The Separation of CC and NC Events in the Sudbury Neutrino Observatory

Jessica A. Dunmore
Hertford College, Oxford

Thesis submitted in partial fulfilment of the requirements
for the degree of Doctor of Philosophy
at the University of Oxford
Hilary Term 2004

The Separation of CC and NC Events in the Sudbury Neutrino Observatory

Jessica A. Dunmore
Hertford College, Oxford

Thesis submitted for the degree of Doctor of Philosophy

Hilary Term 2004

Abstract

The Sudbury Neutrino Observatory (SNO) has shown, by comparing the charged current (CC) and neutral current (NC) neutrino interactions in heavy water, that neutrino flavor conversion is the origin of the "Solar Neutrino Problem." The flavor conversion is well described by the MSW effect which results in an energy-dependent suppression of the solar neutrino flux.

Measuring this suppression without making assumptions about the shape of the ^{8}B solar neutrino energy spectrum requires a technique of separating CC and NC events independent of their energy. The addition of salt to the heavy water of SNO changes the topology of the NC event signal, allowing for statistical separation of CC and NC events.

Different parameterizations of the event topology (or isotropy) are discussed and the parameter yielding the highest separation power between CC and NC events is used in the analysis of data from the salted D_2O phase of SNO. This parameter, β_{14}, utilizes Legendre polynomials to describe the event light distribution.

A correction had to be made to the standard EGS4 package which models electron transport to obtain simulation of events with isotropy parameter values consistent with data. The correction primarily accounts for the missing Mott terms in the electron multiple scattering cross section. The calculation and implementation of this correction are described.

The systematic uncertainty of the isotropy parameterization is determined using various calibration sources. The values presented were used in the published SNO salt data set results [1]. The isotropy values are then calibrated in the Monte Carlo to reduce the systematic uncertainty. The energy dependence of event isotropy is studied and accounted for in the statistical separation. Using maximum likelihood, these calibrated energy-dependent β_{14} distributions yield the following fluxes (in units of 10^6 cm^{-2}s^{-1}):

$$\phi_{\nu_e} = 1.65 \pm 0.06(\text{stat.}) \pm 0.06(\text{syst.})$$
$$\phi_{\nu_{e,\mu,\tau}} = 5.21^{+0.23}_{-0.22}(\text{stat.}) \pm 0.36(\text{syst.}).$$

The calibration of β_{14} results in lower systematic uncertainties than in published SNO results [1]: from 7.2% to 6.7% on the NC flux and from 4.2% to 3.6% on the CC flux.

To my parents....

Acknowledgments

Firstly I must thank **Nick Jelley** who has been an exceptionally supportive supervisor and it has been an absolute pleasure working with him. **Nick** is both professionally and personally a very admirable person.

I am very grateful to **Jeanne Wilson** for the use of her signal extraction code and also for being a great friend. **Charlotte Sims** has also been a great friend and the two of them have made work seem less like work, whether in Oxford, Sudbury, or away at "conferences." Thanks very much to the rest of the Oxford SNO group (**Steve Biller**, **Simon Peeters**, **James Loach**, and **Hok Wan Chan Tseung**) for all of their help and for creating such a friendly and supportive working environment. I will very much miss having two tea breaks a day in the Denys Wilkinson Building with the SNO group and other particle physics graduate students. **Keith Hamilton** and **Thilo Pauly**, especially, have made tea breaks, Thursday pub nights, and summer school much more interesting.

Thanks also to the rest of the **SNO collaboration**. I have received a large amount of help from many people, especially **Kevin Graham**, **Mark Boulay**, and **Neil McCauley**. I'd like to thank **Chris Kyba** for being a good friend and for always being in Sudbury. Thanks to the rest of the **Penn group**, especially **Gene Beier**, for always being welcoming hosts in Philadelphia.

I would like to gratefully acknowledge the financial support of the John G. Martin fellowship, the University of Hartford, the University of Oxford Physics Department, and Hertford College. Thanks especially to **Charles Condon** and **Laurence Gould** and to my college supervisors, **Robin Devenish** and **Pat Roche**.

Thank you to all of my very supportive family and friends, particularly **Nick Melin** for an enormous amount of encouragement and many late night phone calls. Finally, thank you to my parents, **Karen Dunmore**, **Thomas Dunmore**, and **Barbara Urban** for all of their love and support.

Contents

List of Figures

List of Tables

Acronyms

ADC Analog to Digital Converter

AV Acrylic Vessel

CC Charged Current (ν interaction)

CFRIP Correlation Function Ring Inner Product

CL Confidence Level

CPT Charge-Parity-Time

CTC Crate Trigger Card

DAQ Data Acquisition

EGS Electron Gamma Shower code

ES neutrino-electron Elastic Scattering

eCPU embedded CPU

FEC Front End Card

FWHM Full Width at Half Maximum

GTID Global Trigger Identification Number

HV High Voltage

INCO International Nickel COmpany

ITR In-Time Ratio

LMA Large Mixing Angle (MSW solution)

MCPROD Monte Carlo (and data) Production group

MINUIT A standard minimization package

MNS Maki-Nakagawa-Sakata

MSW Mikheyev, Smirnov, and Wolfenstein

MTC/A Master Trigger Card / Analog

MTC/D Master Trigger Card / Digital

NC Neutral Current (ν interaction)

N$_{hit}$ Number of PMT hits in an event

OWL OutWard Looking photomultiplier tube

PE Photo-electron

PDF Probability Density Function

PMT Photomultiplier Tube

PMTIC Photomultiplier Tube Interface Card

PSUP Photomultiplier Support Structure

QHL Q=charge, H=high gain, L=long integration time

QHS Q=charge, H=high gain, S=short integration time

QLL Q=charge, L=low gain, L=long integration time

RMS Root Mean Square

SNO Sudbury Neutrino Observatory

SSM Standard Solar Model

TOF Time-of-flight

UV Ultraviolet

V-A Vector minus Axial

ZDAB ZEBRA Data Acquisition/Analysis Bank

ZEBRA Data management library for FORTRAN

Chapter 1

Neutrino Physics and Astrophysics

1.1 The Neutrino

The neutrino was first postulated by Wolfgang Pauli in 1930 to account for the apparent missing energy and momentum in nuclear β-decay experiments [2]. Adding an antineutrino to the β-decay interactions,

$$(N, Z) \rightarrow (N-1, Z+1) + e^- + \bar{\nu}_e,$$

means that the antineutrino would carry away some of the energy, rather than the emitted electron always carrying energy equal to the reaction Q-value. A few years later, Enrico Fermi formulated a relativistic quantum field theory which described the (weak) interactions involved in β-decay. This theory is analogous to Dirac's theory of quantum electrodynamics and accounted remarkably well for all observed properties of β-decay [3]. An experiment by Wu in 1956 found that the neutrino violates parity maximally as it exists only in a left-handed state [4]. A theory of a weak interaction which acts only on negative helicity particles (V-A theory) was proposed by Gell-Mann and Feynman shortly thereafter [5]. The V-A (vector minus axial) operator of the weak interaction projects only the left-handed component of a particle's wavefunction. In the Standard Model of Particle Physics, the neutrino is presumed to be massless in order to explain its left-handedness in any given frame of reference.

The neutrino was first detected in 1956 by Frederick Reines and collaborators. Antineutrinos from nuclear fission reactors were detected through the process of inverse β-decay:

$$\bar{\nu}_e + p \rightarrow n + e^+.$$

The target was a tank of liquid scintillator and light from the delayed-coincidence signal of the n and e^+ was seen using photomultiplier tubes [6]. For the detection of the neutrino, Reines was awarded the 1995 Nobel Prize in Physics. More sensitive neutrino detectors using the same detection principle have since been developed and are running today [7, 8].

1.2 The Standard Model of Particle Physics

The Standard Model of Particle Physics attempts to describe the basic fundamental particles that exist in the universe and the physics of the interactions between them. There are three forces existing in the Standard Model: electromagnetism, the strong force, and the weak force. The gravitational force, which exists between all particles that have mass, is not yet included in the Standard Model framework. The electromagnetic force exists between particles or fields that have charge or magnetic moments, and the particle that mediates this force is the photon (γ). The strong force exists between particles that have color (quarks) and the mediating particle is the massless gluon (g). This force is responsible for binding the quarks into hadrons and into neutrons and protons within nuclei. The weak force involves the exchange of weak gauge bosons, $W^{\pm}$ and Z^0, and is responsible for nuclear β-decay. The weak interaction is called "weak" because the strength of an interaction at low energies[1] is inversely dependent on the square of the mass of its mediating particle and the weak gauge bosons are very heavy. Refer to Table 1.1 for a summary of these forces.

The Standard Model contains two types of fermionic (spin-1/2) elementary particles: leptons and quarks. The leptons consist of the electron (e^-), muon (μ^-), tau (τ^-), electron neutrino (ν_e), muon neutrino (ν_μ), and tau neutrino (ν_τ). There are six quarks: up, down, strange, charm, top, and bottom (u, d, s, c, t, and b). All have corresponding antiparticles. Properties of these particles are found in Table 1.1. The leptons and quarks are divided into 3 generations according to mass. The first generation contains (u d) and (e ν_e) and these are the only stable particles that constitute matter in the present day universe. The second (c s), (μ ν_μ) and third (b t), (τ ν_τ) generations are created in high energy processes and decay into the first generation particles (with the exception of ν_μ and ν_τ which do not appear to decay). The number of light ($m_\nu < M_Z/2$) neutrino types, or *flavors*, is limited to 3 by observation of the Z^0 boson decay width.

The Standard Model has proved successful in describing interactions between these particles in most experimental tests. The first evidence of deviation from the Standard Model has come from the detection of solar and atmospheric neutrinos.

[1] This is a good approximation for momentum transfer q^2 much less than the mass of the mediating particle M^2. The coupling is actually given as $\propto (q^2 + M^2)^{-1}$.

Standard Model Forces and Mediating Bosons

Force	Mediator	Mediator Mass	Relative Strength[a]
Strong	gluon g	0	1
Electromagnetism	photon γ	0	10^{-2}
Weak	gauge bosons $W^{\pm},\ Z^0$	80.4, 91.2 GeV	10^{-6}

[a]For energies much less than the gauge boson masses.

Fermionic Elementary Particles

		First Generation	Second Generation	Third Generation
Leptons	Particle	electron e	muon μ	tau τ
	Charge	-1	-1	-1
	Mass	0.511 MeV	106 MeV	1,777 MeV
	Particle	electron neutrino ν_e	muon neutrino ν_μ	tau neutrino ν_τ
	Charge	0	0	0
	Mass	<3 eV	<0.19 MeV	<18.2 MeV
Quarks	Particle	up u	charm c	top t
	Charge	+2/3	+2/3	+2/3
	Mass	∼3 MeV	∼1,200 MeV	∼175,000 MeV
	Particle	down d	strange s	bottom b
	Charge	-1/3	-1/3	-1/3
	Mass	∼20 MeV	∼150 MeV	∼4,500 MeV

Table 1.1: Summary of Standard Model particles [9, 10].

1.3 The Solar Neutrino Problem

Experiments devised to detect electron-type neutrinos emitted from the Sun and arriving at the Earth found fewer than expected from solar model calculations. The discrepancy between theoretical calculations and the measured flux became known as the *Solar Neutrino Problem*. It took a long time and a lot of experimental data before it was realized that this problem was due to a misunderstanding of particle physics and not of the modeling of how the Sun produces energy.

1.4 Solar Physics

The theoretical calculation of the flux of solar neutrinos expected at Earth comes from the *Standard Solar Model*[2]. This chapter will describe why the calculated solar neutrino flux is trusted and why it is now believed that the cause of the experimental discrepancy is due to neutrino properties not included in the Standard Model of Particle Physics.

1.4.1 Solar Observables

Solar observables include mass ($M_\odot$), photon luminosity ($L_\odot$), radius ($R_\odot$), age, metal content, and helioseismic data. These observables must be used as inputs into solar models. When modeling how the Sun works, it is very important that the model reproduces these observables. The solar luminosity and central temperature, $(T_c)_\odot$, of the Sun put strong constraints on the solar neutrino flux.

Observable	Value	Observable	Value
$L_\odot$	3.9×10^{26} Js^{-1}	$R_\odot$	7.0×10^{8} m
$M_\odot$	2.0×10^{30} kg	$(T_c)_\odot$	2×10^{7} K

One of the other pieces of astronomical data that significantly constrains the flux of neutrinos comes from helioseismology [11]. The solar surface vibrates with a period of T = 5 min. By studying how the solar surface vibrates, we can infer properties of the solar interior. These vibrations create a "sound" (if amplified by a factor of around 1 million these vibrations would be heard!). The sound speed is dependent on solar temperature and the present He abundance. Helioseismic observations put limits on the temperature profile of the Sun and, consequently, the emitted neutrino fluxes. The fractional difference between the measured and predicted sound speeds is shown in Figure 1.1. If the Standard Solar Model were altered to agree to within 1σ of the neutrino fluxes measured in early solar neutrino experiments, the sound speed prediction would lie more than 8% away from measurements (this is labelled on the plot with an arrow), yet there is less than 0.5% disagreement between the Standard Solar Model prediction and the measurements.

1.4.2 Nuclear Astrophysics

In the nineteenth century, the conversion of gravitational energy into heat was thought to be the sole source of solar luminosity. An estimation for the lifetime of the Sun may

[2] There are a number of solar models; however they are all based on the same underlying principles and thus produce similar results for solar neutrino fluxes.

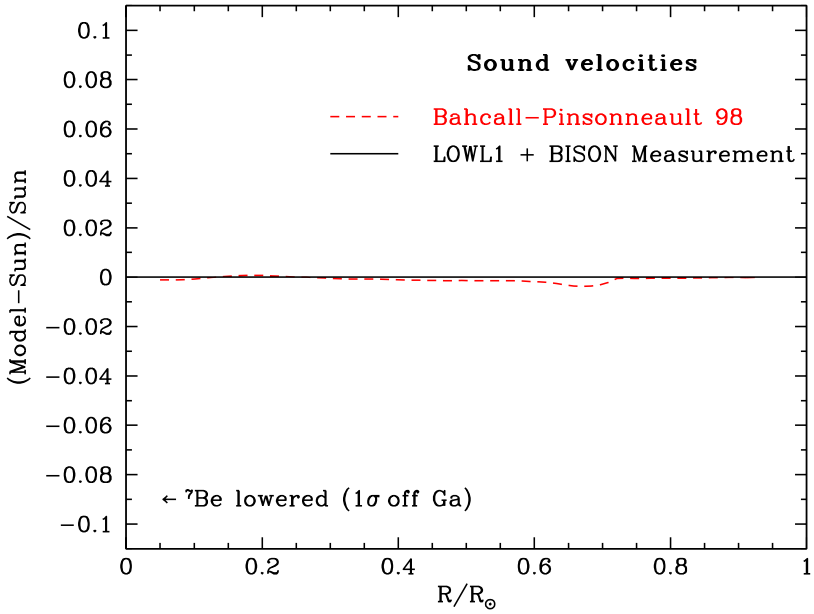

Figure 1.1: The agreement between calculated and measured sound speed in the Sun. Figure from [11].

be obtained using the ratio of gravitational energy to total luminosity[3]:

$$t_{\mathrm{G}} \approx \frac{GM_{\odot}^{2}}{R_{\odot}L_{\odot}} \approx 10^{7}\mathrm{yr}. \tag{1.1}$$

However, terrestrial rocks and fossils suggest that the solar system was formed and the Sun began to shine about 4.5 billion years ago [12]. In order for the Sun to sustain itself for this amount of time, it would need an additional source of energy. At the turn of the century, nuclear radioactivity was discovered and immediately proposed as another source of solar energy. It was later realized that it is not nuclear radioactivity, but *fusion* that produces this energy.

The Sun is a Main Sequence star in a stage of hydrogen burning and produces a flux of electron neutrinos through chains of nuclear fusion. In the pp-chain, protons fuse together to create helium though the reaction

$$4p \rightarrow {}^{4}\mathrm{He} + 2e^{+} + 2\nu_{e} + 26.731\ \mathrm{MeV}.$$

Higher elements are subsequently "burned" through a chain of fusion reactions found in Figure 1.2. A few comments will be made about the neutrino-producing reactions in this chain.

[3] $G = 6.673 \times 10^{-11}\mathrm{m}^{3}\mathrm{kg}^{-1}\mathrm{s}^{-2}$ is the Newtonian gravitational constant.

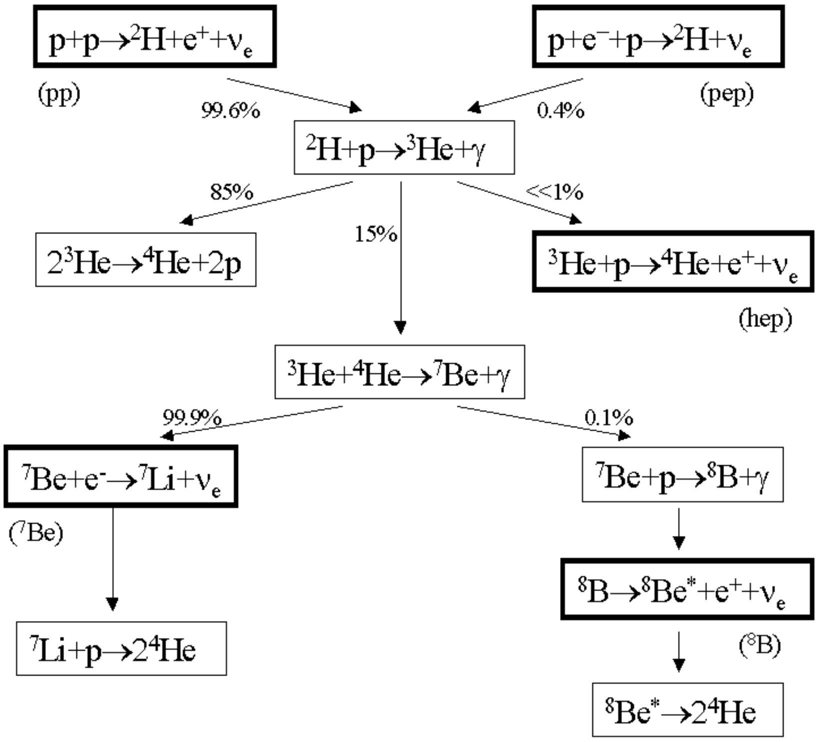

Figure 1.2: The pp-chain.

(pp) $p + p \rightarrow {}^2\mathrm{H} + e^+ + \nu_e$ **and (pep)** $p + e^- + p \rightarrow {}^2\mathrm{H} + \nu_e$

These reactions are calculated accurately using low-energy weak interaction theory and measured properties of proton-proton scattering [12]. It is within the *pp* reaction that the majority of solar neutrinos are produced. *pp* neutrinos have energy $E_\nu \leq 0.42$ MeV and *pep* neutrinos have a monoenergetic energy of 1.44 MeV.

(hep) ${}^3\mathrm{He} + p \rightarrow {}^4\mathrm{He} + e^+ + \nu_e$

The approximate branching fractions of particular channels are determined by the typical cross sections of the type of interaction. Cross sections of electromagnetic interactions are on order of 10^{-3} mb, while weak interactions have cross sections on the order of 10^{-11} mb [10], which is why the *hep* branch occurs much less frequently than ^{3}He+^{3}He or ^{3}He+^{4}He. The neutrinos from this interaction are very energetic (up to 18.77 MeV), but the flux is very low.

(^{7}Be) ${}^7\mathrm{Be} + e^- \rightarrow {}^7\mathrm{Li} + \nu_e$

The rate from this reaction is well known and is calculated easily using weak interaction theory. There are two lines in the ^{7}Be solar neutrino energy spectrum because ^{7}Be can decay to both the ground state and to an excited state of ^{7}Li.

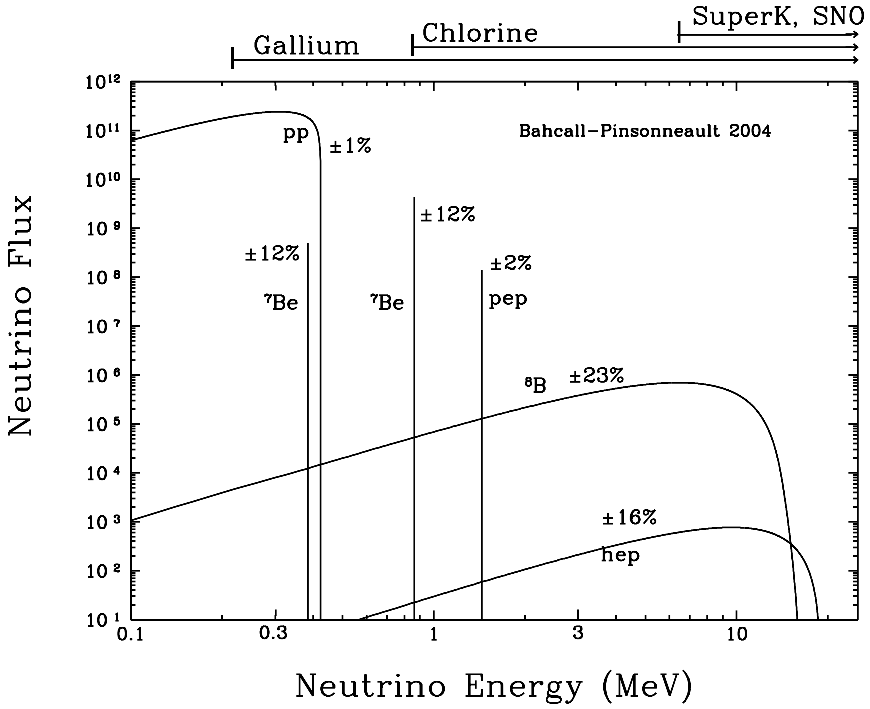

Figure 1.3: Energy dependence of solar neutrino fluxes.

(^{8}B) $^8\mathrm{B} \rightarrow\ ^8\mathrm{Be}^* + e^+ + \nu_e$

The ^{7}Be+p reaction occurs about 1 time in every 5000 terminations of the pp-chain. The subsequent ^{8}B decay can produce neutrinos up to about 15 MeV. The flux of neutrinos from this reaction has the largest uncertainty in the pp-chain as it varies with the 25^{th} power of the core temperature of the Sun. Thus a small change in the core temperature in a solar model results in a large change of this flux. Although the flux of neutrinos produced through this reaction is much lower than that produced by the *pp* reaction, the higher energy of these neutrinos offers more possibility for detection. This was first realized in 1962 by Raymond Davis who has received the 2002 Nobel Prize in physics for his pioneering work on detecting solar neutrinos, along with Masatoshi Koshiba for the detection of neutrinos from Supernova 1987A.

The fluxes of *pp*, *pep*, ^{7}Be, ^{8}B, and *hep* neutrinos are found in Figure 1.3. The approximate energy thresholds of different types of experiments are indicated at the top of the graph to show which solar neutrinos they are capable of detecting.

Solar neutrinos are also emitted in the CNO (carbon-nitrogen-oxygen) cycle. Neutrinos from the reactions in this cycle have energy less than 2 MeV. The total flux is comparable to the *pep* flux, but very small compared to ^{7}Be and *pp* fluxes.

1.4.3 Standard Solar Model ν Flux

The most current calculation of solar neutrino fluxes is from the 2004 Bahcall-Pinsonneault (BP04) solar model [13]. The predicted total flux of ^{8}B solar neutrinos (which are detectable by water Čerenkov detectors such as SNO) is

$$\phi(^8\mathrm{B}) = 5.82 \times (1 \pm 0.23) \times 10^6 \mathrm{cm}^{-2}\mathrm{s}^{-1}. \tag{1.2}$$

The factors contributing most to the uncertainty are[4]

1. the uncertainty on the ^{3}He(^{4}He,γ)^{7}Be cross section (8%) and

2. the uncertainty on the surface heavy element abundances (20%).

Where possible, measured flux results presented in this thesis will be compared to this model; however, many experimental results presented in this chapter are compared to earlier models, BP00[14] or BPB01[15]. Other solar neutrino fluxes may be found in [13].

1.5 Pioneering Solar Neutrino Experiments

The first experiments designed to detect solar neutrinos were radiochemical. In these experiments, radioactive nuclei build up in a target which is exposed for a time commensurate with the half-life of that nucleus. These nuclei are chemically extracted and counted by observing their decay.

Large water Čerenkov experiments were originally designed to search for proton decay. These were later upgraded to detect ^{8}B solar neutrinos.

1.5.1 Chlorine

The Homestake experiment, constructed by Raymond Davis and collaborators, was located 4850 feet underground in the Homestake Gold Mine in South Dakota. This radiochemical experiment used 615 gallons of C_2Cl_4 (a common dry-cleaning fluid) to detect electron-type neutrinos through the interaction

$$\nu_e + {}^{37}\mathrm{Cl} \rightarrow {}^{37}\mathrm{Ar} + e^-.$$

This reaction has a threshold of 814 keV, so it is sensitive to *pep*, ^{7}Be, ^{8}B, *hep*, and CNO solar neutrinos. However, the higher energy ^{8}B neutrinos dominate because of the presence of a 4.98 MeV excited state of ^{37}Ar which has a large cross section since it is the isobaric analogue to ^{37}Cl. The ^{37}Ar decays through electron capture back to ^{37}Cl with a

[4]Previously, the the measured ^{7}Be+p cross section gave the dominant uncertainty on the ^{8}B neutrino flux. This cross section is now well determined [13].

half-life of 35 days. Helium gas was bubbled through the tank to extract the argon, so that the X-rays or Auger electrons[5] emitted from the ^{37}Ar decay could be detected in a proportional counter.

The first results were announced in 1968 and the number of ^{37}Ar decays observed was significantly lower than what was expected from the Standard Solar Model. Almost 30 years of data were collected and the number of neutrinos observed equaled (0.34±0.03) times the expected electron neutrino flux predicted by the 2000 Bahcall-Pinsonneault standard solar model (BP00) [16, 14].

1.5.2 Gallium

The gallium radiochemical experiments, SAGE (Soviet American Gallium Experiment) and GALLEX (GALLium EXperiment) detected electron neutrinos through the interaction

$$\nu_e + {}^{71}\mathrm{Ga} \rightarrow {}^{71}\mathrm{Ge} + e^-.$$

This interaction has a threshold of 233 keV, so it is possible to detect *pp*, ^{7}Be, ^{8}B, *hep*, and CNO solar neutrinos. The ^{71}Ge nuclei decay solely by electron capture with a half-life of 11.4 days. The Ge was extracted about every 30 days and observed for 6 months to count the X-rays and Auger electrons emitted in the decays.

GNO (Gallium Neutrino Observatory) is an upgrade to GALLEX with improved systematic uncertainty and is still taking data. Combined SAGE, GALLEX, and GNO measurements have found 0.55±0.03 of the expected neutrino flux.

1.5.3 Water Čerenkov

Kamiokande

The Kamiokande (for Kamioka Nucleon Decay Experiment) detector was initially built to search for proton decay. It consisted of a large cylindrical tank filled with 2140 tonnes of water, surrounded by almost 1000 20-inch photomultiplier tubes (PMTs). Kamiokande was upgraded in 1985 (becoming Kamiokande II) to detect neutrinos through elastic scattering on electrons

$$\nu_x + e^- \rightarrow \nu_x + e^-.$$

In this reaction, relativistic electrons are created and the Čerenkov radiation that they emit (see Section 2.1) is detected by the PMTs. This experiment was sensitive to all flavors of neutrinos, $x = e, \mu, \tau$, but the sensitivity to ν_e is about six times greater than to $\nu_{\mu,\tau}$. The direction of the resultant electron is strongly peaked in the forward direction

[5] An Auger electron is created when the ^{37}Ar nucleus captures an electron from its K shell. The hole in the K shell is filled by an electron in an outer (e.g. L_1) shell and the extra energy is transfered to an $L_{2,3}$ electron which is ejected from the atom.

of the incoming neutrino. Only ^{8}B neutrinos were detectable with the Kamiokande II energy threshold and about one half of the predicted flux was observed.

Super-K

A larger and improved version of Kamiokande, named Super-K (for Super-Kamiokande), became operational in 1996. In a 1496-day data set with a total energy range of 5–20 MeV, 22,400 solar neutrinos were observed, consistent with a fit to $\cos\theta_\odot$, which is the angle of the fit event with respect to the Sun, while 48,200 were expected.

Experiment	Energy Threshold	Measured/SSM	Reference
Homestake	0.814 MeV	0.34 ± 0.03	[17]
SAGE+GALLEX/GNO	0.233 MeV	0.55 ± 0.03	[17]
Super-K	5–20 MeV	0.47 ± 0.02	[17]

Table 1.2: Pre-SNO solar neutrino data.

1.6 Solar Neutrino Oscillations

A particle physics solution to the Solar Neutrino Problem is possible if the electron type neutrinos produced in the Sun are able to transform into non-electron types of neutrinos[6]. Neutrino *flavor* states ($\nu_l = \nu_e, \nu_\mu, \nu_\tau$) are states which correspond to the charged leptons, e, μ, and τ. Each neutrino flavor state is able to interact with its corresponding lepton, forming the charged currents. The neutrino *mass* states (ν_1, ν_2, ν_3) correspond to states with masses m_1, m_2, and m_3. Neutrino mixing may occur if the flavor states do not match the mass eigenstates. The flavor states are, instead, linear combinations of the mass eigenstates in which

$$|\nu_l\rangle = U_{MNS}\ |\nu_i\rangle, \quad \text{where } l = e, \mu, \tau, \quad i = 1, 2, 3, \tag{1.3}$$

where the mixing parameters U_{MNS} form the MNS (for Maki-Nakagawa-Sakata) matrix

$$U_{MNS} = \begin{pmatrix} U_{e1} & U_{e2} & U_{e3} \\ U_{\mu 1} & U_{\mu 2} & U_{\mu 3} \\ U_{\tau 1} & U_{\tau 2} & U_{\tau 3} \end{pmatrix}. \tag{1.4}$$

1.6.1 Two Neutrino Mixing in a Vacuum

Because U_{e3} is close to zero, solar neutrino oscillations may be very well approximated by two neutrino mixing, $\nu_e \leftrightarrow \nu_\alpha$, where ν_α is a non-electron flavor neutrino state. In

[6] Neutrino mixing and oscillations were first proposed by B. Pontecorvo in 1957 [18].

this case,

$$U_v = \begin{pmatrix} \cos\theta_v & \sin\theta_v \\ -\sin\theta_v & \cos\theta_v \end{pmatrix}. \tag{1.5}$$

This gives

$$\begin{aligned} |\nu_e\rangle &= \cos\theta_v \; |\nu_{1v}\rangle + \sin\theta_v \; |\nu_{2v}\rangle, \\ |\nu_\alpha\rangle &= -\sin\theta_v \; |\nu_{1v}\rangle + \cos\theta_v \; |\nu_{2v}\rangle. \end{aligned} \tag{1.6}$$

Here, θ_v is the vacuum mixing angle and the subscript $_v$ on the mass states indicates eigenstates in a vacuum. From (1.6) we also have

$$\begin{aligned} |\nu_{1v}\rangle &= \cos\theta_v \; |\nu_e\rangle - \sin\theta_v \; |\nu_\alpha\rangle, \\ |\nu_{2v}\rangle &= \sin\theta_v \; |\nu_e\rangle + \cos\theta_v \; |\nu_\alpha\rangle. \end{aligned} \tag{1.7}$$

The flavor eigenstates are eigenstates of the weak interaction Hamiltonian. The vacuum mass eigenstates are eigenstates of the Hamiltonian for vacuum propagation and must satisfy the Schrödinger Equation

$$i \, \frac{d}{dt} \begin{pmatrix} |\nu_{1v}\rangle \\ |\nu_{2v}\rangle \end{pmatrix} = \begin{pmatrix} E_1 & 0 \\ 0 & E_2 \end{pmatrix} \begin{pmatrix} |\nu_{1v}\rangle \\ |\nu_{2v}\rangle \end{pmatrix}. \tag{1.8}$$

The solution to this wave equation is

$$\begin{aligned} |\nu_{1v}(t)\rangle &= e^{(-iE_1 t)} \; |\nu_{1v}(0)\rangle, \\ |\nu_{2v}(t)\rangle &= e^{(-iE_2 t)} \; |\nu_{2v}(0)\rangle. \end{aligned} \tag{1.9}$$

Neutrinos are produced and detected as flavor states, but propagate as states with definite mass.

Survival Probability

The two mass eigenstates are assumed to have equal momentum[7], p. If $m_1 \neq m_2$, then the two vacuum mass eigenstates will propagate with different energies. This means that a neutrino created as ν_e at time $t = 0$ will have different components of ν_{1v} and ν_{2v} when it is detected at some time t, and therefore, some non-zero probability of being detected as ν_α. The probability of the neutrino being detected at t as ν_e is given by $P(\nu_e \to \nu_e) = |\langle \nu_e | \nu_e(t) \rangle|^2$. Combining (1.6) and (1.9) we have

$$\begin{aligned} |\nu_e(t)\rangle &= \cos\theta_v \exp(-iE_1 t)|\nu_{1v}\rangle + \sin\theta_v \exp(-iE_2 t)|\nu_{2v}\rangle \\ &= e^{-iE_1 t} \left(\cos\theta_v |\nu_{1v}\rangle + \sin\theta_v \exp(i\Delta m^2 t/2E_\nu)|\nu_{2v}\rangle \right), \end{aligned} \tag{1.10}$$

[7] A more sophisticated treatment involving wavepackets is given by Kayser [19].

where

$$E_1 - E_2 \approx \frac{m_1^2 - m_2^2}{2p} \approx \frac{m_1^2 - m_2^2}{2E_\nu} \equiv \frac{\Delta m^2}{2E_\nu} \quad (\text{for } p \approx E_\nu >> m_1, m_2). \tag{1.11}$$

Using the above relations and the orthonormality relation $\langle \nu_i | \nu_j \rangle = \delta_{ij}$, the ν_e survival probability may be derived:

$$\begin{aligned}
P(\nu_e \to \nu_e) &= |\cos\theta_v \langle \nu_e | \nu_{1v} \rangle + \sin\theta_v \langle \nu_e | \nu_{2v} \rangle \; e^{i\Delta m^2 t/2E_\nu}|^2 \\
&= |\cos^2\theta_v + \sin^2\theta_v \; e^{i\Delta m^2 t/2E_\nu}|^2 \\
&= \cos^4\theta_v + \sin^4\theta_v + \cos^2\theta_v \sin^2\theta_v \; (e^{i\Delta m^2 t/2E_\nu} + e^{-i\Delta m^2 t/2E_\nu}) \\
&= 1 - 2\cos^2\theta_v \sin^2\theta_v + 2\cos^2\theta_v \sin^2\theta_v \cos\left(\frac{\Delta m^2 L}{2E_\nu}\right) \\
&= 1 - 4\cos^2\theta_v \sin^2\theta_v \sin^2\left(\frac{\Delta m^2 L}{4E_\nu}\right) \\
&= 1 - \sin^2 2\theta_v \sin^2\left(\frac{\Delta m^2 L}{4E_\nu}\right) \\
&= 1 - P(\nu_e \to \nu_\alpha),
\end{aligned} \tag{1.12}$$

where the identities $\cos x = \frac{1}{2}(e^{ix} + e^{-ix})$, $\sin^2\theta = \frac{1}{2}(1 - \cos 2\theta)$ and $\cos^2\theta = \frac{1}{2}(1 + \cos 2\theta)$ have been used and t has been replaced with L, the distance from the source of the ν_e's, since the neutrinos are moving very close to the speed of light.

Oscillation Length

Because of the term $\sin^2\left(\frac{\Delta m^2 L}{4E_\nu}\right) = \sin^2 \pi \frac{L}{L_v}$ in (1.12), the survival probability oscillates with distance from the source. The *vacuum oscillation length* is defined as

$$L_v = \frac{4\pi E_\nu}{\Delta m^2}. \tag{1.13}$$

This is the distance traveled by a neutrino before it returns to its initial ν_e state. The mixing angle $\sin^2 2\theta_v$ determines the amplitude of the oscillation while Δm^2 affects the oscillation length.

Neutrinos from an Extended Source

For an extended source such as the Sun, where electron neutrinos are created over large distances, the average survival probability is given by

$$P(\nu_e \to \nu_e)_{\text{avg}} = 1 - \frac{1}{2}\sin^2 2\theta_v, \tag{1.14}$$

since the average of $\sin^2\left(\frac{\Delta m^2 L}{4E_\nu}\right)$ is 1/2. This probability is never less than one half. So, vacuum oscillations cannot account for the larger discrepancies seen by solar neutrino experiments (found in Table 1.2).

1.6.2 Matter Effects

When traveling through matter, neutrino propagation is affected by its interactions with that matter. At low energies, only coherent elastic forward scattering is relevant, and is described by the potentials V_e and V_α. There is a difference between these two potentials because matter is composed of electrons and not muons or taus, and thus, ν_e's may interact via neutral current *and* charged current scattering ($\nu_e e^- \rightarrow \nu_e e^-$) while ν_α's may interact via neutral currents only. This potential difference is given by the *matter oscillation term*

$$V = V_e - V_\alpha = \sqrt{2} G_F n_e, \tag{1.15}$$

where G_F is the Fermi coupling constant and n_e is the number density of electrons. The potential difference leads to an additional phase difference with time, t, in the neutrino oscillation system: $\Delta\phi_{matter} = Vt$. The *refraction length*, at which the additional matter phase equals 2π is given by

$$L_m = \frac{2\pi}{V} = \frac{\sqrt{2}\pi}{G_F n_e}. \tag{1.16}$$

The additional term in the electron neutrino phase causes the relative phase between the ν_e and ν_α states to change with distance. The interference between the two states may be totally destructive, totally constructive, or somewhere in between.

In the presence of matter, the Hamiltonian is changed:

$$\mathcal{H}_0 \rightarrow \mathcal{H} = \mathcal{H}_0 + V, \tag{1.17}$$

where $\mathcal{H}_0$ is the Hamiltonian in vacuum. The diagonalization of $\mathcal{H}$ leads to a new form for the ν_e survival probability (in the case of constant electron density) [20, 21, 22]

$$P_{\mathrm{MSW}}(\nu_e \rightarrow \nu_e) = 1 - \sin^2 2\theta_m \sin^2\left(\frac{\pi L D_m}{L_v}\right), \tag{1.18}$$

where

$$\sin^2 2\theta_m = \frac{\sin^2 2\theta_v}{D_m^2},$$

$$D_m^2 = \sin^2 2\theta_v + (L_v/L_m - \cos 2\theta_v)^2,$$

$$\frac{L_v}{L_m} = \frac{2\sqrt{2} G_F n_e E_\nu}{\Delta m^2}.$$

The mixing parameter $\sin^2 2\theta_m$ is dependent on the ratio of the oscillation and refraction lengths (i.e. the ratio of vacuum to matter effects), L_v/L_m, and thus, is dependent on matter density and neutrino energy.

Resonance

A resonance occurs for $L_v/L_m = \cos 2\theta_v$ at which point the mixing becomes maximal ($\sin^2 2\theta_m = 1$). In the varying density of the Sun, there exists a layer at which this resonance occurs. As neutrinos travel through the Sun, it is within this resonance layer that flavor transition mainly occurs [23]. The resonance amplitude is independent of the vacuum mixing angle, θ_v, so a neutrino will have a very high probability of transforming into another flavor of neutrino even if the *in vacuo* probability for doing so is very small.

Adiabacity

In matter with varying density, $n_e = n_e(t)$, the mixing angle changes over the course of neutrino propagation. If the density changes slowly enough (this is the *adiabacity condition*) the transitions $\nu_{1m} \nleftrightarrow \nu_{2m}$ may be neglected and ν_{1m} and ν_{2m} propagate independently. Because the mixing angle is dependent on electron density, the flavor admixtures of ν_{1m} and ν_{2m} will vary with changing density. In the high density of the Sun, neutrinos with flavor state $|\nu_e\rangle$ are created. Here $|\nu_e\rangle$ is approximately the same as the heavier mass eigenstate $|\nu_{2m}\rangle$ because $\sin\theta_m$ is high. As the neutrino travels out of the Sun, the density slowly decreases and the flavor state remains close to $|\nu_{2m}\rangle$. When the neutrino emerges from the Sun into what is almost a vacuum, the neutrino is close to the vacuum eigenstate $|\nu_{2v}\rangle$, which is close to $|\nu_\alpha\rangle$ [24]. Hence, the electron neutrinos are converted to another flavor. This transition is shown in Figure 1.4 (where ν_α is labeled ν_x). The transformation of one neutrino flavor to another within a medium of varying density is the MSW effect (for Mikheyev-Smirnov-Wolfenstein) [20]. With this effect, an *energy-dependent* suppression of the solar neutrino flux is possible.

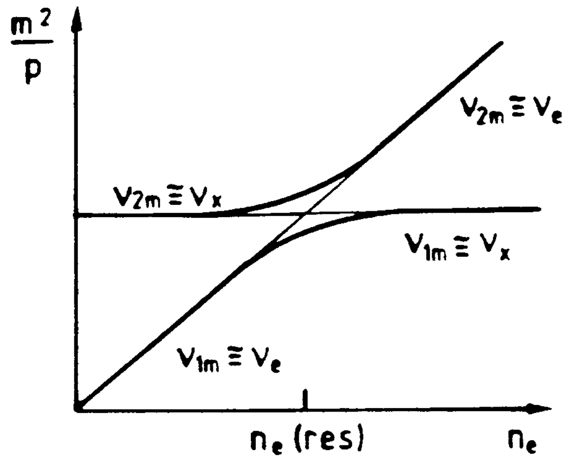

Figure 1.4: Flavor change for a electron neutrino traveling in a medium with varying electron density n_e [12].

1.7 Results from the Sudbury Neutrino Observatory

The first solar neutrino detectors were built to "enable us to see into the interior of a star and thus verify directly the hypothesis of nuclear energy generation in stars" [25]. The Sudbury Neutrino Observatory (SNO) was built to test the hypothesis that electron neutrinos produced in the Sun experience flavor transformation by detecting not only the flux of electron-type neutrinos arriving at the Earth, but also the *total* flux of all active[8] neutrinos arriving at the Earth. This is feasible by detecting neutrino interactions in heavy water (D_2O). SNO observes ^{8}B solar neutrinos through three processes[9]:

1. The charged current (CC) interaction which provides a measure of the number of electron-type solar neutrinos only.
2. The neutral current (NC) interaction which yields a measure of the total ^{8}B solar neutrino flux, regardless of flavor.
3. The elastic scattering (ES) interaction which measures all three flavors of active neutrinos, but is more sensitive to electron flavor neutrinos.

SNO is the first detector able to observe $\nu_{\mu,\tau}$ *appearance* through the comparison of these three measurements. In particular, if the neutrino flux inferred from the NC measurement differs from that inferred from the CC measurement, there is evidence that there exists a $\nu_{\mu,\tau}$ component of the solar neutrino flux.

In 2002, after 306.4 days of live-time acquired within about 3 years of operation, SNO released results of its pure D_2O phase. The number of events found and the inferred ^{8}B neutrino fluxes are given in Table 1.3 for each of the three measurements [26]. A kinetic energy threshold of 5 MeV is used; however, neutrinos with energy greater than 2.22 MeV are capable of creating a signal from the NC interaction. All three signals are observed through Čerenkov light detection and are not distinguishable on an event-by-event basis. Maximum likelihood signal extraction techniques are used to obtain the number of events belonging to each of the three interactions above.

From this information the electron and non-electron flavor components of the solar neutrino flux may be determined:

$$\begin{aligned} \phi_e &= 1.76^{+0.05}_{-0.05}(\text{stat.})^{+0.09}_{-0.09}(\text{syst.}) \times 10^6 \text{ cm}^{-2}\text{s}^{-1} \\ \phi_{\mu\tau} &= 3.41^{+0.45}_{-0.45}(\text{stat.})^{+0.48}_{-0.45}(\text{syst.}) \times 10^6 \text{ cm}^{-2}\text{s}^{-1}. \end{aligned} \tag{1.19}$$

Figure 1.5 shows the flux of non-electron flavor active neutrinos ($\phi_{\mu\tau}$) versus the flux of electron neutrinos (ϕ_e) deduced from the SNO measurements.

[8] *Active* meaning left-handed neutrinos which may experience weak interactions, as opposed to *sterile* right-handed neutrinos which may not be detected because they do not interact with matter. Sterile neutrinos will be briefly discussed in Section 1.12.2.

[9] The SNO detector and its three measurements are described in more detail in Chapter 2.

Signal	Number of Events	^{8}B ν flux ($\times 10^6$ cm^{-2} s^{-1})
CC	$1967.7^{+61.9}_{-60.9}$	$1.76^{+0.11}_{-0.10}$
NC	$576.5^{+26.4}_{-25.6}$	$5.13^{+0.64}_{-0.61}$
ES	$263.6^{+49.5}_{-48.9}$	2.39 ± 0.26

Table 1.3: Summary of the three neutrino measurements made in the pure D_2O phase of SNO. The quoted uncertainties are the statistical and systematic uncertainties added in quadrature.

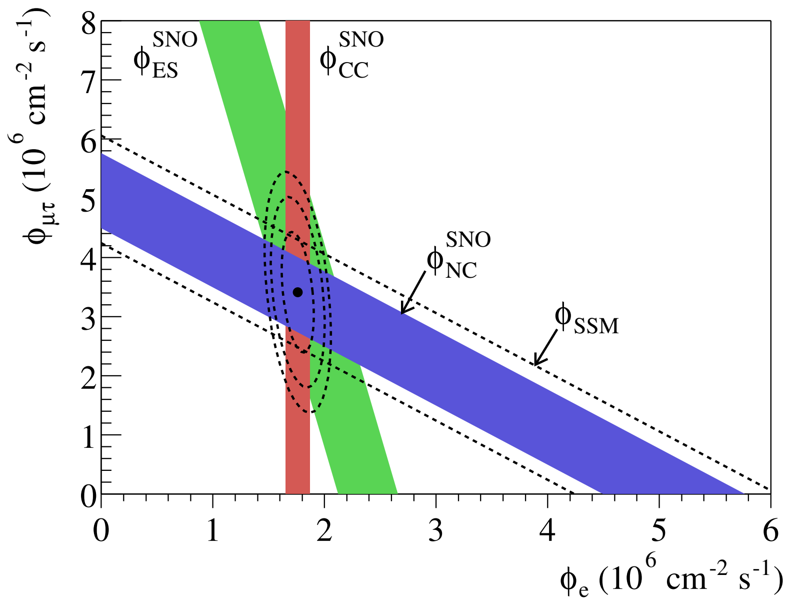

Figure 1.5: Flux of non-electron flavor ($\nu_{\mu,\tau}$) ^{8}B solar neutrinos versus flux of electron flavor neutrinos deduced from the three SNO neutrino measurements [26]. The widths of the bands correspond to $\pm 1\sigma$ errors. The dashed diagonal lines are the predicted flux from the BPB01 Standard Solar Model (SSM) [15].

The MSW oscillation parameters, Δm^2 and $\tan^2\theta_v$[10] are displayed in Figure 1.6. Combined with all other solar neutrino experiments, the SNO data strongly prefer the LMA (large mixing angle) solution to the solar neutrino problem. Data from the salt phase of SNO, which will be presented later in this thesis, has been released and it further reduces the contours in Figure 1.6 to just the LMA region [1].

1.8 Results from KamLAND

KamLAND is a detector located next door to Super-K in the Kamioka Mine, Japan which observes antineutrinos emitted from nuclear reactors [8]. The reactors, which

[10] Here $\Delta m^2 = m_2^2 - m_1^2$. Using $\tan^2\theta_v$ rather than $\sin^2 2\theta_v$ shows if $\theta_v > \pi/4$ ($\sin^2 2\theta_v$ is symmetric about $\pi/4$). In this case, Δm^2 would be less than 0 and $m_1^2 > m_2^2$.

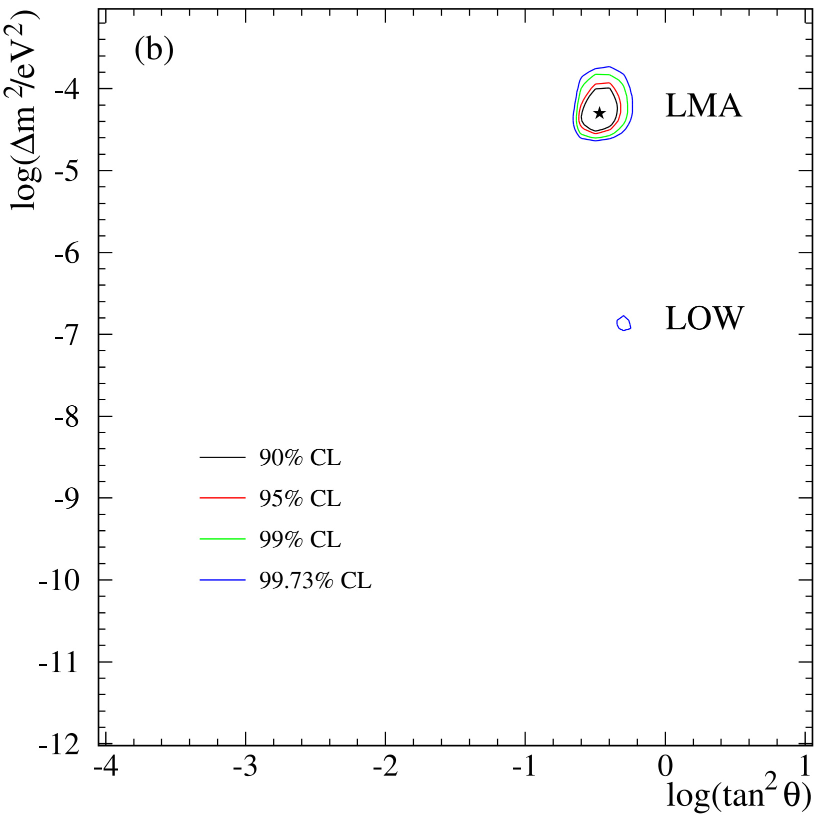

Figure 1.6: MSW contours after the SNO pure D_2O results (from [27]).

produce almost 7% of the world's nuclear power, are located an average of 175 km from the detector. The active region of the detector consists of a nylon balloon filled with 1000 tonnes of liquid scintillator and is surrounded by 1325 17-inch PMTs. Antineutrinos are detected through the interaction

$$\bar{\nu}_e + p \rightarrow n + e^+. \tag{1.20}$$

Scintillation light resulting from the positron ionization and the positron-electron annihilation is observed, followed by a 2.2 MeV signal from neutron capture on a proton. This delayed coincidence signal is very effective in ensuring a high signal-to-noise ratio. A threshold of 2.6 MeV was chosen to avoid geoneutrinos. KamLAND observed $0.611 \pm 0.085(\text{stat.}) \pm 0.041(\text{syst.})$ of the expected flux assuming no oscillations [8]. This measurement confirms the LMA solution to the solar neutrino problem (assuming charge-parity-time, CPT, conservation). The measurement of the electron antineutrino survival probability, in fact, divides the LMA region into two separate regions with different Δm^2 ranges.

Figure 1.7 shows the MSW contours with the KamLAND and SNO salted D_2O data included. The best fit solar neutrino oscillation parameters from all solar data and

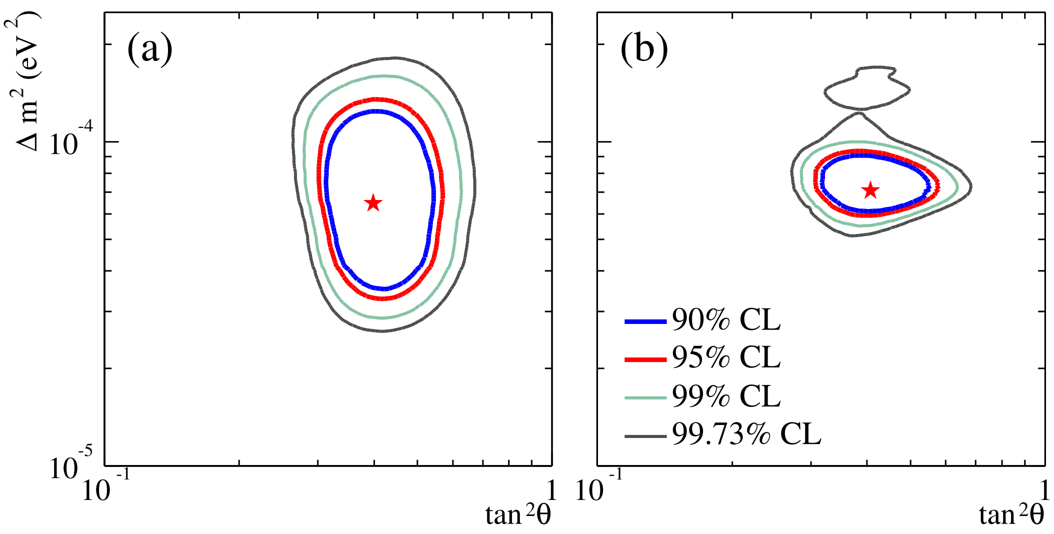

Figure 1.7: MSW contours after SNO salted D_2O results: (a) solar data only and (b) including KamLAND results [1].

KamLAND data are [1]

- $\Delta m^2_{12} = 7.1^{+1.0}_{-0.3} \times 10^{-5}$ eV^2
- $\theta_{12} = 32.5^{+1.7}_{-1.6}$ degrees.

1.9 LMA Solution to the Solar Neutrino Problem

SNO has determined that neutrino flavor change occurs in the LMA (large mixing angle) region of neutrino mixing phase space and this has since been confirmed by KamLAND.

According to the LMA solution, electron neutrinos travel several thousand oscillation lengths and undergo adiabatic conversion in the Sun. For the LMA solution, the MSW ν_e survival probability may be rewritten [28, 29]

$$P_{\mathrm{LMA}}(\nu_e \to \nu_e) = \frac{1}{2} + \frac{1}{2}\cos 2\theta_m \cos 2\theta_v, \tag{1.21}$$

where

$$\cos 2\theta_m = \frac{\cos 2\theta_v - L_v/L_m}{\sqrt{(\cos 2\theta_v - L_v/L_m)^2 + \sin^2 2\theta_v}}.$$

There are three energy regions with different effects:

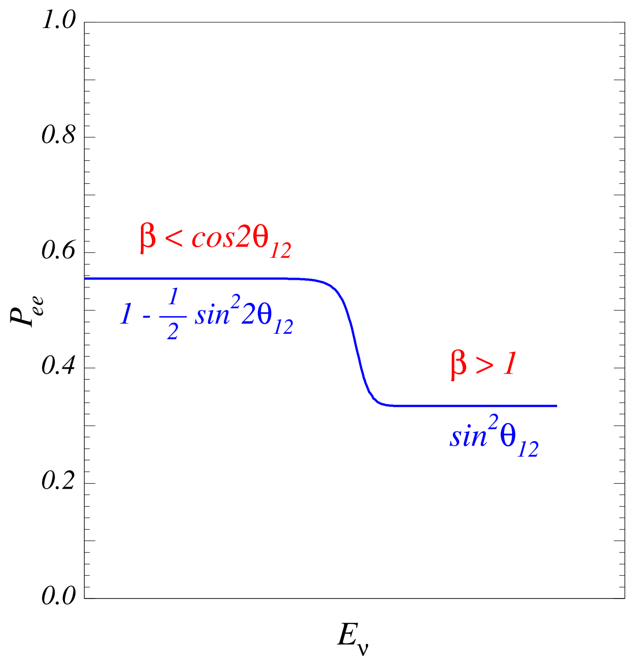

Figure 1.8: LMA electron neutrino survival probability as a function of energy [17]. Here, $\beta = L_v/L_m$.

1. **High energy region** ($E > 10$ MeV): the adiabatic (MSW) conversion occurs with small oscillation effect. Here, $L_v/L_m >> 1$ and $\cos 2\theta_m \approx -1$, so the survival probability may be approximated as[11]

$$P(\nu_e \to \nu_e) = \sin^2\theta_v = \sin^2\theta_{12}. \tag{1.22}$$

2. **Intermediate energy region** ($E \sim 2 - 10$ MeV): the oscillation effect is significant. For $E \sim 2$ MeV, neutrinos are produced on resonance.

3. **Low energy region** ($E < 2$ MeV): vacuum oscillations with small matter corrections occur. Here, $L_v/L_m << \cos 2\theta_v$, so $\cos 2\theta_m \approx \cos 2\theta_v = \cos 2\theta_{12}$. The survival probability corresponds to vacuum oscillations, also found in (1.14):

$$P(\nu_e \to \nu_e) = 1 - \frac{1}{2}\sin^2 2\theta_{12}. \tag{1.23}$$

Figure 1.8 shows the electron neutrino survival probability as a function of neutrino energy for the LMA oscillation solution.

[11] The vacuum mixing angle θ_v is normally written as θ_{12} (or just simply θ). The subscript v was added earlier to easily distinguish this angle from θ_m, but from this point on, it will be referred to as θ_{12}.

1.10 Three Neutrino Mixing

In Section 1.6.1, solar neutrino oscillations were approximated in the two flavor scenario. Of course, however, there are three active flavors of neutrinos and, thus, three mixing angles and three mass differences. The full U_{MNS} matrix may be written [29]

$$\begin{aligned} U_{MNS} &= U_{23}U_{13}U_{12} \\ &= \begin{pmatrix} 1 & 0 & 0 \\ 0 & c_{23} & s_{23} \\ 0 & -s_{23} & c_{23} \end{pmatrix} \begin{pmatrix} c_{13} & 0 & s_{13}e^{-i\delta} \\ 0 & 1 & 0 \\ -s_{13}e^{+i\delta} & 0 & c_{13} \end{pmatrix} \begin{pmatrix} c_{12} & s_{12} & 0 \\ -s_{12} & c_{12} & 0 \\ 0 & 0 & 1 \end{pmatrix}, \end{aligned} \tag{1.24}$$

$$c_{ij} = \cos\theta_{ij}, \;\; s_{ij} = \sin\theta_{ij}.$$

The first and third parts of (1.24) contain variables recognizable in atmospheric and solar neutrino oscillations. The middle part contains the CP-phase δ. If the CP-phase is nonzero, then charge-parity violation might be observable in the neutrino sector. In order to measure the CP-phase, θ_{13} must be large enough.

For solar neutrinos, the atmospheric component is averaged out and the ν_e survival probability for 3-flavor oscillations takes the form [29]

$$P_{ee}^{3\nu} \cong \sin^4\theta_{13} + \cos^4\theta_{13} P_{ee}^{2\nu}, \tag{1.25}$$

where $P_{ee}^{2\nu}$ is the two neutrino MSW ν_e survival probability found in (1.18). The value of θ_{13} is constrained by solar neutrino data because large values of θ_{13} would suppress the energy dependence of the survival probability. The value of θ_{13} is also constrained by atmospheric neutrino data because it adds a $\nu_\mu \leftrightarrow \nu_e$ contribution to the oscillations. The most stringent constraints come from reactor experiments. The combined analysis of atmospheric, solar, and reactor data place a limit $\sin^2\theta_{13} < 0.05$ at 3σ [30].

1.11 Other Neutrino Oscillation Experiments

There are numerous neutrino oscillation experiments. Presented in this section are a selection of experiments that have already contributed significantly to what is known about neutrino oscillations or are likely to make significant contributions.

1.11.1 Atmospheric

In 1998 the Super-K collaboration announced that they had found evidence for neutrino mass[12] [31]. Super-K observes atmospheric neutrinos which result from the collision of

[12]The variation of ν_μ suppression with zenith angle (or path length) is evidence for neutrino mass and is consistent with the oscillation hypothesis.

cosmic rays with O and N nuclei in the Earth's atmosphere. These collisions produce mostly pions and some kaons which decay to neutrinos through e.g.

$$\begin{aligned} \pi^+ &\rightarrow \mu^+ + \nu_\mu \\ &\quad\rightarrow e^+ + \nu_e + \bar{\nu}_\mu . \end{aligned} \tag{1.26}$$

The ratio N(ν_μ):N(ν_e) is therefore expected to be ∼2:1.

Super-K found a deficit of ν_μ and no enhancement of ν_e, implying a $\nu_\mu \leftrightarrow \nu_\tau$ transformation. Also observed is a zenith angle dependence of the ν_μ suppression. The best fit oscillation parameters from the Super-K result are [32]

- $|\Delta m^2_{23}| = 2.5 \times 10^{-3}$ eV^2
- $\sin^2 2\theta_{23} = 1.0$ ($\sin^2 2\theta_{23} > 0.96$ (90% CL)).

1.11.2 Long Baseline

MINOS

MINOS [33], a 735 km long-baseline experiment between the Fermilab Main Injector and the Soudan Mine, will be able to test the oscillation hypothesis posed by the results of studying atmospheric neutrinos – that the ν_μ deficit is due to $\nu_\mu \rightarrow \nu_\tau$ – and make precision measurements of the atmospheric neutrino oscillation parameters. Limits will be placed on the probability of $\nu_\mu \rightarrow \nu_{sterile}$[13]. The primary measurement of MINOS is ν_μ disappearance, but it will also be sensitive to ν_e appearance. MINOS should have the sensitivity to observe the oscillatory behavior from the first oscillation maximum.

K2K

K2K is a 250 km long-baseline experiment which detects ν_μ produced at the KEK beam facility at the Super-K detector. The K2K experiment has observed ν_μ disappearance: it detected 56 ν_μ's, while $80^{+6.2}_{-5.4}$ were expected [34]. A near detector, consisting of a 1 kilo-tonne Čerenkov detector and a fine-grained muon detector, is utilized to reduce the uncertainty on the expected flux at Super-K. The best fit oscillation parameters from the K2K analysis are in agreement with those suggested by atmospheric neutrinos.

T2K

T2K will detect neutrinos from the 50 GeV JHF proton synchrotron 295 km away at the Super-K detector. The neutrino beam will be produced in an off-axis configuration to narrow the energy distribution of the detected neutrinos. The peak neutrino energy is

[13] Sterile neutrinos ($\nu_{sterile}$) will be discussed briefly in Section 1.12.2.

$\sim$0.8 GeV, chosen to optimize the sensitivity to neutrino oscillations. The sensitivity to $\nu_\mu \to \nu_e$ discovery at $\Delta m^2_{13} \approx 3 \times 10^{-3}$ eV^2 is expected to be down to $\sin^2 2\theta_{13} \approx 0.006$ [35].

1.11.3 Reactor

Like the KamLAND experiment described earlier, reactor experiments detect $\bar{\nu}_e$ from nuclear reactors. Earlier reactor experiments, with shorter baselines, placed many exclusion limits on neutrino oscillation regions. The CHOOZ detector in France excludes atmospheric $\nu_\mu \leftrightarrow \nu_e$ mixing and places the limit [7]

- $\sin^2 2\theta_{13} < 0.10$ (90% C.L.) for $\Delta m^2_{13} \gtrsim 2 \times 10^{-3}$ eV^2.

New reactor experiments are being proposed to make a precise measurement of θ_{13} by searching for $\bar{\nu}_e$ disappearance. The limit on θ_{13} will depend upon precision measurements of $\sin^2 2\theta_{23}$ from K2K and MINOS. The expected sensitivity to θ_{13} of reactor experiments after 3 years of running is $\sin^2 2\theta_{13} < 0.01$ at 90% C.L. for $\Delta m^2_{13} = 2.5\times10^{-3}$eV^2 [36]. Measuring θ_{13} using reactors will complement the ν_e appearance searches using ν_μ beams, such as T2K.

1.11.4 Short Baseline

LSND

The LSND experiment performed a search for $\bar{\nu}_e$ appearance by bombarding a tank of liquid scintillator with $\bar{\nu}_\mu$'s. The $\bar{\nu}_\mu$'s were created by smashing protons into a beam dump which created pions which then decayed through

$$\begin{aligned} \pi^+ \to& \mu^+ + \nu_\mu \\ &\to e^+ + \nu_e + \bar{\nu}_\mu. \end{aligned} \tag{1.27}$$

If $\bar{\nu}_\mu$ oscillates to $\bar{\nu}_e$, then the $\bar{\nu}_e$'s will be detected through $\bar{\nu}_e + p \to n + e^+$. In the data from 1993–1999, an excess of 87.9 ± 22.4(stat.) $\pm$ 6.0(syst.) e^+'s was observed [37]. This excess results in oscillation parameters:

- $\Delta m^2 = (0.2 - 2)$ eV^2
- Best fit $\sin^2 2\theta = 0.003$.

This cannot be accommodated by the 3×3 mixing scheme, as one would expect that a third Δm^2 could be inferred from the other two Δm^2, yet this value is inconsistent with the values found from solar and atmospheric neutrino mixing:

$$\begin{gathered} \sum \Delta m^2 = (m_2^2 - m_1^2) + (m_3^2 - m_2^2) + (m_1^2 - m_3^2) = 0, \\ \text{but } \Delta m^2(\text{solar}) + \Delta m^2(\text{atmos.}) + \Delta m^2(\text{LSND}) \neq 0. \end{gathered} \tag{1.28}$$

KARMEN

KARMEN was used to check the LSND result. It observed the delayed coincidence of a positron followed by γ's emitted from the capture of the free n. KARMEN observed 15 candidate events, but expected a background of 15.8 ± 0.5 e^+'s, which means that there was no oscillation excess found [38]. KARMEN excludes much, but not all, of the LSND oscillation phase space.

BooNE

MiniBooNE is the first phase of the BooNE experiment. MiniBooNE is an 800 tonne detector filled with mineral oil which will detect neutrinos from a beam created 500 meters away at the Fermilab booster. MiniBooNE has been optimized to positively confirm or refute the LSND signal. If the signal is observed, a second detector will be built at a distance appropriate to optimally measure the oscillation parameters and to search for CP and CPT violation.

1.12 Status of Neutrino Physics

1.12.1 Oscillation Knowns and Unknowns

What we know from experimental data includes [1, 31, 30]

1. Total of 3 light ν flavors: ν_e, ν_μ, ν_τ.
2. $\Delta m^2_{12} = 7.1^{+1.0}_{-0.3} \times 10^{-5}$ eV^2.
3. $|\Delta m^2_{23}| \sim 2 \times 10^{-3}$ eV^2.
4. $\theta_{12} = 32.5^{+1.7}_{-1.6}$ degrees.
5. $\sin^2 2\theta_{23} \sim 1$.
6. $\sin^2 2\theta_{13} < 0.05$.

What we do not know includes

1. The sign of $|\Delta m^2_{23}|$.
2. How small $\sin^2 2\theta_{13}$ really is.
3. If the CP-phase δ is non-zero and large enough to be observable.
4. If oscillations into sterile neutrinos occur.

1.12.2 Unresolved Issues

In the Standard Model of Particle Physics, neutrinos are assumed to have zero mass. Now that it has been determined that neutrinos change flavor, and thus have mass, mechanisms to incorporate this mass into the Standard Model of Particle Physics must be considered.

Nature of Neutrinos

Dirac Neutrinos

The Dirac neutrino would be analogous to the Dirac electron, having four independent states: left- and right-handed particle (ν_R, ν_L) and antiparticle ($\bar{\nu}_L, \bar{\nu}_R$) states. In this regime, two new particles would need to be added to the Standard Model. These particles would be *sterile* since neutrinos interact via the weak interaction only and the weak interaction only works on left-(right-)handed (anti)particles. The sterile neutrinos could have masses different to their ν_L and $\bar{\nu}_R$ counterparts, which would have interesting implications for cosmology. Correspondingly, cosmological arguments place limits on the existence of sterile neutrinos. If the LSND results are confirmed, there are three Δm^2 which would imply the existence of sterile neutrinos; however, solar and atmospheric data strongly reject the sterile neutrino hypothesis [32].

Majorana Neutrinos

Majorana particles have just two particle states as they are their own antiparticles. If neutrinos are Majorana particles, this could be confirmed by a positive signal of neutrinoless double beta decay ($0\nu\beta\beta$):

$$N(n,p) \rightarrow N(n-2,p+2) + 2e^{-}. \tag{1.29}$$

Normally two neutrinos are emitted in a double beta decay reaction; however, in the case of $0\nu\beta\beta$ decay, a right-handed $\bar{\nu}_{eR}$ released in the decay of a neutron is reabsorbed by another neutron as a left-handed ν_{eL}. This process violates lepton number conservation and requires that the neutrino and antineutrino are identical [39].

Neutrino Mass Mechanism

It is a mystery why the neutrino mass is so small. One possibility is to add a right-handed neutrino to the Standard Model. Then ν_L and ν_R may form a Dirac mass term similar to that for charged leptons and quarks. However, to obtain a neutrino with mass in the eV range requires this mass term to be "unnaturally small" given the symmetries in the Standard Model. The Seesaw Mechanism[14] requires the addition of a singlet Majorana mass term for the right-handed neutrino and the resulting mass matrix has the form

[14] For a more complete description see [40, 41].

$$(\bar{\nu}_L \bar{\nu}_R^c) \left(\begin{array}{cc} 0 & m_D \\ m_D^\dagger & M_R \end{array} \right) \left(\begin{array}{c} \nu_L^c \\ \nu_R \end{array} \right). \tag{1.30}$$

M_R is not constrained by standard model symmetries so its scale may be much higher than the weak scale. Diagonalizing the mass matrix gives a light Majorana mass to the left-handed neutrino,

$$m_L = m_D M_R^{-1} m_D^\dagger. \tag{1.31}$$

Mass Hierarchy

As pointed out in the Section 1.12.1, the sign of $\Delta m_{23}^2 \equiv (m_2^2 - m_3^2)$ is unknown. It has not been determined that m_3^2 is necessarily larger than m_2^2. There are two possible hierarchies of the neutrino masses.
Normal hierarchy:

$$m_1^2 < m_2^2 << m_3^2.$$

Inverse hierarchy:

$$m_2^2 > m_1^2 >> m_3^2.$$

Because a difference between $P(\bar{\nu}_e \leftrightarrow \bar{\nu}_\mu)$ and $P(\nu_e \leftrightarrow \nu_\mu)$ is dependent on the sign of Δm_{23}^2, strong correlations are expected to exist between measured values of Δm_{23}^2 and δ.

If $\sin^2 2\theta_{13}$ is larger than ~ 0.01, then *superbeams*, which are high intensity ν_μ beams, would be able to measure the sign of Δm_{23}^2 and δ. Correlations between these two measurements would be reduced by using two or more baselines [42].

1.13 Summary

There have been numerous contributions to the field of neutrino physics since their first detection by Reines and Cowen 40 years ago. The Sudbury Neutrino Observatory has provided direct evidence of neutrino flavor mixing and thus has solved the "Solar Neutrino Problem." SNO has also contributed to our knowledge of stellar evolution by providing the first measurement of the total active ^{8}B solar neutrino flux. The ^{8}B neutrinos, however, account for a very small fraction of the total solar neutrino flux. More than 98% of the predicted flux lies below 1 MeV. There is still much to be learned from solar neutrino experiments which have sensitivity to lower energy neutrinos.

SNO may be able to further reduce its uncertainty on the solar neutrino mixing parameters in its third phase of operation (briefly described in Chapter 2) which has a different detector configuration and systematic uncertainties. The atmospheric neutrino mixing parameters will be confirmed by MINOS and the uncertainties reduced by MINOS and the continuation of Super-K. A handle on θ_{13} and the CP-phase will be gained through future reactor, long baseline, and superbeam experiments.

Chapter 2

The SNO Detector

The Sudbury Neutrino Observatory (SNO) was designed to detect neutrinos produced by the fusion reactions which power the Sun. The Sun produces electron-type neutrinos only, but SNO has the capability of detecting all three active neutrino flavors (ν_e, ν_μ, and ν_τ). The crucial elements of SNO are *heavy water, size, cleanliness*, and *depth*. SNO is a Čerenkov detector filled with heavy water which allows it to see what other Čerenkov detectors do not distinguish: non-electron type neutrinos[1]. Neutrinos have an extremely low interaction cross section because they interact via weak interactions only. To detect a significant number of neutrinos, the detector must be quite large. SNO's target is 1 kilo-tonne of heavy water contained within a 12 m-diameter sphere. Of the trillions of neutrinos that pass through each second, only about 10 interact within the heavy water each day[2]. The water must be as free from impurities as possible in order to see neutrino signals above radioactive background signals. Unshielded neutrino detectors would be swamped by particles from cosmic rays. The SNO detector is located in the INCO Ltd. Creighton mine[3] near Sudbury, Ontario, Canada. The center of the detector is 2039 meters below the Earth's surface. At this depth, only about 100 cosmic ray muons pass through the detector each day.

2.1 Čerenkov Radiation

Charged particles traveling through a medium with a refractive index n at a velocity that is greater than the speed of light in that medium (c/n) emit Čerenkov radiation. The number of Čerenkov photons emitted per unit track length per unit wavelength λ

[1] H_2O Čerenkov detectors see ν_μ's and ν_τ's with about $\frac{1}{6}$ the probability of seeing ν_e's, but the signals are completely indistinguishable.

[2] Within analysis cuts.

[3] Creighton is an active nickel mine.

is given by

$$\frac{d^2N}{dxd\lambda} = \frac{2\pi\alpha Z^2}{\lambda^2}\left(1 - \frac{1}{\beta^2 n^2}\right), \tag{2.1}$$

where $\alpha \approx \frac{1}{137}$ is the fine structure constant, $\beta = v/c$, and Z is the charge of the relativistic particle [43]. The light is emitted at the Čerenkov angle, $\theta_C = \cos^{-1}(1/\beta n)$, relative to the momentum vector of the relativistic particle.

Electrons created in neutrino reactions in the SNO detector that are traveling faster than the speed of light in heavy water[4] emit photons with intensity $I(\lambda) \propto 1/\lambda\, d\lambda$ at a Čerenkov angle of around 42°. In the energy region of interest in the SNO detector (about 5–15 MeV), about 220 photons are emitted per MeV within the detected wavelength region. The electrons emit Čerenkov light until their speed drops below c/n; this cutoff occurs at a kinetic energy of 262 keV for electrons in water. These Čerenkov photons are detected by a geodesic array of 8 inch Hamamatsu photomultiplier tubes (PMTs). However, only a fraction of them are seen due to the coverage and collection efficiency of the PMTs and the attenuation of light in the detector media.

2.2 Detector Design

The 1000 tonnes of heavy water are on loan from the Atomic Energy of Canada Ltd. The heavy water is contained inside a 6 m-radius acrylic sphere, the Acrylic Vessel (AV) [44]. Surrounding the AV is a geodesic stainless steel structure 17.8 m in diameter, known as the PSUP (for Pmt SUPport structure), which holds 9438 PMTs looking in towards the D_2O[5]. To improve the light collection efficiency of these PMTs, 27 cm-diameter light concentrators (or *reflectors*) are mounted on each PMT. The PMT-reflector combination provides a phototube coverage of about 54% [44]. The light collection is approximately flat out to an angle of about 50° and rapidly decreases beyond this angle [45]. The maximum angle of incidence of detected photons on the PMT-reflector combination is about 60°.

In addition to the inward-looking PMTs, the PSUP also holds 91 outward looking PMTs (called OWLs) used as muon veto tubes.

To shield the inner detector from natural radioactivity found in both the walls of the cavern and the PSUP, the AV and PSUP are surrounded by 7000 tonnes of ultra-pure light water contained in a barrel-shaped cavity. See Figure 2.1 for a schematic view of the detector.

[4]The index of refraction is wavelength dependent and the average n in heavy water is about 1.32.
[5]Over time, some PMTs have been taken off-line due to break down.

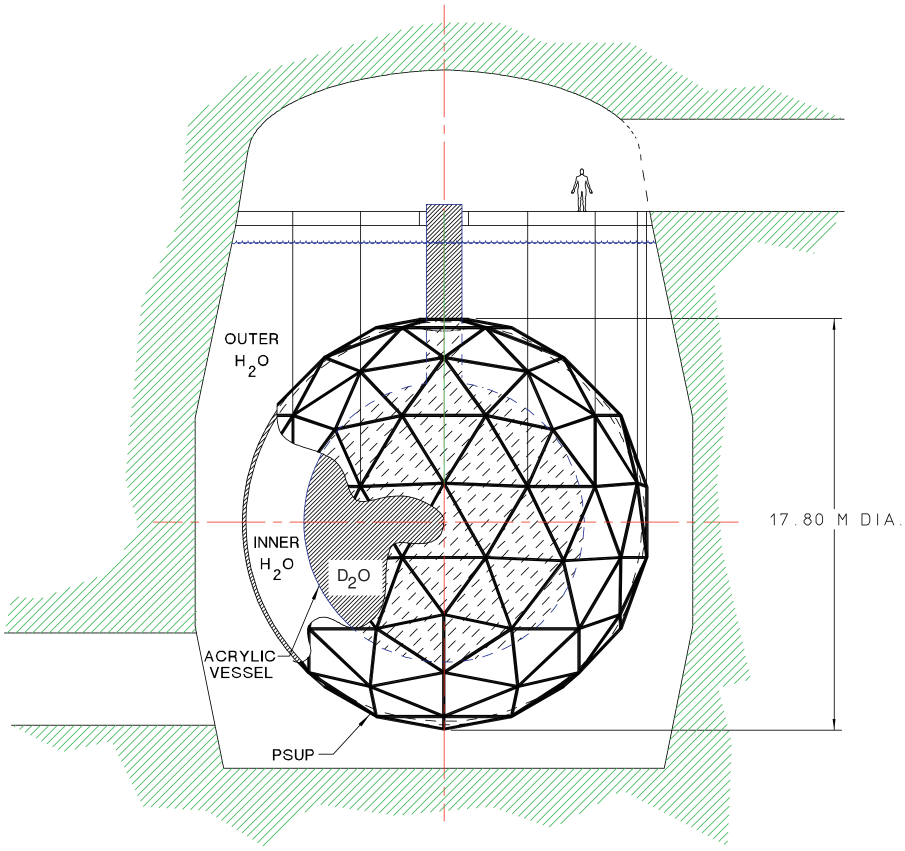

Figure 2.1: Schematic view of SNO detector [44].

2.3 Electronics

The accessible area on top of the detector is referred to as the *deck* and all PMT electronics are stored here. The electronics are responsible for measuring and storing hit time and charge information from PMT pulses. A trigger is generated if coincident PMT signals satisfy triggering requirements and the stored information is read out and classified as an event.

2.3.1 Layout

The layout of the SNO detector electronics is as follows:

- Each PMT cable leads into one of 19 crates located in racks situated about the deck.

- Eight PMT cables attach to a *Paddle Card.*

- Four paddle cards are mounted on a *PMT Interface Card* (PMTIC) located at the back of the crate which controls the high voltage for the PMTs. The HV for eight PMTs is turned on or off at one time through relays on the PMTIC.

- The PMT signals are sent from the PMTIC to a *Front End Card* (FEC) which contains four *Daughter Cards.* A Daughter Card digitizes the signals and stores time and charge information for eight PMTs by storing charges on buffer capacitors. Each FEC processes 32 channels and is companion to a PMTIC, to which it is connected by a customized backplane.

- Each crate holds 16 FECs and PMTICs and is, thus, able to process up to 512 PMTs.

See Figure 2.2 for a pictorial representation of the PMT electronics layout [45].

2.3.2 Data Acquisition and Triggering

A photon striking a PMT cathode has some (angular-dependent) probability of producing a photoelectron which is accelerated to the first dynode and then multiplied down the dynode chain producing a 2–3 ns wide pulse of about 4 mV in amplitude. The pulse travels along the PMT cable to the rear of the SNO electronics, the PMTIC. The signal continues to the FEC where it encounters a discriminator. The discriminator produces a 100 ns pulse if the PMT pulse amplitude is greater than the discriminator setting. The 100 ns trigger pulses from all 32 channels are summed on the FEC, and all 16 summed triggers from the FECs are summed in the *Crate Trigger Card* (CTC). Each of the 19 CTCs signals are sent to the *Master Trigger Card/Analog* (MTC/A) located in the *Timing Rack* VME crate. There the signals are finally summed into an analog pulse with an amplitude proportional to the total number of PMTs that have fired within 100 ns of one another. Because the PMT array is 17 m in diameter, different photons from the same interaction in the D_2O may differ in travel time to the PMTs by as much as 66 ns, or longer if they undergo reflections, thus the 100 ns pulse catches prompt and reflected light.

There are three discriminators on the MTC/A: LOW, MED, and HI. If the summed pulse exceeds the threshold for one of these three discriminators, the MTC/A sends a pulse to the *Master Trigger Card/Digital* (MTC/D) also located in the Timing Rack. If the MTC/D receives a signal from a trigger that it is configured to look for, a *Global Trigger* is sent to all crates. The timing and charge information from each tube is digitized and stored on the FECs.

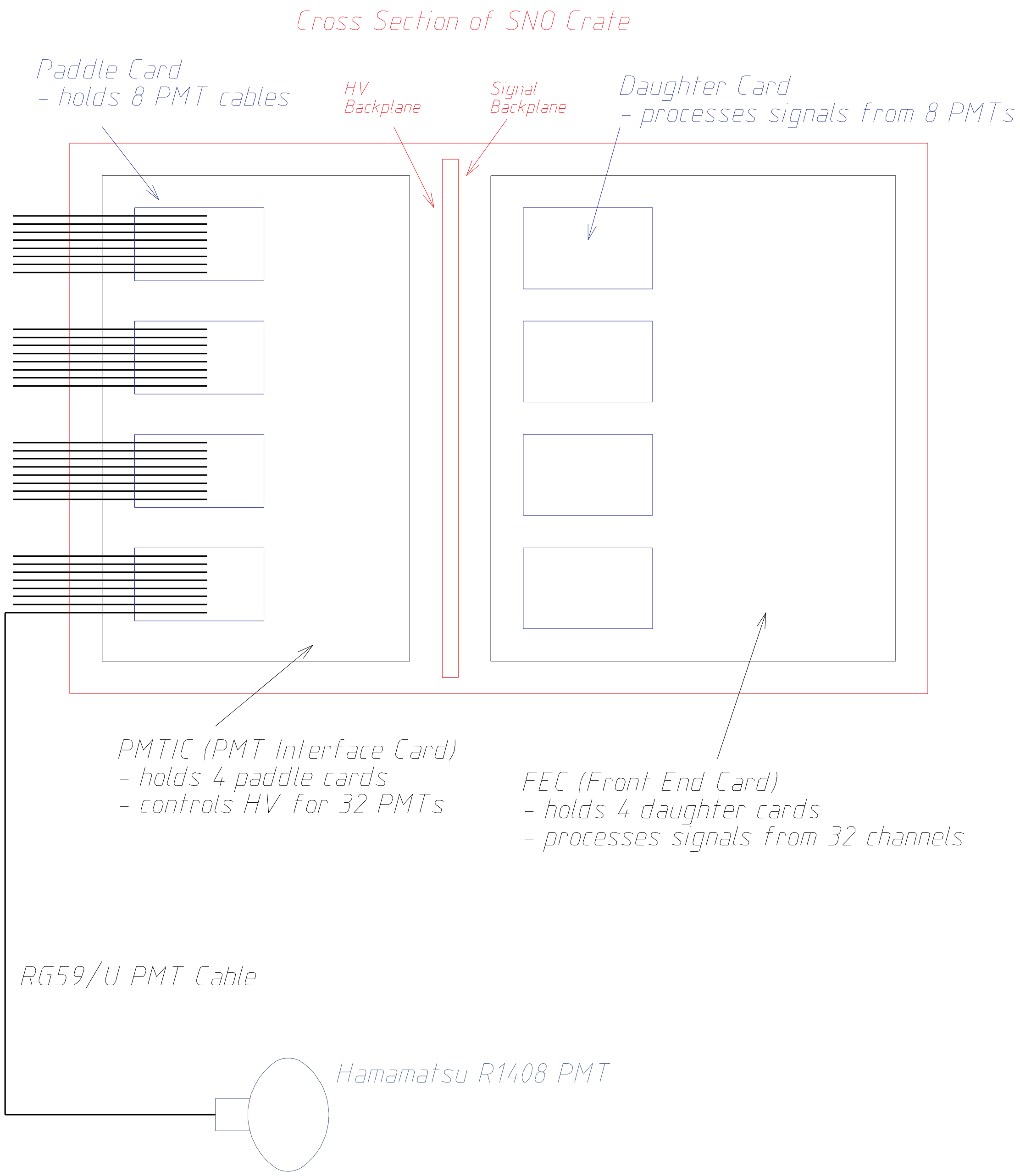

Figure 2.2: Schematic cross section of PMT crate showing the orientation of Paddle Cards, PMTICs, FECs (Motherboards) and Daughter Cards [45].

Each crate contains a backplane which runs between the PMTICs and FECs. The CTC is located here, as well as an $XL2$ interface card, which reads out the data from the crate. Each $XL2$ is connected to a companion $XL1$ card located on the backplane of the Timing Rack. The Timing Rack backplane also contains a single board computer, called the $eCPU$ (for embedded CPU), which reads out the data. For each valid global trigger, the data stored are:

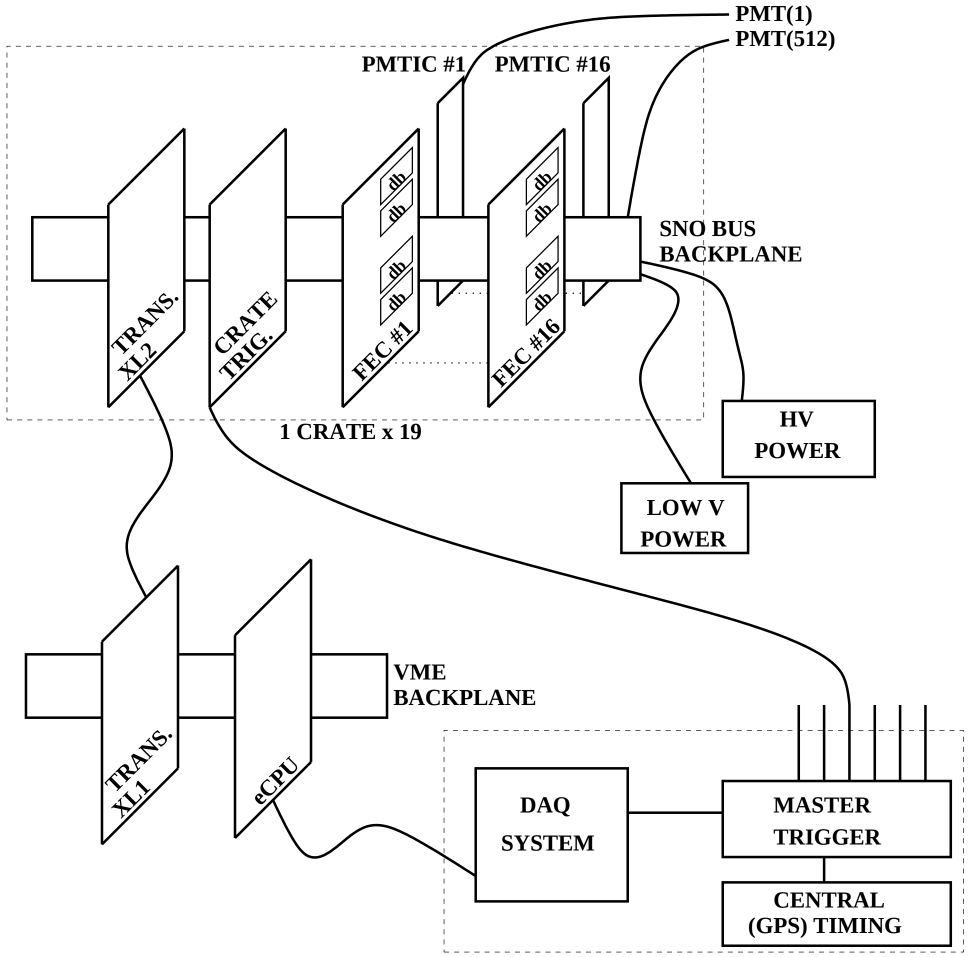

Figure 2.3: Diagram of SNO data acquisition electronics [44].

1. a digitized time for each fired PMT
2. three digitized charges for each fired PMT
3. a unique identification number (GTID)
4. a global trigger time recorded by 10 MHz and 50 MHz clocks
5. a unique identifier for each fired PMT

The data are transferred from the eCPU to a Sun computer (labelled as *DAQ System* in the above picture) where the data are built into data `zdab` files, which are written to tapes. A diagram of the flow of SNO data acquisition (PMT pulse to tape) is shown in Figure 2.3.

2.4 Neutrino Interactions in D_2O

2.4.1 The Charged Current Interaction

Only electron-type neutrinos interact via the charged current (CC) interaction,

$$\nu_e + d \rightarrow p + p + e^-.$$

These neutrinos must have an energy greater than the interaction threshold of 1.44 MeV. Exchange of a W boson converts a neutron in the deuterium nucleus to a free proton by changing a down quark into an up quark. The momenta of the resulting protons are very small, so the energy of the recoil electron created in this interaction is closely related to the incident neutrino energy. Thus, the energy spectrum of ^{8}B solar neutrinos may be measured.

The angular distribution of the electron is weakly correlated to that of the neutrino direction with the form [46, 47]

$$f(\theta_\odot) \cong 1 - \frac{v_e}{3c}\cos\theta_\odot \approx 1 - 0.345\cos\theta_\odot, \tag{2.2}$$

where v_e is the initial speed of the recoil electron and $\theta_\odot$ is the electron direction with respect to the direction of the neutrino which has been emitted from the Sun.

Nearly all of the recoil electrons are moving faster than the speed of light in the D_2O, so they emit Čerenkov light which is detected by the PMTs.

2.4.2 The Neutral Current Interaction

The neutral current (NC) interaction is equally sensitive to all three active flavors of neutrinos,

$$\nu_x + d \rightarrow n + p + \nu_x.$$

The energy threshold is the binding energy of the deuteron, 2.22 MeV. The signal of this interaction comes from the freed neutron, and there are three methods (corresponding to three phases of detector configuration) by which the neutron is detected.

1. Pure D_2O The neutron captures on deuterium, forming an excited state of tritium which then releases a single 6.25 MeV γ-ray.

2. Salted D_2O NaCl is added to the D_2O. The neutron captures on ^{35}Cl, producing ^{36}Cl* which consequently releases a γ-cascade totaling 8.6 MeV in energy.

In these two phases in which the detection principle is neutron capture, the emitted γ's primarily Compton scatter electrons which emit light if over the Čerenkov threshold.

3. D_2O+NCDs Neutral Current Detectors (NCDs) are added to the D_2O after the salt is removed. The NCDs are ^{3}He-filled proportional counters which capture the neutron through the reaction $^3\mathrm{He}(n,p)^3\mathrm{H}$. The proton and the triton produce ionization which is detected on the anode wire, giving a clear neutron signal[6].

The NC interaction gives no spectral or directional information about the incoming neutrinos; however, the rate of this interaction (in comparison with the CC interaction) is the most important measurement in SNO. This rate gives a measure of the total flux of ^{8}B neutrinos from the Sun. A discrepancy between inferred NC and CC fluxes is an indication of non-electron-type neutrinos reaching Earth from the Sun. This discrepancy is evidence for neutrino flavor change, which may be explained by the neutrino oscillation hypothesis.

2.4.3 The Elastic Scattering Interaction

Also present in SNO is neutrino-electron elastic scattering,

$$\nu_x + e^- \rightarrow \nu_x + e^-.$$

The elastic scattering (ES) reaction occurs for all three active neutrinos, but it is more sensitive to electron-type neutrinos since they are able to interact with electrons via exchange of charged W bosons in addition to the neutral Z boson exchange. Because it is an elastic collision, the reaction has no threshold. Its differential cross section comes straight from electroweak theory [48]:

$$\begin{aligned} \frac{d\sigma}{dT_e} &= \frac{2G_F^2 m_e}{\pi}\left[g_L^2 + g_R^2\left(1-\frac{T_e}{E_\nu}\right)^2 - g_L g_R\left(\frac{m_e T_e}{E_\nu^2}\right)\right] \\ &(g_L = (\pm\frac{1}{2} + \sin^2\theta_W),\ g_R = \sin^2\theta_W,\ \sin^2\theta_W = 0.23), \end{aligned} \tag{2.3}$$

where G_F, m_e, T_e, and E_ν are respectively the Fermi coupling constant, the electron rest mass, the electron recoil kinetic energy, and the incoming neutrino energy. The upper sign in g_L is for ν_e's (scattering through charged and neutral current exchange) and the lower sign is for ν_μ's and ν_τ's (scattering through neutral currents only).

The elastic scattering cross section is relatively small compared to that of the CC and NC interactions and the cross section for electron type neutrinos is approximately 6.5 times higher than the cross section for the other neutrino types.

The Čerenkov light emitted from relativistic recoil electrons is detected in SNO. The direction of these electrons is highly correlated with that of the incoming neutrino as displayed in Figure 2.4. The ES interaction also occurs in the light water region surrounding the acrylic vessel. Light water Čerenkov detectors detect neutrinos through the ES interaction only.

[6] Roughly 50% of the neutron signals on the NCDs are clearly from neutrons; the rest of the signals might be separated from α background using analysis of pulse shapes.

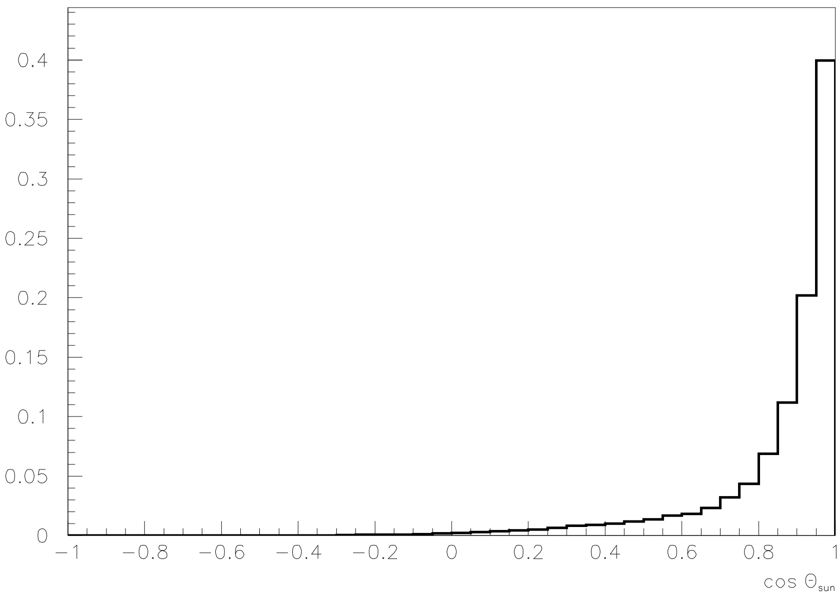

Figure 2.4: Angular distribution of electrons from the ES interaction with respect to the direction of the incoming neutrino, which is coming from the Sun.

2.4.4 Antineutrino Interactions

Antineutrinos may be observed in the D_2O through the interaction,

$$\bar{\nu}_e + d \rightarrow n + n + e^+. \tag{2.4}$$

The signature of this reaction is Čerenkov light from positron-electron annihilation in delayed coincidence with light from neutron capture.

Placing an upper limit on the number of extraterrestrial $\bar{\nu}_e$'s interacting through (2.4) is interesting because it constrains the spin flavor precession hypothesis which is an alternative to MSW neutrino flavor change. In this process, a left-handed Majorana ν_{eL} may be converted to a right-handed $\bar{\nu}_{xR}$ if there exists a large magnetic moment of the electron neutrino which would interact with the solar magnetic field [49]. The SNO limit on the $\bar{\nu}_e$ flux may be found in [50].

Antineutrinos may also interact in the light water through

$$\bar{\nu}_e + p \rightarrow n + e^+, \tag{2.5}$$

but observation of this is unlikely since SNO's neutron detection capability is principally within the D_2O.

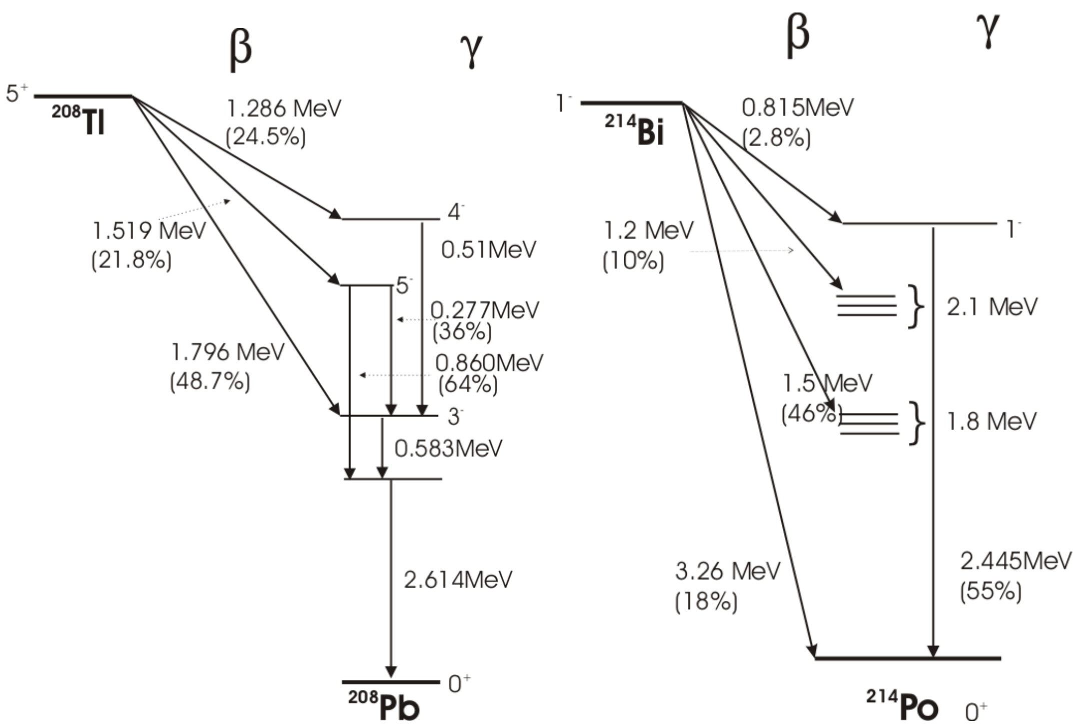

Figure 2.5: ^{208}Tl and ^{214}Bi decay diagrams. Figures provided by C. Sims.

2.5 Backgrounds

The most troublesome background to the neutrino signals in SNO comes from natural radioactivity in the heavy water, the light water, and everything surrounding the detector. Daughters of ^{232}Th and ^{238}U produce low energy Čerenkov events limiting how far the energy threshold may be lowered. These chains also produce γ's, some of which are energetic enough to break apart the deuteron into its component proton and neutron. This free neutron is a background to the neutral current signal. The ^{232}Th and ^{238}U decay chains may be found in Appendix A. Discussed in this section are Čerenkov light-producing backgrounds only. Instrumental backgrounds are discussed briefly in Chapter 5 and in much more detail in [51]. Estimates of the Čerenkov backgrounds will be discussed in Chapter 5.

Low Energy Čerenkov Background

The low energy threshold of SNO is limited by the Čerenkov background from decay products of ^{232}Th and ^{238}U. In particular, a 2.6 MeV γ is emitted from almost every β-decay of ^{208}Tl in the ^{232}Th chain and ^{214}Bi in the ^{238}U chain β-decays emitting an electron with maximum energy of 3.26 MeV. Gammas from these decay chains contribute to this background primarily by Compton scattering electrons. Decay diagrams of ^{208}Tl and ^{214}Bi are found in Figure 2.5.

Internal Neutron Production by $d(\gamma, n)p$

Gammas above the deuteron binding energy, 2.22 MeV, come from daughters in the ^{232}Th and ^{238}U decay chains. A 2.614 MeV γ comes from almost every β-decay of ^{208}Tl. For $\sim$2% of every ^{214}Bi β-decay a γ with energy greater than 2.2 MeV is produced. Upper limits of $< 3.7\times10^{-15}$ gTh/gD$_2$O and $< 4.5\times10^{-14}$ gU/gD$_2$O are placed to limit the background from these chains to less than one neutron per day in the D$_2$O volume from each chain.

External Neutron Production

Gammas from activity in the light water and acrylic vessel are potential sources of neutron background since they can photodisintegrate deuterium. Also, radon daughters that were deposited on the acrylic vessel during construction can instigate (α, n) reactions on carbon and oxygen nuclei. Enough of these neutrons are captured in the salted D$_2$O that they must be accounted for in the neutrino data set. The appearance of these neutrons peaks at the AV and their radial profile is very different from that of NC events. This allows for the amount of these external neutrons to be extracted by fitting for their characteristic radial profile.

AV Events

Nearly isotropic events have been observed in SNO data and appear to emanate from the Acrylic Vessel (hence, they are referred to as *AV* events[7]) [52]. The light-producing mechanism of the AV events is uncertain. One possibility is that light is produced by stress relief of the acrylic. Another theory is that bubbles form on the acrylic and release isotropic light when they detach [53]. The removal of these events is discussed in Chapter 5.

2.6 SNO Monte Carlo and Analysis Code

SNOMAN (SNO Monte Carlo and ANalysis) is the primary Monte Carlo and analysis package of the SNO collaboration [54]. It has been developed using FORTRAN 77 and the ZEBRA memory manager [55]. SNOMAN provides Monte Carlo simulation of

[7] These have also been known as *Leslie* events, named for the first person to investigate them, Hamish Leslie.

events in the SNO detector, as well as data processing capability. SNOMAN uses the EGS4 (Electron-Gamma Shower) system to model the propagation of electrons, γ-rays, and Čerenkov photons [56]. The MCNP package is used to model neutron transport [57]. SNOMAN contains a detailed description of the SNO geometry, PMT response, electronics, trigger system, and data acquisition system. It also contains important analysis tools for calibration, reconstruction, and event filtering.

A database is maintained containing constants used for detector simulation and calibration. When raw data are unpacked and read into SNOMAN, the software applies calibration constants which are valid for the times of the particular events in that data.

2.7 SNO Observables

For any charged particle producing Čerenkov light in the detector, the following event quantities may be determined from the measured PMT times, charges, and positions:

1. position vertex
2. direction
3. energy
4. isotropy

The event vertex is determined by measuring the relative times that PMTs are fired. The direction is determined by the angular positions of the hit PMTs about the fit vertex. The energy is closely proportional to the amount of light detected by the PMTs [58]. The first three of these observables will be discussed briefly in the following sections, while the event isotropy is the main topic of this thesis.

2.7.1 Event Vertex and Direction

Vertex reconstruction is based on the relative timing of PMTs which have fired in an event. A timing residual for each fired PMT i is defined as

$$t_i^{res} = (t_i - t_{fit}) - |\mathbf{r}_{fit} - \mathbf{r}_i|/c_{avg}, \tag{2.6}$$

where t_i is the time at which PMT i fired, t_{fit} is the fitted event time, $\mathbf{r}_{fit}$ is the fitted event position vector, $\mathbf{r}_i$ is the position vector of PMT i, and c_{avg} is the mean group velocity. A timing residual histogram from data obtained during a run in which the ^{16}N calibration source[8] was placed at the center of the detector (this is often referred to as

[8]The ^{16}N calibration source is discussed in Section 2.8.4.

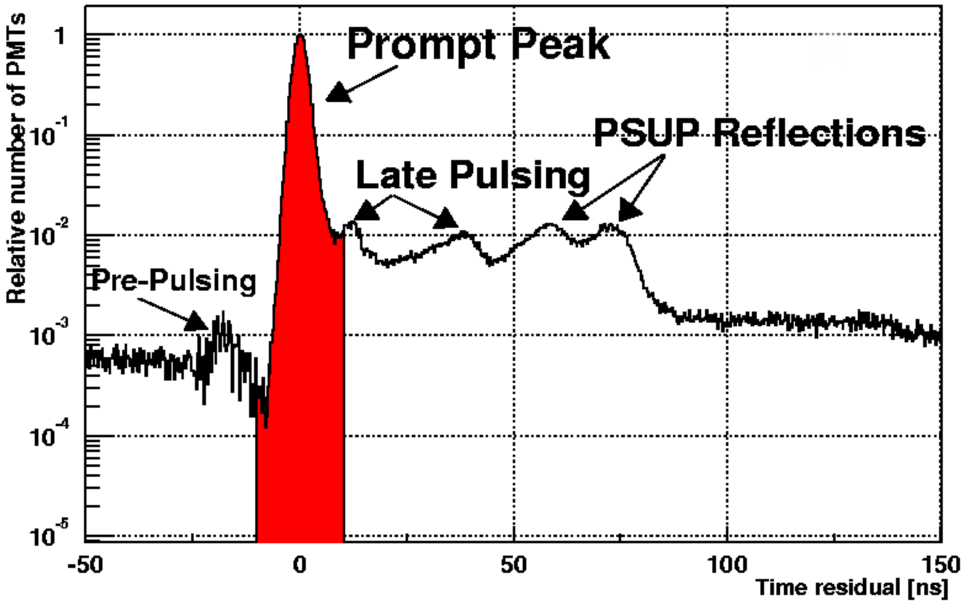

Figure 2.6: Timing residual histogram for central ^{16}N data. Figure from [59].

a *central run*) is displayed in Figure 2.6 (note that the y-axis has a logarithmic scale). The width of the prompt peak is due to the intrinsic PMT timing resolution of about 1.5 ns. The pre-pulsing and late pulsing peaks are properties of the PMTs and do not vary with source position. However, the PSUP reflections vary with source position and are most prominent for central runs.

To find the event vertex $(t_{fit}, \mathbf{r}_{fit})$, a simple fitter minimizes

$$\chi^2 = \sum_i \frac{(t_i^{res})^2}{\sigma^2}, \tag{2.7}$$

where the value σ is the PMT timing resolution.

GRID Fitter

The GRID fitter (designed by M. Moorhead [60] and improved by X. Chen [61]), utilizes probability density functions (PDFs) of timing residuals obtained from Monte Carlo simulation. The event vertex is found using maximum likelihood techniques. The likelihood function is described by

$$\mathcal{L}_{vertex} = \prod_{i=0}^{N} P(t_i^{res}), \tag{2.8}$$

where $P(t_i^{res})$ is probability of PMT i having a timing residual t_i^{res}. The negative logarithm of (2.8) is minimized at each point in a 3D position grid. The $(t_{fit}, \mathbf{r}_{fit})$ with the lowest $-\log \mathcal{L}_{vertex}$ is then used to seed a 4D minimization of (2.8) using MINUIT [62, 63].

QPDF Fitter

The QPDF Fitter, designed by M. Boulay [59], is also a maximum likelihood fitter, but significantly faster than the GRID fitter. Timing residual histograms derived from Monte Carlo simulation and from laserball calibration data are used as probability density functions for each PMT. A timing cut of ± 50 ns from the mean PMT hit time is imposed to reduce random PMT noise and light scattered from the PSUP. Like the GRID fitter, $-\log \mathcal{L}_{vertex}$ is minimized to find the most probable event vertex. A description of how this minimization is achieved is found in [59].

The event direction $(\theta_{fit}, \phi_{fit})$ is also found by minimizing a likelihood function created from PDFs based on the angular distribution of Čerenkov photons from the fitted event vertex. The distribution of the angles, θ_i, between the event direction and each fired PMT is peaked at the Čerenkov angle. Scattering of the electron smears the photon direction about this angle. The distribution of azimuthal angle ϕ_i is expected to be flat.

The accuracy of the vertex reconstruction is limited by (i) uncertainty in the arrival time of photons on the PMTs, (ii) a few hits resulting from PMT noise in an event (the dark rate noise is about 593 Hz [59]), and (iii) Rayleigh scattering of the Čerenkov photons in the water. The vertex resolution determined using Monte Carlo simulation is found to be about 30 cm. The multiple scattering of the electron results in a poor determination of event direction which has a resolution of about 20°.

In-Time Ratio (ITR)

The In-Time Ratio (ITR) is the number of hits falling within a time window of -2.5 to 5.0 ns divided by the total number of calibrated PMT hits. For many SNO analyses, a cut is placed on this quantity after event reconstruction.

2.7.2 Energy Reconstruction

$\mathbf{N}_{hit}$

The most basic measure of energy is simply the number of photomultiplier tubes that are hit in an event. N_{hit} is defined as the number of PMTs hit within a time window of 100 ns. This value depends on the number of Čerenkov photons produced by a relativistic electron and the response of the detector at the origin of these photons. The value has been found to scale linearly with the energy of the charged particle creating the Čerenkov photons [58]. There are roughly 8 PMT hits per 1 MeV of kinetic energy, although this number has decreased slowly over time.

Energy Response Function (RSP)

RSP gives a measure of the electron energy by incorporating the detector's response[9]. RSP uses the number of prompt PMT hits in an event as the primary estimator of event energy. It uses a time window of ±10 ns, chosen so that Čerenkov photons reflected from the PSUP are not used. To avoid using hits which may be due to electronic pickup, RSP places a charge threshold of 8 counts above pedestal.

The quantity $\langle N_{win} \rangle$ is defined to be the mean number of prompt hits for each ^{16}N run and the *effective* number of prompt PMT hits (N_{eff}) is then defined as

$$N_{eff} = (\langle N_{win} \rangle - N_{dark}) \cdot \frac{\text{Total number of PMTs in MC}}{\text{Number of PMTs on during run}}, \tag{2.9}$$

where N_{dark} is the PMT dark count in the prompt time window (about 0.11 hits). The ratio is to account for the effect of the number of enabled PMTs changing between runs.

The scaling between N_{eff} and the electron energy is determined using Monte Carlo. RSP calculates the optical response of SNO for a given event vertex and direction. The number of prompt hits for a Čerenkov event occurring anywhere in the heavy water region is corrected to the equivalent number of hits at the center before the N_{eff} to energy scaling is applied. RSP also corrects for small changes in the PMT effective efficiency over time. The uncertainty on the energy scaling is determined to be 1.1% [1].

Effective Kinetic Energy (T_{eff})

Often referred to in this thesis is effective kinetic energy, T_{eff}. This is defined as RSP energy minus 0.511 MeV (the electron rest mass). A plot of T_{eff} versus N_{hit} is shown in Figure 2.7. The correlation between N_{hit} and T_{eff} is not exactly one because for a given electron energy, the number of PMTs that fire depends on Poisson statistics and the event direction and position at which the event occurred.

2.8 Calibrations

Performing frequent calibrations over the entire lifetime of the detector ensures that the most accurate measurements of the observable event quantities are made. Calibrations are used to determine electronic properties, optical properties, and the detector response to physical signals.

[9] RSP was developed by M. Boulay and more information on this energy measure is available in [59].

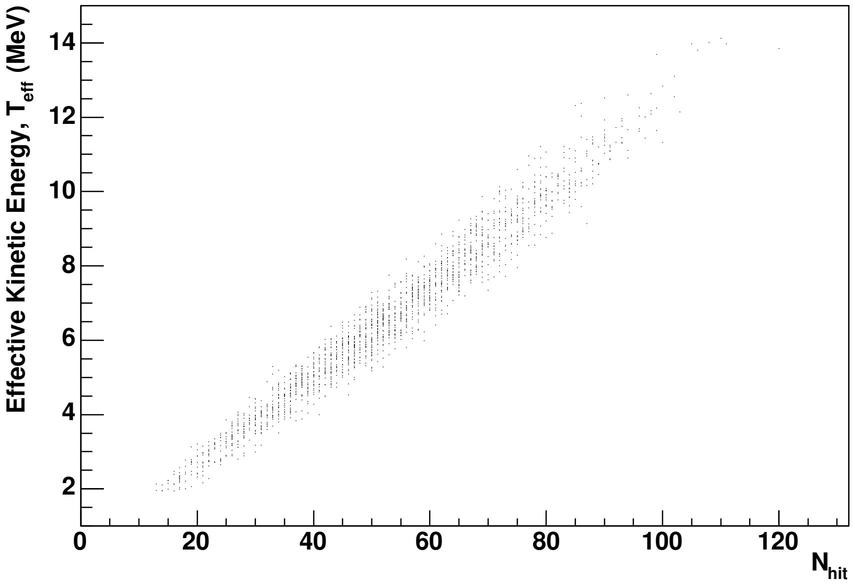

Figure 2.7: Effective kinetic energy (T_{eff}) versus N_{hit} for CC events.

Calibration sources are deployed through the *glovebox*, which envelops the top of the AV neck and is accessible from a clean room on the deck.

2.8.1 Electronics Calibration

Each FEC contains four analog-to-digital converters (ADCs) for charge and time measurements. When a PMT triggers the discriminator, the time to amplitude converter (TAC) is started. The ADCs continue to store charge until a global trigger signal is received or the system runs out of time (about 400 ns) and resets. Once a global trigger signal is received, the time of firing and the charge deposited in the PMT are stored. The charge signal is integrated over two time windows (70 and 400 ns) to obtain prompt (Čerenkov light traveling directly to the PMTs) and late (reflected) light. Three integrated charge signals are stored: QHS, QHL, and QLL.[10] Each channel has 16 banks of storage cells consisting of four capacitors inside of a chip, on which the four measurements are stored. Calibrations must be generated for each cell.

There are two electronics calibrations performed bi-weekly which obtain the following information for each cell in each channel:

1. Pedestal Calibration: the number of ADC counts present when no charge is collected (called the *pedestal* values),

[10] Q stands for charge, the second letter (H=high or L=low) refers to the gain, and the third letter (S=short or L=long) stands for the integration time.

2. Time Slope Calibration: the slope corresponding to time (TAC) versus ADC counts.

These are necessary to convert charge ADC counts to pedestal corrected counts above zero and time ADC counts into nanoseconds.

A photoelectron (PE) has a mean of about 32 ADC counts above pedestal[11] and most PMT discriminators are set at $\sim$1/4 PE. For the pedestal calibration, each of the 16 cells are "pinged" 10 times. The channel fires via front end logic and a Global Trigger is issued by the central timing rack. The integrator starts to integrate with no charge from the PMT. The pedestal calibrations are done with a 150 ns delay, which corresponds to a time measurement of 1850 ADC counts. There are a number of checks done to validate this calibration. The pedestal mean and width of the 10 pings for each cell are calculated. Acceptable values for the pedestal means are 300–900 ADC counts for charge and 1350–2400 counts for TAC. Also the values are compared to the values from the previous pedestal calibration.

The TAC time slopes are obtained by varying the time between pedestal pulses and the global trigger. Each cell is measured for 31 time values.

Before the electronics were cooled with a fan upgrade in December 2000, the electronics calibration was dependent on the rate at which events are read out from a cell in a channel. It was necessary to apply a correction to PMT times from low rate (neutrino) data to make the times consistent with high rate (calibration) data. The data from the salted D_2O phase have all been acquired since this fan upgrade, and it is shown in Appendix E that this correction is not necessary since the cooling of the electronics.

2.8.2 PMT Calibration

Each PMT must be calibrated for individual properties such as cable delays, gain, and discriminator walk. Discriminator walk is the phenomenon of a discriminator's firing time being dependent on the size of the PMT pulse which fires that discriminator [64]. When a larger charge is deposited on a PMT, the pulse crosses the discriminator earlier because it has the same rise time[12] as a smaller pulse, but a larger amplitude. The size of the correction for this effect is in the range of 0–5 ns, which is determined from data obtained from deploying an isotropic light source, called the *laserball*, which is briefly described in the next section. This correction also accounts for offsets to individual ECA times due to cable delays.

The number of ADC counts above pedestal that corresponds to one photoelectron varies between PMTs [64]. A gain calibration is applied to convert charge units into

[11] The number of ADC counts varies and might lie anywhere between 8 and 160.

[12] Rise time is defined as the amount of time required for a pulse to rise from 10% to 90% of its peak amplitude.

units proportional to the number of photoelectrons. The laserball source is run at low light level to obtain this calibration, but with sets of channels gated so that data can be taken that would fall below discriminator values.

Once the electronics and PMT calibrations have been applied, the PMT timing is calibrated to approximately 1.5 ns.

2.8.3 Optical Calibration

Measurements of the attenuation coefficients in the D_2O, H_2O, and AV are made as a function of wavelength using data obtained from the laserball. The laserball consists of a pulsed dye laser connected with a fiber-optic cable to a diffuser ball with a diameter of 10 cm. The wavelength of the isotropically emitted photons has selectable values within the range of 360–700 nm.

The angular response of the PMTs is measured by deploying the laserball source in many locations in the detector at a number of wavelengths. An optics model is fitted to these data and the optical properties are extracted.

Rayleigh scattering is measured by fixing a mask on the laserball which has a small hole at the bottom so that a collimated beam is formed. From the distribution of detected photons, the scattering may be determined [65].

2.8.4 Energy Calibration

An important part of the detector's optical response not measured by the laserball is the PMT quantum efficiency, which is the probability that a photoelectron is produced and detected when a photon strikes the PMT. The quantum efficiency is wavelength dependent due to the wavelength-dependence of the PMT photocathode and the reflectivity of the reflectors. The quantum efficiency must be measured with a light source that always produces the same amount of light and an ^{16}N γ-ray source has been chosen for this task. The ^{16}N is produced via (n, p) on the oxygen nuclei in CO_2 gas and β-decays to an excited state of ^{16}O which emits a 6.13 MeV γ-ray. The β provides a tag for the 6.13 MeV γ-ray which produces a Čerenkov light-emitting electron primarily through Compton scattering. Because the source always produces the same energy γ, it produces (on average) the same light output and, thus, allows for a calibration of the efficiency for light detection by the PMTs. The *effective quantum efficiency* can change with time (due to changes in the reflectors, changes in the PMT gain, etc.), so it is necessary to do the ^{16}N calibration regularly.

The ^{16}N source produces a Compton scattered electron with an energy of roughly 5 MeV and is used to give a calibration of the response of the detector to an electron of this energy (for example, the number of PMTs fired within a certain window of time).

This response varies by $\sim 10\%$ with position of the source within the AV and also varies slightly with time.

For the detector response at high energies, a source is used which produces a 19.8 MeV γ-ray from the reaction

$$p + t \rightarrow {}^{4}\mathrm{He} + \gamma.$$

2.8.5 Neutron Calibration

To calibrate neutron detection efficiency, an encapsulated ^{252}Cf fission source is used [66]. Each fission decay of ^{252}Cf produces on average 3.7676 ± 0.0047 neutrons. The energy distribution of the resulting γ-cascade from the capture of these neutrons agrees well with Monte Carlo predictions. ^{252}Cf data may be cleaned using the Burst Analysis method [67], which removes the first event in each neutron "burst" defined by a specific time window. The first event in each "burst" typically contains a considerable fraction of γ's.

2.8.6 Background Calibration

In the salt phase, low energy calibration is achieved from ^{24}Na decay. Neutrons produced via photodisintegration of deuterium by a "strong" Th γ source capture on ^{23}Na producing ^{24}Na* which decays with a half life of 15 hours.

Untriggered thorium and uranium chain sources, encapsulated in acrylic, are used to measure the detector's response to low energy backgrounds caused from nuclei in the ^{232}Th and ^{238}U chains. Also, radon has been injected into the D_2O to measure the detector response to radon. Background levels and the methods used to obtain them are discussed in Chapter 5.

2.9 Water Systems

Maintaining low levels of radioactive contamination in the light water and heavy water regions of the SNO detector is critical for the experiment. The low energy background "wall" of Čerenkov light produced by electrons and γ's from radioactive contaminants places a lower limit on the energy which may be accurately analyzed. A more detailed description of water systems in SNO is available in [44].

Heavy Water System

The heavy water system is responsible for purifying and assaying the D_2O. Before the D_2O was added to the AV, it was passed through ion-exchange columns to remove ionic impurities such as K and passed through a reverse osmosis system. D_2O in the AV is recirculated and passed through ion absorption columns to reduce impurities to very low levels. Before returning to the AV, the water passes through an ultrafiltration unit to remove any fine particles introduced by assays for radioactive content and other chemical properties of the water. Radiochemical assays are made using loaded filters to extract ions. One method [68] uses microfilters coated with HTiO to remove Th, Pb, and Ra. The Ra is eluted from the filters and counted by observing $\beta - \alpha$ coincidences from its decay. In another method [69] the D_2O is passed through a column of MnO_x beads and radium is identified using alpha spectroscopy on the emanated radon. Radon is also extracted directly from the water and counted [44].

Light Water System

The H_2O used in SNO comes initially from a plant that serves the mine. The water is first deaerated to removed dissolved O_2 and N_2. It then enters a series of filters to remove large and fine particles and softeners to remove Ca, Mg, and Fe. Initially, the water was then passed through a reverse osmosis system to achieve ultra-filtration, but this system is no longer used. The water is then exposed to mercury UV lamps to kill bacteria, passed through ion-exchange, degassed to remove O_2 and Rn, regassed with N_2, and cooled to 10°C before entering the detector. To maintain the highest purity levels, the light water is continually recirculated, monitored, and re-passed through the light water purification system beginning with the UV unit. There are 1700 tonnes of water between the AV and the PMT support structure and 5700 tonnes between the support structure and the cavity walls. A plastic, slightly porous barrier separates these regions. Radio assays are also carried out on the light water.

Cover Gas System

Radon-rich mine air can enter the H_2O and D_2O from leaks above the detector. Nitrogen gas, boiled off from a liquid nitrogen dewar, provides a physical barrier between the detector water volume and laboratory air to maintain acceptable radon levels in the water.

2.10 Addition of Salt

In June 2001, SNO entered its second phase of operation by adding two tonnes of NaCl to the 1000 tonnes of pure D_2O in the detector. The salt serves to enhance the detection of the neutral current signal. In the salted D_2O, neutrons are most likely to capture on ^{35}Cl, producing a γ-cascade with total energy of 8.6 MeV and an average of 2–3 emitted γ's.

Changes to the Neutron Signal

The neutron capture efficiency versus radial position is shown in Figure 2.8 for both the pure D_2O phase and salt phase. The volume-weighted neutron capture efficiency increases from 30% in pure D_2O to around 83% in the salted D_2O. As a result, the path length of the neutron decreases and the probability of neutron capture on the acrylic vessel (which does not produce a visible signature) is reduced. This flattens the radial profile of the neutrons, which was more distinctive from the CC and ES profiles in the pure D_2O phase. The change to the radial profile is obvious in Figure 2.9. Table 2.1 summarizes the changes to the neutron detection as a result of the NaCl being added to the D_2O[13].

	Pure D_2O	Salted D_2O
Neutron Diffusion Length	110 cm	30 cm
Volume-weighted Capture Efficiency	30%	83%
Volume-weighted Detection Efficiency	14.4%	39.9%

Table 2.1: Effect of salt addition on neutron detection. For the detection efficiency, a lower limit placed on effective electron kinetic energy is 5.0 MeV for the pure D_2O phase and 5.5 MeV for the salted D_2O phase and a fiducial volume of radius 550 cm is used for both phases [1, 26].

The higher capture efficiency increases the amplitude of the neutral current signal. The higher energy release for neutron capture on ^{35}Cl shifts the signal to higher energies relative to the NC spectrum observed in pure D_2O. This is demonstrated in Figure 2.10 which shows the predicted energy distributions for the NC signal in both salt and pure D_2O and the CC signal, which is the same in both detector scenarios.

Neutral current events are likely to produce more than one cone of Čerenkov light from the γ-cascade in salted D_2O, so the events are typically more isotropic than single-ring electron events. Thus, the isotropy of an event becomes a powerful tool to separate the NC signal from CC and ES signals.

Radioactivity and Background from Salted D_2O

Internal radioactivity creates neutron background to the neutral current signal. Before the salt was added to the heavy water, it was purified by flow over MnO_x and HTiO which reduced its thorium and uranium concentrations by a factor of about 100. Table 2.2

[13] Diffusion length is defined as the distance between the point at which the neutron becomes thermal and the point of its final capture.

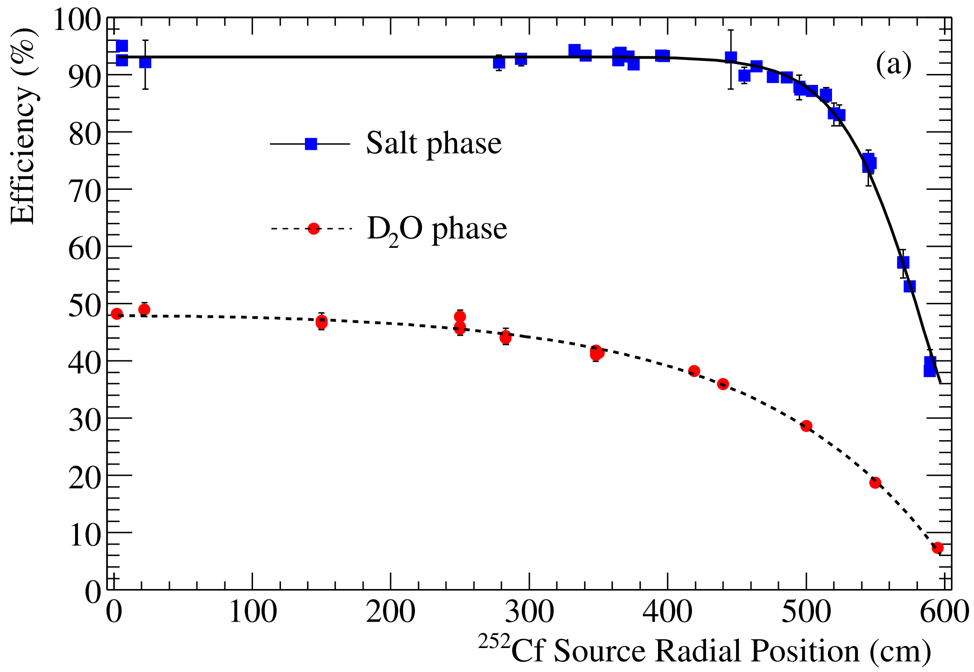

Figure 2.8: Neutron capture efficiency for the pure D_2O and salted D_2O phases.

gives the target purity and the measured values of radioactivity in the pure D_2O [26] and in the salted D_2O. Additional neutron background in the salt phase comes from the activation of sodium and this is further discussed in Chapter 5. The average rate of neutron production from activity in the salted D_2O is $0.72^{+0.24}_{-0.23}$ neutrons per day [1].

Source	Limit (yields < 1 n/day)	Pure D_2O (measured)	Salted D_2O (measured)
^{232}Th	$< 3.7\times10^{-15}$g/g D_2O	1.6×10^{-15}g/g D_2O	1.0×10^{-15}g/g salt D_2O
^{238}U	$< 4.5\times10^{-14}$g/g D_2O	1.8×10^{-14}g/g D_2O	7.7×10^{-15}g/g salt D_2O

Table 2.2: Thorium and uranium concentrations in pure D_2O and salted D_2O. The values for salted D_2O are preliminary [70].

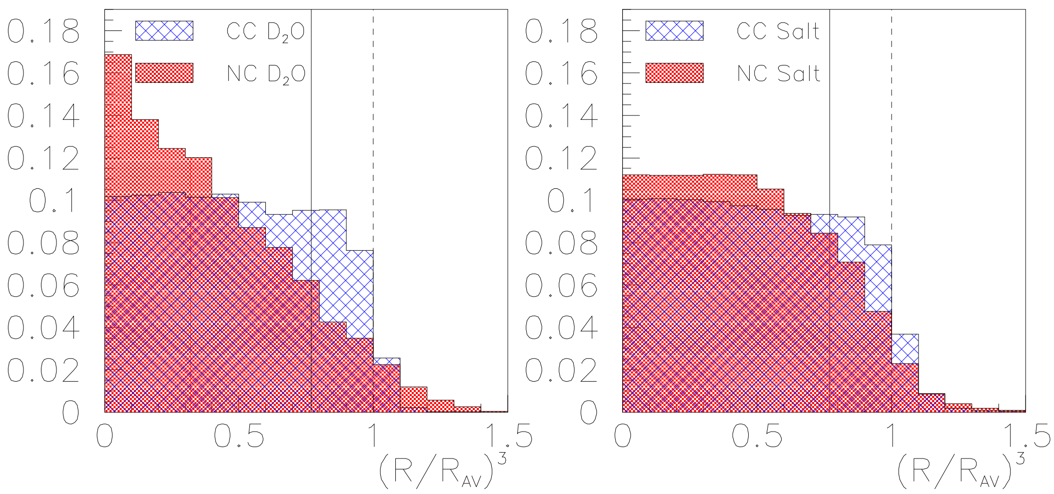

Figure 2.9: Radial profile of CC and NC events in the pure D_2O and salted D_2O phases. The dashed line indicates the position of the AV and the solid line indicates a fiducial volume of radius 550 cm.

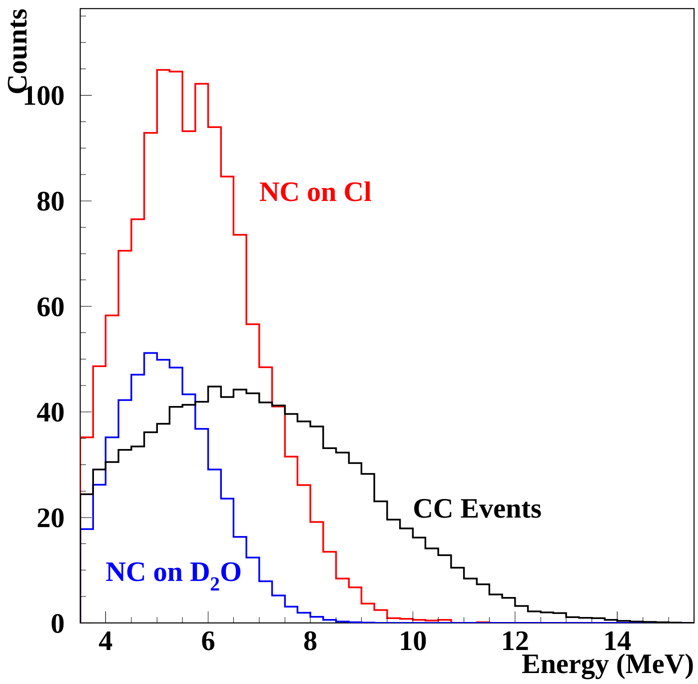

Figure 2.10: The predicted energy spectra after one year of running for the NC signal in both pure and salted D_2O and for the CC signal which remains the same in both scenarios.

Chapter 3

Isotropy Parameters

As explained in Section 1.6.2, the MSW effect may distort the energy spectrum of electron neutrinos emitted from the Sun. Two major goals of SNO are measurement of the spectrum using the detected electrons from the charged current (CC) interaction and limits on the oscillation parameters Δm^2_{12} and θ_{12} which are related to the ratio of the fluxes inferred from the CC and neutral current (NC) rates (which is equivalent to the ν_e survival probability integrated over the detector energy threshold). The energy spectrum of charged current electrons is closely related to that of the incoming neutrinos. The neutral current energy spectrum is dependent on the Q-value of the neutron capture reaction only (6.25 MeV in pure D_2O and 8.6 MeV in salted D_2O) and the rate leads to a measure of the flux of all active ^8B neutrinos over 2.2 MeV.

In the pure D_2O phase of SNO, the characteristic energy spectra of CC and NC events (displayed in Figure 2.10) was the most powerful parameter with which to statistically separate the two event signals. The analysis therefore relied on assumptions about the energy dependence of the ν_e survival probability[1]. In the salted D_2O phase of SNO, we are able to exploit the difference in event topologies between CC and NC events so that it is unnecessary to use the predicted solar neutrino energy spectrum. Using topology rather than energy to statistically separate the signals allows for model-*independent* measurement of the charged current energy spectrum and derived limits on Δm^2_{12} and θ_{12}.

3.1 Event Signatures

This section explains the difference between electron and neutron event topology in the salted D_2O phase of SNO. The signatures of the two types of events are not so distinct that they may be separated on an event-by-event basis; however, the topology of an event may be parameterized and used to statistically separate the two event classes.

[1] No flavor transformation and undistorted ν_e energy spectrum were assumed [47].

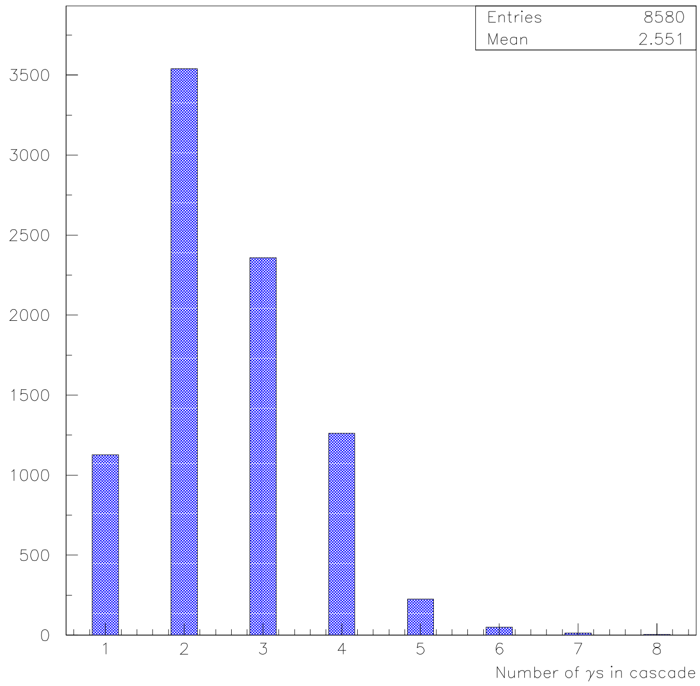

Figure 3.1: Distribution of ^{36}Cl γ multiplicity from neutron capture on ^{35}Cl.

The signal of a charged current or elastic scattering event in the SNO detector is a ring-like pattern of PMT hits created by a single Čerenkov light-producing relativistic electron. The majority of the hits lie at about 42° (the Čerenkov angle) from the direction of the electron. However, the ring pattern is significantly broadened by multiple scattering of the electron.

During the salted D_2O phase of SNO neutral current events create a number of rings when a neutron captured on ^{35}Cl causes a γ-cascade as the excited ^{36}Cl nucleus decays to its ground state[2]. The γ's predominantly Compton scatter electrons which then produce Čerenkov light. The decay scheme of ^{36}Cl is quite complicated because it has a large number of levels in its decay to the ground state (details may be found in [71]). The distribution of the number of γ's above the Čerenkov threshold in a cascade resulting from neutron capture on ^{35}Cl is displayed in Figure 3.1. The mean multiplicity is about 2.5 γ's. It is also possible that a higher energy γ will produce more than one Čerenkov light-emitting electron through scattering. However, in many cases the majority of the energy is carried away by one dominant γ, so the neutron and electron event topologies are not so distinct.

[2] In the pure D_2O phase, neutrons capture on deuterium and the resulting excited tritium emits one γ-ray.

Figures 3.2(a) and 3.2(b) show the SNO event display for neutrino candidates from the salt data set. The events chosen have a relatively high number of hit PMTs so that the Čerenkov cones are clearly visible. The geodesic grid lines show the shape of the structure which holds the PMTs (the PSUP). The colors of the lines, stretching from the fit vertex to all of the hit PMTs, indicate the time that the PMT was fired relative to the fit event time. The timing distributions are below the geodesics. The first event is a single-ring event. The few stray hits are most likely due to scattering and random PMT noise. The second event has a much more isotropic light distribution, implying that there were several Čerenkov cones produced, but it is difficult to tell exactly how many. More typical events have lower statistics and the rings are even less clear.

A typical Čerenkov event in the SNO detector contains less than 100 detected photons. With such small statistics it is difficult to recognize the number of rings especially with the large smearing of the rings due to scattering. There also exists the probability that a neutron event will contain only one ring. Therefore, it is not possible to distinguish between electron-type (CC and ES) and neutron-type (NC) signals on an event-by-event basis. However, the distribution of fired PMTs is typically more isotropic for neutral current events than for electron-type events. The angular distribution of PMT hits in an event may be used to characterize the *isotropy* of an event. A parameterization of the isotropy may be used to statistically separate the two event types using maximum likelihood techniques. The isotropy of CC and ES signals is expected to be the same and it is possible to statistically separate ES from CC and NC signals using the event direction with respect to the Sun [47]. So, the use of isotropy to statistically separate CC and NC events only will be studied here.

Three parameters used to quantify event isotropy are defined and compared in this chapter:

- $\langle\theta_{ij}\rangle$
- $\beta_{14} = \beta_1 + 4\beta_4$
- $\mathcal{L}_\theta$

Numerous other isotropy parameters were studied in [72, 73, 74] and one of these, CFRIP, is also described in this chapter.

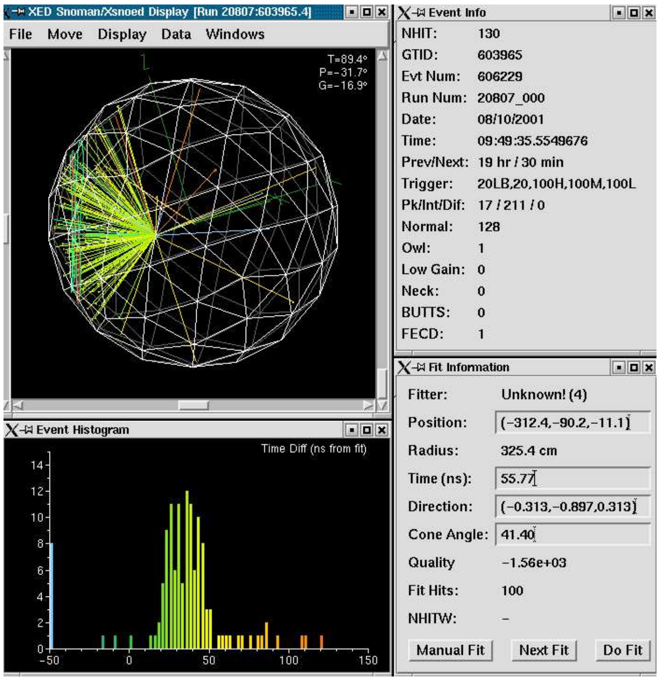

(a) Single ring neutrino candidate.

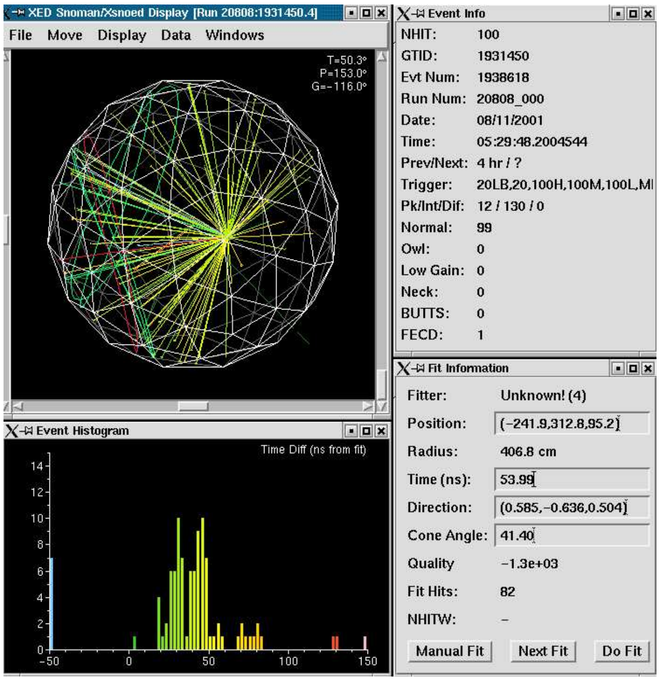

(b) Multiple ring neutrino candidate.

Figure 3.2: Event display for events from the salt data set.

3.2 Definition of Separability

Given normalized probability density functions (PDFs) A and B of a particular parameter for two event classes, a measure of the separation power of the parameter can be obtained from the overlap of the two PDFs [75] (the derivation of the overlap is given in Appendix B). The overlap of two PDFs with N bins is given by

$$A \otimes B = \sum_{i=1}^{N} \frac{A_i B_i}{aA_i + bB_i}, \tag{3.1}$$

where a and b are the fraction of the number of events belonging to each of the distributions A and B, where $a+b=1$. A_i and B_i are the probabilities of an event of each event class lying in bin i where $\sum_i A_i = \sum_i B_i = 1$. Also, $A \otimes A = B \otimes B = 1$. The separation, $\mathcal{S}$, is given by $\mathcal{S} = (1 - A \otimes B)$, and this value lies between 0 and 1. A value of $\mathcal{S} = 0$ means that the distributions completely overlap; a value of $\mathcal{S} = 1$ means that they are completely distinguishable and event-by-event separation may be achieved. This measure is used in this chapter to compare the different isotropy parameters. Examples of $A \otimes B$ values are shown in Figure 3.3. The calculated values of separability quoted were all made assuming there are $\sim$ 2000 events of each type (CC and NC). However, the distributions shown have higher statistics.

It is shown in Appendix B that the overlap is related to the uncertainty on the extracted numbers of events from the two classes, N_A and N_B, obtained from a χ^2 fit[3] of a data set D which has N_D events and is composed of contributions from A and B. The uncertainty on N_A is given by

$$\sigma_{N_A}^2 = \frac{aN(1 - aA \otimes B)}{1 - A \otimes B}. \tag{3.2}$$

3.3 Monte Carlo Specifics

This study of isotropy parameters was carried out entirely using Monte Carlo. SNOMAN version 4.0191 was used to create 200,000 electrons and γ-cascades. The electrons were generated isotropically throughout the salted D_2O with energies corresponding to the CC energy spectrum. The γ-cascades were also generated isotropically throughout the salted D_2O and have energies corresponding to γ's resulting from neutron capture on ^{35}Cl. The Monte Carlo includes 2 mg/g D_2O of salt (NaCl) added to the heavy water.

A cut is placed on all Monte Carlo events to accept only those which have at least 40 PMT hits ($N_{hit} \geq 40$). This corresponds to roughly 5 MeV in total energy. Unless

[3] To separate CC and NC events in the SNO data sets, maximum likelihood fitting is used which, in the limit of large statistics, gives the same result as χ^2 minimization [76].

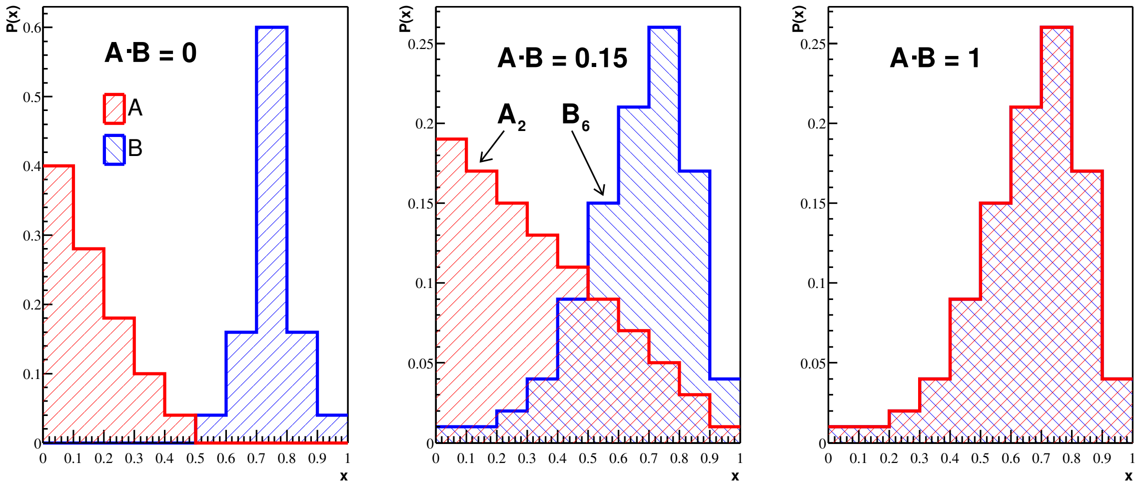

Figure 3.3: The overlap, $A \otimes B$, for histograms A and B.

otherwise specified, all studies in this section were carried out with the Grid Fitter [60, 61], which is briefly discussed in Section 2.7.1. Reflected photons and PMT noise can weaken the separating power between single and multi-ring events by making events appear more isotropic. To reduce this effect, a time cut is implemented so that most of these hits are not included in the isotropy calculation. This cut is given by

$$|d_i - (c/n)(t_i - t_{fit})| \leq 200 \text{ cm}, \tag{3.3}$$

where d_i is the distance between PMT i and the fit vertex, t_{fit} is the fitted time of the event, t_i is the firing time of PMT i, and c/n is the mean group speed of light. All times are in nanoseconds and distances are in centimeters. The left-hand side of (3.3) is closely related to the timing residual described in Chapter 2. The hits accepted by (3.3) roughly fall into the area that is shaded red in Figure 2.6. Figures 3.2(a) and 3.2(b) show distributions of PMT hit times.

3.4 Definition of Event Axes

Refer to Figure 3.4, which is a pictorial representation of a number of PMT hits in a single ring Čerenkov event. The event's fit vertex and normalized direction, $\mathbf{u}$, are shown. The vector $\mathbf{r}_i$ extends from the fit event vertex to hit i and $\mathbf{r}_j$ to hit j. Using these vectors, the following quantities may be defined:

$$\theta_{ij} = \text{angle between hits } i \text{ and } j \text{ from fit vertex} \tag{3.4}$$

$$\theta_i = \text{angle between hit } i \text{ and event direction from fit vertex} \tag{3.5}$$

$$\cos\theta_i = \frac{\mathbf{u}\cdot\mathbf{r}_i}{|\mathbf{r}_i|}. \tag{3.6}$$

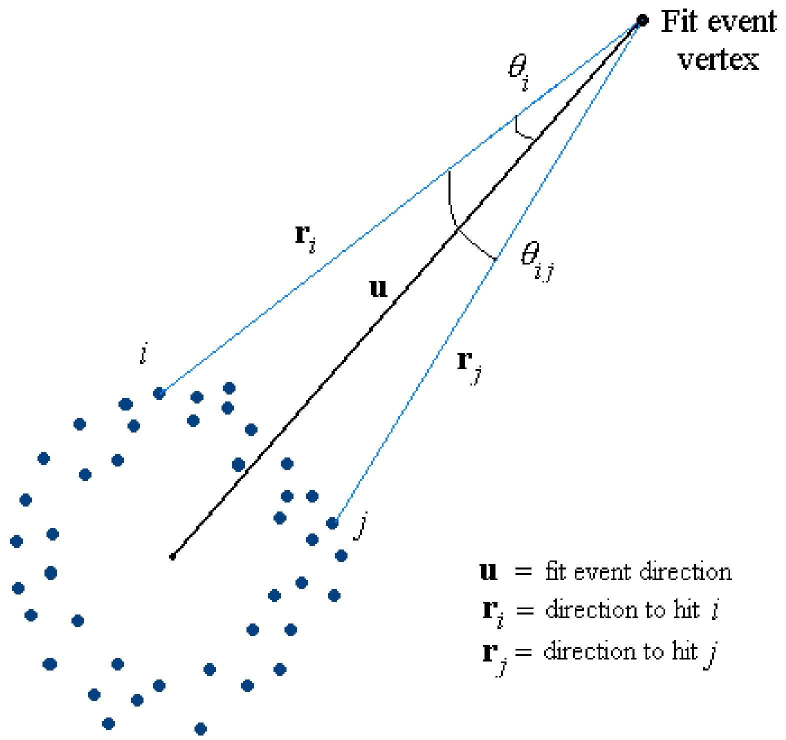

Figure 3.4: Diagram of relevant angles in a single ring Čerenkov event (in a typical event, the ring is significantly smeared through multiple scattering of the electron).

3.5 Isotropy Parameters Defined

3.5.1 $\langle\theta_{ij}\rangle$

The parameter $\langle\theta_{ij}\rangle$ is defined as the average angle between all PMT hits in an event, relative to the fitted vertex:

$$\langle\theta_{ij}\rangle = \frac{2}{N(N-1)}\left[\sum_{i=1}^{N-1}\sum_{j=i+1}^{N}\theta_{ij}\right]. \tag{3.7}$$

Distributions of $\langle\theta_{ij}\rangle$ are displayed in Figure 3.5 for charged current and neutral current events. The number in the plot indicates the separability of the two distributions (which is described in Section 3.2). Notice that the NC events have higher $\langle\theta_{ij}\rangle$ values because of the greater number of large angles in multi-ring events.

This parameter has been used in SNO analyses to separate low energy background signals from ^{214}Bi β-decays and γ-emitting ^{208}Tl β-decays [77, 78].

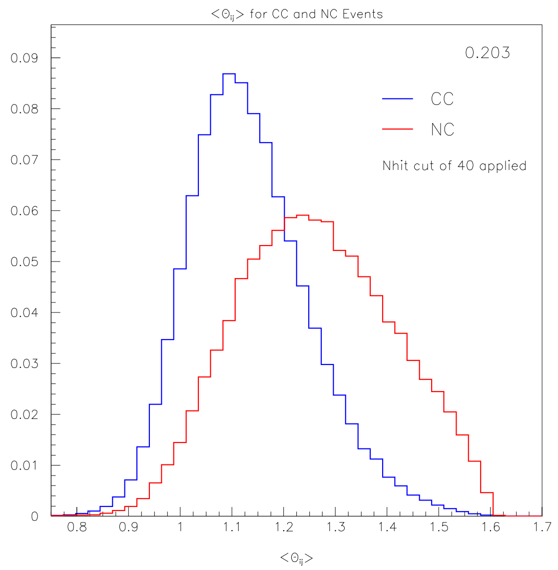

Figure 3.5: Distributions of $\langle\theta_{ij}\rangle$ for CC and NC events. The number in the upper right-hand corner indicates the separability, $\mathcal{S}$, of the two distributions.

3.5.2 Legendre Polynomial (Beta) Parameters

The following is a continuation of work contained in theses by M. Thorman [75] and S. Brice [79].

Let $f(\theta, \phi)$ be a normalized, continuous distribution of Čerenkov light. This distribution may be expanded using a linear combination of orthogonal spherical harmonics,

$$f(\theta, \phi) = \sum_{l=0}^{\infty} \sum_{m=-l}^{l} \alpha_{lm} Y_{lm}^{*}(\theta, \phi) \tag{3.8}$$

where

$$\alpha_{lm} = \int f(\theta, \phi) Y_{lm}(\theta, \phi) d\Omega \tag{3.9}$$

as given by the orthonormality of $Y_{lm}(\theta, \phi)$.

Applying the normalization condition, $\int f(\theta, \phi) d\Omega = 1$, we have the expansion parameters, α_{lm}, as simply the average value of $Y_{lm}(\theta, \phi)$ over the distribution.

The set of PMT hits in an event is a discrete sample from this distribution so the expansion parameters may be estimated by averaging over the N individual hits,

$$\alpha_{lm} = \frac{1}{N} \sum_{i=1}^{N} Y_{lm}(\theta_i, \phi_i). \tag{3.10}$$

Define a set of rotational invariants, the beta parameters, to be

$$\beta_l'' = \sum_m |\alpha_{lm}|^2. \tag{3.11}$$

Using the estimate for α_{lm}, we have

$$\sum_m |\alpha_{lm}|^2 = \frac{1}{N^2} \sum_{i,j} \sum_m Y_{lm}(\theta_i, \phi_i) Y_{lm}^{*}(\theta_j, \phi_j) \tag{3.12}$$

and thus, by the Spherical Harmonic Addition Theorem,

$$\beta_l'' = \frac{2l+1}{4\pi N^2} \sum_{ij} P_l(\cos\theta_{ij}), \tag{3.13}$$

where θ_{ij} is the angle between the hits labelled i and j and P_l are Legendre polynomials. The first six Legendre polynomials are listed in Appendix C.

Altering (3.13) to avoid a double summation and to avoid including the angle between each hit and itself, we are left with

$$\beta_l' = \frac{2l+1}{2\pi N(N-1)} \left[\sum_{i=1}^{N-1} \sum_{j=i+1}^{N} P_l(\cos\theta_{ij}) \right]. \tag{3.14}$$

For simplicity, we remove a factor of $(2l+1)/4\pi$ and use

$$\beta_l = \frac{2}{N(N-1)}\left[\sum_{i=1}^{N-1}\sum_{j=i+1}^{N} P_l(\cos\theta_{ij})\right]. \tag{3.15}$$

The β_l quantities are rotationally invariant parameters which give us information about the spatial hit pattern of an event. Note that β_1 is closely related to $\langle\theta_{ij}\rangle$, except that it involves the average *cosine* of the angle between hits, rather than just the angle.

Figure 3.6 shows distributions of the first five harmonic beta parameters for charged current and neutral current events. Again, the numbers in the plots indicate the separability of the distributions. Note that in the case of the beta parameters, lower values of β_i indicate greater isotropy (the reverse is true for $\langle\theta_{ij}\rangle$ distributions).

Figure 3.6 shows that β_1 gives the best separability between the two event classes (approximately the same as $\langle\theta_{ij}\rangle$). β_2 and β_3 give almost no separation, while β_4 and β_5 give some.

The first six Legendre polynomials are displayed in Figure 3.7. Perfect single ring events have an average Čerenkov angle of 42° and the maximum angle between

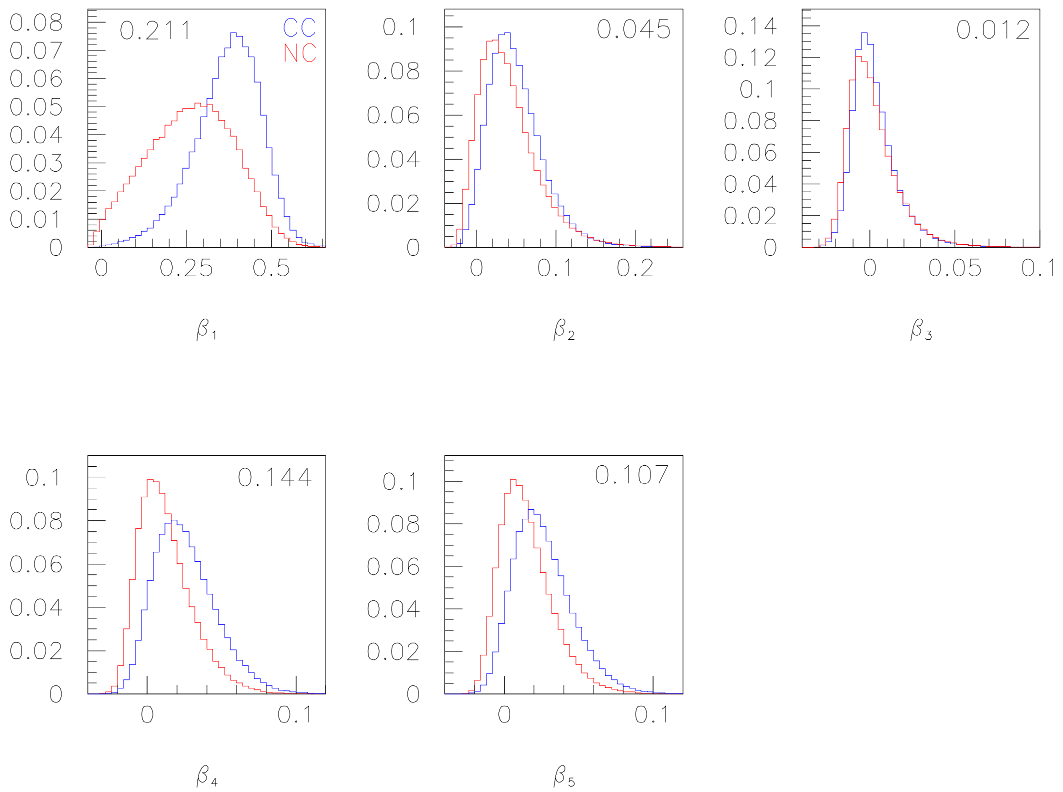

Figure 3.6: The Legendre Polynomial (Beta) Parameters β_1 to β_5 for CC and NC events. The numbers in each plot represent the separability between the two PDFs.

two hits is 84° ($\cos 84°=0.10$). Figure 3.8 shows the distribution of $\cos\theta_{ij}$ values for a number of charged current and neutral current events. Noticeable, particularly in the CC distribution, is the "knee" at $\cos\theta_{ij}=0.10$. It is also apparent that there are a lot of angles between PMT hits that are greater than twice the Čerenkov angle, particularly for NC events.

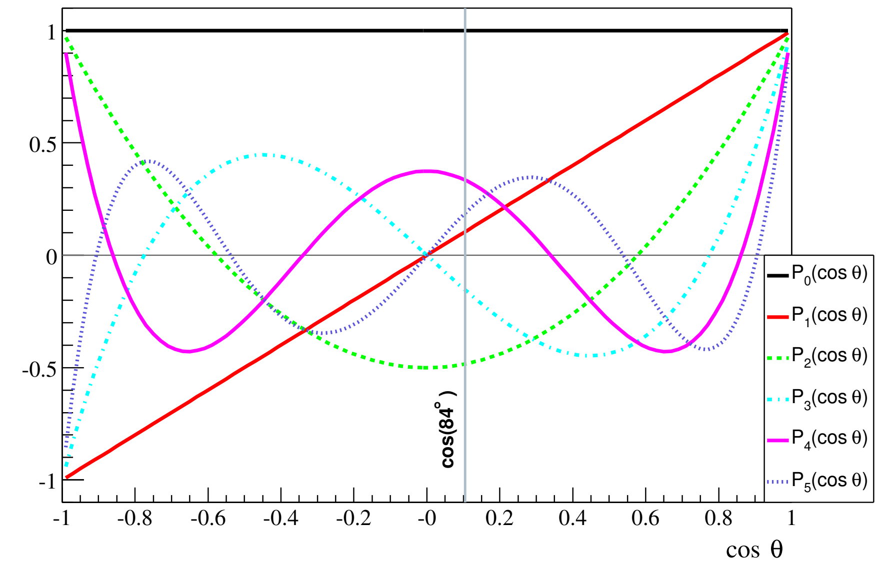

Figure 3.7: The first six Legendre Polynomials.

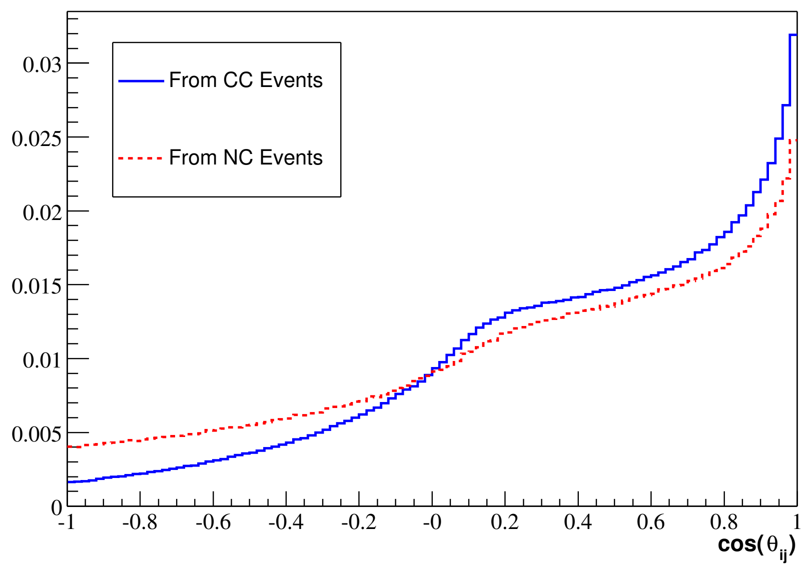

Figure 3.8: Distribution of $\cos\theta_{ij}$ values from CC and NC events.

Enhanced separability may be obtained using linear combinations of β_1 and β_4 or β_5. Figure 3.9 shows different linear combinations of β_1 and β_4. From these plots it is clear that $\beta_1 + 4\beta_4$ gives the best separation. A similar study was also done using linear combinations of β_1 and β_5 which gave slightly less separability.

Figure 3.10 shows various contour plots:

- β_4 vs. β_1
- β_5 vs. β_1
- β_5 vs. β_4
- β_5 vs. $\beta_1 + 4\beta_4$

The lines indicate constant values of $\beta_1 + 4\beta_4$, $\beta_1 + 4\beta_5$, and $\beta_1 + 4\beta_4 + 1.5\beta_5$, respectively. The upper left-hand plot visually helps to explain why $\beta_1 + 4\beta_4$ gives the greatest separation (as opposed to other linear combinations of β_1 and β_4). The lines

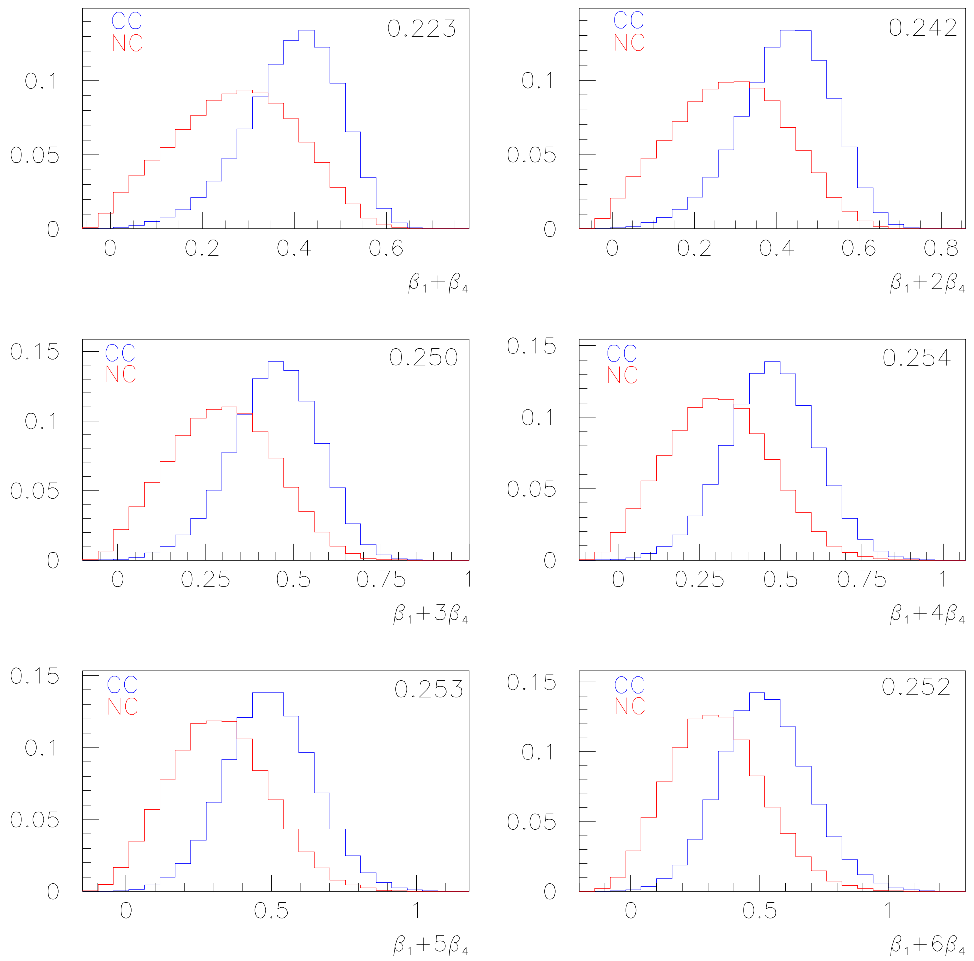

Figure 3.9: Linear combinations of β_1 and β_4. The numbers in the plots give the separability.

run almost optimally between the peaks of the CC and NC contours and thus optimal separation is achieved by projection along these lines. A similar combination of β_1 and β_5 is nearly as effective. However, adding any amount of β_5 to $\beta_1 + 4\beta_4$ does not improve the separability significantly ($+1.5\beta_5$ gave the optimal separability which was only $\sim$1% better than $\beta_1 + 4\beta_4$ alone). This is most likely because β_4 and β_5 are strongly correlated, as can be seen in the bottom left-hand plot. The contour plot of β_5 versus $\beta_1 + 4\beta_4$ shows that the separability was not increased much by adding in β_5 because most of the power is in $\beta_1 + 4\beta_4$. The lines could be rotated to vertical and there would be almost as much separation between the two signals. Including β_2 or β_3 to $\beta_1 + 4\beta_4$ does not increase the separability, as expected from Figure 3.6. From this point on, $\beta_1 + 4\beta_4$ will be referred to as β_{14}.

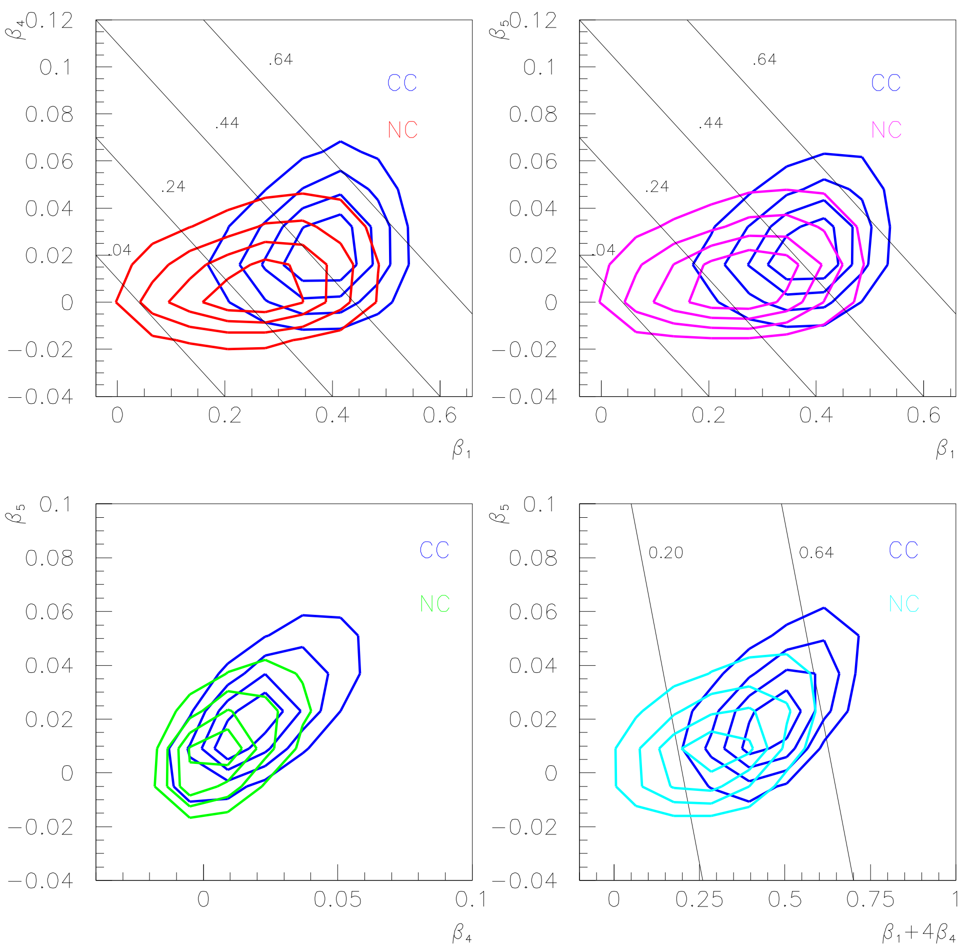

Figure 3.10: Contour plots of β_4 vs. β_1, β_5 vs. β_1, β_5 vs. β_4, and β_5 vs. $\beta_1 + 4\beta_4$. The numbers show the values for lines with constant $\beta_1 + 4\beta_4$, $\beta_1 + 4\beta_5$, and $\beta_1 + 4\beta_4 + 1.5\beta_5$.

3.5.3 $\mathcal{L}_\theta$

The value $\cos\theta_i$ is the cosine of the angle between the fitted direction of an event and a PMT hit from the fitted vertex. Each event will have a number of values for this parameter equal to the number of PMT hits. It would be expected that distributions of this parameter should peak around the cosine of the Čerenkov angle, particularly for CC events, and should be more spread out for NC events as the hits are more isotropic due to the multiple number of γ's producing Čerenkov rings. Distributions of $\cos\theta_i$ for CC and NC events are found in Figure 3.11. The distributions are normalized and only events which have more than 40 PMT hits are used.

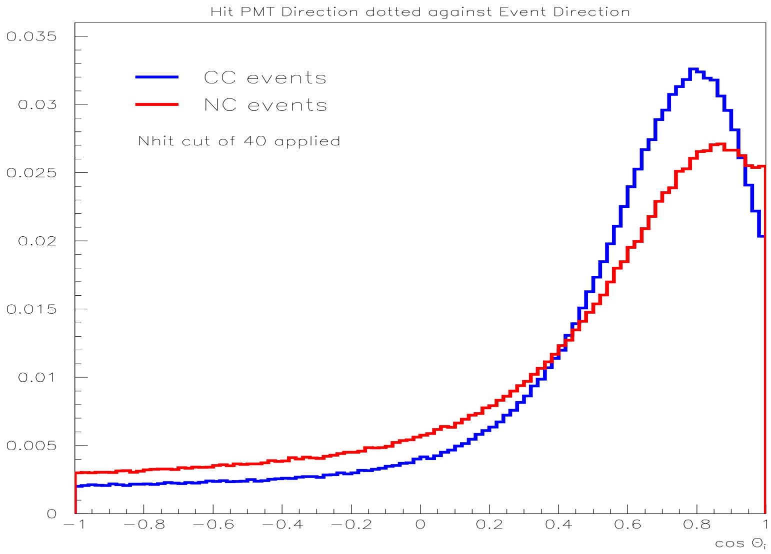

Figure 3.11: Distributions of $\cos\theta_i$ for CC and NC events.

There is quite a bit of overlap between these two distributions, which means that these distributions themselves are not very useful PDFs for signal extraction. Let us define a likelihood ratio for an event which is the relative probability of the distribution of $\cos\theta_i$ values for that event belonging to the CC or NC event distribution. This likelihood ratio is given by

$$\mathcal{R}_\theta = \prod_{i=1}^{N} \frac{P_{CC}(x_i)}{P_{NC}(x_i)}, \tag{3.16}$$

where x_i=$\cos\theta_i$, $\mathrm{P}_{CC}(x)$ and $\mathrm{P}_{NC}(x)$ are the normalized probability density functions for $\cos\theta_i$, and we are summing over the number of PMT hits in the event, N. For computational simplicity, it is the logarithm of this ratio which is used,

$$\mathcal{L}_\theta = \ln(\mathcal{R}_\theta) = \sum_i \ln(P_{CC}(x_i)) - \sum_i \ln(P_{NC}(x_i)). \tag{3.17}$$

Distributions of $\cos\theta_i$ have an energy dependence, displayed in Figure 3.12 where $\cos\theta_i$ is plotted for different N_{hit} ranges [4]. Parameterized probability density functions of $\cos\theta_i$ were found by fitting skewed Gaussian functions with the form found in (3.18) to each of the N_{hit}-divided $\cos\theta_i$ distributions.

$$f(\cos\theta_i) = A \cdot \exp\left[\frac{-(B-x)^2}{2(C+Dx+Ex^2)}\right] \tag{3.18}$$

The parameters A, B, C, D, and E were found as a function of N_{hit}. The N_{hit}-dependent PDFs were then used to calculate the likelihood ratio, $\mathcal{L}_\theta$. From (3.17), this value should be positive for CC events and negative for NC events. The $\mathcal{L}_\theta$ distributions are found in Figure 3.13.

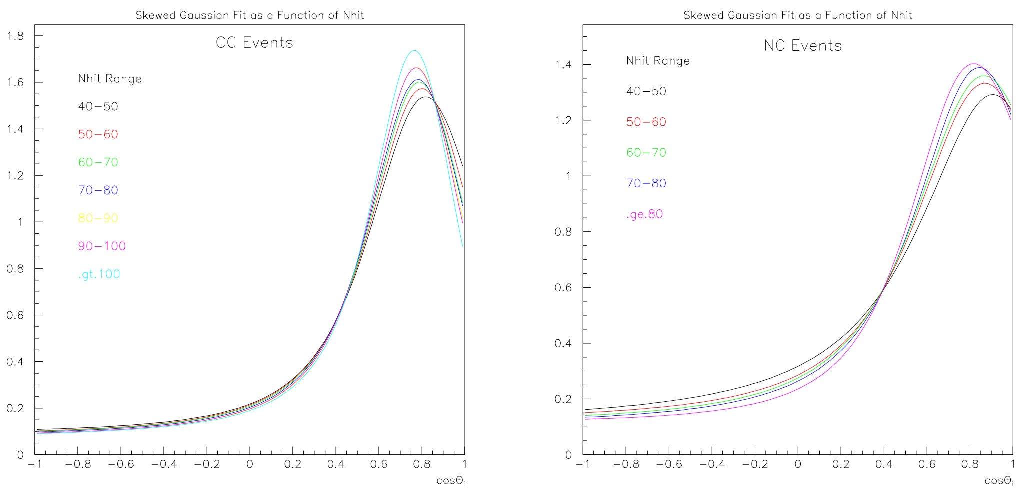

(a) CC Events

(b) NC Events

Figure 3.12: N_{hit}-dependent distributions of $\cos\theta_i$. Arbitrary units on the y-axis.

3.5.4 CFRIP

Another isotropy parameter, called CFRIP (for Correlation Function Ring Inner Product) was developed at the University of Pennsylvania by Bill Heintzelman [73, 74]. This parameter utilizes *correlation functions*, which are essentially distributions of the cosines of angles between all pairs of hits in an event with respect to the fit event vertex. These are shown in Figure 3.8 for CC and NC events. Correlation functions are created for each

[4] The energy dependence of β_{14} will also be shown in Chapter 7.

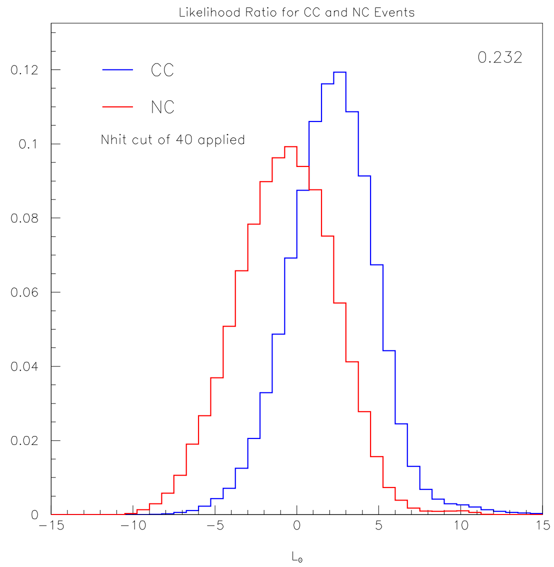

Figure 3.13: Distributions of $\mathcal{L}_\theta$ for CC and NC events. The number in the upper right-hand corner indicates the separability of the two distributions.

event in a data set and compared with the correlation function for an ideal ring which would be created by an electron emitting Čerenkov light in a perfect cone of half-angle 42° and a width of about 8°. The value of CFRIP for an event is the dot (or inner) product of the event correlation function with the standard function. The *inner product*, defined as $\sum_{i=1}^{N} \epsilon_i \rho_i$, where N is the number of bins in the correlation functions, ϵ_i is the number of angles in the i^{th} bin of the normalized correlation function for the event, and ρ_i is the fraction in the i^{th} bin of the normalized perfect cone correlation function. This parameter has a separability comparable to that of the other parameters discussed in this chapter. Comparisons may be found in [74].

3.6 Summary of Isotropy Parameter Separabilities

In this section, the separabilities for the three different angular parameters are compared. The comparison is made for different energy ranges (the energy estimator N_{hit} is chosen). The isotropy of an event has some dependence on the energy of that event. Higher energy electrons have straighter tracks, so the Čerenkov cone is better defined and the distribution of PMT hits is less isotropic and more peaked at the Čerenkov angle, as evident in Figure 3.12. The dependence is stronger for neutrons since events with a large multiplicity have a lower energy because more energy is lost in Compton scattering because of the Čerenkov energy threshold. The energy dependence of β_{14} is studied in detail in Chapter 7, where 2-dimensional energy-dependent isotropy PDFs are created.

Table 3.1 gives the separability between CC and NC event distributions of each isotropy parameter for various N_{hit} ranges. It is clear that the Legendre polynomial parameter, β_{14}, gives the highest separability for practically all N_{hit} ranges.

N_{hit} Range	$\langle\theta_{ij}\rangle$	β_{14}	$\mathcal{L}_\theta$
40-50	0.230	0.313	0.243
50-60	0.185	0.212	0.179
60-70	0.164	0.189	0.181
70-80	0.198	0.225	0.223
$\geq$80	0.128	0.178	0.188
$\geq$40	0.203	0.256	0.232

Table 3.1: Separability between CC and NC distributions for different isotropy parameters.

A very nice study was conducted by Jeanne Wilson to determine which isotropy parameter gives the lowest statistical uncertainty on the extracted number of CC and NC events obtained using maximum likelihood signal extraction[5] [88]. One hundred simulated "data" sets containing 300 CC and 300 NC events were created and the numbers of CC (N_{CC}) and NC (N_{NC}) events were then extracted using likelihood maximization. The various isotropy parameters found in Table 3.2 were used as PDFs in addition to characteristic PDFs of the radial fit position (R^3_{fit}) and the event direction with respect to the Sun ($\cos\theta_\odot$). Not only was β_{14} studied, but also various other combinations of the Legendre polynomial parameters β_1 and β_4. One of the main purposes of this study was to determine if the statistical uncertainty on N_{CC} and N_{NC} would decrease if a two dimensional PDF of β_4 vs. β_1 were used, as opposed to a one dimensional $\beta_1 + 4\beta_4$ PDF. Also studied was the use of separate 1D PDFs of β_1 and β_4. Because there is an energy dependence on the isotropy parameters, which will be studied in detail in Chapter 7, a narrow kinetic energy range of $5.5 \leq T_{eff} \leq 6.5$ MeV was used. The statistical uncertainties on the extracted number of CC and NC events are given in Table 3.2.

It is clear that β_{14} gives less uncertainty than β_1 alone. Using separate PDFs for β_1 and β_4 results in less uncertainty, but this does not take into consideration correlations between the two which could cause a bias in the fit results. Combining β_1 and β_4 in a 2D PDF produces slightly less uncertainty than using β_{14}, however, the difference is very small and it would be far more difficult to include the energy dependence in a 2D PDF. Using β_{14} yields a slightly lower uncertainty than both $\langle\theta_{ij}\rangle$ and CFRIP ($\mathcal{L}_\theta$ was not used in this study).

Using the values of separability calculated with (3.1), the expected statistical uncertainties on the fit values N_{CC} and N_{NC} for each isotropy parameter are given by (3.2).

[5] Maximum likelihood signal extraction and the code used for this study (written by J. Wilson) will be discussed in more detail in Chapter 8.

Isotropy PDFs	Mean Uncertainty	
	N_{CC}	N_{NC}
β_4	42.30	42.08
β_1	31.26	31.64
β_{14}	29.02	29.23
2D $\beta_4$vs. β_1	28.78	28.90
1D β_1 and 1D β_4	27.18	27.20
θ_{ij}	31.12	31.48
CFRIP	30.05	30.29

Table 3.2: Mean statistical uncertainty on the number of extracted CC and NC events using different isotropy parameters. The data sets contained 300 of each event type within the range $5.5 \leq T_{eff} \leq 6.5$ MeV.

Isotropy PDFs	Separability	Predicted Uncertainty $N_{CC} = N_{NC}$
β_4	0.144	34.5
β_1	0.211	29.3
β_{14}	0.254	27.2
θ_{ij}	0.203	29.8

Table 3.3: Predicted uncertainty on extracted number of CC and NC events for different isotropy parameters, calculated using Equation 3.2. The separability was calculated with a cut on low energy events only ($N_{hit} > 40$). The extracted uncertainties are given in Table 3.2.

These values are found in Table 3.3 and are lower than that found by the maximum likelihood fit. The separabilities used to calculate the expected uncertainties in Table 3.3 were calculated using isotropy distributions which contained events over a wide energy range (also a larger number of events was used). Because of the energy dependence of isotropy, the isotropy PDFs created have energy information in them, which may make the isotropy separability appear higher than it really is. This would result in a lower uncertainty on the fit values, as would using a larger number of events. The separability values also assume sufficient statistics for χ^2 minimization to be equivalent to maximum likelihood. This will not have been satisfied in the tails of the distributions in this study; however, the separabilities give the uncertainties to $< 10\%$ (except for β_4) and, more importantly for this study, correctly predict the relative uncertainties for the different isotropy parameters.

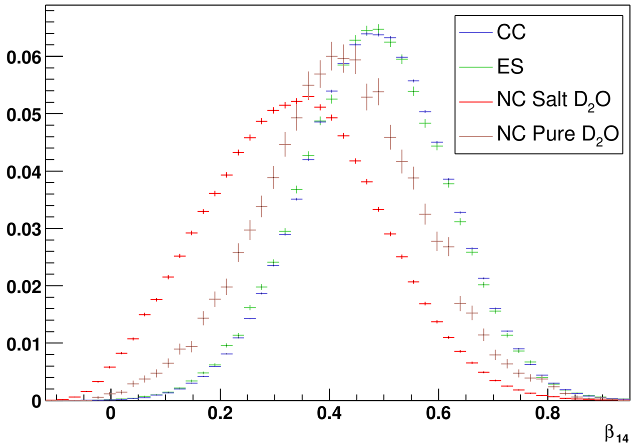

Figure 3.14: Normalized β_{14} distributions in the pure and salted D_2O phases.

3.7 Selection of Isotropy Parameter

The isotropy parameter chosen for the signal extraction of the data from the salt phase of SNO in this thesis is β_{14} because it has the highest separation power of the 1D parameters developed and studied at Oxford. The 1D β_{14} PDF is chosen instead of a 2D β_4 vs. β_1 PDF as it has essentially the same separation power and it is easier to quantify the energy dependence of the isotropy.

β_{14} was also chosen for the published analyses of the salt phase data [1, 50]. The decision was mainly between $\langle\theta_{ij}\rangle$, β_{14}, and CFRIP. These parameters all have comparable separation powers, but β_{14} is the most easily parameterized, which, as detailed in Chapter 6, is an advantage when determining systematic uncertainties. In particular, the CC distribution is well described by a symmetric Gaussian. This makes the parameterization over the full energy range easier.

3.8 β_{14} Distributions in Pure and Salt D_2O

Figure 3.14 shows the β_{14} distributions for CC and ES events (which are approximately the same, except for a small difference due to the different energy spectra of the CC and ES signals) and NC events in both pure and salted D_2O. The CC and ES distributions are the same in both phases as the detection principle is unchanged (Čerenkov light from a relativistic electron is detected). The NC distribution is much less distinct from CC in the pure D_2O phase than in the salted D_2O phase because there is only one γ emitted in neutron capture on deuterium, while there are a number of γ's emitted when a neutron captures on ^{35}Cl. The single γ signal in the pure D_2O phase is similar to the signal made by the ^{16}N source which also emits one γ.

Chapter 4

Correction to EGS4 in SNOMAN

4.1 Discrepancy between Data and Monte Carlo

Initial comparisons between calibration data and Monte Carlo isotropy distributions revealed a small, but notable discrepancy. ^{16}N calibration data showed that the data were less isotropic than the ^{16}N Monte Carlo. The $\langle\theta_{ij}\rangle$ and β_{14} distributions for a central ^{16}N run are shown in Figure 4.1. The mean values of the $\langle\theta_{ij}\rangle$ and β_{14} distributions and the fractional discrepancies between data and Monte Carlo are found in Table 4.1.[1] The discrepancy is higher for mean β_{14} because the cosines of the angles are being used[2].

Parameter	Data	MC	Discrepancy
Mean $\langle\theta_{ij}\rangle$	1.160 ± 0.0003	1.171 ± 0.0003	0.9%
Mean β_{14}	0.4155 ± 0.0003	0.4049 ± 0.0007	-2.4%

Table 4.1: Mean values of isotropy distributions for central ^{16}N data and Monte Carlo.

It was discovered that the Monte Carlo $\cos\theta_i$ distributions contained more backscattered angles than the data. Checks were done to ensure that the Rayleigh scattering of Čerenkov photons was not being overestimated in the Monte Carlo, and in fact, it was slightly *under*estimated [65]. The discrepancy could not be explained by optics modeling. A closer look at distributions of electron scattering angles revealed that the Monte Carlo simulation of SNO events is *highly* sensitive to the modeling of electron transport.

[1] Although β_{14} was chosen for the main analysis in this thesis and that of the collaboration, $\langle\theta_{ij}\rangle$ has been used in many previous studies, including this one on making a correction to scattering angles in the Monte Carlo.

[2] $\beta_{14} \approx \beta_1 = \langle\cos\theta_{ij}\rangle$.

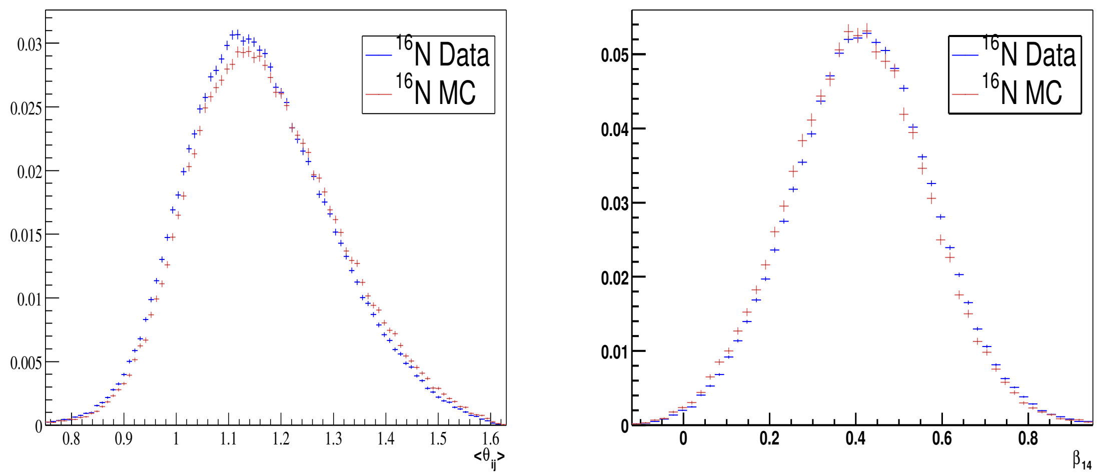

(a) $\langle\theta_{ij}\rangle$ (b) β_{14}

Figure 4.1: Data and Monte Carlo isotropy distributions from a central ^{16}N run.

4.2 Multiple Scattering in EGS4

Electron transport is handled within SNOMAN by EGS4. Elastic collisions with atomic nuclei are modeled using Molière's theory of multiple scattering as formulated by Bethe [56, 80]. Underlying Molière theory is the Rutherford scattering cross section

$$\sigma = \left(\frac{Ze^2}{2m_ec^2}\right)\frac{1-\beta^2}{\beta^4}\csc^4\left(\frac{\theta}{2}\right) \tag{4.1}$$

which neglects the spin of electrons. For spin-1/2 Dirac electrons, additional terms formulated by Mott [81] and revised in [82] must be included. The electron scattering cross section in EGS4 neglects these terms. The Mott terms slightly reduce the amount of large angle scattering; and in the ultra-relativistic limit of $\beta \to 1$, scattering through 180° is prohibited with the inclusion of the Mott terms. SNOMAN therefore overestimates the large angle scattering and consequently the amount of Čerenkov light emitted in the backwards hemisphere.

The EGS code has been upgraded since it was installed in SNOMAN and also substantially rewritten. The latest version, EGSnrc [83], has a more sophisticated treatment of multiple scattering than EGS4, incorporating the Mott terms in the scattering cross section as well as improvements to the approximations employed. The effect of including the Mott terms is the most significant.

4.3 The Mott Terms in the Scattering Cross Section

The performance of EGS4 in modeling electron multiple scattering was validated by comparison with an entirely different analytic calculation using the Goudsmit and Saunderson treatment of multiple scattering [84]. In both cases the multiple scattering of electrons was represented by screened Rutherford scattering, the cross section of which is given in 4.1. Including the effect of spin, the relativistic single scattering cross section formulated by Mott [82] and revised by McKinley and Feshbach [82] is the Rutherford formula multiplied by a factor $M(\theta, \beta, Z)$ given by

$$M(\theta, \beta, Z) = 1 - \beta^2 \sin^2 \frac{\theta}{2} + \pi\beta \frac{Ze^2}{\hbar c} \sin \frac{\theta}{2} \left(1 - \sin \frac{\theta}{2}\right)$$

where θ is the single scattering angle and Z the charge of the scattering nucleus. This factor is one for θ equal to zero and $1 - \beta^2$ for θ equal to π.

The Goudsmit and Saunderson method, as implemented in [84], was modified to calculate the effects of the Mott terms on the angular distribution of Čerenkov photons [85]. The angular distribution with the Mott terms present is a little tighter than with pure Rutherford scattering. For 5 MeV electrons the fraction of photons emitted into the backward hemisphere was reduced by 0.0078 when the Mott factor was included. A numerical calculation drawing θ_i and θ_j from the photon angular distribution, with azimuthal symmetry about the direction of the original electron, yielded a decrease in $\langle\theta_{ij}\rangle$ by 1%. However, the distribution of $\langle\theta_{ij}\rangle$ is not correct and for this a Monte Carlo of the electron trajectory is required.

A Monte Carlo program was written by S. West[3] in which the electron is propagated from one collision to the next until its speed v is less than the Čerenkov cut-off c/n, where n is the refractive index of water [85]. The average value of $\langle\theta_{ij}\rangle$ for 5 MeV electrons in water with this Monte Carlo was checked against the Goudsmit-Saunderson value. The percentage of light observed in the backward hemisphere with and without the Mott terms was found to be very similar to that obtained using the Goudsmit-Saunderson method. Figure 4.2 shows the angular distribution of electrons after passing through 0.1056 cm of water. The tighter distribution is the one calculated with the Mott terms. For comparison, the distribution of multiple scattering angles from EGS4 is also shown. EGS4 contains additional physics processes, such as Møller scattering, which are not included in the Monte Carlo written by S. West. Therefore, the EGS4 and Mott-free Monte Carlo scattering distributions are not expected to line up exactly.

The Monte Carlo gave the average value of $\langle\theta_{ij}\rangle$ for 5 MeV electrons as 1.096 ± 0.001 radians (without Mott) and 1.086 ± 0.001 radians (with Mott), a change of 0.9%. This

[3]The work presented in this chapter was completed by the author in collaboration with S. West, N. Jelley, and M. Bowler and presented in [86].

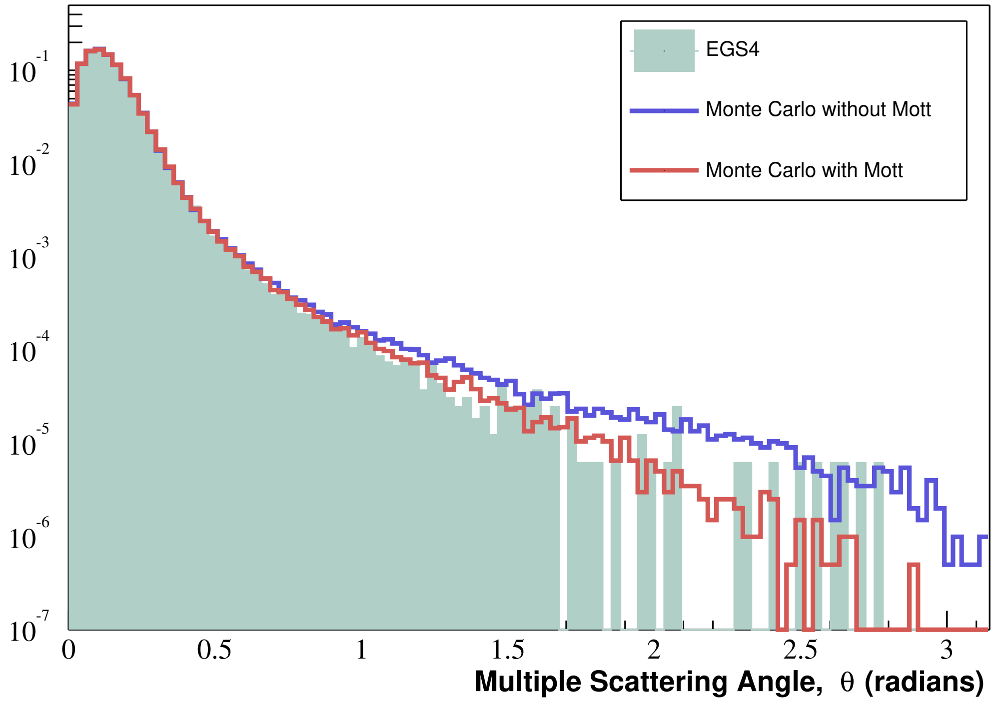

Figure 4.2: Angular distribution of 5 MeV electrons after passing through 0.1056 cm of water. Normalized to 1.

is the same percentage difference seen between data and SNOMAN in the values for ^{16}N calibration events, which give a light output approximately equivalent to an electron with an energy of $\sim$5 MeV. The actual θ_{ij} values given by this Monte Carlo calculation, however are several percent lower than those seen in the SNO data and SNOMAN Monte Carlo due to neglect of other physical processes such as delta rays from Møller scattering. These are included in EGS4, so a correction to EGS4 for the neglect of the Mott terms (and the improved approximations of EGSnrc) is required to simulate the SNO data more accurately.

4.4 The EGS4 Multiple Scattering Correction

In EGS4, an electron is propagated a step length x at which point its direction is changed by an angle θ. This angle is drawn from a probability density function $F_n(\theta)$ for electrons multiply scattered by a (screened) Coulomb potential with no Mott terms (this distribution is shown in Figure 4.2). The probability $P_n(\theta)$ that the electron would have scattered through a larger angle is given by $\int_\theta^\pi F_n(\theta) d\cos\theta$. For an angle ϕ drawn from a probability density function $F_m(\theta)$ that includes the Mott terms, the corresponding

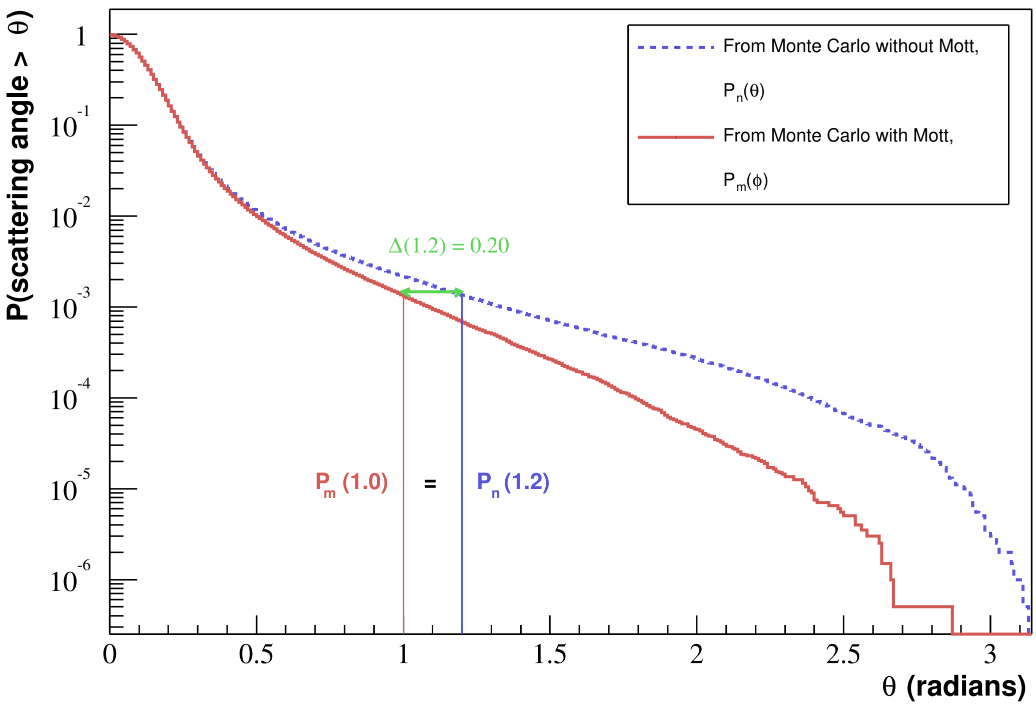

Figure 4.3: The integrated multiple scattering angle distributions show the probability of the multiple scattering angle being greater than angle θ for 5 MeV electrons after passing through 0.1056 cm of water, obtained from Monte Carlo generated with (P_m) and without (P_n) Mott terms.

probability $P_m(\phi)$ is given by $\int_\phi^\pi F_m(\theta) d\cos\theta$. When $P_m(\phi) = P_n(\theta)$, the angle ϕ is the one that would have been drawn by EGS4 had it been using the probability density function $F_m(\theta)$ rather than $F_n(\theta)$. The difference $\Delta(\theta) = (\theta - \phi)$ gives the correction that has to be applied in EGS4 after each step length x.

The probability distributions $P_m(\phi)$ and $P_n(\theta)$, shown in Figure 4.3, were calculated using the Monte Carlo program and a correction file was generated giving the amount $\Delta(\theta)$ to be subtracted from the EGS4 angle θ for a number of different step lengths x and electron kinetic energies, T. A simple example of $\Delta(\theta)$ is shown in Figure 4.3. Figure 4.4 shows the correction, $\Delta(\theta)$, for a number of step lengths (0.005 to 0.04 cm) used in EGS4 for 2 MeV kinetic energy electrons. As can be seen, particularly for large angles, the correction is approximately step length independent.

4.4.1 Analytic Correction

For large angles the probabilities $P_m(\theta)$ and $P_n(\theta)$ are much larger than the probabilities for two successive scatters through $\theta/2$, $(P_m(\theta/2))^2$ and $(P_n(\theta/2))^2$, so $F_m(\theta)$ and $F_n(\theta)$

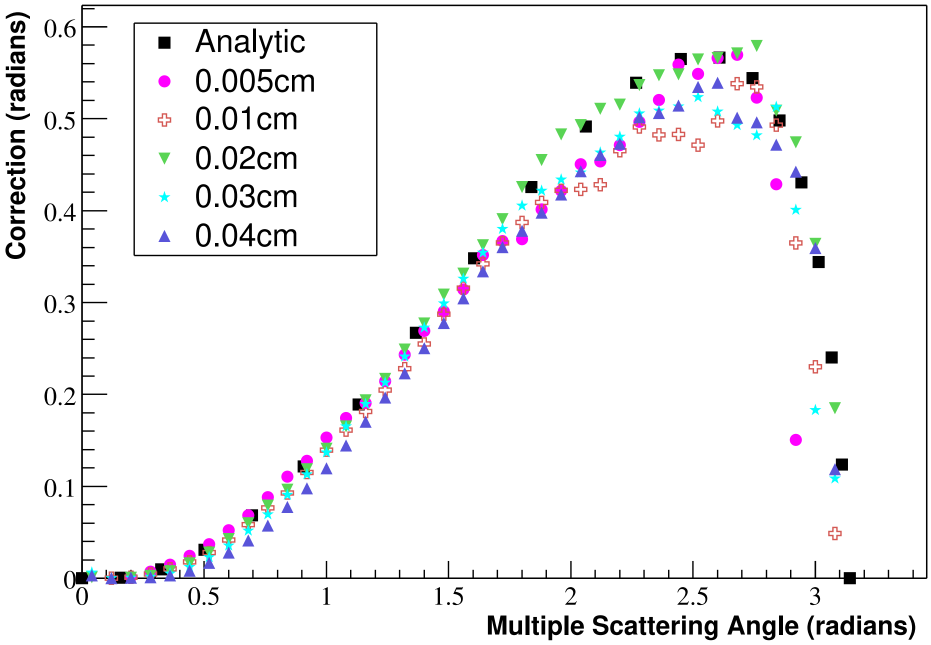

Figure 4.4: Step dependence of Mott correction for 2 MeV electrons

are likely to be well approximated by the single scattering probabilities[4]. These are given by $n\sigma_m x$ and $n\sigma_n x$, where σ_m and σ_n are the single scattering cross sections with and without the Mott terms, respectively, n is the number of scattering atoms per unit volume and x is the step length. The cross sections σ_m and σ_n are related by

$$\sigma_m = M(\theta, \beta, Z)\sigma_n = M(\theta, \beta, Z)G(T)\sin^{-4}\left(\frac{\theta}{2}\right) \tag{4.2}$$

where $G(T)$ is a function of the electron kinetic energy. The condition on the probabilities, $P_m(\phi) = P_n(\theta)$, is therefore equivalent to

$$\int_{\phi}^{\pi} M(\theta, \beta, Z)\sin^{-4}\left(\frac{\theta}{2}\right) d\cos\theta = \int_{\theta}^{\pi} \sin^{-4}\left(\frac{\theta}{2}\right) d\cos\theta \tag{4.3}$$

which leads to an equation relating $y_m = \sin^{-1}(\phi/2)$ and $y_n = \sin^{-1}(\theta/2)$

$$y_m^2 + 2\pi\beta\frac{Ze^2}{\hbar c}(y_m - 1) - 2\left(\beta^2 + \pi\beta\frac{Ze^2}{\hbar c}\right)\ln(y_m) = y_n^2 \tag{4.4}$$

Solving this equation gives the correction $\Delta(\theta) = (\theta - \phi)$ that has to be applied in EGS4 after each step in the approximation of single scattering being dominant. (As the scattering molecules are D_2O, an effective Z=7.63 is used in the Mott term.) This

[4]This small angle approximation was derived by Nick Jelley.

Energy	Avg. Step Length	Energy	Avg. Step Length
0.3 MeV	0.0042 cm	3.5 MeV	0.0501 cm
0.5 MeV	0.0080 cm	5.0 MeV	0.0637 cm
1.0 MeV	0.0171 cm	8.0 MeV	0.0808 cm
2.0 MeV	0.0324 cm	12.0 MeV	0.0962 cm

Table 4.2: Average EGS4 step lengths for various electron kinetic energies.

analytic correction at energies where β is close to one is effectively energy independent. The analytic correction is also step length independent.

In Figure 4.4 the analytic correction (black squares) for 2 MeV electrons is in reasonable agreement with that obtained with the Monte Carlo program, particularly at large angles for all step lengths, and provides an approximate verification of the Monte Carlo calculation at these angles. For small angles and longer step lengths the Monte Carlo correction is less than the single scattering approximation and reflects the increased importance of multiple scattering in determining the probability density functions.

4.4.2 Energy Dependence of Correction

The angular dependence of the Monte Carlo correction shows an approximately monotonic dependence on electron kinetic energy, T. The Monte Carlo correction was calculated for a number of energies between 0.3 MeV and 12 MeV using the average EGS4 step length for that energy (found in Table 4.2). Figure 4.5 shows the analytic correction (dashed lines) and the correction obtained using the average step length (points), together with a fit (solid black lines) to the final correction[5] which was installed in EGS4.

The easiest way to implement the correction to the EGS4 multiple scattering angles is to parameterize it as a function of energy. A reasonable fit to the analytic correction is given by $A(\pi-\theta)^B\theta^C$, so that the corrected angle becomes

$$\theta_{corr} = \theta - A(\pi-\theta)^B\theta^C, \tag{4.5}$$

where A, B, and C are dependent on T. The θ^C factor ensures that the correction is zero at $\theta = 0$ and the $(\pi-\theta)^B$ factor ensures that the correction goes to zero at $\theta = \pi$. The parameterization to the final correction is

$$\theta_{corr} = \theta - A(\pi-\theta)^B\theta^C[1 - 1.1e^{-\theta/(\theta+D)}], \tag{4.6}$$

where A, B, C, and D are dependent on T. The extra factor is included to decrease the correction at small angles and was found by dividing the calculated correction at each

[5]The correction chosen to alter the EGS4 angles is approximately midway between the analytic and the average step length corrections and tuned to agree with EGSnrc at 5 MeV (as discussed in Section 4.5). This will be referred to as the *final correction*.

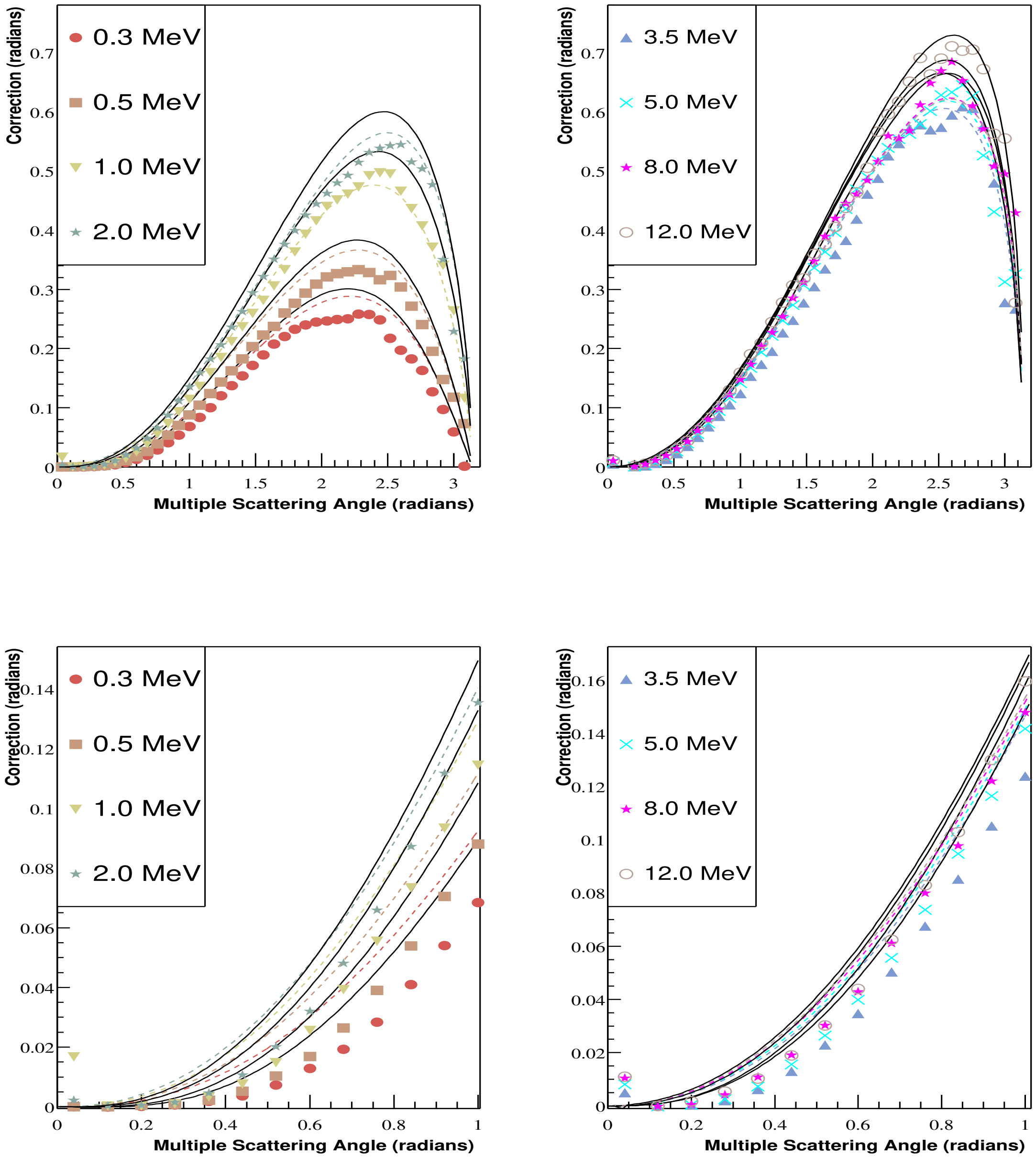

Figure 4.5: Multiple scattering angle correction for different electron energies. Markers are the correction calculated using the average EGS4 step length for that energy. Dashed lines are the analytic correction. Black lines are the final correction installed in EGS4.

angle by the fit given by (4.5) and fitting that ratio. The different elements of this fit are shown in Figure 4.6.

For some energies, the fit to the correction is poor at large angles; however, for the step lengths taken in EGS4, angles greater than 2 radians are very rarely selected

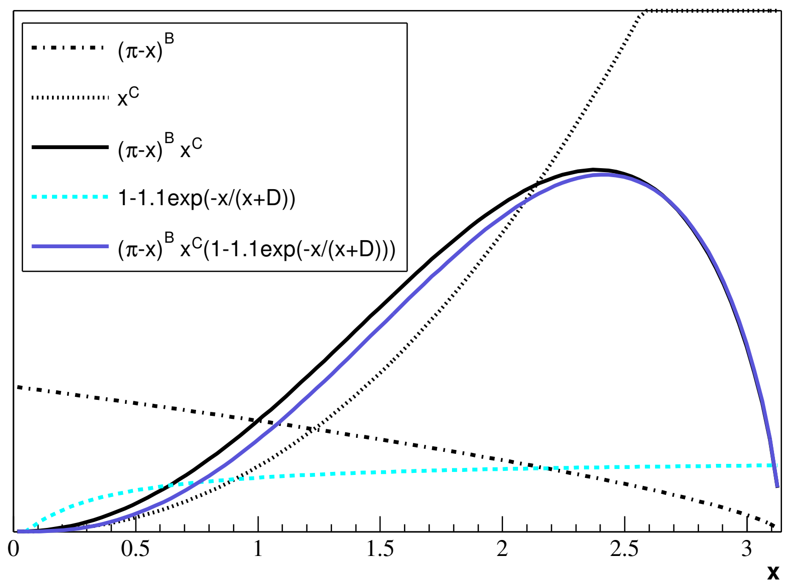

Figure 4.6: Fit to scattering angle correction, divided into each of its components. The normalization of each of the functions is arbitrary.

(as seen in Figure 4.2 which has a logarithmic y-axis) so the fit to EGS4 angles above 2 radians is not critical. In fact, the correction was turned off for $\theta > 2$ and no difference was seen in the resulting isotropy distributions. The energy dependence of the fit is displayed in Figure 4.7. The parameter C was fixed to 2.2; the energy dependence of the other parameters is given in Section 4.6.

As shown in Figure 4.5, the overall decrease in the correction as β becomes much less than one is reproduced by the analytic approximation. A routine, which utilizes the AUSGAB function in EGS4, was added to EGS4 to apply the correction to the multiple scattering angle after each step. This code may be found in Appendix D. The electron angular distribution and the mean values of $\langle\theta_{ij}\rangle$ and of β_{14} were calculated with and without the various corrections for a number of electron energies and are compared to data in the following sections.

4.5 Comparisons with EGSnrc and Data

The multiple scattering angles in EGS4 must be corrected not only for the neglect of the Mott terms, but also for the improvements made to approximations in EGSnrc. Dave Rogers has run EGSnrc and EGS4 to calculate the angular distribution of 5 MeV (kinetic energy) electrons passing through 1 cm of water and also of 2 MeV electrons passing through 4 mm of water [87]. The percentage increase in the number of 5 MeV

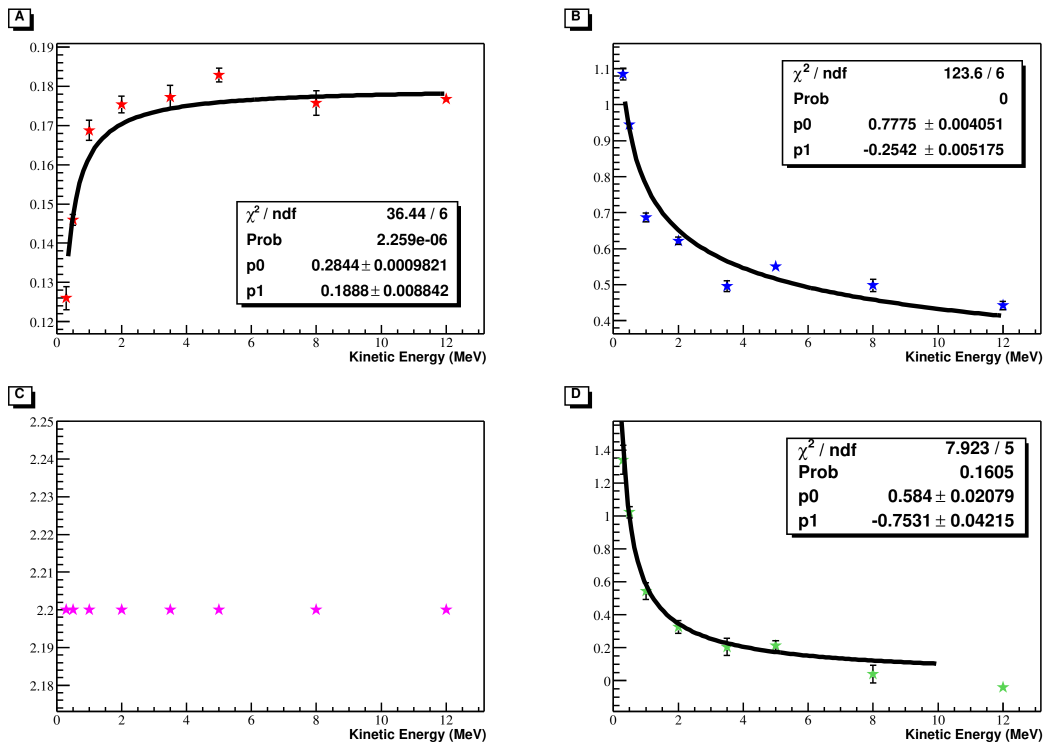

Figure 4.7: Energy dependence of correction to EGS4 multiple scattering angles.

electrons that pass through 1 cm of water (without being scattered into the backwards hemisphere) using EGSnrc with Mott compared with using EGS4 is 1.2%. Distributions of the emerging angles are shown in Figure 4.8 where "spin on" refers to EGSnrc with the Mott terms included and "spin off" refers to EGSnrc without the Mott terms. For 2 MeV electrons passing through 4 mm of water the corresponding percentage increase is 2–3%, made up of ∼4% from including the Mott terms and ∼-1.5% from the other changes in EGSnrc. For comparison, the percentage increases calculated by including Mott terms in the simpler Monte Carlo code discussed in Section 4.3 were 1.3% and 1.9% for the 5 MeV and 2 MeV cases, respectively [85].

The excess of PMT hits in the backwards hemisphere (with respect to event direction) was shown to be the main reason for the discrepancy between calibration data and Monte Carlo isotropy parameter values. The increased number of forward scattering angles observed by EGSnrc with the Mott terms reduces the amount of light observed in the backwards hemisphere. Therefore, it is important that the difference between the fraction of scatters in the forward hemisphere in ESG4 and EGSnrc is reproduced by the correction to EGS4.

The result of applying the correction obtained by using the average EGS4 step length was to increase the percentage of 5 MeV electrons passing through 1 cm of water by 0.9%, while applying the analytic correction increased the percentage by 1.3%. For

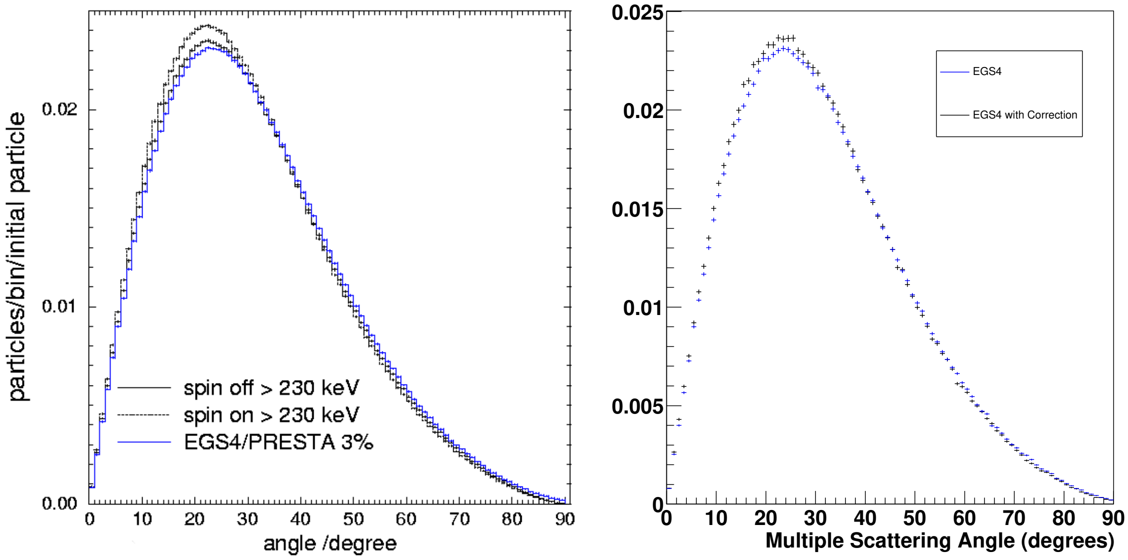

Figure 4.8: Multiple scattering angles for 5 MeV electrons passing through 1 cm of H_2O. The left-hand plot shows results from EGS4 and EGSnrc with (spin on) and without (spin off) Mott scattering terms. The right-hand plot shows results from EGS4 and EGS4 with the correction found in Equation 4.6.

2 MeV electrons passing through 4 mm of water the corresponding increases were 1.9% (average step length) and 3.4% (analytic). The effect of applying these corrections for 5 MeV electrons on mean $\langle\theta_{ij}\rangle$ is to decrease the value by 0.88% and 1.15% and on mean β_{14} to increase the value by 2.06% and 3.07%, respectively.

A correction midway between the analytic and average step length corrections was tuned by multiplying it by a factor of 1.1 to achieve the best overall agreement with the EGSnrc results for 5 MeV electrons. The result on the emerging angular distribution for this correction is shown in the right-hand plot in Figure 4.8. The blue histogram in each of the plots is the same, as they are both distributions from EGS4. We do not expect the "EGS4 with correction" distribution to exactly match "EGSnrc with spin on" because EGSnrc includes more differences to the scattering angles than just the effect of including the Mott terms (as seen by the difference between the EGS4 distribution and "EGSnrc with spin off"). However, we have tuned our correction so that the *difference in the integrals* between EGS4 and "EGSnrc with spin on" and between EGS4 and "EGS4 with correction" are the same. Applying this correction increases the fraction of 5 MeV electrons emerging through 1 cm of water by 1.18% and 2 MeV electrons passing through 4 mm of water by 2.64%. Mean $\langle\theta_{ij}\rangle$ for 5 MeV electrons decreases by -0.97% and mean β_{14} increases by 2.48%. The effect of applying this final correction to EGS4 scattering angles on β_{14} is shown in Figure 4.9. All of the percentage differences quoted in this chapter are summarized in Tables 4.3 and 4.4.

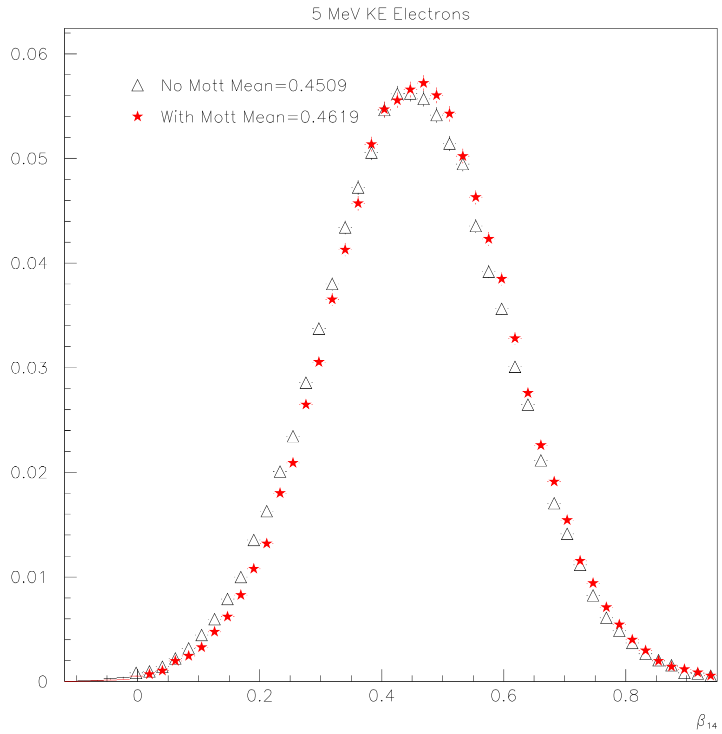

Figure 4.9: Effect of multiple scattering angle correction on β_{14} for 5 MeV electrons.

	EGSnrc	Simple MC	Avg Step	Analytic	Final
2 MeV e^-	**2-3%**	1.9%	1.9%	3.4%	**2.64%**
5 MeV e^-	**1.2%**	1.3%	0.9%	1.3%	**1.18%**

Table 4.3: Fractional discrepancy between number of electrons emerging in the forward direction from a slab of H_2O from Monte Carlo with unmodified EGS4 (except in the case of the Simple MC which does not utilize EGS4 and the comparison is between code with and without Mott scattering terms) and Monte Carlo with corrected multiple scattering angles.

	Data	Simple MC	Avg Step	Analytic	Final
Mean $\langle\theta_{ij}\rangle$	**-0.9%**	-0.9%	-0.88%	-1.15%	**-0.97%**
Mean β_{14}	**2.4%**		2.06%	3.07%	**2.48%**

Table 4.4: Discrepancy between mean isotropy parameter values for 5 MeV electrons from Monte Carlo with unmodified EGS4 (except in the case of the Simple MC where the comparison is between code with and without Mott scattering terms) and Monte Carlo with corrected multiple scattering angles (except for the data, of course, which comes from the ^{16}N calibration source placed in the center of the D_2O region).

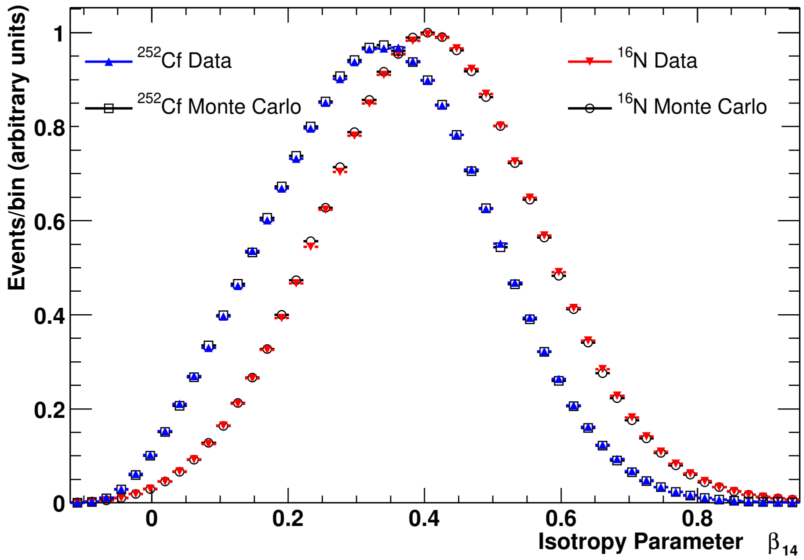

Figure 4.10: Agreement between ^{16}N and ^{252}Cf data and Monte Carlo β_{14} distributions.

4.6 Final Correction

The final correction, which is 10% larger than that midway between the analytic and the average step length correction, was installed in EGS4 and the corrected multiple scattering angles are given by

$$\theta_{corr} = \theta - A(\pi - \theta)^B \theta^C [1 - 1.1e^{-\theta/(\theta+D)}], \tag{4.7}$$

where

$$\begin{aligned} A &= 0.308(1 - e^{-T/(T+0.19)}) \\ B &= 0.78T^{-\frac{1}{4}} \\ C &= 2.2 \\ D &= 0.58T^{-\frac{3}{4}}. \end{aligned} \tag{4.8}$$

When this correction is applied to EGS4 the resulting Monte Carlo β_{14} distributions for ^{16}N and ^{252}Cf sources agree very well with data, as can be seen in Figure 4.10. These distributions include all selected ^{16}N and ^{252}Cf runs taken before the submission of [1]. The merged runs have been weighted so that, effectively, the number of events is evenly distributed throughout the detector volume.

The mean values of β_{14} for different ^{16}N and ^{252}Cf radial positions also are in improved agreement, as displayed in Figures 4.11 and 4.12[6]. While the agreement near the acrylic vessel for ^{252}Cf is good, it is less good for ^{16}N suggesting that this disagreement is

[6]Note that these plots were created with an earlier version of the detector simulation than the version

caused by inaccurate modeling of ^{16}N events near the acrylic vessel. There is also a slight variation seen amongst points at the same radius which reflects a small z-dependence in the mean value of β_{14}.

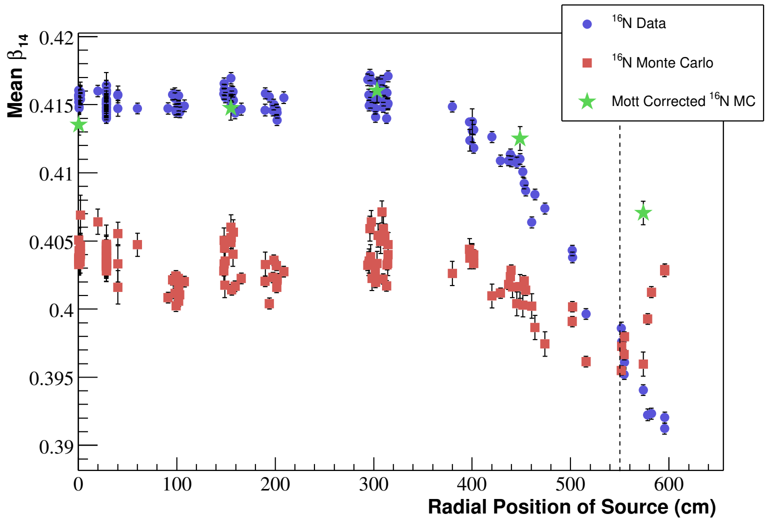

Figure 4.11: Effect of correction on mean β_{14} for ^{16}N events versus source radial position. The dashed line corresponds to the fiducial volume.

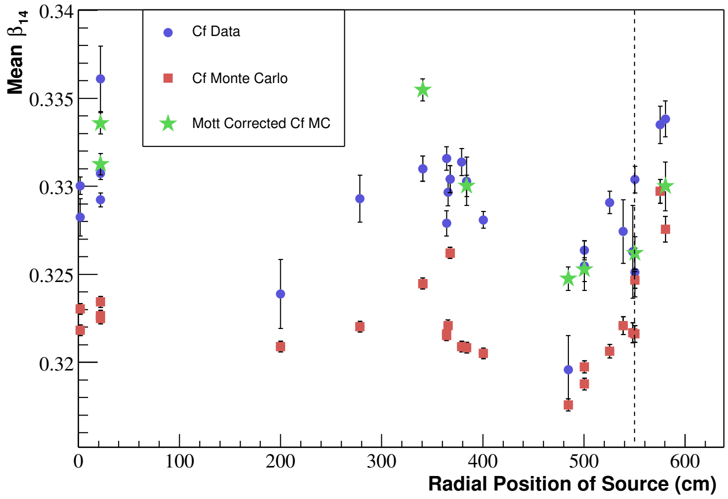

Figure 4.12: Effect of correction on mean β_{14} for ^{252}Cf events vs. source radial position.

used to compare calibration data and Monte Carlo in Chapter 6. The mean β_{14} values are slightly lower in the more recently processed data and Monte Carlo as a result of improvements made to modeling of the optics; however, the difference between data and Monte Carlo with or without the correction from this chapter remains essentially the same in both versions.

Chapter 5

Backgrounds and Analysis Cuts

The data set from the salted D_2O phase contains about 10 solar neutrinos per day within analysis cuts. However, the trigger rate of the detector is about 20 events per second [47]. The majority of these triggers come from low-energy Čerenkov events resulting from natural radioactivity in and surrounding the detector. Many also come from instrumental background, and various cuts are placed on the data to remove these unphysical events.

There is one instrumental background of uncertain origin which is slightly more difficult to distinguish from neutrino events. The signal from this background is an isotropic light distribution and these events were removed from the pure D_2O data set using a parameterization of isotropy. The feasibility of this in the salt phase is studied and found to remove too many neutrons. However, it is possible to remove the majority of this background using a fiducial volume cut [52].

Events that are not reconstructed well by the fitters must also be removed from the data set. A significant number of these events tend to have a well confined light distribution with respect to the fit vertex in which most angles θ_{ij} between hits i and j are close to zero. Such misreconstructed events may be removed from the data set by placing a cut on the isotropy parameter.

This chapter presents the selected cuts on β_{14}, as well as the fraction of neutrino events which are lost (referred to as *sacrifice*) due to these cuts. Sacrifice is calculated using ^{16}N and ^{8}Li data and CC and ES Monte Carlo for electron-type events and ^{252}Cf data for neutron events. *Contamination* is the number of background events in the accepted neutrino signal region.

Also presented are estimates of radioactive background using isotropy distributions. Concentrations of ^{232}Th and ^{238}U in the D_2O may be determined by analyzing the isotropy of the Čerenkov light created from their decay products.

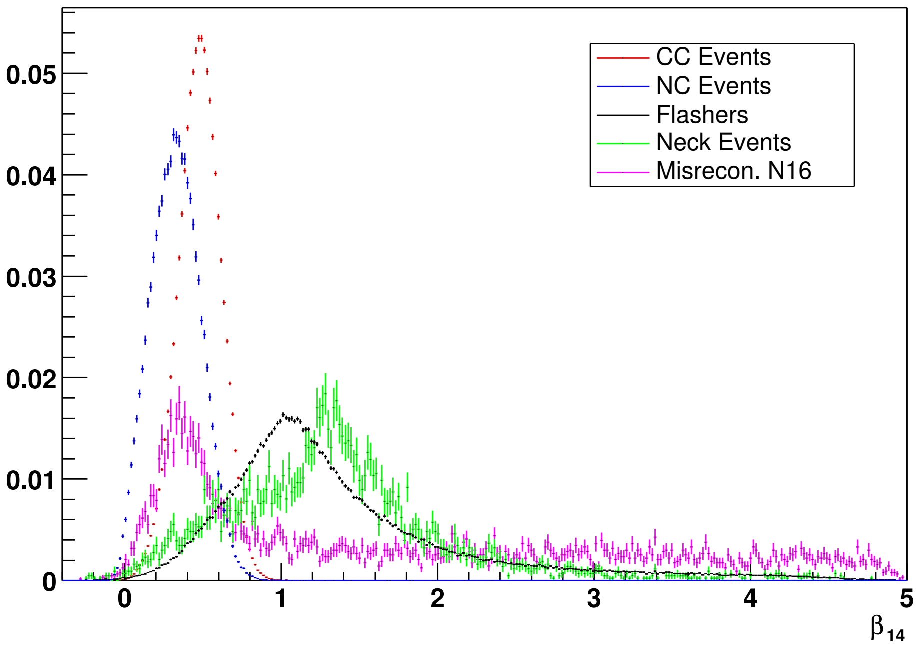

Figure 5.1: Comparison of β_{14} for signal events and backgrounds in the salt phase. Note that the maximum value attainable for β_{14} is 5.0 and *high* values of β_{14} imply *low* isotropy. Each of the distributions is normalized to one.

5.1 Instrumental Background Removal

Instrumental backgrounds are those due not to radioactive decay, but to the detector components [51]. The PMTs occasionally give off pulses of light that are detected on the near and opposite sides of the detector. These events, called *flashers*, are the most numerous type of light-producing instrumental background. They are characterized by an early cluster of hit PMTs and later light on the opposite side of the detector. This characteristic signature makes them easily removable from the data set. Events emanating from the neck of the SNO detector are referred to as *neck events*. The origin of this background is uncertain, but static discharge from the acrylic is one likely possibility [51]. Light is produced in the neck which is also seen at the bottom of the detector. Neck events are vetoed by specially installed PMTs surrounding the neck which fire in coincidence with the PMTs at the bottom of the detector.

For a description of other such backgrounds and techniques for their removal see [51]. The β_{14} distributions for flashers and neck events are shown in Figure 5.1. The distribution for flashers is approximately symmetric about β_{14}=1, which means that they have a very contained light distribution. Neck events also tend to have relatively high values of β_{14}. These distributions were studied to determine whether or not there was a lot of power in using β_{14} to distinguish these backgrounds. Although, statistically the distributions are quite different from the neutrino signals, β_{14} would not be effective for the removal of flashers and neck events. Instead, these are removed by the techniques described in [51].

5.2 Using Isotropy to Remove Unwanted Events

In the pure D_2O phase of SNO, the isotropy parameter $\langle\theta_{ij}\rangle$ was used to remove misreconstructed neutrino-induced events and nearly isotropic events which reconstruct at the acrylic vessel (AV events) [89]. In the salt phase, an isotropy parameter may still be used to remove misreconstructed events, but placing a cut on high-isotropy (low β_{14}) events would remove many neutrons from the data set. Figure 5.2 shows β_4 vs. β_1 for neutrino candidate events in the pure D_2O phase of SNO. A radial cut of $R_{fit} < 550$ cm and a cut on kinetic energy of $5 < T_{eff} < 20$ MeV are applied. The red stars indicate accepted events with the same cuts applied as in the published pure D_2O data set [26]. The three light blue squares are events cut by ITR < 0.55. Green points are events cut by a $\langle\theta_{ij}\rangle > 0.75$ cut. The events cut by the high $\langle\theta_{ij}\rangle$ cut of 1.45 are shown in blue.

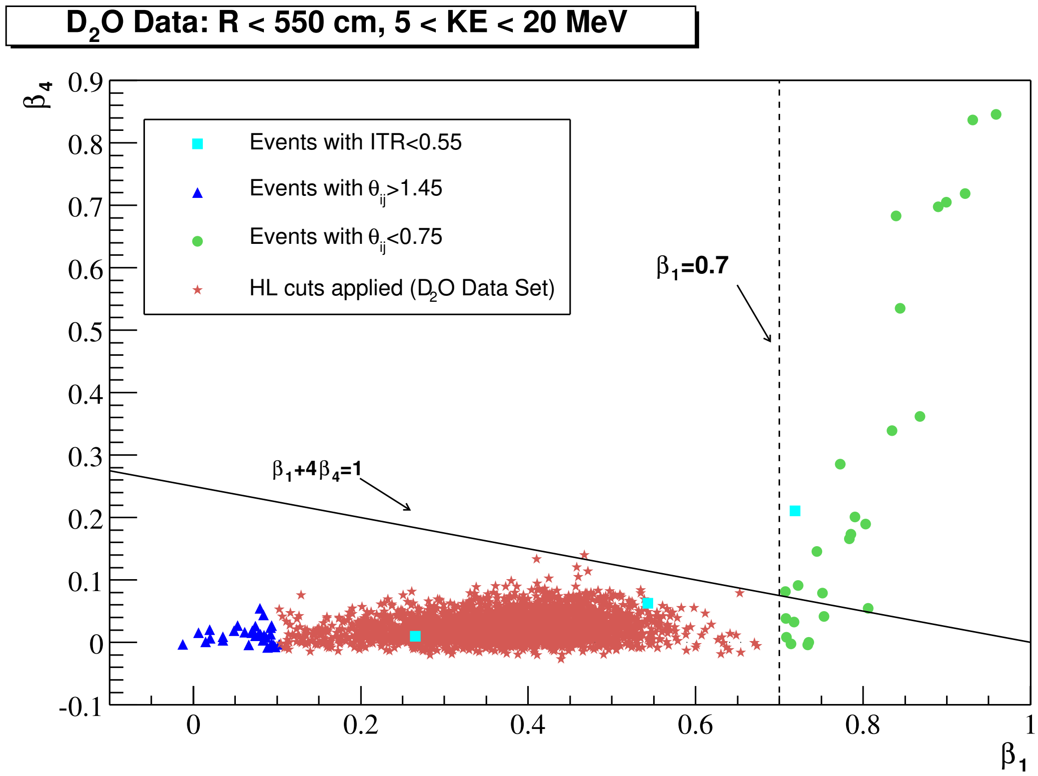

Figure 5.2: β_4 vs. β_1 for data from the pure D_2O phase.

5.2.1 Misreconstructed Events

To remove misreconstructed events, a high cut must be placed on the isotropy parameter formed using the Legendre polynomial parameters (note that this was a *low* cut on $\langle\theta_{ij}\rangle$). Referring to the plot of the Legendre Polynomials in Figure 3.7, one can see that in order to have a large value of β_4, an event must have a very contained light distribution. To have $\beta_4 > 0.5$, the PMT hits must have an average angular separation of less than 20°, so large β_4 values are a clear indication of misreconstructed events. Cutting on β_1, the same events would be removed as by the cut on $\langle\theta_{ij}\rangle$ since they are directly related. However, we are using β_{14} as the isotropy distribution in signal extraction, so the cut should be placed on this parameter. The β_{14} cut removes fewer events, as shown in Figure 5.2; however, it must be determined if these are neutrino events that have reconstructed accurately and should be retained in the data set. This may be done by looking at calibration data and signal Monte Carlo.

The next plots show the result of placing a cut of $(\beta_1 + 4\beta_4) \leq 1$ and a cut on β_1 which corresponds to the $\langle\theta_{ij}\rangle$ cut in the pure D_2O data set on CC and NC Monte Carlo and on Cf data. Figure 5.3 shows β_4 vs. β_1 for Cf data from runs at the center of the detector and at z=-500 cm. Figure 5.4 shows β_4 vs. β_1 for signal Monte Carlo. A cut placed on either β_{14} or β_1 yields a very small sacrifice. These are not the final sacrifice numbers, as a more detailed calculation of sacrifice has been performed with the finally determined limits on β_{14} [52].

Figure 5.1 shows a normalized distribution of β_{14} for misreconstructed ^{16}N events[1] compared to that of CC and NC Monte Carlo. The misreconstructed events have β_{14} values all the way up to the maximum value of 5.0. Figure 5.5 shows β_{14} and β_1 versus the difference between fit (R_{fit}) and generated (R_{gen}) radial positions for CC and NC Monte Carlo events which have been generated throughout the D_2O region ($0 \leq R_{gen} \leq 600$ cm). The same cuts are applied as in Figure 5.4, including a cut of $R_{fit} < 550$ cm, which is why the distribution is slightly asymmetric. From this plot, it is clear that a high cut on the β_{14} distributions is useful for removing highly misreconstructed events. Note that neutron events have higher values of $(R_{fit} - R_{gen})$ due to the distance traveled by the neutron and the subsequent distance traveled by the γ's emitted after the neutron capture.

5.2.2 AV Events

AV events reconstruct near the acrylic vessel and characteristically have an isotropic light distribution. It is uncertain how these events are produced, but one possibility is that

[1] For this particular distribution (in Figure 5.1), two high-radius ^{16}N runs were chosen and events reconstructing more than 250 cm away from the source are plotted.

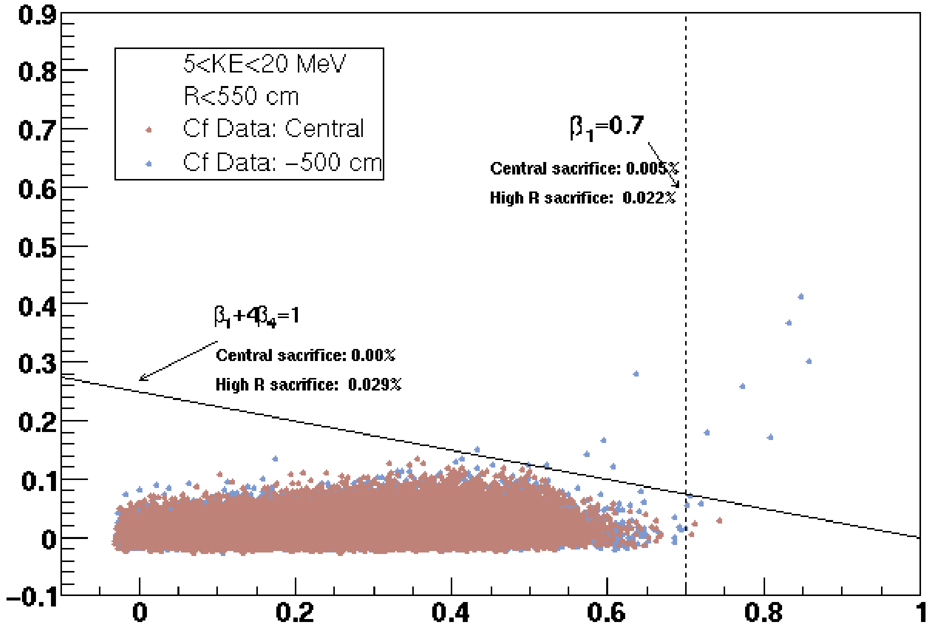

Figure 5.3: β_4 (y-axis) versus β_1 (x-axis) for Cf runs in salted D_2O.

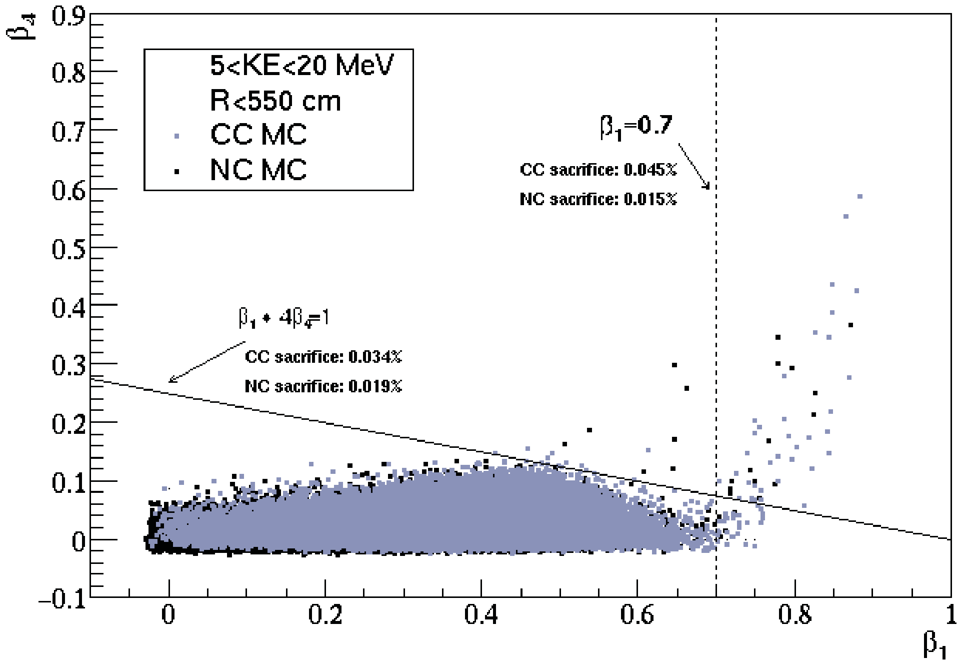

Figure 5.4: β_4 versus β_1 for CC and NC signal MC in salted D_2O.

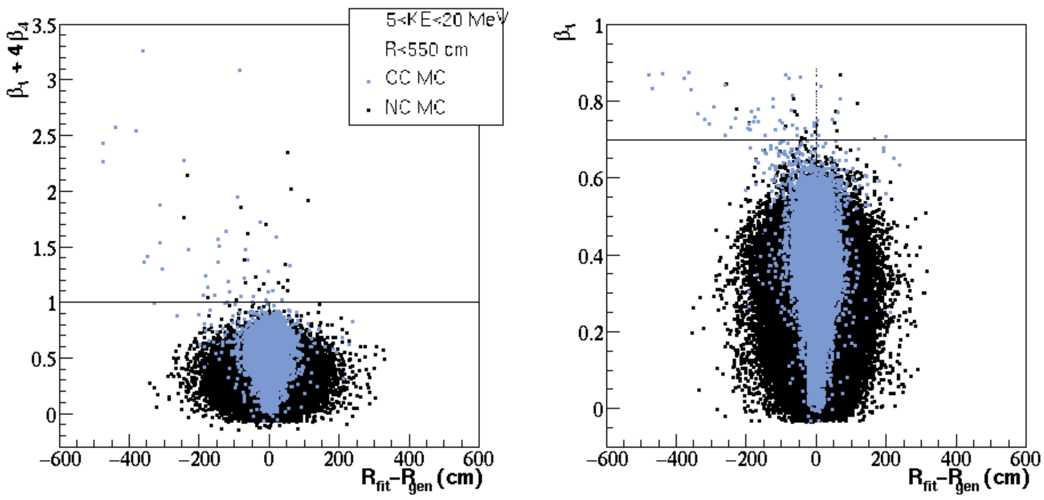

Figure 5.5: β_{14} (left) and β_1 (right) values versus radial misreconstruction ($R_{fit} - R_{gen}$) of signal Monte Carlo.

they come from stress relief in the acrylic. Another is they result from bubbles forming on the acrylic and when these detach, light is emitted. Figure 5.6(a) shows how the AV events feature prominently in the pure D_2O data set. The black lines in show the data featured in Figure 5.2 from the pure D_2O phase. The solid line is for data reconstructing near the AV ($525 < R_{fit} < 765$ cm) and the dashed line is for data reconstructing within the fiducial volume ($R_{fit} < 550$ cm). For reference, Monte Carlo distributions of charged current and neutral current events in *salted* D_2O are included, so that one can see how low in β_1 these distributions extend. The normalizations are arbitrary, except for an attempt to normalize the CC distributions to the D_2O data distributions. Note that the pure D_2O data set contains mostly CC events and neutron events are less isotropic (higher β_{14} values) in this phase than in the salt phase as demonstrated in Figure 3.14. This is why the data for events reconstructing within the fiducial volume agrees well with the CC Monte Carlo, although the statistics on the number of data events are low.

Isotropic AV events are clearly seen in the data reconstructed near the AV by the bump centered at β_1=0. These events were removed in the pure D_2O data set by placing a high cut on $\langle\theta_{ij}\rangle$. The same cannot be done for salt data, because the neutron signal would be significantly reduced. Also, the isotropy parameter β_{14} smears this bump, making the AV events less distinguishable from neutron-induced events, as shown in Figure 5.6(b). Fortunately nearly all of these events may be removed with an appropriate fiducial volume cut [52]. A limit is placed on the number of these events by analyzing the pure D_2O data and is included as an error on the extracted neutral current and charged current rates[2].

[2]Because these events are approximately isotropic it is expected that they would be mistaken for NC

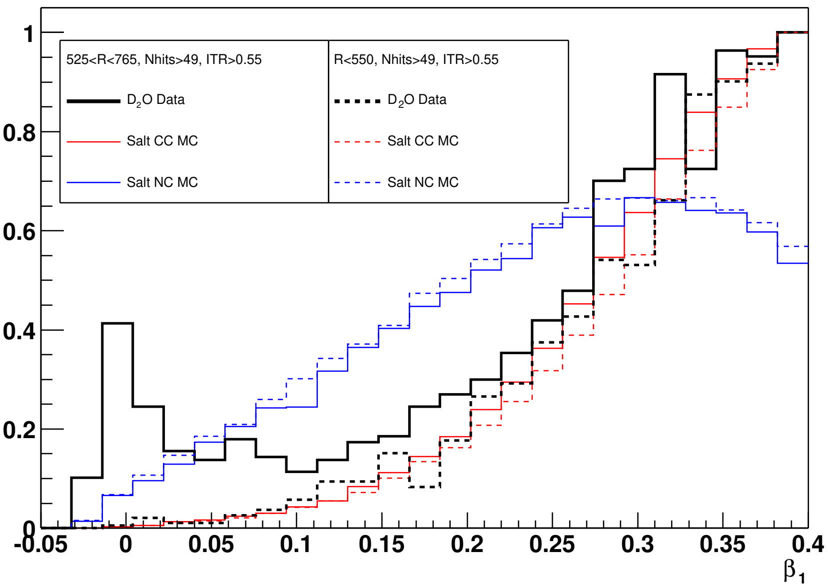

(a) β_1

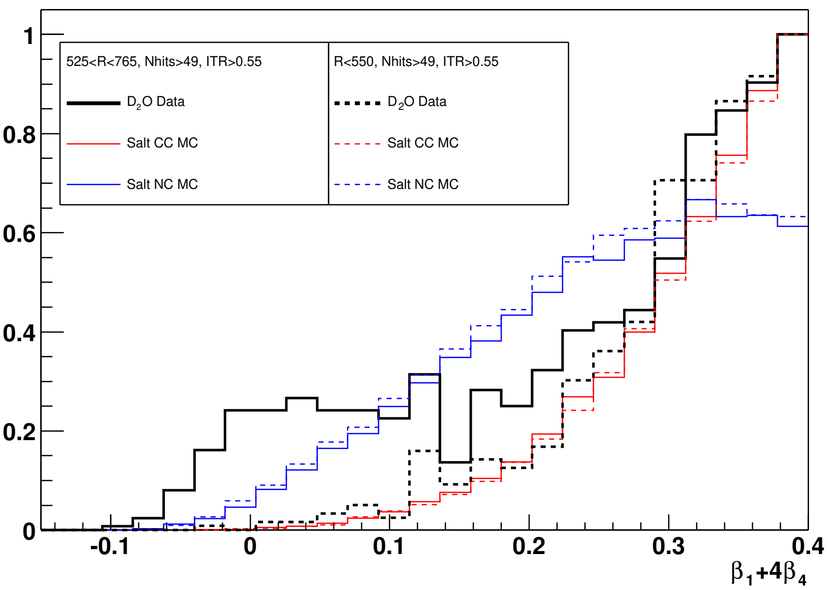

(b) β_{14}

Figure 5.6: Comparison of β_1 and β_{14} distributions for neutrino signals and AV events. Arbitrary units on y-axis.

events; however, the energies are more consistent with CC events, which is why they contribute to an error on the CC rate as well as on the NC rate.

5.2.3 β_{14} Cuts

Figure 5.7 shows zoomed-in logarithmic versions of Figure 5.1. Based on these figures, a lower limit of β_{14}=-0.12 and an upper limit of β_{14}=0.95 have been chosen. The instrumental backgrounds do not show any alarming features at either of these two points. At the low end, there is almost no signal lost due to the β_{14} cut. At the high end there is virtually no neutron signal lost, but a very small fraction of the charged current signal is lost. However, it is beneficial to have a more stringent limit on the high end of β_{14} to reduce the number of misreconstructed events.

The sacrifice due to the limits placed on β_{14} is $(0.480 \pm 0.002)\%$ for ^{16}N data and $(0.344 \pm 0.002)\%$ for ^{252}Cf data [52]. The total sacrifice due to *all* cuts placed on the neutrino data set (within a total energy range of 6 to 20 MeV) is found in Table 5.1.

Signal	Total Sacrifice
CC	$0.57^{+16}_{-11}\%$
ES	$0.86^{+21}_{-17}\%$
NC	$0.68^{+16}_{-11}\%$

Table 5.1: Expected sacrifice of the salted D_2O neutrino data set. Values from [52].

5.3 Using Isotropy to Estimate Backgrounds

5.3.1 Natural Radioactivity

Low energy Čerenkov background and γ's with energies high enough to photodisintegrate the deuteron result from natural contamination of ^{232}Th and ^{238}U and their decay chain products in the light and heavy water and detector components. Two *ex situ* techniques are used to determine the average levels of ^{232}Th and ^{238}U in the D_2O. Radium ions are extracted chemically from the heavy water onto either MnO_x [69] or HTiO [68]. Radon daughters are then released by the radium and identified using alpha spectroscopy for the MnO_x technique, while for HTiO the radium is concentrated and detected through β-α coincidences. Another method is through the extraction of radon directly from the water [44].

Another measurement is provided by analyzing the Čerenkov light produced by the radioactive decays. In the analysis window of 4.5–5.0 MeV, the Čerenkov light from ^{214}Bi in the uranium chain is dominated by β-decay to the ground state of ^{214}Pb while that from ^{208}Tl in the thorium chain is dominated by the Čerenkov light from a β and a number of γ's with maximum energy of 2.6 MeV. Both decay chains, found in Figure 2.5, contain γ's with energy greater than 2.2 MeV which is large enough to split up the deuteron. Because of the higher number of Čerenkov light-producing particles

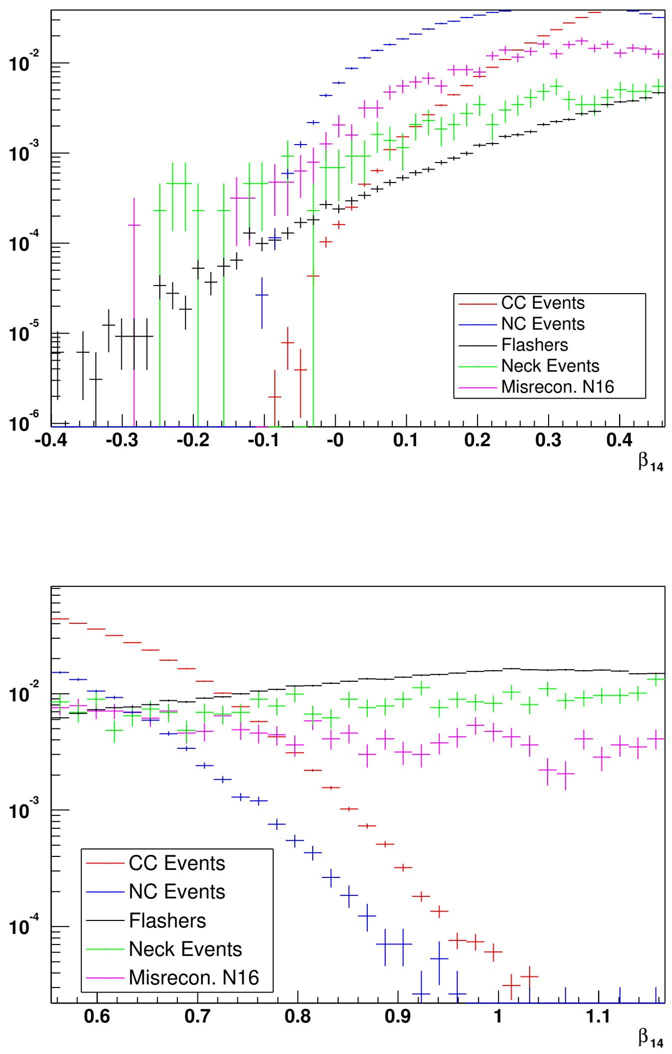

Figure 5.7: Determination of low and high β_{14} limits.

emitted, the ^{208}Tl events are typically more isotropic than the ^{214}Bi events and may be statistically separated using β_{14} isotropy distributions. With ^{24}Na as a background (see Section 5.3.2), a distribution for sodium events must also be included in this extraction. This comes from the sodium activation calibration and its amplitude is calculated and fixed. Neutrino signal must also be fitted out to obtain the correct amounts of ^{214}Bi and ^{208}Tl. Distributions of β_{14} for ^{214}Bi, ^{208}Tl, and ^{23}Na are displayed in Figure 5.8. These distributions are quite well known because ^{214}Bi Monte Carlo is calibrated using the radon injection data and ^{208}Tl is verified by the agreement between ^{24}Na data and Monte Carlo (the two nuclei have similar decay chains). The numbers extracted from this analysis are in agreement with those from the chemical measurements.

5.3.2 Sodium Activation

Sodium in the salt added to the D_2O may become naturally activated by neutron capture. The ^{23}Na captures a neutron and becomes ^{24}Na*, which decays with a half-life of 15 hours. The ^{24}Na* emits a 1.4 MeV β and two γ's. One of the γ's has an energy of 2.75 MeV, so it has the potential to photodisintegrate the deuteron, producing a free neutron which is background to the neutral current signal.

The sodium also creates an advantage for calibrating the detector. The ^{24}Na may be used as a containerless low energy calibration source. A source of γ-rays from a Th source was added to the heavy water and removed. The γ's photodisintegrate the deuterons, creating free neutrons which capture on ^{23}Na. The ^{24}Na* decays as described above. The N_{hit} distributions for the calibration data and Monte Carlo are in very good agreement. This gives a great deal of confidence into how well the backgrounds are modeled in SNO. The decay of ^{24}Na* is quite similar to that of ^{208}Tl, so the excellent modeling of this decay implies that both the decay chains and the resulting neutron and Čerenkov background are modeled well.

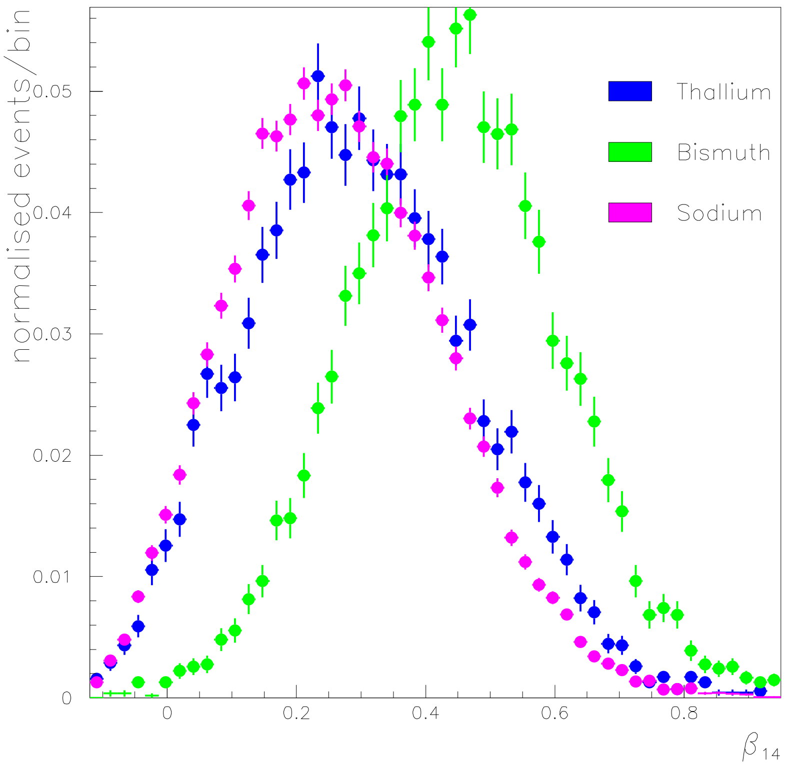

Figure 5.8: β_{14} distributions for low energy background events. Figure provided by C. Sims.

Chapter 6

Systematic Uncertainties of β_{14}

6.1 Definition of Systematic Uncertainty

We gain a good deal of *certainty* in the detector response to physical data by deploying calibration sources. Results of calibration data are fed into the Monte Carlo. For example, as explained in Chapter 4, it was through the comparison of data and Monte Carlo that we realized that the EGS4 code utilized in the SNO Monte Carlo was missing a term that was crucial for accurate simulation of event isotropy. Optical constants, neutron detection efficiency, and energy response are all determined using calibration sources. These pieces of information go into the SNO Monte Carlo so that neutrino and background events may be simulated as accurately as possible. Characteristic distributions, such as isotropy and energy, may then be formed for the different types of events. However, there will always be some sort of uncertainty in these distributions due to what we cannot learn about the detector response from calibration sources.

Statistical uncertainties are the result of fluctuations arising from the fact that the measurement is based on a finite number of observations with Poisson type fluctuations [90]. *Systematic uncertainties* arise from the uncertainties associated with the nature of obtaining the measurement. Although the data sets from SNO are not that large (a few thousand events) by particle physics standards, the results are limited not by statistics but by systematic uncertainties.

Just as calibration sources help us to understand the detector response, they also help us to determine what we don't know. The systematic uncertainties of SNO are normally determined using the data from calibration sources, most of which are placed at discrete locations throughout the detector.

Primarily, the ^{16}N source is used to assign systematic uncertainty to the isotropy distributions. The β_{14} distribution for the ^{16}N source is well approximated by a Gaussian. For each ^{16}N run i, the β_{14} distribution is fit to obtain the mean μ_i and width σ_i. To get the mean value of μ for the ^{16}N runs, we average over the total number of selected ^{16}N runs and the uncertainty on μ comes from the variation amongst the different measurements μ_i from the different runs. The measurement of μ_i for a run might be dependent, for example, on the location of the source and/or the time at which the run was taken. Also, different measurements taken at the same position under the same detector conditions will not be exactly the same due to statistical fluctuations. See for example Figure 6.3, which shows the mean value of β_{14} (μ_i) versus the radial position ($(R_{Source}/R_{AV})^3 \equiv (R_{Source}/600\text{ cm})^3$) of the source. It is clear that there is variation

(a) between data and Monte Carlo,

(b) as a function of radial position, and

(c) between measurements taken at nominally the same position.

In this chapter, the systematic uncertainty will be calculated to account for all three of the above points. In the next chapter, it will be shown that the β_{14} values may be corrected to reduce errors arising from points (a) and (b). However, statistical deviations such as (c) are not something that might be reduced.

The general formula used to calculate the *volume-weighted* fractional systematic uncertainty of a parameter p (such as the mean μ described above) is given as follows:

$$\sigma_p = \frac{\sum_i \frac{V_k}{\sigma_i^2 N_k} \left(\frac{p_i^{Data} - p_i^{MC}}{p_i^{MC}}\right)^2}{\sum_i \frac{V_k}{\sigma_i^2 N_k}}, \tag{6.1}$$

where

- the radial distribution of the source positions is broken up into k shells between 0 and the fiducial volume,
- each run i falls into one of the k shells,
- V_k = fractional volume of shell k,
- N_k = number of runs in shell k,
- p_i^{Data} is the parameter value (e.g. the mean of a Gaussian) for the data from run i,
- p_i^{MC} is the parameter value for the Monte Carlo of run i, and
- σ_i^2 is the fit error on parameter p_i for run i and is defined as:

$$\sigma_i^2 = \left[\sigma\left(\frac{p_i^{Data} - p_i^{MC}}{p_i^{MC}}\right)\right]^2 = \left(\frac{p_i^{Data}}{p_i^{MC}}\right)^2 \left[\left(\frac{\sigma_i^{Data}}{p_i^{Data}}\right)^2 + \left(\frac{\sigma_i^{MC}}{p_i^{MC}}\right)^2\right].$$

This formula essentially averages the fractional difference between data and Monte Carlo $(p_i^{Data} - p_i^{MC})/p_i^{MC}$ in each volume shell and weights the uncertainty such that an equal contribution of the fractional difference is made from each shell. Also included is a weighting corresponding to the error on parameter value for each run, $(1/\sigma_i^2)$. This means that runs with more accurate parameter values (most likely because there are more statistics in that run) will be weighted more highly than other runs.

The probability density functions used in the signal extraction in this thesis come from signal Monte Carlo (for reasons discussed in Chapter 7), so it is important that the difference between data and Monte Carlo be included in the systematic uncertainty of β_{14}. The calculation of systematic uncertainty on CC and ES β_{14} distributins comes from ^{16}N data comparison with Monte Carlo. The uncertainty on the NC β_{14} distribution is assigned using ^{252}Cf data and MC comparison. ^{252}Cf is also used to gain more information on the energy dependence of the uncertainty. The CC data from the pure D_2O phase gives information on the energy dependence of the uncertainty, although the statistics are very limited. The systematic uncertainty at low energies may be checked with the data from the radon injection.

The following questions need to be addressed in assigning the systematic uncertainties on isotropy parameters:

1. Is the systematic uncertainty different between electrons, γ's, and neutrons?

2. Is the systematic uncertainty energy dependent?

3. Does the systematic uncertainty change with time?

All of the above should be investigated, but is important to recognize which should be included in the systematic uncertainty of β_{14}. For example, we wish to know if β_{14} values change over time (this would likely be due to a decreasing collection efficiency of the PMTs). If there is a variation, but this variation is modeled by the Monte Carlo, then it does not contribute to the uncertainty.

6.2 Systematic Uncertainties from ^{16}N Data

Cuts applied to triggered ^{16}N data and MC are found in Table 6.1. A cut was placed on high z (upper hemisphere of the detector) runs because the isotropy of events reconstructing near the neck where there are no PMTs is quite different to that of events reconstructing elsewhere. The volume for which the neck influences the isotropy is quite small, but that area has several calibration runs because runs are often carried out along the $z = 0$ axis. Including these runs would bias the the systematic studies of high radius

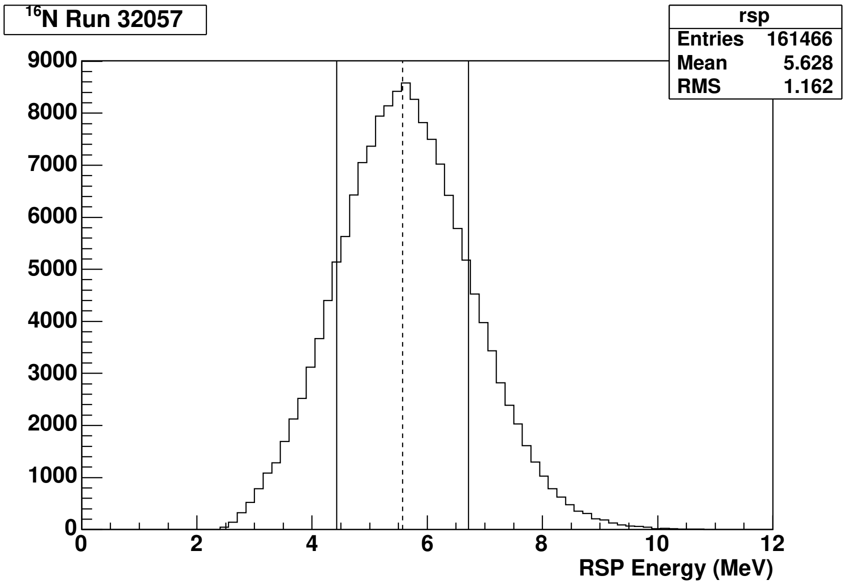

Figure 6.1: RSP energy (E_{eff}) distribution for ^{16}N run 32057. The dashed line is the mean value of the distribution and the solid lines are $\pm$ 1 RMS from the mean.

Field	Low Cut	High Cut
Energy	Mean E_{eff}-RMS	Mean E_{eff}+RMS
Fit Radius	-	600 cm
Fit z Position	-	+300 cm
ITR	0.55	-
β_{14}	-0.12	0.95

Table 6.1: Cuts applied to ^{16}N data.

calibration runs. The distribution of RSP energies, E_{eff}, for one ^{16}N run is displayed in Figure 6.1; the solid lines are the boundaries of the energy cut for this run.

One-dimensional β_{14} histograms from each run were fit with a Gaussian to obtain values for the mean and width. An example of this fit is shown in Figure 6.2. The fit mean and width of the data and Monte Carlo for each run is plotted versus the source radial position in Figures 6.3 and 6.4. The fractional differences between ^{16}N data and MC for β_{14} fit means and widths are displayed in Figure 6.5. The Monte Carlo slightly underestimates the β_{14} values at the center of the detector by about 1%, and further into the volume the agreement between data and Monte Carlo becomes better. Beyond 500 cm, the Monte Carlo overestimates the β_{14} values. The volume-weighted systematic uncertainty calculation found in (6.1) is used because the difference between data and Monte Carlo is dependent on radial position. There does not appear to be a radial dependence on the difference between data and MC for the width, but the same calculation is used for consistency.

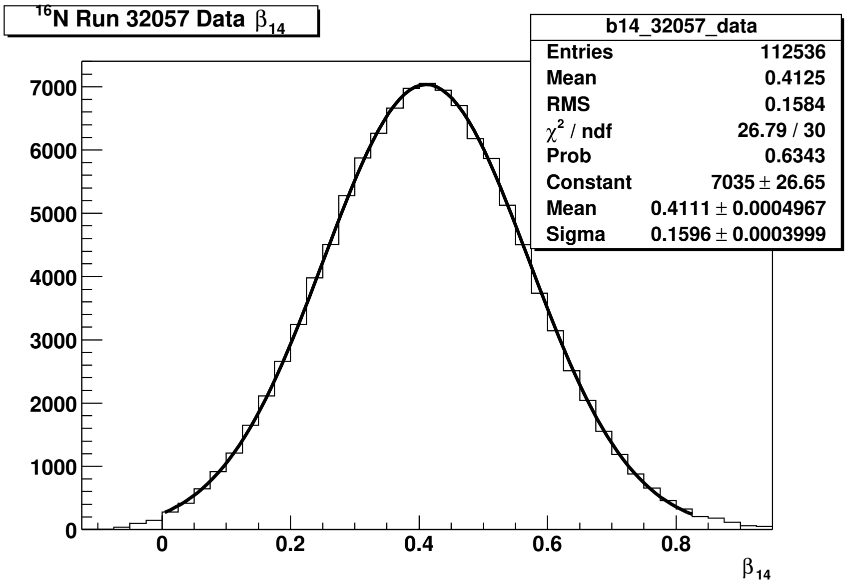

Figure 6.2: A Gaussian fit to β_{14} distribution from ^{16}N run 32057.

The systematic uncertainty on the fit parameters is calculated using Equation 6.1. Table 6.2 shows this measure for various fiducial radii. The systematic uncertainty appears to be consistent to a radius of approximately 560 cm. A number of factors contribute to the selection of fiducial volume including removal of low energy Čerenkov AV events, fraction of neutrino events sacrificed, and consistency of various systematic uncertainties. A fiducial volume of radius 550 cm has been used in most SNO analyses and will be used for the data analysis in this thesis. Therefore, the systematic uncertainty applied to CC and ES β_{14} distributions is 0.85% for the mean and 0.94% for the width.

Fiducial Radius	σ_B (mean)	σ_C (width)
440.00 cm	0.81%	0.91%
510.00 cm	0.81%	0.96%
530.00 cm	0.81%	0.92%
550.00 cm	**0.85%**	**0.94%**
560.00 cm	0.85%	0.94%
580.00 cm	0.90%	0.95%
600.00 cm	1.04%	0.95%

Table 6.2: Systematic uncertainty on β_{14} fit parameters for various fiducial volumes.

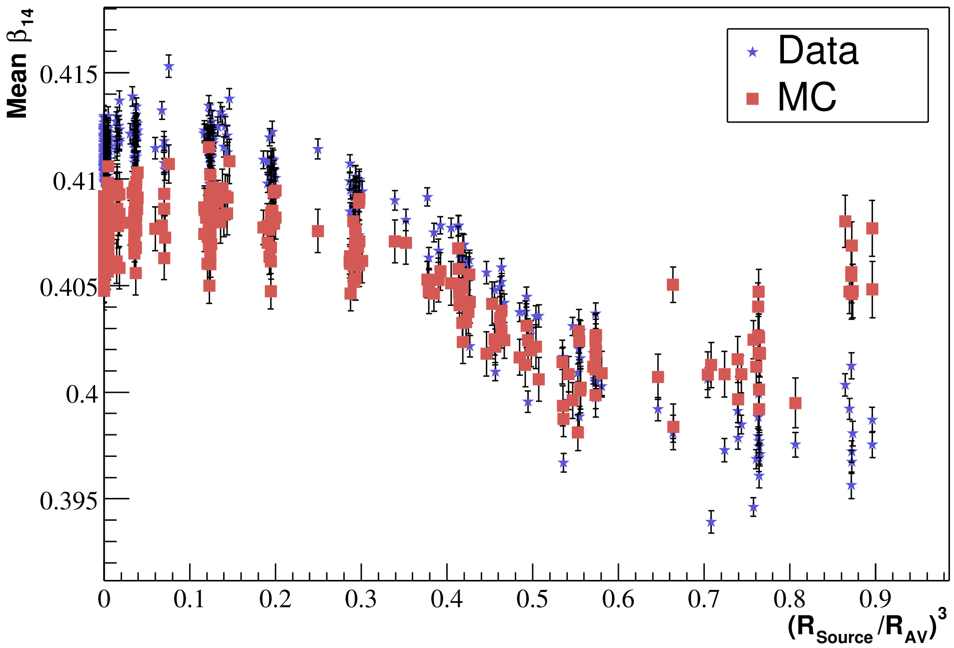

Figure 6.3: Mean β_{14} versus source radial position for ^{16}N data and MC.

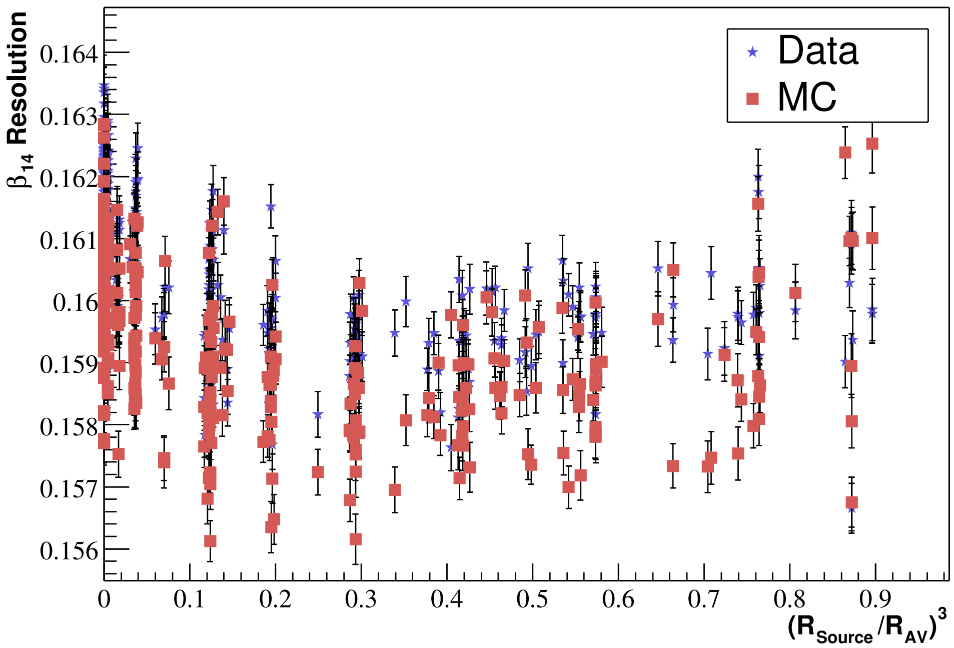

Figure 6.4: β_{14} resolution versus source radial position for ^{16}N data and MC.

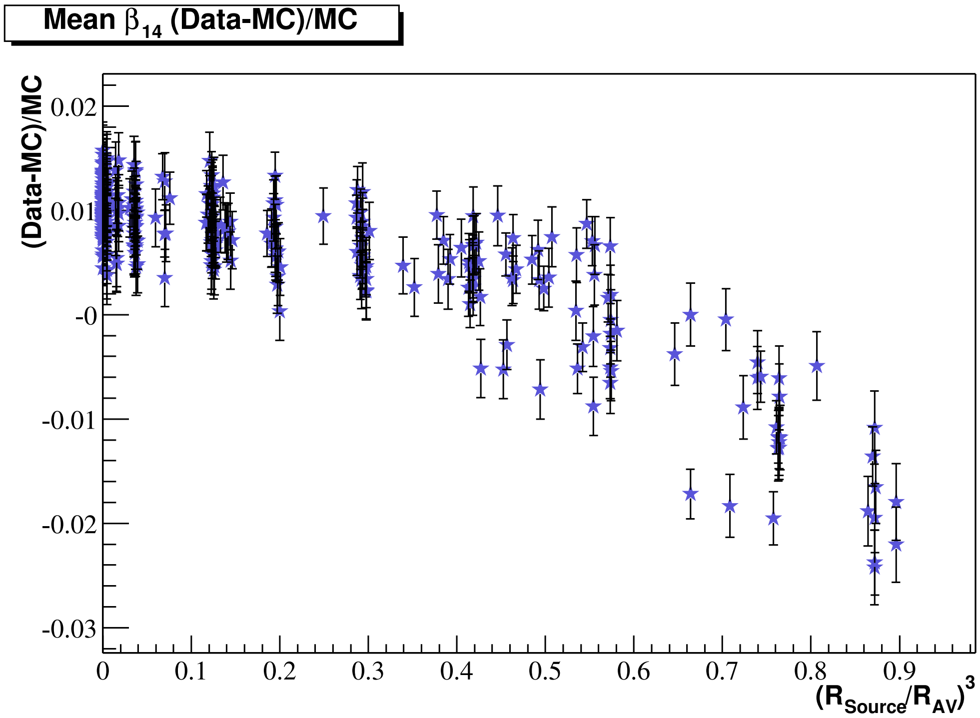

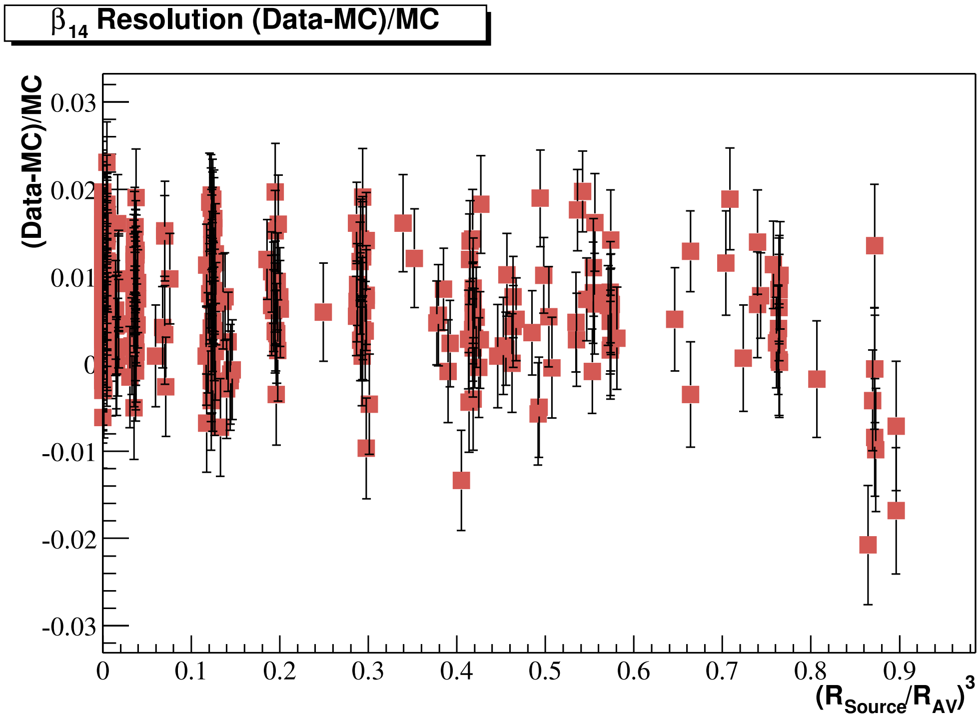

Figure 6.5: Fractional difference between ^{16}N data and Monte Carlo β_{14} fit means and resolutions versus source radial position.

6.2.1 Variation of β_{14} Fit Parameters with Time

Figure 6.6 shows that the mean value of β_{14} for ^{16}N is consistent over time. Julian date is used where "Day 1" in SNOMAN corresponds to Jan. 1, 1975, 0 hours UTC. The first run was taken on July 26, 2001 (Julian date 9704), the final run on Sept. 3, 2003 (Julian date 10473). The resolution appears to increase over time in both the data and Monte Carlo with approximately the same slope. This is most likely due to the decreased light collection of the PMTs over time which is mainly due to increased attenuation in the heavy water and reduced reflection by the PMT concentrators.

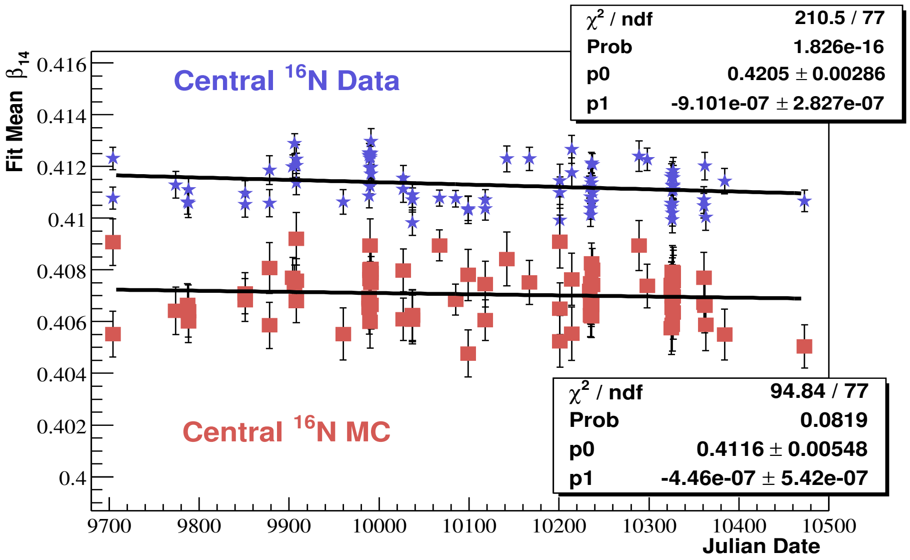

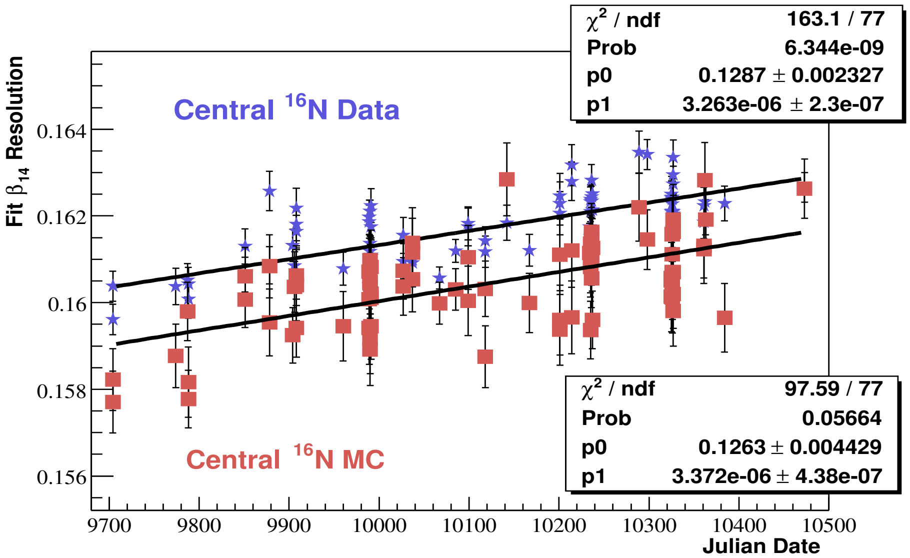

Figure 6.6: Mean and resolution of β_{14} versus Julian date.

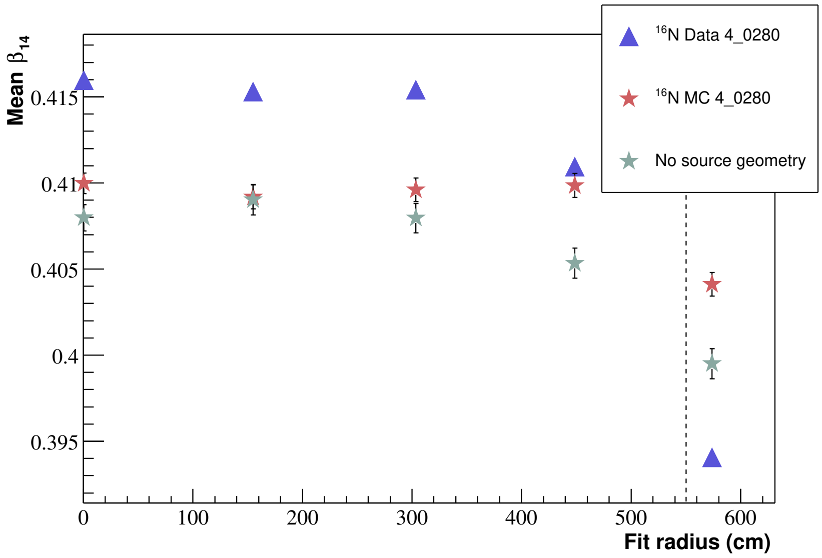

Figure 6.7: Mean β_{14} versus fit radial position with ^{16}N source geometry turned on and off in the Monte Carlo.

6.2.2 ^{16}N Source Effects

^{16}N Monte Carlo was generated with the source geometry removed and the results are shown in Figure 6.7[1]. With the source geometry removed, β_{14} decreases (events become more isotropic) due to the fact that there is no source to shield light. The volume-weighted difference between source on and off is 0.8%. Thus, if the error on the modeling of the source were as high as 25% this would result in a small error of 0.2% on the mean value of β_{14}.

6.2.3 Energy Dependence of Uncertainty from ^{16}N

Using the ^{16}N source data and Monte Carlo, the energy dependence was studied two different ways. First, the ^{16}N events from each run were divided up into specific energy ranges and the systematic uncertainty was calculated for each effective kinetic energy (T_{eff}) range. Next, the events were divided up into energy ranges about the mean T_{eff} of each run, μ. The value σ refers to the RMS of the energy distribution. For reference, central run 20674 has μ = 5.061 and σ = 1.149. In this case, each energy range has approximately the same statistics. These energies ranges are shown visibly in Figure 6.8[2]. The uncertainties on the mean, σ_B, and width, σ_C, fit parameters are

[1]Note that the data and MC for this comparison were generated with a different production than in the previous sections. The correction to the EGS4 multiple scattering angles is included in the Monte Carlo, but the most recent optics constants for the salt phase are not used.

[2]This distribution looks different from the one in Figure 6.1 because the RSP energy distributions have been smoothed in more recently processed data and Monte Carlo. The means are different because

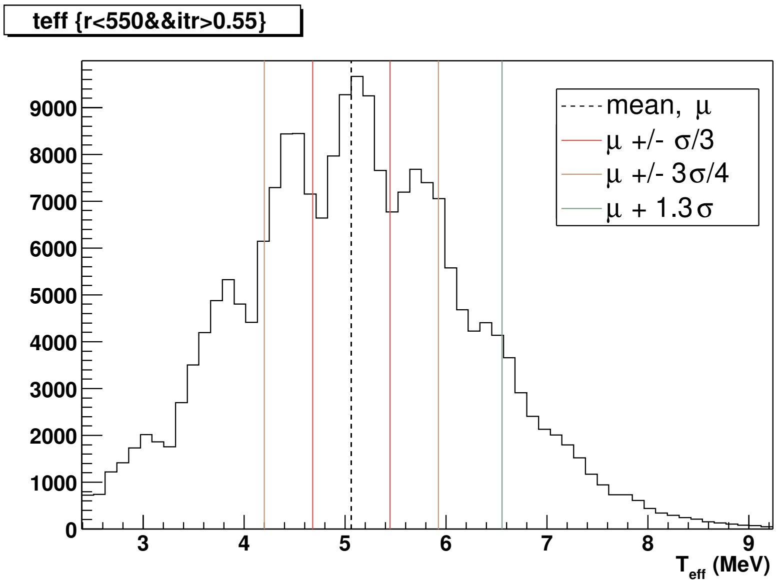

Figure 6.8: Effective kinetic energy distribution from ^{16}N Run 20674.

T_{eff} Range	Central Data Mean β_{14}	σ_B (mean)	σ_C (width)
4.0-5.0 MeV	0.399	1.05%	1.21%
5.0-6.0 MeV	0.424	0.86%	0.81%
5.5-6.5 MeV	0.434	0.92%	0.95%
6.0-7.0 MeV	0.444	1.03%	1.12%
7.0-10.0 MeV	0.457	1.88%	1.81%
$(\mu - 3\sigma/4, \mu - \sigma/3)$	0.398	1.20%	1.93%
$(\mu - \sigma/3, \mu)$	0.408	1.13%	1.88%
$(\mu, \mu + \sigma/3)$	0.418	0.97%	1.46%
$(\mu + \sigma/3, \mu + 3\sigma/4)$	0.429	0.92%	1.27%
$(\mu + 3\sigma/4, \mu + 1.3\sigma)$	0.441	1.10%	1.48%
$> \mu + 1.3\sigma$	0.453	1.41%	1.46%

Table 6.3: Systematic uncertainty for various cuts on effective kinetic energy.

displayed in Table 6.3. A fiducial volume cut of 550 cm was applied and the mean value of β_{14} for central ^{16}N data is included for reference only.

Note that ^{16}N events are more isotropic than single electron events due to multiple scattering of the 6.13 MeV γ. A single electron of 5 MeV (close to the mean kinetic energy from ^{16}N) has a mean β_{14} value of 0.47 and a 6.5 MeV electron has a mean β_{14} value of 0.48, while mean β_{14} for ^{16}N data increases over this range from 0.41 to 0.44. This is because the Čerenkov light from ^{16}N events with higher effective energies is dominantly from one (relatively) high energy electron, and thus it more closely resembles that from single electron events. The agreement between data and Monte Carlo for events with

kinetic energy is displayed here, while *total* energy is displayed in Figure 6.1.

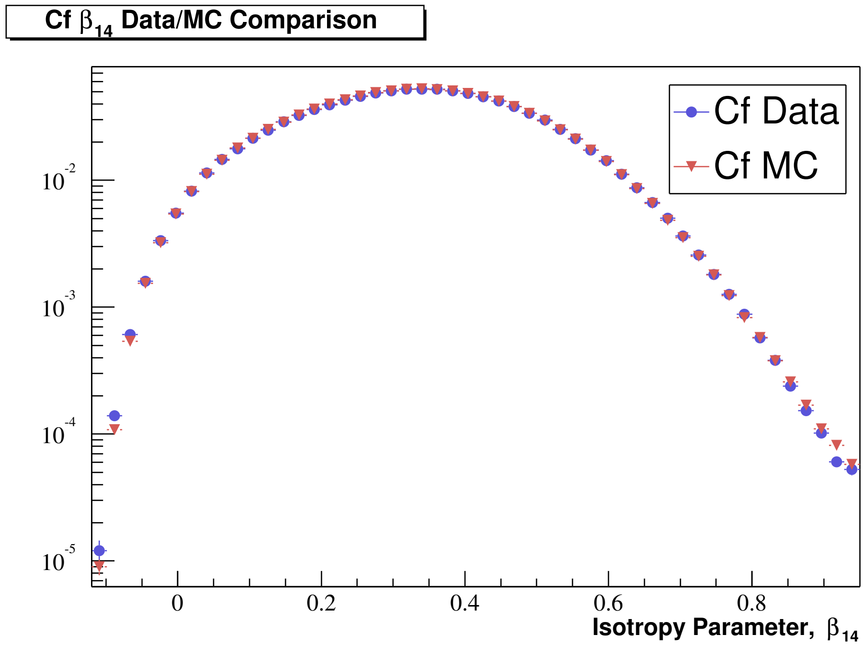

Figure 6.9: β_{14} (merged over T_{eff} range 5.5–20 MeV) for Cf data and MC.

different T_{eff} values, with no significant increase in σ_B, is an indication that the ^{16}N source is modeled well, i.e. the γ interactions, subsequent electron multiple scattering, and Čerenkov light production is accurately reproduced. This implies that the Monte Carlo is also modeling pure electron events well.

6.3 Systematic Uncertainties from ^{252}Cf Data

Figure 6.9 shows the excellent agreement between data and MC β_{14} distributions on a logarithmic scale. The β_{14} distributions for each Cf run were fit using Equation 6.2 which is described in detail in Chapter 7,

$$A \cdot \exp\left[-0.5\left(\frac{x-B}{C}\right)^2\right] \cdot \left[1+\left(\frac{0.1}{x-D}\right)^4\right]^{-1}. \tag{6.2}$$

The fit parameters B, C, and D are displayed versus source radial position in Figures 6.10, 6.11 and 6.12. The fractional differences between data and Monte Carlo are displayed in 6.13. For a fiducial volume of radius 550 cm and a T_{eff} threshold of 5.5 MeV, the volume-weighted uncertainty from Cf data is 0.48% for the mean B, 0.67% for the width C, and 2.77% for parameter D. We are not particularly concerned with the uncertainty on parameter D because it has little effect on the PDF.

6.3.1 Energy Dependence of Uncertainty from ^{252}Cf

Cf events were divided into different energy ranges and the systematic uncertainty for the fit mean and width were calculated for each energy range. The results are found in Table 6.4. There does not seem to be a significant dependence on the systematic uncertainty as a function of energy.

T_{eff} Range	σ_B (mean)	σ_C (width)
5.0-6.0 MeV	1.68%	0.80%
5.5-6.5 MeV	1.21%	0.72%
6.0-7.0 MeV	0.64%	0.75%
6.5-7.5 MeV	0.53%	0.77%
7.0-8.0 MeV	0.55%	0.98%
7.5-8.5 MeV	0.58%	1.32%
≥5 MeV	0.67%	0.66%
≥5.5 MeV	**0.48%**	**0.67%**
≥6 MeV	0.34%	0.77%

Table 6.4: Systematic uncertainty for various effective kinetic energy cuts from a volume-weighted Cf data/MC comparison with a fiducial volume of radius 550 cm.

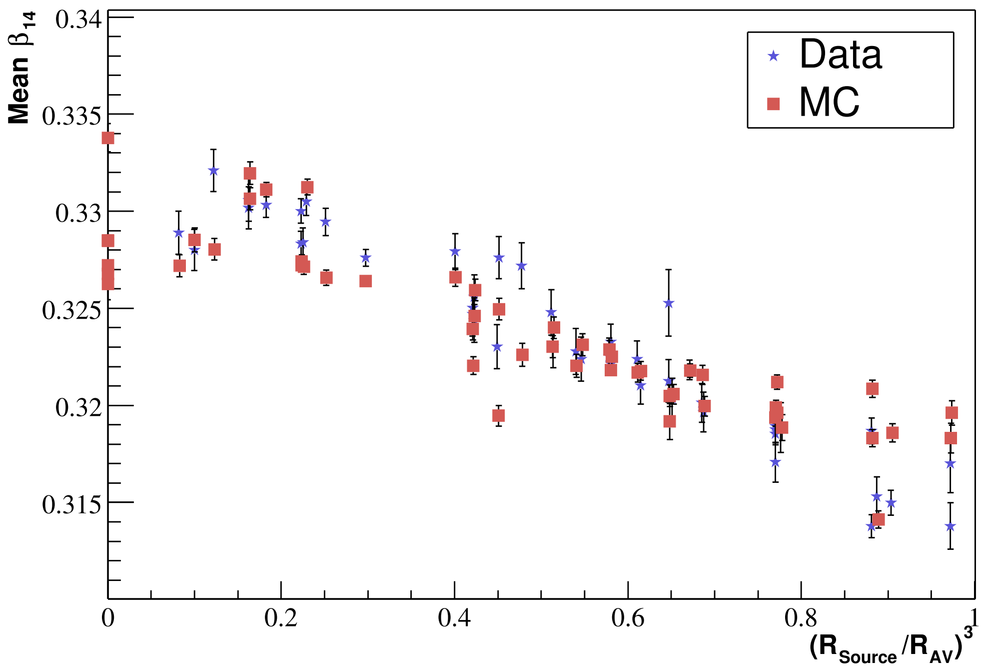

Figure 6.10: Mean β_{14} (fit parameter B) versus source radial position for ^{252}Cf data and MC.

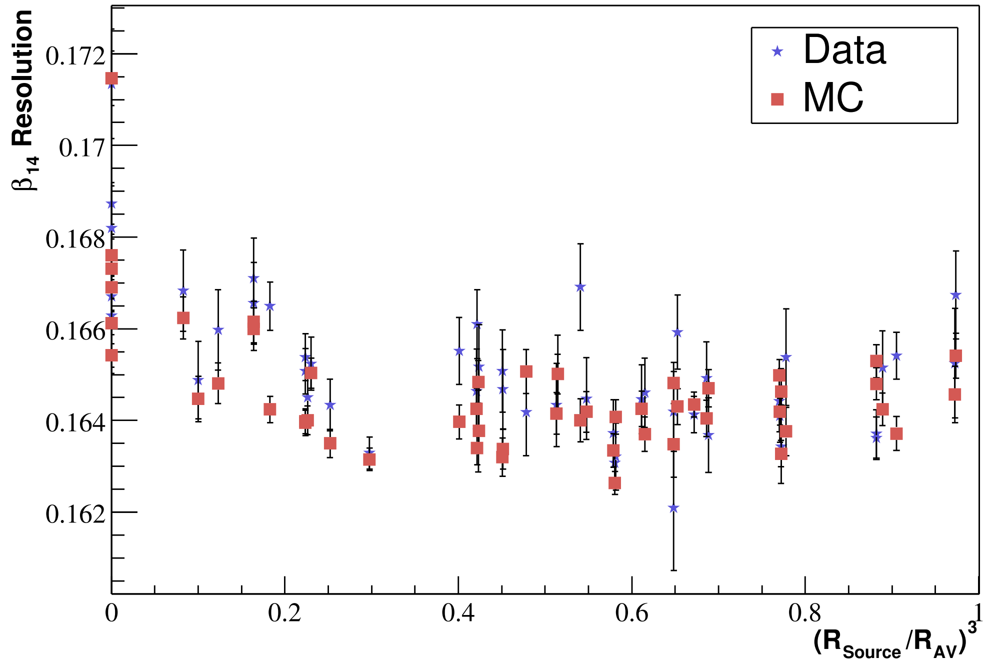

Figure 6.11: β_{14} fit parameter C versus source radial position for ^{252}Cf data and MC.

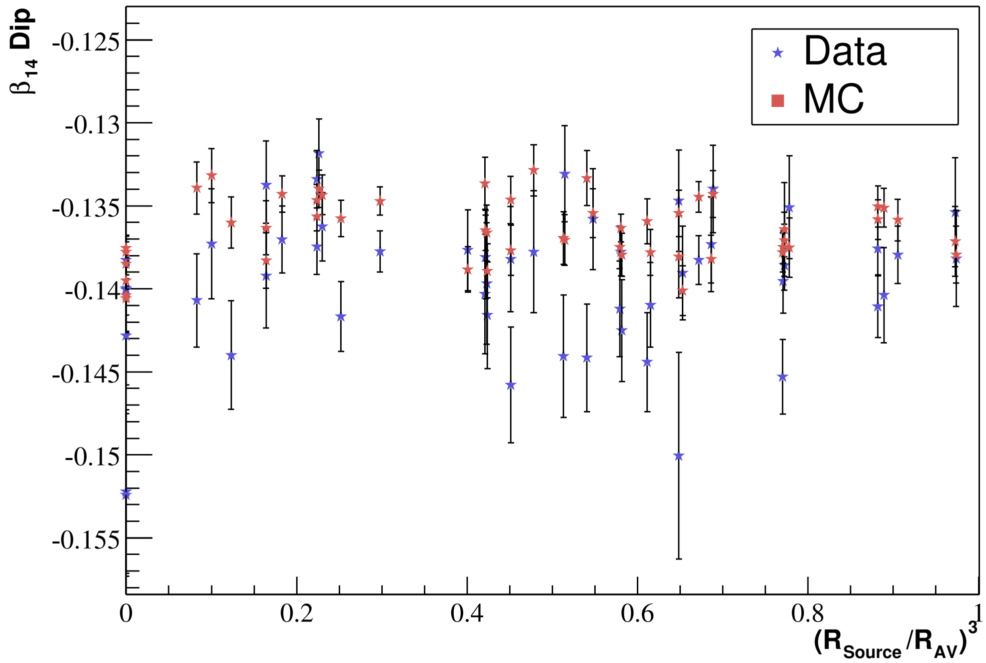

Figure 6.12: β_{14} fit parameter D versus source radial position for ^{252}Cf data and MC.

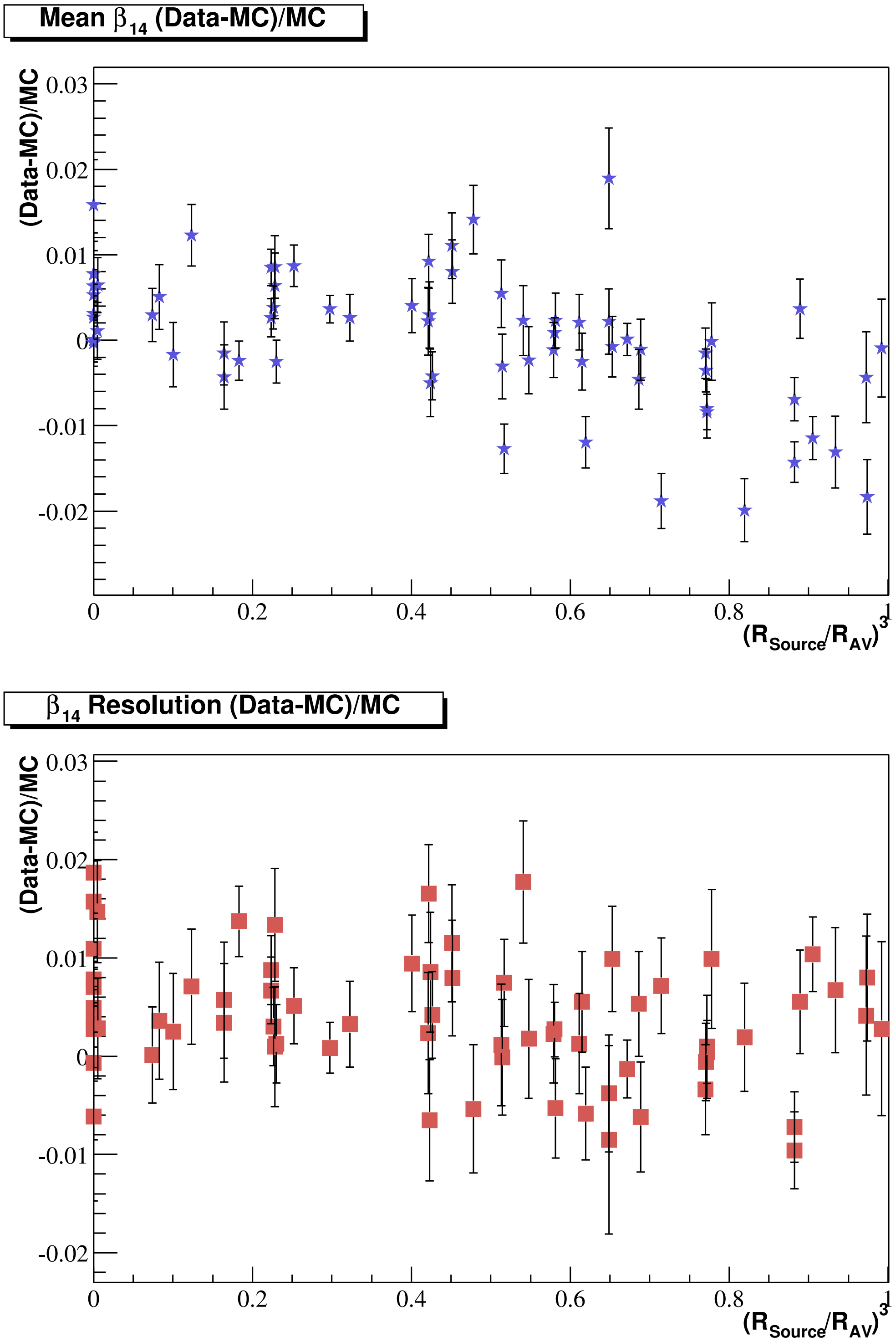

Figure 6.13: Fractional difference between ^{252}Cf data and Monte Carlo β_{14} fit means and resolutions versus source radial position.

6.3.2 Time Dependence of Cf Data and Monte Carlo

Figure 6.14 shows the fit mean values of ^{252}Cf β_{14} distributions over time for the data and the Monte Carlo. There is no clear time dependence on ^{252}Cf β_{14} mean.

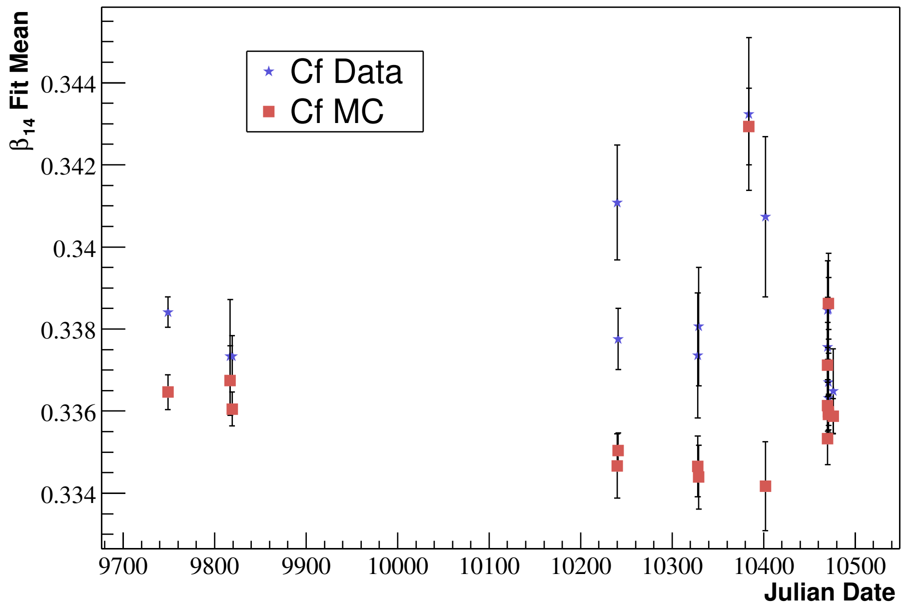

Figure 6.14: Mean β_{14} from Cf data and MC versus Julian date.

6.4 Additional β_{14} Systematic Studies

6.4.1 Pure D_2O Data

The data from the pure D_2O phase of SNO were processed using SNOMAN version 4.0196 with the correction to the EGS4 multiple scattering angles included. The cuts in Table 6.5 were used. The lower cut on energy is to remove most of the neutrons in the data set.

Field	Low Cut	High Cut
Effective KE	7.0 MeV	20.0 MeV
Fit Radius	-	550 cm
ITR	0.55	-
β_{14}	0.05	0.95

Table 6.5: Cuts applied to pure D_2O data.

Figure 6.15 shows the β_{14} distributions for the data and Monte Carlo using these cuts. The distributions were fit with Gaussians. Because the data are already distributed

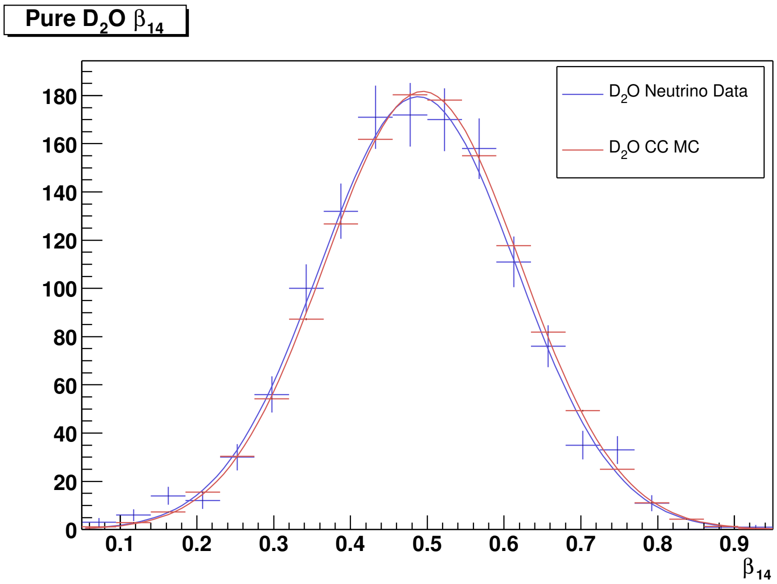

Figure 6.15: β_{14} for pure D_2O data and MC.

evenly throughout the volume, the volume weighted calculation was not used for the systematic uncertainty. The percentage difference between the mean value of β_{14} for the data and MC is 1.19% and the uncertainty on the width is 0.39%. The systematic uncertainties for various effective kinetic energy bins are found in Table 6.6.

The statistics are very limited, particularly when dividing the data up into energy bins, so it is difficult to draw strong conclusions from these numbers. It can be noted, however, that there is no alarmingly large systematic uncertainty at higher energies.

T_{eff} Range	Data Mean β_{14}	σ_B (mean)	σ_C (width)
7.0 - 8.0	0.4822	0.40%	2.31%
8.0 - 9.0	0.4860	1.36%	2.91%
9.0 - 11.0	0.4869	1.99%	1.81%
7.0 - 20.0	0.4860	**1.19%**	**0.39%**

Table 6.6: Systematic uncertainty for various effective kinetic energy cuts from pure D_2O data/MC comparison with a fiducial radius of 550 cm.

6.4.2 Radon Injection

Radon was injected into the salted D_2O to in order to study the detector response to low energy Čerenkov background. The heavy water was circulated after the injection to spread the radon approximately uniformly throughout the AV. This calibration has the advantage that there are no systematic uncertainties associated with it due to a source

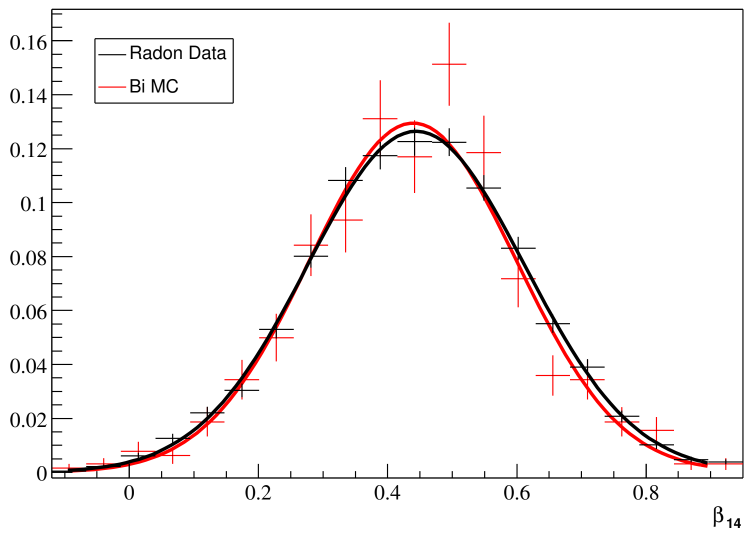

Figure 6.16: β_{14} for Rn data and Bi MC.

container. Data from the radon injection into the salted D_2O was compared with ^{214}Bi Monte Carlo. The cuts used are found in Table 6.7.

Field	Low Cut	High Cut
T_{eff}	4.0	4.5
Fit Radius	-	450 cm
ITR	0.55	-
β_{14}	-0.12	0.95

Table 6.7: Cuts applied to Rn data and Bi MC.

Figure 6.16 shows the data and MC β_{14} distributions. Fitting a Gaussian to the β_{14} histograms, the mean value from the radon data is 0.444 and the mean from the MC is 0.439, yielding a difference of 0.6%. Again, statistics are very limited, but the agreement between data and Monte Carlo implies that there is not a large systematic uncertainty at lower energies.

6.5 Summary of β_{14} Systematic Uncertainties

The systematic uncertainty seems to be fairly consistent between electrons, neutrons, and γ's (from ^{16}N). It may be expected that the uncertainty be less for neutrons because β_{14} is a measure of the *overall* isotropy of an event, not just how cone-like it is. For neutron capture on ^{35}Cl, an average of 2–3 γ's are produced. Therefore, the value of β_{14} is partly determined by the isotropy of the decay, as well as by the modeling of the

Čerenkov cone. The same is true for ^{16}N events, but to a lesser extent. The systematic uncertainties derived from a Cf data/MC comparison are slightly less than that derived from ^{16}N, but the values are close.

Due to limited statistics, it is difficult to get an accurate determination of the energy dependence of the β_{14} systematic uncertainty. It may be concluded, however, that there does not appear to be a strong energy dependence of the β_{14} systematic uncertainty.

The dependence of β_{14} with time is negligible. Any variation would, however, be included in the ^{16}N data versus MC calculation of systematic uncertainty. In Section 6.2.2, it was shown that large effects in source modeling would not have large effects on β_{14}.

The ^{16}N data/MC comparison is used to assign systematics for the CC and ES PDFs. The Cf data/MC comparison is used to assign systematics to the neutron PDF. A summary of the systematic uncertainties for β_{14} PDFs is found in Table 6.8. In the following chapter, the β_{14} values will be calibrated and the systematic uncertainties reduced.

Source	σ_B (mean)	σ_C (width)	Apply To
^{16}N data vs. MC	0.87%	0.97%	Electron PDFs
Cf data vs. MC	0.48%	0.67%	Neutron PDFs

Table 6.8: Summary of β_{14} systematic uncertainties.

Chapter 7

Energy Dependent Isotropy PDFs

With the addition of salt to the heavy water it is possible to obtain a measurement of the ^{8}B solar neutrino flux and energy spectrum without any dependence on solar models. In the pure D_2O phase, characteristic energy distributions are the most effective way to separate the CC and NC signals; and to separate ES events, the fit direction of events with respect to the Sun ($\cos\theta_\odot$) is the most effective. For the salt data, the isotropy distributions are just as effective as the energy distributions at separating CC and NC events and they allow for the separation to be done without assumptions about the ^{8}B solar neutrino energy spectrum[1].

One-dimensional probability density functions (PDFs) for β_{14}, kinetic energy (T_{eff}), and $\cos\theta_\odot$ are displayed in Figures 7.1, 7.2, and 7.3. We wish to use the β_{14} distributions in the signal extraction of salt data; however, isotropy distributions have a small but significant dependence on energy. Therefore, 2-dimensional PDFs of β_{14} versus T_{eff} must be used. The distribution of $\cos\theta_\odot$ is nearly energy-independent, so 1D PDFs may be used.

Isotropy PDFs may be created using either calibration data or Monte Carlo simulation of the neutrino signals. If the Monte Carlo agrees well with data it is preferable to use the Monte Carlo because extrapolation between positions in the detector not accessible by calibration sources is possible. A discrepancy between calibration data and Monte Carlo was initially discovered, but the majority of this discrepancy was reconciled by correcting the angular distribution of electron scattering in the Monte Carlo to account for missing Mott terms in the EGS4 electron scattering cross section and other improvements which have been included in the more recent EGSnrc, as described in Chapter 4.

Even after the correction to the multiple scattering angles, there is still a small residual discrepancy between calibration data and Monte Carlo. From Figure 6.5 it is

[1] Some separation in the pure D_2O phase is possible using the different radial distributions but the resulting errors on the spectrum and flux are relatively large.

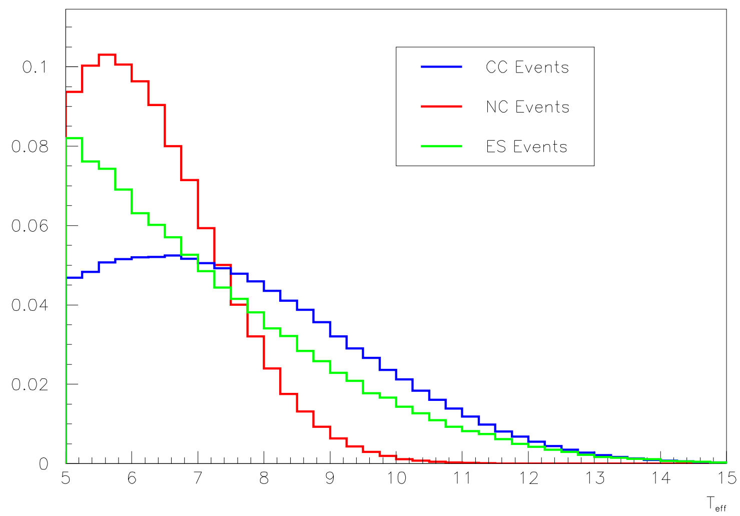

Figure 7.1: T_{eff} PDFs for neutrino signals in salted D_2O, normalized to unity.

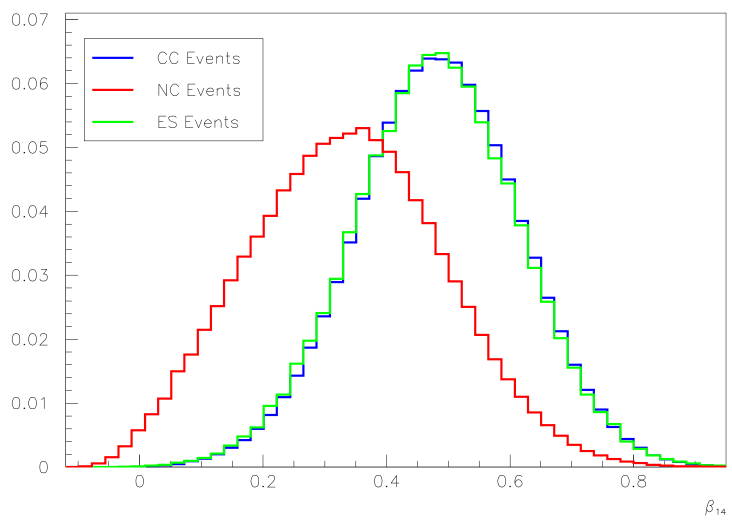

Figure 7.2: β_{14} PDFs for neutrino signals in salted D_2O, normalized to unity.

clear that there is a radially dependent difference between data and Monte Carlo β_{14} values for ^{16}N events. This radial dependence also exists for the difference between ^{252}Cf data and Monte Carlo, but it is less. The difference between data and Monte Carlo may be fit as a function of radial position and this fit used to shift the Monte Carlo values to agree with data. PDFs will be created both with and without shifting the β_{14} values for CC, ES, NC, and external neutron PDFs.

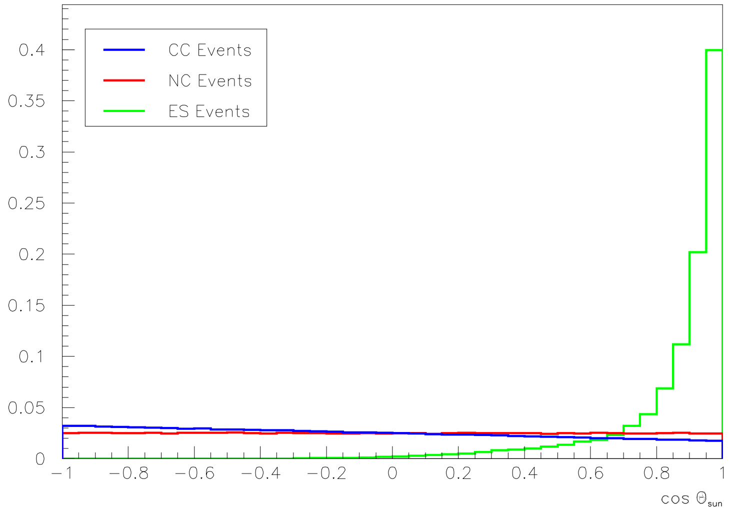

Figure 7.3: $\cos\theta_\odot$ PDFs for neutrino signals in salted D_2O, normalized to unity.

7.1 Radial Dependence of β_{14}

Before creating the radially dependent shift to β_{14} values, an attempt will be made to understand why β_{14} is dependent on how far an event reconstructs from the acrylic vessel and why the *difference* between data and Monte Carlo is dependent on radial fit position.

Figure 7.4 shows the radial dependence of β_{14} for different types of events: electrons (in 1 MeV effective kinetic energy ranges from 4–16 MeV), ^{16}N γ's, and neutrons. It appears that with increasing isotropy values, the radial dependence becomes stronger. Also, the discrepancy between data and Monte Carlo is more substantial for less isotropic events (^{16}N is less isotropic than the ^{252}Cf neutrons). This is clear from Figure 7.4, many figures in Chapter 6, and the calculation of systematic uncertainty using ^{16}N and ^{252}Cf data/MC. It can therefore be assumed that applying a radially dependent shift to β_{14} values for electron-type events based on the difference between ^{16}N data and Monte Carlo will not be too extreme.

First, however, it would be prudent to try to understand the behavior of ^{16}N Monte Carlo β_{14} values at high radii. There is a slight upturn past the fiducial volume of radius 550 cm which is not visible in any of the other distributions. An investigation was carried out to determine if there is a difference in isotropy between inward and outward going events. *Inward* meaning from the source towards the center of the detector volume; *outward* meaning directly towards the AV and PMTs. The measure of the direction of

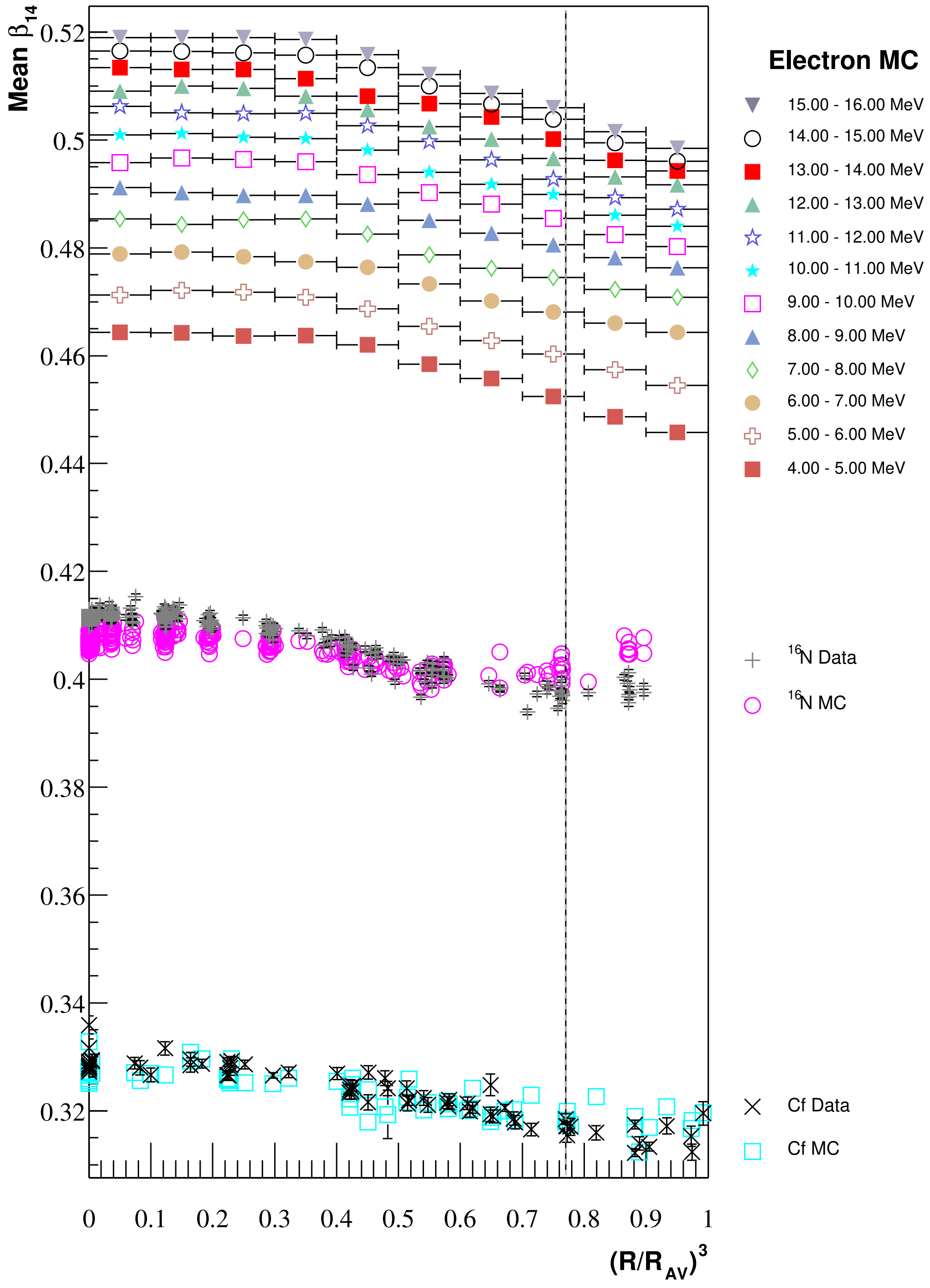

Figure 7.4: Radial dependence of mean β_{14} for events of different energies. Increased values of β_{14} indicate lower isotropy.

an event with respect to the center of the detector is given by

$$\frac{\mathbf{u}\cdot\mathbf{r}}{|\mathbf{r}|} = \cos\theta, \tag{7.1}$$

where $\mathbf{u}$ is the normalized (unit vector) direction of the event, $\mathbf{r}$ is the radial position of the fit vertex, and θ is the angle between these two vectors. Positive values ($\theta < 90°$) indicate outward going events and inward going events have negative values ($\theta > 90°$). The distance between the event vertex and the PMTs is larger for inward going events than for outward going events. Figure 7.5 shows a simple diagram of $\mathbf{u}\cdot\mathbf{r}$ for an outward moving particle.

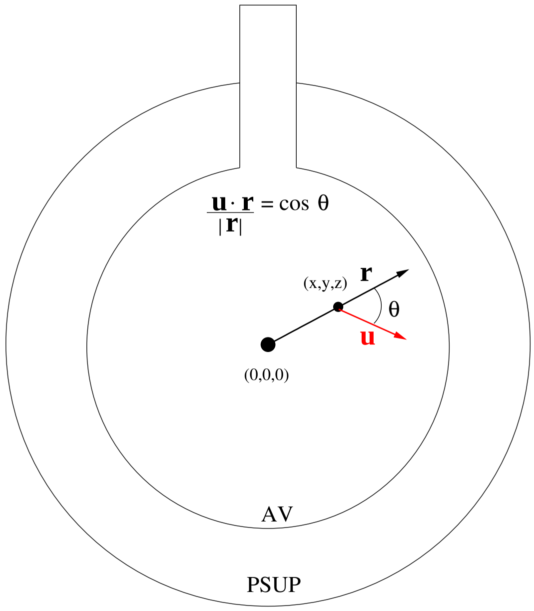

Figure 7.5: Diagram of $\mathbf{u}\cdot\mathbf{r}$ for an outward going event.

Figures 7.6 and 7.7 show mean β_{14} versus radial source position for inward and outward going ^{16}N and ^{252}Cf events. The ^{16}N plot shows that inward going events are modeled well by the Monte Carlo, except for a very small underestimation of the mean value, and the mean β_{14} values have no radial dependence. The outward going events, however, have a significant radial dependence on β_{14} and this is not well modeled by the MC after about 475 cm. This may be due to an inaccurate modeling of the scattering of photons passing through the AV at large angles. Thus, the effect of the AV on the isotropy becomes more significant the closer to the AV an event occurs. However, this discrepancy requires further investigation.

The ^{252}Cf plot shows that inward going events are well modeled by the MC within the fiducial volume of radius 550 cm. There is not much of a radial dependence on inward going events, except for some behavior near the center, which is well modeled by the MC. Like the ^{16}N data, there is a strong radial dependence of mean β_{14} for outward going events that the MC gets wrong after about 475 cm.

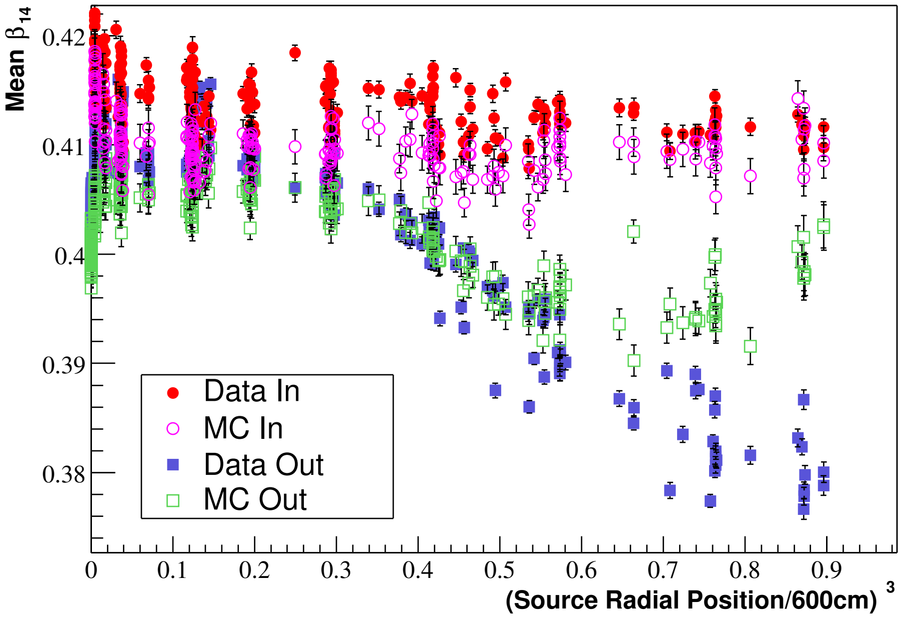

Figure 7.6: The dependence of ^{16}N mean β_{14} on $\mathbf{u}\cdot\mathbf{r}$.

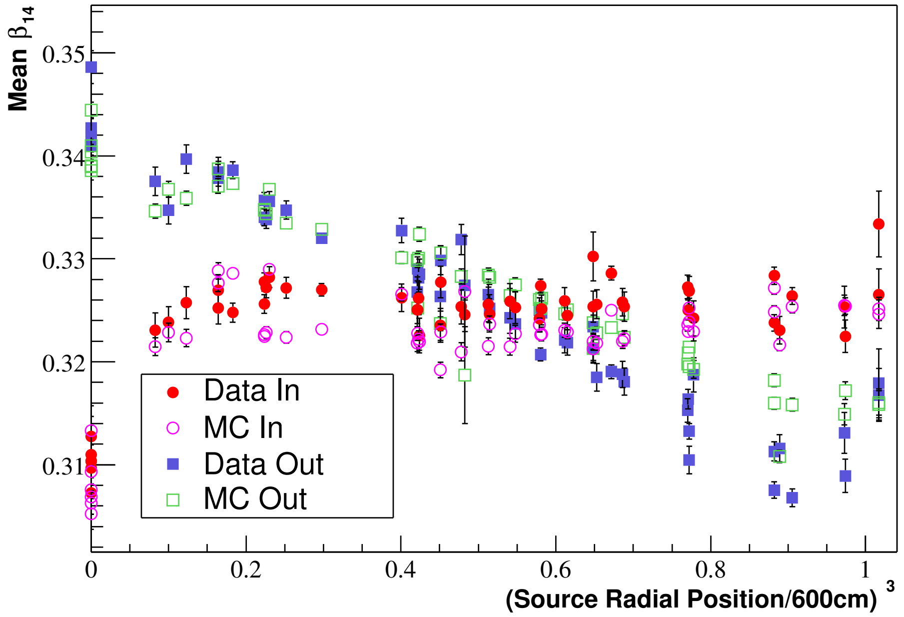

Figure 7.7: The dependence of ^{252}Cf mean β_{14} on $\mathbf{u}\cdot\mathbf{r}$.

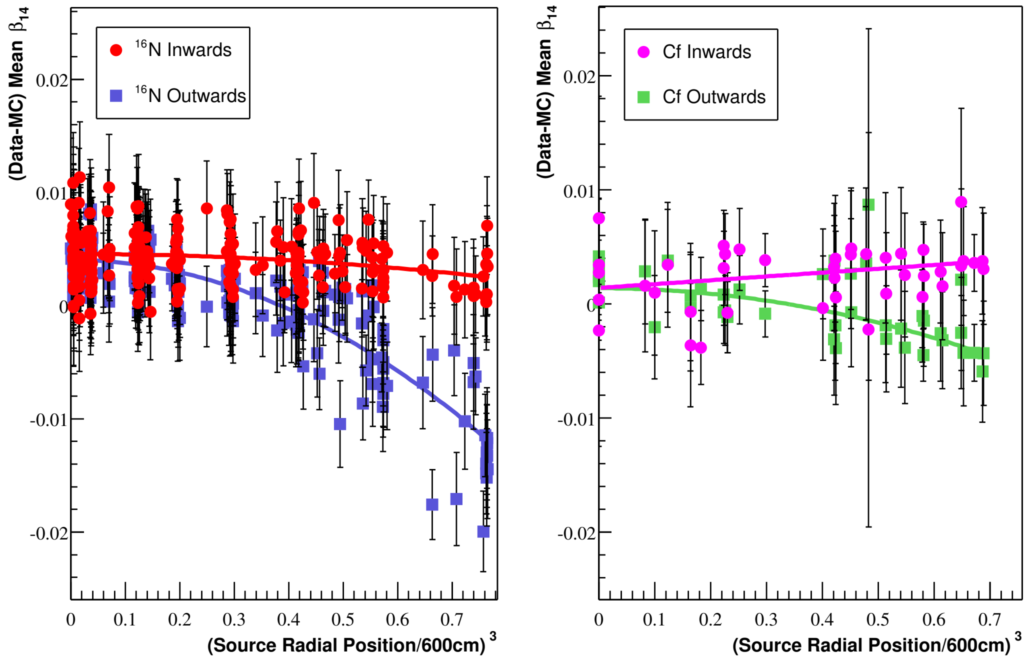

Figure 7.8: Mean β_{14} shifts between ^{16}N and ^{252}Cf data and Monte Carlo.

Based on this investigation, it has been decided to perform separate shifts to electron (CC and ES) and neutron (NC) event β_{14} values. The shift will depend on whether the event direction is inwards or outwards and on the reconstructed radial vertex of the event. Polynomials were fit to the difference between the data and Monte Carlo mean β_{14} values. Figure 7.8 shows these different shifts. For electron events, the following shifts will be applied to the Monte Carlo:

Electron Events

$$\begin{aligned} \textbf{Inward} \quad \beta'_{14} &= \beta_{14} + 0.0046 - 0.0035(R_{fit}/R_{AV})^6 \\ \textbf{Outward} \quad \beta'_{14} &= \beta_{14} + 0.0040 - 0.0272(R_{fit}/R_{AV})^6 \end{aligned} \tag{7.2}$$

Neutron Events

$$\begin{aligned} \textbf{Inward} \quad \beta'_{14} &= \beta_{14} + 0.0014 + 0.0034(R_{fit}/R_{AV})^3 \\ \textbf{Outward} \quad \beta'_{14} &= \beta_{14} + 0.0014 - 0.0121(R_{fit}/R_{AV})^6 \end{aligned} \tag{7.3}$$

In this chapter, analytic PDFs are provided both with and without this correction. Also, systematic uncertainties for the corrected PDFs are given. In the next chapter, maximum likelihood signal extraction are performed using both corrected and uncorrected PDFs.

7.2 Systematic Uncertainties for Calibrated β_{14}

Using the same method as in Chapter 6, the systematic uncertainties were recalculated for the calibrated β_{14} PDFs. ^{16}N and ^{252}Cf Monte Carlo were regenerated with the shifted β_{14} values given in (7.2) and (7.3). The significantly reduced uncertainties are found in Table 7.1 (the systematic uncertainties of the uncalibrated β_{14} distributions are found in Table 6.8). The Monte Carlo β_{14} values were shifted to make the mean β_{14} values for calibration runs agree with the data. The width was not taken into account, which explains why there is little change to the newly calculated uncertainty on the width, σ_C. The mean values of the calibrated β_{14} distributions for ^{16}N are plotted versus radial source position in Figure 7.9. Figures 7.10 and 7.11 show the new fractional differences between data and Monte Carlo mean β_{14} values for ^{16}N and ^{252}Cf.

Source	σ_B (mean)	σ_C (width)	Apply To
^{16}N data vs. MC	0.56%	0.92%	Electron PDFs
Cf data vs. MC	0.32%	0.64%	Neutron PDFs

Table 7.1: Systematic uncertainties for calibrated β_{14} PDFs.

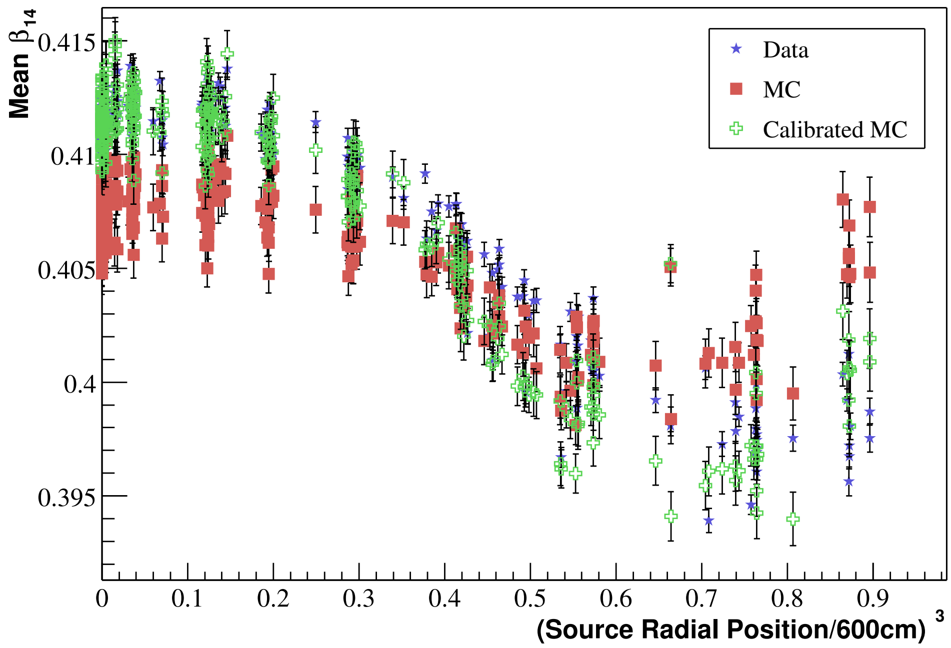

Figure 7.9: Mean β_{14} versus ^{16}N source radial position for data, MC, and MC with calibrated β_{14} values.

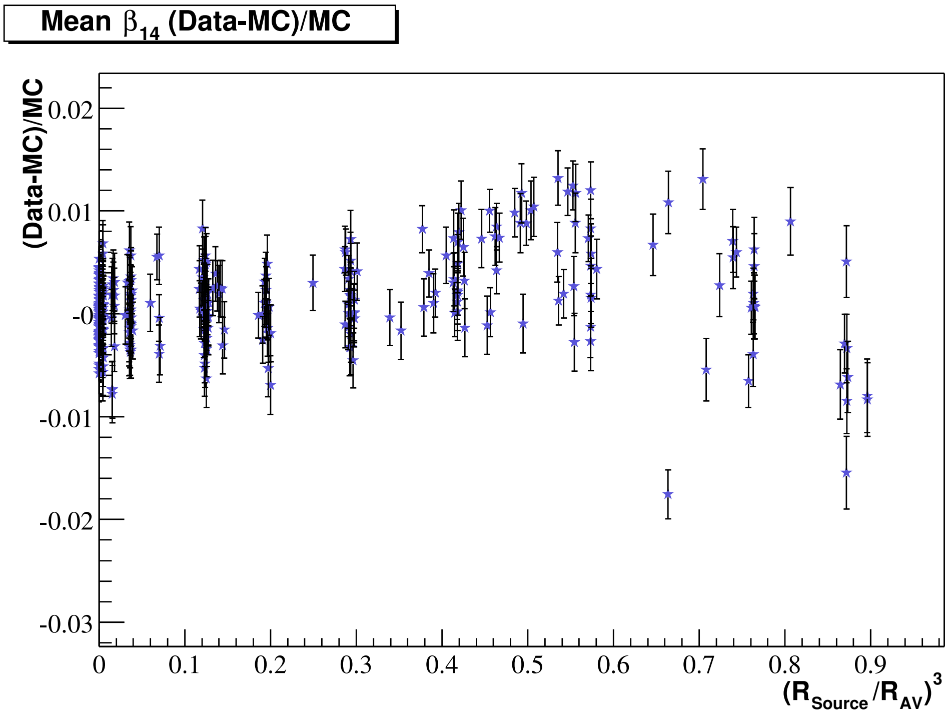

Figure 7.10: Fractional difference between fit means of ^{16}N data and MC with calibrated β_{14} values versus radial source position.

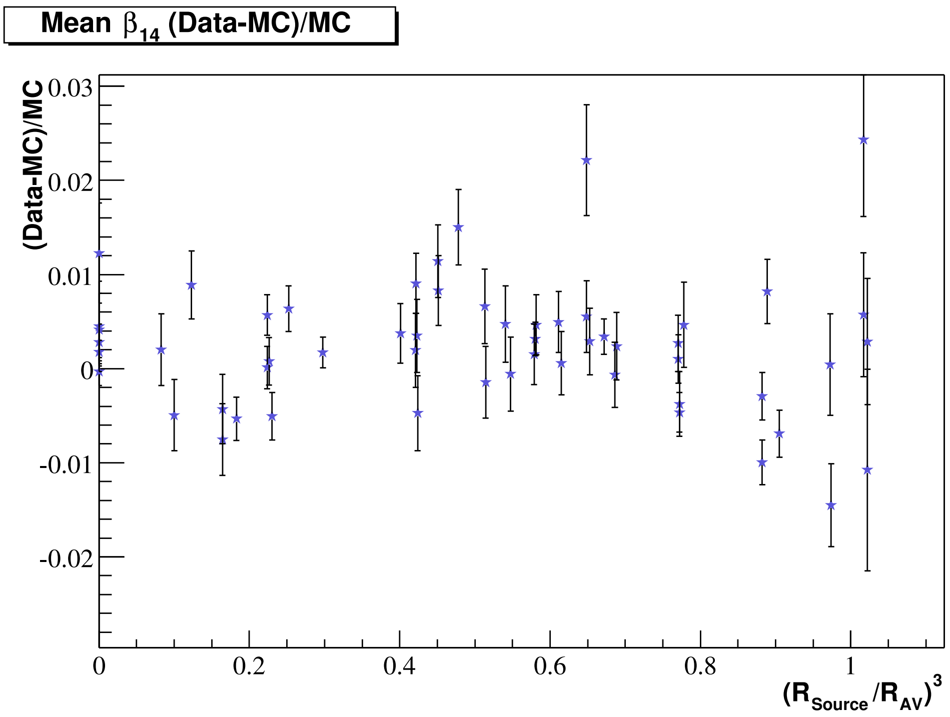

Figure 7.11: Fractional difference between fit means of Cf data and MC with calibrated β_{14} values versus radial source position.

7.3 Monte Carlo and Cuts

Charged current, elastic scattering, neutral current, and monoenergetic electron Monte Carlo were generated by MCPROD[2] using SNOMAN version 4.0285 mimicking the salt data set (1212 runs between run numbers 20684 and 33520), but with higher statistics (the production rate given the BPB01 Standard Solar Model [15] was scaled by a factor of 200). The QPDF fitter [59] was used for reconstruction. Cuts applied to the Monte Carlo to create PDFs for signal extraction are found in Table 7.2. The correction to EGS4, described in Chapter 4, was included in this Monte Carlo.

Field	Low Cut	High Cut
ITR	0.55	-
β_{14}	-0.12	0.95
Fiducial Radius	-	550 cm

Table 7.2: Cuts applied to signal Monte Carlo.

7.3.1 Types of PDFs

Binned PDFs

Binned PDFs may be easily formed using Monte Carlo simulation. Although high statistics are required, binned PDFs have the advantage that all known detector effects are simultaneously modeled and, as a result, correlations between different parameters are automatically included. MCPROD has generated sufficient Monte Carlo so that limited statistics are not an issue.

Analytic PDFs

Whether binned or analytic PDFs are used in signal extraction, it is useful to form analytic PDFs in order to determine systematic uncertainties. Systematic uncertainties on a given parameter may affect the shapes of the PDFs for that parameter. The effect of this uncertainty on the extracted number of events is obtained by perturbing the PDFs. For example, if there is uncertainty on the mean value of a PDF, the PDF is shifted to the left and to the right of the mean by the one standard deviation uncertainty. The perturbed PDF is then used in the signal extraction and the difference in the extracted number of events gives the systematic uncertainty on that extracted number (leading to a systematic uncertainty on the neutrino flux). It is usually easier to perturb the PDFs if there is an analytic form describing the PDFs. Analytic PDFs are derived in

[2]MCPROD is a group within the SNO collaboration responsible for the production of "standard" data and Monte Carlo which is available to all members of SNO.

this chapter; however binned PDFs will be used in the signal extraction in Chapter 8 because the normalization of two-dimensional analytic PDFs (necessary for the energy-dependent β_{14} PDF) is difficult to implement correctly with the tools available at the time of writing.

7.4 Electron PDF

The signal from the charged current and elastic scattering interactions is a relativistic, Čerenkov light-emitting electron. For these electron-producing signals, there is mainly the ^{16}N source, creating Compton-scattered electrons (with energy of ~ 5 MeV) from 6.13 MeV γ's, available for calibration. There is no appropriate source yielding higher energy electrons, except for a ^{8}Li source, which decays to the same state of ^{8}Be as ^{8}B. However, this source is not very well modeled by the Monte Carlo [91]. The ^{16}N source cannot be used to create the charged current and elastic scattering isotropy PDFs because the isotropy parameters differ for pure electron events and γ events[3]. Also, the isotropy parameters have an energy dependence and the CC and ES signals have very different energy distributions than the ^{16}N source. Thus signal Monte Carlo only is used to create energy dependent isotropy PDFs.

Monoenergetic electron Monte Carlo generated isotropically throughout the D_2O volume and over a range of energies from 4–20 MeV is used to produce electron β_{14} PDFs. This was chosen instead of CC and ES Monte Carlo to get higher statistics at high energies. There is no expected difference between β_{14} distributions for CC and ES signals, unless integrated over the CC and ES energy spectra.

7.4.1 Energy Dependence and Fit to Electron PDFs

Gaussians were fit to 1D β_{14} distributions divided into a number of energy slices. The energy dependence of each fit parameter is displayed in Figure 7.12. The plot in the upper left-hand corner of Figure 7.12 is the fit to the β_{14} distribution for electrons with kinetic energies of 6.0–6.5 MeV. Fortunately, the energy dependence of the Gaussian parameters is parameterized quite easily so that a 2-dimensional analytic energy-dependent β_{14} PDF may be formed.

The analytic form for the electron β_{14} versus T_{eff} PDFs is

$$A \cdot \exp\left[-0.5\left(\frac{x-B}{C}\right)^2\right] \tag{7.4}$$

where

[3]However, comparison between ^{16}N MC and data has been used (see Chapter 6) to infer that the MC is modeling single ~ 5 MeV electrons well.

for uncorrected MC:

$$
\begin{aligned}
A &= 1.62 + 0.272\ T_{eff} - 0.0148\ T_{eff}^2 + 0.00030\ T_{eff}^3 \\
B &= 0.427 + 0.00854\ T_{eff} - 0.000178\ T_{eff}^2 \\
C &= 0.107 + 0.348 \exp[-T_{eff}^{0.46}].
\end{aligned}
$$

for MC corrected with (7.2):

$$
\begin{aligned}
A &= 1.68 + 0.258\ T_{eff} - 0.0138\ T_{eff}^2 + 0.00027\ T_{eff}^3 \\
B &= 0.426 + 0.00841\ T_{eff} - 0.000173\ T_{eff}^2 \\
C &= 0.109 + 0.353 \exp[-T_{eff}^{0.47}].
\end{aligned}
$$

The 2-dimensional analytic PDF is displayed in Figure 7.14, along with 2D binned CC and ES PDFs in Figure 7.13. It is clear that the mean of β_{14} increases and its width decreases with increasing energy. This is because electrons with higher energy tend to have straighter tracks. Thus, the Čerenkov cone is more contained, making the mean β_{14} value for high energy events higher which indicates less event isotropy. The smaller amount of scattering for high energy events is also reflected in the decreased width.

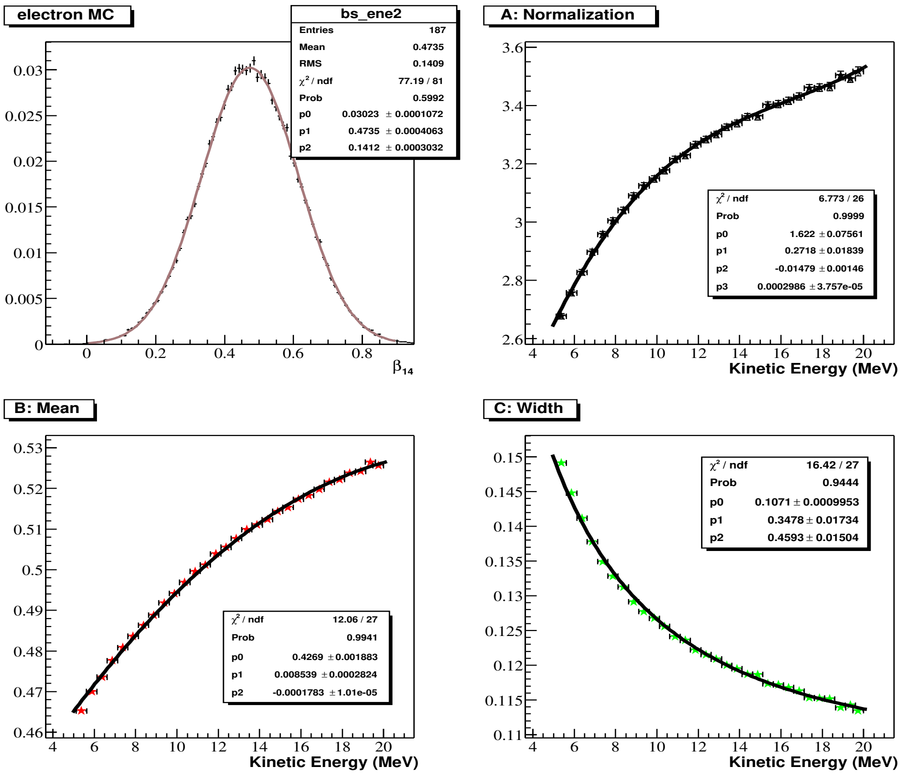

Figure 7.12: Gaussian fit parameters to β_{14} vs. effective kinetic energy for electron MC. The error bars on the x-axis are the bin widths and the error bars on the y-axis are the errors obtained in the Gaussian fits.

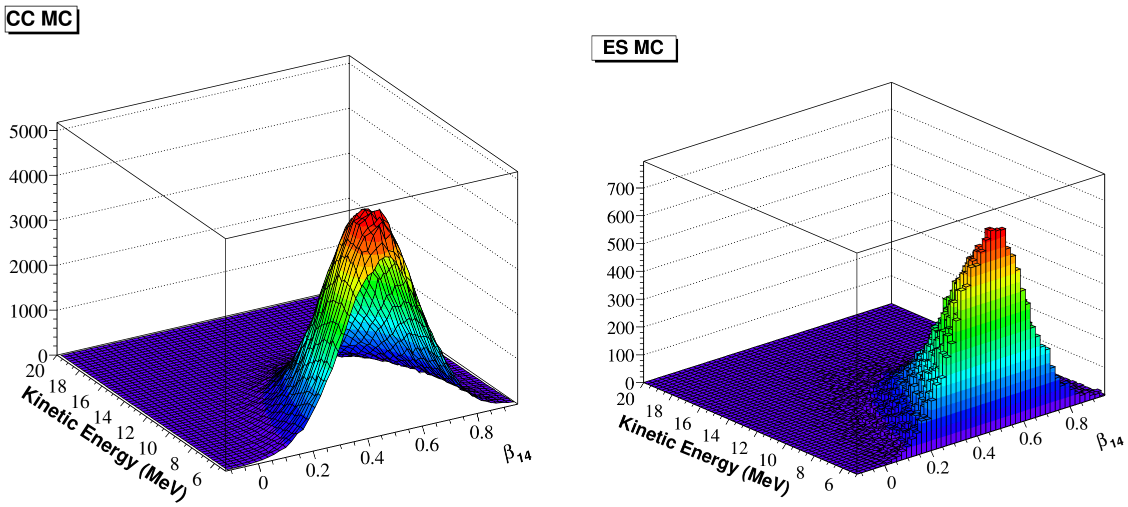

Figure 7.13: Binned CC and ES β_{14} versus T_{eff} PDFs.

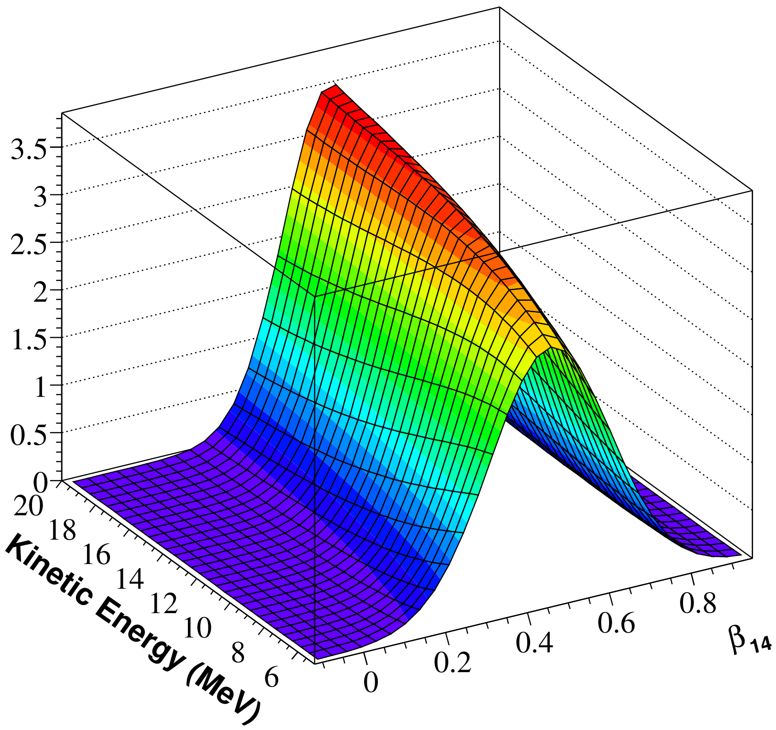

Figure 7.14: Analytic electron β_{14} versus T_{eff} PDF.

7.5 Neutron PDF

A PDF for neutron events may be created using either Monte Carlo or Cf data which has been weighted over the D_2O volume. The neutral current signal creates free neutrons in the detector, which capture on chlorine in the salted D_2O, yielding a cascade of γ's. The ^{252}Cf fission source models this signal well; however, the source is placed at discrete locations throughout the D_2O, so the PDF created from this source may not adequately mimic the isotropically distributed NC signal. Cosmic ray muons passing through the detector emit bremsstrahlung photons, some of which are energetic enough to photodisintegrate the deuteron, producing neutrons [92]. Neutrons following muons are removed with a timing cut. These may also be used to create a neutron PDF which does sample the entire D_2O region; however the statistics from these neutrons is very limited.

The neutral current PDF is created using NC Monte Carlo. Because of the good agreement between Cf data and Monte Carlo, it is sensible to use the NC Monte Carlo rather than data to ensure that source effects are not an issue. Also, the NC Monte Carlo also incorporates any variance with time that the isotropy distribution might have. Differences between calibration data and Monte Carlo may be studied and accounted for in the systematic uncertainty on the finally extracted flux.

7.5.1 Energy Dependence and Fit to Neutron PDFs

Because the effective energy of neutron events is correlated with the number of γ's emitted in the de-excitation of ^{36}Cl*, the neutron β_{14} distribution is much more strongly dependent on energy than the electron β_{14} distribution. The higher the number of γ's that result from the ^{36}Cl* de-excitation, the more energy gets lost in the Compton scattering of electrons because of the Čerenkov threshold, and thus, a lower effective energy is observed for events with higher isotropy. A reasonable fit to neutron β_{14} distributions is

$$A \cdot \exp\left[-0.5\left(\frac{x-B}{C}\right)^2\right] \cdot \left[1+\left(\frac{0.1}{x-D}\right)^4\right]^{-1} \tag{7.5}$$

where the parameters A, B, C, and D are dependent on energy. This function is a Gaussian multiplied by a function which skews the left-hand side of the Gaussian, but not the right. This function is visible in Figure 7.15 as a black line. This plot shows the β_{14} distribution for NC events with energy between 6.0 and 6.5 MeV. The blue line is a Gaussian and the red line is the blue Gaussian multiplied by the black function. This functional form was chosen after fitting one-dimensional β_{14} distributions with a Gaussian, then dividing the histogrammed distribution by the fit Gaussian. That difference was then fit with the function that analytically mimics a step function. Figure 7.16

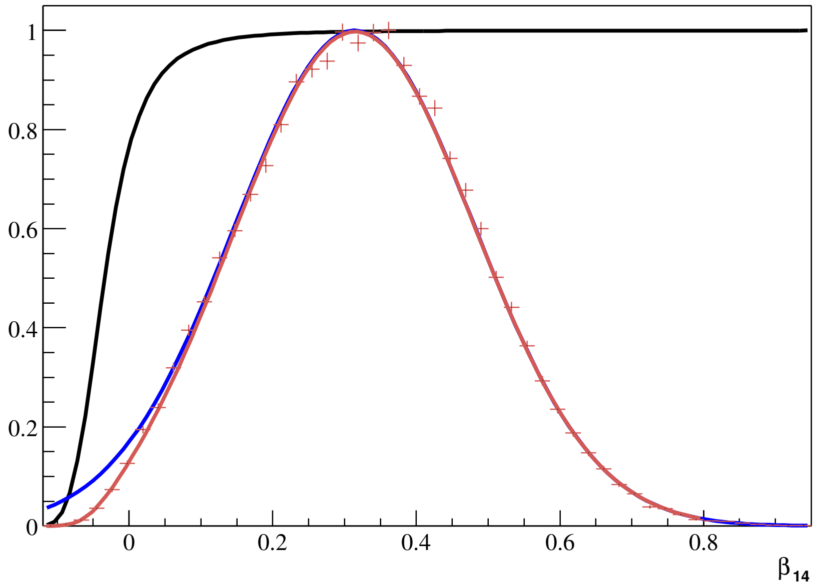

Figure 7.15: Fit to β_{14} for neutrons with effective kinetic energy of 6.0–6.5 MeV.

shows the fit parameters as a function of energy and Figure 7.17 shows the 2-dimensional binned and analytic neutron β_{14} versus T_{eff} PDFs.

The parameter values as a function of effective kinetic energy for the NC Monte Carlo PDF are

for uncorrected MC:

$$\begin{aligned} A &= 1.9 + 0.088\ T_{eff} \\ B &= 0.076 + 0.045\ T_{eff} - 0.0012\ T_{eff}^2 \\ C &= 0.24 - 0.016\ T_{eff} + 0.00063\ T_{eff}^2 \\ D &= -0.33 + 0.048\ T_{eff} - 0.0026\ T_{eff}^2 \end{aligned} \tag{7.6}$$

for MC corrected with (7.3):

$$\begin{aligned} A &= 1.9 + 0.087\ T_{eff} \\ B &= 0.074 + 0.046\ T_{eff} - 0.0013\ T_{eff}^2 \\ C &= 0.25 - 0.017\ T_{eff} + 0.00074\ T_{eff}^2 \\ D &= -0.24 + 0.020\ T_{eff} - 0.00045\ T_{eff}^2. \end{aligned} \tag{7.7}$$

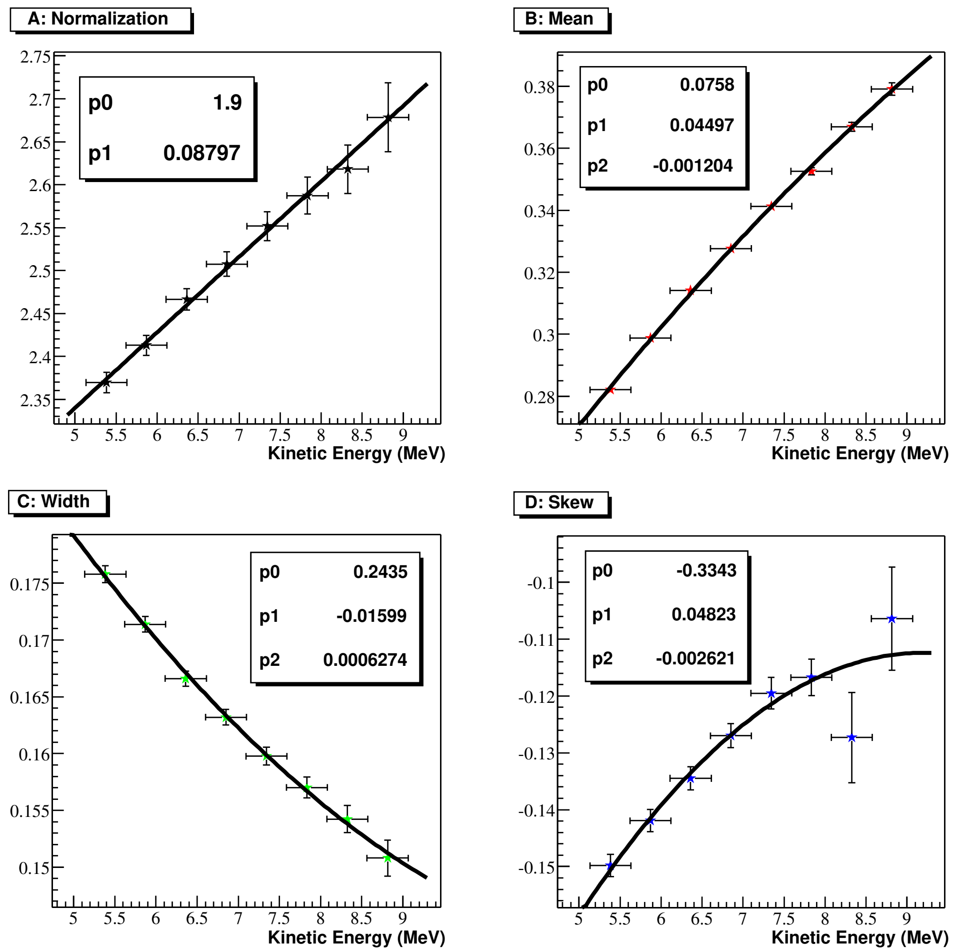

Figure 7.16: Neutron fit parameters as a function of effective kinetic energy. The error bars on the x-axis are the bin widths and the error bars on the y-axis are the errors obtained in the fits.

7.6 Summary

Calibration of β_{14} values reduces the systematic uncertainty of the β_{14} distributions which will be used in maximum likelihood signal extraction. The systematic uncertainties for uncalibrated and calibrated electron and neutron β_{14} PDFs are found in Table 7.3.

The presented analytic PDFs are valid for a fiducial volume of radius 550 cm and kinetic energy ranges of 5.5–20 MeV for electron events and 5.0–9.5 MeV for neutron events. The energy-dependent analytic functions for the electron and neutron signal β_{14} PDFs must be multiplied by the CC, ES, or NC (arising from the $^{36}Cl^{*}$ γ-cascade) spectral distribution to be complete for a maximum likelihood fit with constrained energy spectra.

One dimensional β_{14} PDFs from electron and neutron Monte Carlo generated throughout the D_2O volume are found in Figure 7.18.

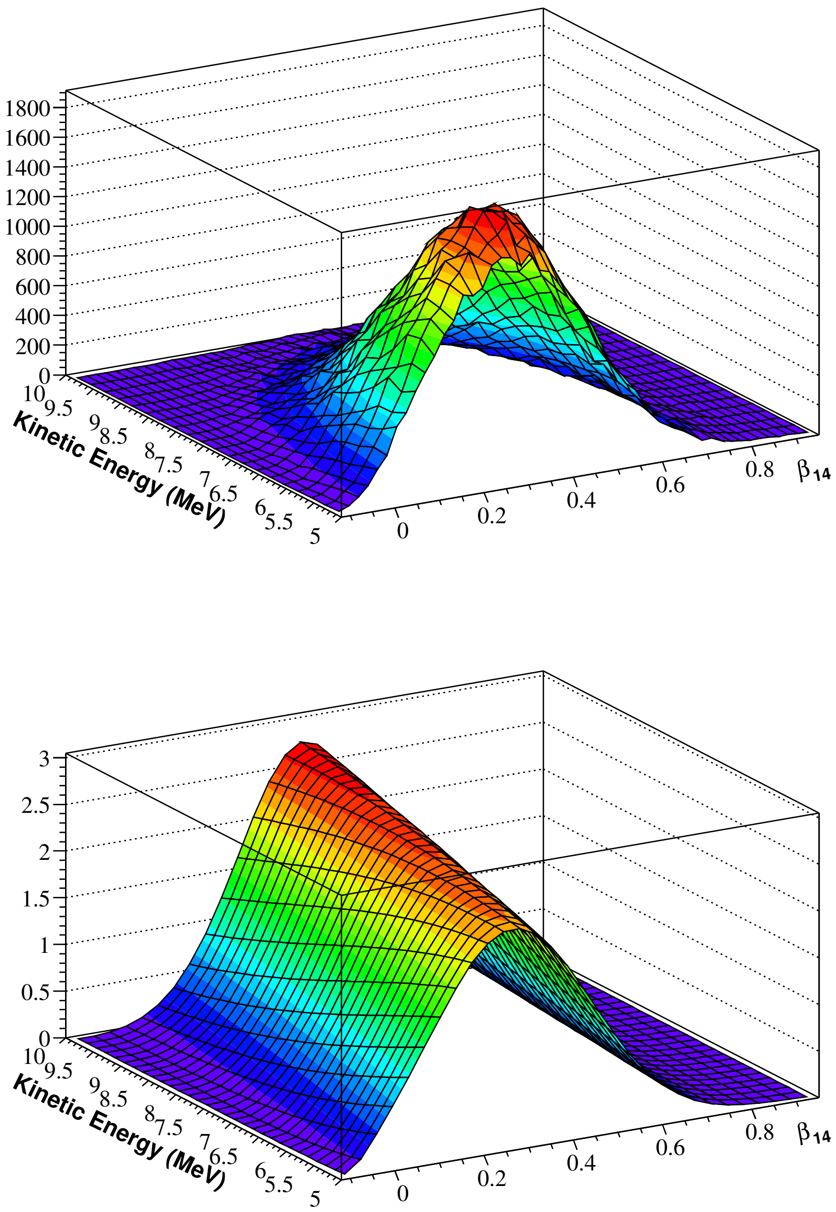

Figure 7.17: Binned and analytic neutron β_{14} versus T_{eff} PDFs. The top binned PDF has the NC energy spectrum folded in. The analytic PDF is normalized to 1 for every 0.5 MeV in energy.

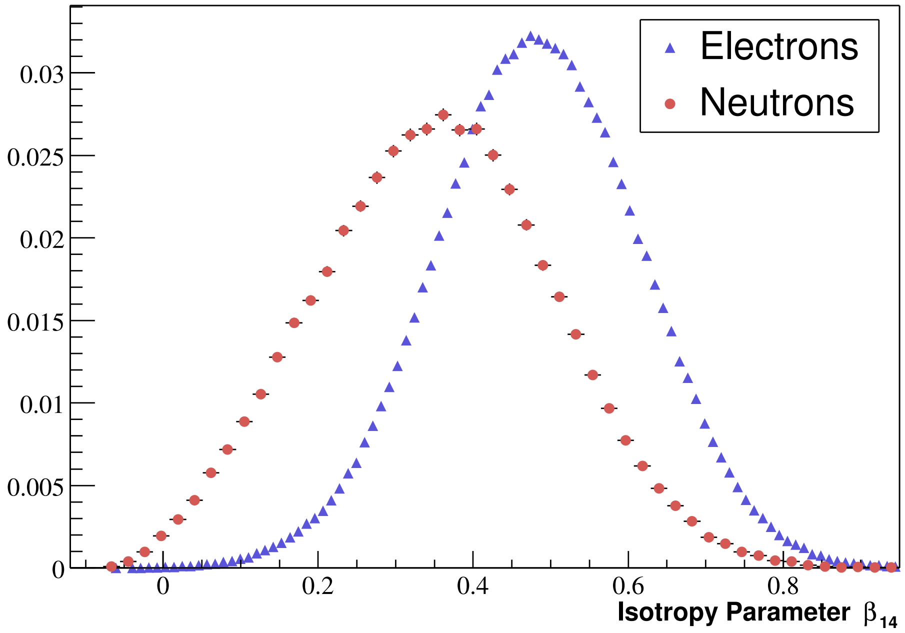

Figure 7.18: β_{14} for NC and electron Monte Carlo.

Source	σ_B (mean)	σ_C (width)	Apply To
For Uncalibrated β_{14}			
^{16}N data vs. MC	0.87%	0.97%	Electron β_{14} PDFs
Cf data vs. MC	0.48%	0.67%	Neutron β_{14} PDFs
For Calibrated β_{14}			
^{16}N data vs. cal. MC	0.56%	0.92%	Electron β_{14} PDFs
Cf data vs. cal. MC	0.32%	0.64%	Neutron β_{14} PDFs

Table 7.3: Summary of β_{14} systematic uncertainties.

Chapter 8

Measuring the Neutral Current Flux

8.1 Maximum Likelihood Fitting

The number of events belonging to each signal type (CC, ES, NC) in the salt data set is determined using extended maximum likelihood estimation. In maximum likelihood estimation, a *likelihood function* is calculated for a given set of data. The likelihood of a set of data is essentially the probability of obtaining that particular data set given expected probability distributions that compose that data.

The parameters used to separate the signals in the salt data set are effective kinetic energy (T_{eff}), a parameterization of the event isotropy (β_{14}), the fitted angle of an event with respect to the Sun ($\cos\theta_{\odot}$), and radial fit position (R^3_{fit}). Each signal type has a probability density function (PDF) for these parameters obtained through Monte Carlo simulation. Given probability density functions P_s $=P_s(T_{eff}, \beta_{14}, \cos\theta_{\odot}, R^3)$, where s=CC,ES,NC,bkgd[1], a data set D with N events may be described as a linear combination of these 4-dimensional PDFs:

$$D(T_{eff}, \beta_{14}, \cos\theta_{\odot}, R^3_{fit}) = \sum_s a_s P_s(T_{eff}, \beta_{14}, \cos\theta_{\odot}, R^3_{fit}). \tag{8.1}$$

For PDFs normalized to unity, the likelihood function is given by

$$L = \prod_{i=1}^{N} \sum_s a_s P_{si}, \tag{8.2}$$

where P_{si} is the probability of event i belonging to signal s given its values of $T_{eff}, \beta_{14}, \cos\theta_{\odot}$, and R^3_{fit}.

[1] P_{bkgd} is the PDF for some type of background events and there may be more than one of these. If there exists an estimation for the number of background events (e.g. from determination of ^{232}Th and ^{238}U concentrations), the amplitude a_{bkgd} is fixed in the likelihood function. If the number of background events is unknown (such as for external neutrons), it may also be determined in the signal extraction.

The measured number of events N in counting experiments, such as SNO, is a Poisson random variable with distribution

$$f(N) = \frac{\nu^N}{N!}e^{-\nu}, \tag{8.3}$$

where ν is the expectation value of the number of events. For data with this type of distribution, the likelihood function becomes the product of the Poisson probability to find N and the likelihood function found in (8.2). The *extended log likelihood function* for this data set is defined as [93]

$$\mathcal{L} \equiv \ln(L) = \sum_{i=1}^{N} \ln\left(\sum_s a_s P_{si}\right) - \sum_s a_s, \tag{8.4}$$

where the best set of weights, $a_{\mathrm{CC}}, a_{\mathrm{ES}}, a_{\mathrm{NC}}, a_{\mathrm{bkgd}}$, maximize $\mathcal{L}$. The logarithm is taken because maximizing $\ln(L)$ yields the same result as maximizing L, but it is more easily calculated. The summation over these weights removes the constraint on the total number of events N and, instead, the total number of events becomes the sum of independent Poisson variables with expectation values a_s.

P_s is a 4-dimensional probability density function and it is not computationally practical to determine P_s for every point in the 4D space. Because $\cos\theta_\odot$ and R^3_{fit} are essentially uncorrelated[2] with the other parameters, they may be factored out and P_s rewritten

$$P_s(T_{eff}, \beta_{14}, \cos\theta_\odot, R^3_{fit}) = \mathcal{B}_s(T_{eff}, \beta_{14})\mathcal{C}_s(\cos\theta_\odot)\mathcal{R}_s(R^3_{fit}). \tag{8.5}$$

The extended maximum likelihood approach is a simultaneous fit to the T_{eff}, β_{14}, $\cos\theta_\odot$, and R^3_{fit} distributions.

8.2 Selection of PDFs

Maximum likelihood signal extraction is performed to extract the number of CC, ES, NC, and external neutron background events. As discussed in Chapter 7, the following binned PDFs will be used:

1. Energy-dependent β_{14} PDFs have the greatest power to separate electron-type events (CC and ES) from neutron events (NC and external neutrons). These distributions are pictured in Figures 7.13 and 7.17.

2. PDFs of $\cos\theta_\odot$ have the greatest power to separate the forward-peaked ES events. See Figure 7.3 for the $\cos\theta_\odot$ PDFs.

[2] β_{14} is slightly correlated with R_{fit} and the effect of this correlation is shown to give only a small bias (on the order of $\sim 1\%$) on the extracted number of NC events [88]. A 3-dimensional PDF would reduce this bias.

3. Radial (R^3_{fit}) PDFs have power to separate the external neutrons since they are created near the AV. The radial distribution of electron-type events is flat and the NC radial distribution is mostly flat, but falls off slightly towards the AV. These distributions are pictured in Figure 2.9.

These characteristic PDFs are created for each of the signals using Monte Carlo simulation.

8.3 Signal Extraction Specifications

The maximum likelihood extraction is carried out using code written and tested by Jeanne Wilson [88]. It uses MINUIT [63] to maximize the extended likelihood function found in (8.4).

An energy *constrained* fit is one in which an energy PDF is included in the signal extraction. The problem with doing an energy constrained fit is that the CC and ES energy spectra are sensitive to MSW distortions. SNO measures the number of events belonging to each signal type which then give the flux of electron neutrinos and the flux of *all* active neutrinos. From these fluxes, the MSW oscillation parameters Δm^2_{12} and θ_{12} may be determined. Therefore, we do not wish to make any assumptions about these parameters in our signal extraction.

An *unconstrained* fit is one in which the numbers of each event type are determined in a number of energy bins, n_{spec}. In this case the number of parameters to fit for is

$$\begin{aligned}
&n_{spec} \text{ for the number of CC events in each spectral bin}\\
&+ n_{spec} \text{ for the number of ES events in each spectral bin}\\
&+ 1 \text{ for the total number of NC events}\\
&+ 1 \text{ for the total number of external neutron events}\\
&= 2n_{spec} + 2
\end{aligned}$$

Constraining the energy distribution of NC events is allowed because it does not depend on the neutrino energy spectrum. Any neutrino with energy above 2.22 MeV may interact through the neutral current interaction and the observed energy is from the $^{36}\text{Cl}^*$ γ-cascade.

Because of the energy dependence of β_{14} it is desirable to use small energy bins. However, the code must perform a maximization over a ($2n_{spec}$+2)-dimensional likelihood space, so too many spectral bins would be very computationally intensive. Also, because the measure of energy in the SNO detector is discrete in nature (the effective kinetic energy, T_{eff}, is derived from the number of hit PMT tubes, N_{hit}), it is not sensible to have too fine energy bins. So, it was decided to perform the signal extraction using

1-MeV spectral bins. Above 13 MeV, there is very little data, so one larger spectral bin is used for higher energy events. A total of 9 spectral bins was used: eight 1 MeV bins between 5.5 and 13.5 MeV and one bin between 13.5 and 20.0 MeV. Thus, the signal extraction code simultaneously fits for 20 free parameters[3].

A Note on Analytic PDFs

In the summary of Chapter 7 it was noted that for the energy-*constrained* signal extraction, the energy-dependent β_{14} PDF for each signal must be multiplied by its respective energy distribution (because the normalizations of the β_{14} distributions are constant with energy in the functions given in (7.4)–(7.7)). In the case of the energy-*unconstrained* fit, the 2D analytic β_{14} PDF must be integrated over the energy in each spectral bin to create 1D β_{14} PDFs valid for each spectral bin. Given small enough spectral bins, this should not bias the extraction in any significant way. The available signal extraction code does not have the capability to create these integrated 1D PDFs from the 2D energy-dependent analytic forms. In order to use the energy-dependent analytic forms for β_{14}, this feature would need to be added. For this reason, the signal extraction in this thesis is performed using binned PDFs.

8.4 Signal Extraction Results

8.4.1 Blind Data Set

To guard against introducing biases into the analysis, or tuning the analysis to give expected results, three blindness criteria were applied when developing the analysis of the salt data set. The schemes were chosen to blind the NC flux in particular.

Inclusion of Muon Followers

A background to the neutral current signal is from neutrons which are created after a cosmic ray muon passes through the detector (these are also discussed in Section 7.5). Neutrons following muons are normally removed using a 20 second timing cut. However, for the salt data, a "hole" was placed in this timing cut to allow some of the neutrons to be included in the neutrino data set.

Fudge to NC Cross Section

The cross section for NC events was scaled by an unknown factor in the Monte Carlo.

[3] The running time of the code for 20 parameters is about 2.5 hours, while for 0.5-MeV bins up to 13.5 MeV (36 parameters), the code takes close to 30 hours.

Blind Data Set, Uncalibrated β_{14}			
Signal	Number	+ Error	- Error
CC	1565.3	71.4	70.6
ES	205.0	25.2	24.3
NC	1981.9	80.3	79.2
Ext. n	105.8	40.4	39.5

Blind Data Set, Calibrated β_{14}			
Signal	Number	+ Error	- Error
CC	1545.2	71.2	70.4
ES	203.3	25.1	24.2
NC	2002.1	80.4	79.3
Ext. n	107.4	40.5	39.6

Table 8.1: Numbers of events extracted from blind data set using both uncalibrated and calibrated β_{14} PDFs. Errors quoted are the 1σ statistical uncertainties.

Statistical Blindness

An unknown fraction ($< 30\%$) of candidate neutrino events was held back from the analyzed data set.

These three blindness criteria were held until the analysis techniques used to obtain the results in [47] were fixed. There are two main differences between the published analysis in [47] and the analysis in this thesis:

1. the entire salt data set is included here (results are to be released shortly by the SNO collaboration including all selected data from the salt phase) and

2. the calibration of β_{14} values (which is unique to this thesis).

It was decided to perform the signal extraction using calibrated and uncalibrated β_{14} values on the blind data set to see if there are notable differences which should be investigated before carrying out the signal extraction on the fully cleaned data set. The results of the two signal extractions on the blind data set are found in Table 8.1 and plotted in Figure 8.1.

There are no large difference between the extracted numbers using the calibrated and uncalibrated β_{14} PDFs. Using the calibrated PDFs, the number of CC events is about 20 lower (resulting in more neutron events), but there is a statistical uncertainty of about 70 events. The number of ES events is consistent using both types of PDFs. It can therefore be concluded that using calibrated β_{14} PDFs does not cause any significant change in the number of extracted events; however, the difference between data and Monte Carlo is smaller resulting in reduced systematic uncertainty.

Looking at the plots in Figure 8.1, there is possibly a small "bump" centered at β_{14}=0. We do expect there to be some small contamination of AV events in the data set which have an isotropic light distribution ($\beta_{14}\approx 0$), but the upper limit on this background contribution ($<$ 8 events is an estimate based on the number presented in [1]) is much smaller than what is observed here. Most likely this "bump" is no more than a statistical fluctuation.

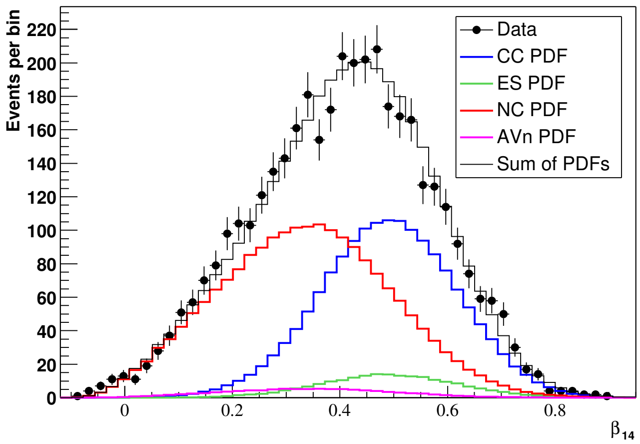

(a) Uncalibrated β_{14}.

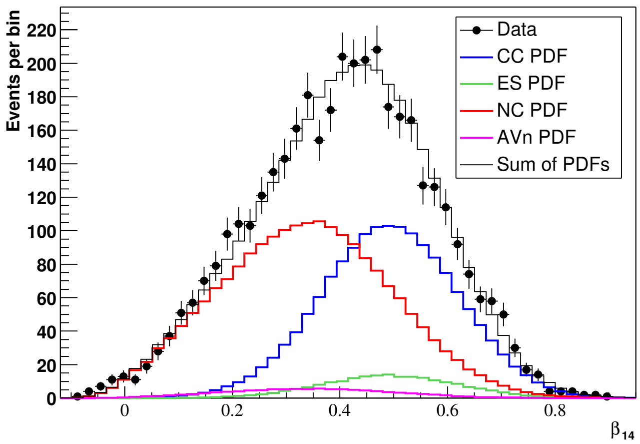

(b) Calibrated β_{14}.

Figure 8.1: Maximum likelihood results on blind data set using (a) uncalibrated β_{14} PDFs and (b) calibrated β_{14} PDFs. Each PDF is scaled by the extracted number of events.

Because there were no large differences in the extracted number of events using the uncalibrated and calibrated β_{14} PDFs, the blindness constraints were removed and the number of events for each signal type extracted for the entire cleaned salt data set.

8.4.2 Full Clean Data Set

The same signal extractions were performed as above, but with all of the blindness constraints on the data removed. The full salt data set contains 4750 candidate neutrino

Full Data Set, Uncalibrated β_{14}			
Signal	Number	+ Error	- Error
CC	2148.6	79.7	78.9
ES	285.2	28.7	27.7
NC	2178.6	86.9	85.8
Ext. n	135.5	43.6	42.6

Full Data Set, Calibrated β_{14}			
Signal	Number	+ Error	- Error
CC	2125.0	79.5	78.8
ES	283.3	28.6	27.6
NC	2203.5	87.1	85.9
Ext. n	136.3	43.6	42.8

Table 8.2: Numbers of events extracted from the full (unblind) salt data set using both uncalibrated and calibrated β_{14} PDFs. Errors quoted are the 1σ statistical uncertainties.

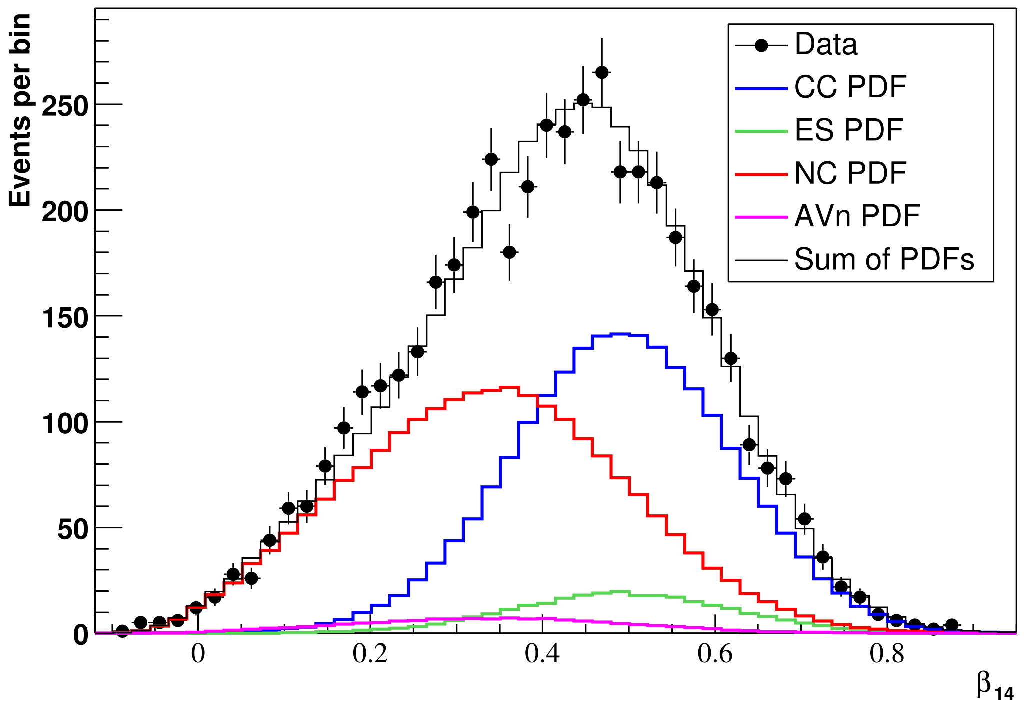

Figure 8.2: Maximum likelihood results on full salt data set using calibrated β_{14} PDFs. Each PDF is scaled by the extracted number of events.

events detected over 391.43 live days between July 26, 2001 and August 28, 2003. The results are found in Table 8.2. Figure 8.2 shows the calibrated β_{14} PDFs scaled by the extracted number of events for each of the signal types along with the data. The apparent "bump" centered at β_{14}=0 observed in the blind data β_{14} distribution (Figure 8.1) is no longer visible which implies that it was most likely a statistical fluctuation. The possibility of it being associated with the hole in the muon follower cut has not yet been investigated.

8.5 Statistical Uncertainty on Event Numbers

In the limit of large statistics, the likelihood function becomes Gaussian about the maximum value. For any measured value with a Gaussian statistical error, the probability that the actual value is within one standard deviation (1σ) of the measured number is 68.3%. In maximum likelihood, the one standard deviation uncertainty on the number of extracted event numbers (N_{CC}, N_{NC}, etc.) is given by the point at which the likelihood decreases by one-half. Even if the likelihood function is not a Gaussian function of the fit parameters, the central confidence interval $[N^{min} - \sigma_-, N^{min} + \sigma_+]$ may still be defined by the point at which the likelihood function decreases by 1/2 on either side [93].

8.6 Systematic Uncertainty on Event Numbers

Certain systematic uncertainties (such as on the isotropy distributions, discussed in Chapter 6) have the effect of changing the shapes of the signal PDFs, which affects the number of extracted events for each signal type. Systematic uncertainties, particularly on energy threshold and fiducial volume, may also contribute to the signal *acceptance* within the data cuts [95].

The effects of systematic uncertainties on the extracted numbers of events is determined by perturbing the PDFs and again performing the signal extraction. The easiest way to perturb the PDFs is to use analytic PDFs and change the parameters of the analytic form based on their uncertainty. However, for the signal extraction in this chapter it has been decided to use binned PDFs because of the reason discussed in Section 8.3. The binned PDFs are perturbed based on the analytic fits derived in Chapter 7 and the uncertainty on the fit parameters. To simplify the perturbation, the uncertainty on parameter D in the neutron β_{14} fit (7.5) is assumed negligible. Referring to Figure 7.15, it is clear that any uncertainty in this parameter would affect the β_{14} distributions only at low values of β_{14} where there is very little expected contribution in the data from CC and ES events. The systematic uncertainties on the mean and width of β_{14} distributions were determined in Chapter 6 using comparison of ^{16}N and ^{252}Cf data with Monte Carlo. The uncertainties on the two fit parameters are assumed to be uncorrelated. To account for these uncertainties, four perturbed β_{14} PDFs were created for each signal:

1. $\beta_{14} + \sigma_{\text{Mean}}$
2. $\beta_{14} - \sigma_{\text{Mean}}$
3. $\bar{\beta}_{14} + (\beta_{14} - \bar{\beta}_{14})(1 + \sigma_{\text{Width}})$
4. $\bar{\beta}_{14} + (\beta_{14} - \bar{\beta}_{14})(1 - \sigma_{\text{Width}})$

where $\bar{\beta}_{14}$ is the mean value of β_{14} for the particular signal. The fit mean values and their uncertainties are found in Table 8.3. Figure 8.3 shows the CC and NC β_{14} distributions with shifted ($\pm\sigma_{\text{Mean}}$) and smeared width values. Each perturbed PDF was checked to

Uncalibrated β_{14}				
Signal	Fit Parameter		Syst. Uncert.	
	Mean	Width	σ_{Mean}	σ_{Width}
CC	0.4828	0.1332	0.87%	0.97%
ES	0.4793	0.1350	0.87%	0.97%
NC	0.3350	0.1571	0.48%	0.67%
Ext. N	0.3417	0.1582	0.48%	0.67%

Calibrated β_{14}				
Signal	Fit Parameter		Syst. Uncert.	
	Mean	Width	σ_{Mean}	σ_{Width}
CC	0.4842	0.1334	0.56%	0.92%
ES	0.4807	0.1352	0.56%	0.92%
NC	0.3358	0.1571	0.32%	0.64%
Ext. N	0.3427	0.1584	0.32%	0.64%

Table 8.3: β_{14} means and widths from signal PDFs (integrated over full energy spectra) and systematic uncertainties.

ensure that it had the correctly altered mean and width. The systematic uncertainties on the extracted numbers are not quoted here, because they are redundant with the systematic uncertainties found on the fluxes which are given in Section 8.7.2.

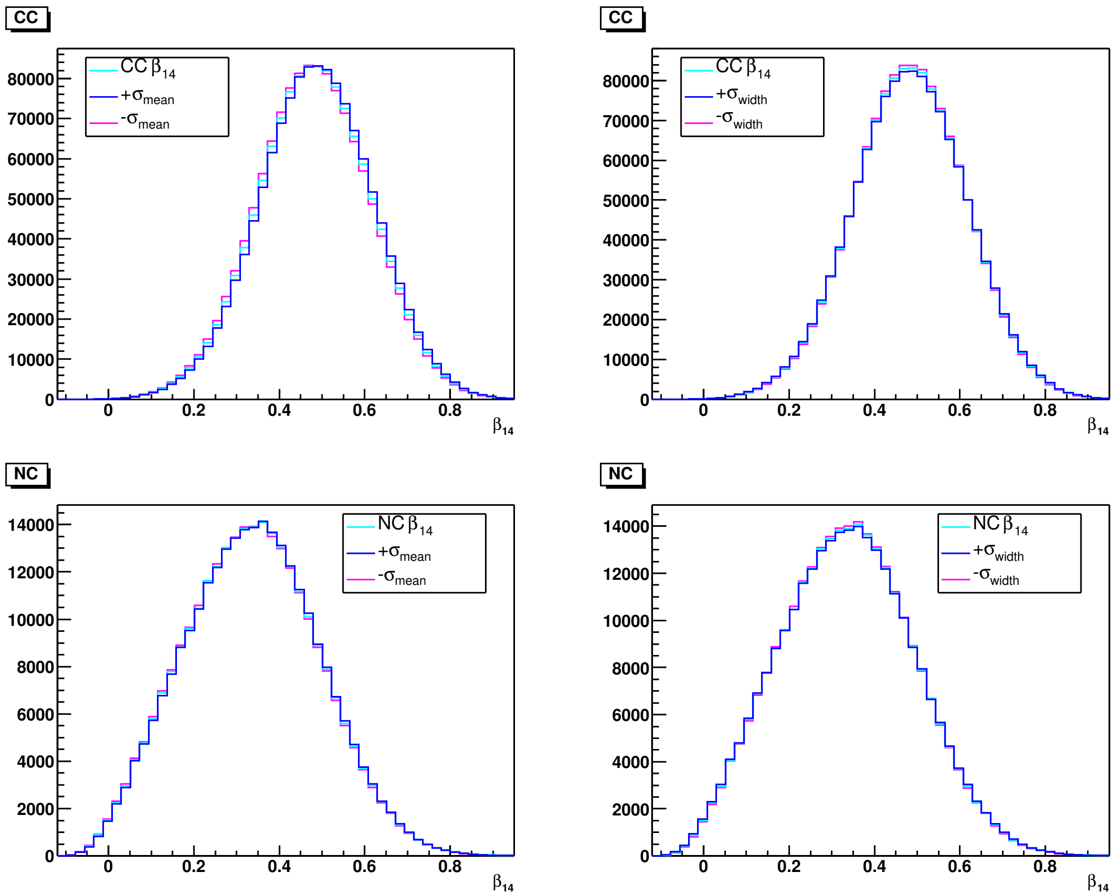

Figure 8.3: CC and NC β_{14} distributions with perturbed means and widths.

8.7 Calculation of Fluxes

We now wish to obtain the solar neutrino flux based on the numbers of events extracted in Section 8.4. The event numbers are compared to that expected by Monte Carlo simulation within the signal region which is:

$$\boxed{\begin{array}{c} 5.5\text{ MeV} \leq T_{eff} \leq 20.0\text{ MeV}, \\ -0.12 \leq \beta_{14} \leq 0.95, \\ -1 \leq \cos\theta_{\odot} \leq 1, \\ R^3_{fit} \leq 550\text{ cm}. \end{array}}$$

Generally, the number of neutrino signal events is related to the flux by:

$$\mathcal{R} = \frac{N_s}{t} = \epsilon_s \phi_s \sigma_s \mathcal{N}_t \tag{8.6}$$

where

- $\mathcal{R}$ is the count rate
- N_s is the number of events belonging to signal type s
- t is the amount of data-taking livetime over which the data were obtained
- ϵ_s is the detection efficiency for signal type s
- ϕ_s is the neutrino flux creating events of type s
- σ_s is the cross section for signal type s
- $\mathcal{N}_t$ is the number of target deuterons (for CC or NC) or electrons (for ES).

Signal events are generated using information on the cross sections[4] [94] and number of targets in the Monte Carlo. The flux assumed in the Monte Carlo is from the BPB01 Standard Solar Model prediction [15] (5.15×10^6 cm^{-2}s^{-1}). Thus, we may compare the number of extracted events to the numbers expected by the Monte Carlo to obtain the inferred fluxes for each event type. For the flux inferred from the number of NC events, a calculated value for the predicted number of neutrons is used rather than the Monte Carlo prediction because the capture efficiency is not accurate in the Monte Carlo.

A Monte Carlo simulation is generated for each of the 1212 runs (between run numbers 20684 and 33520) in the salted D_2O data set. The Monte Carlo has the same livetime as the data, except that corrections must be made for the time cut following muons and other sources of data loss [96]. A number of other corrections must also be

[4] The cross sections do not include radiative corrections arising from higher than leading order Feynman diagrams, but the energy-dependent effects of these are included in the signal extraction code.

made to account for minor inaccuracies in the Monte Carlo. Each correction is detailed below. The flux inferred from the measurement of signal s=CC,ES is given by [95, 97]

$$\phi_s = \frac{N_s}{N_s^{MC}} \cdot \frac{1}{MC_{corr}} \cdot \left(\frac{1}{1-\text{Sacrifice}}\right) \cdot Y \cdot \frac{t}{t'} \cdot \frac{\sigma_s}{\sigma'_s} \cdot \frac{1}{\mathcal{N}_{\text{O,Na,Cl}}} \cdot \frac{\mathcal{N}_t}{\mathcal{N}'_t} \cdot \phi_{\nu_e}^{MC}, \tag{8.7}$$

and the flux inferred from the NC measurement is given by

$$\phi_{\text{NC}} = \frac{1}{\mathcal{R}_{\text{NC}}} \cdot \frac{(N_{\text{NC}} - N_{\text{IntN}})}{t'} \cdot \left(\frac{1}{1-\text{Sacrifice}}\right) \cdot \frac{1}{\epsilon_{\text{NC}}} \cdot \frac{\sigma_{\text{NC}}}{\sigma'_{\text{NC}}} \cdot \phi_{\nu_e}^{MC}, \tag{8.8}$$

where

- N_s is the number of extracted events of type s, given in Table 8.2.
- N_s^{MC} is the number of Monte Carlo simulated events within the signal region, given in Table 8.5.
- MC_{corr} is a correction to account for errors in the Monte Carlo propagation of Čerenkov photons which result in a lower number of events within the signal region.
- Sacrifice is the amount of signal removed due to data cleaning.
- Y=200 is the scale factor with which the Monte Carlo was generated.
- t = 398.59 days is the total length of time during the runs in the salt data set.
- t' = 391.43 days is the corrected livetime after deadtime due to the muon follower cut and data loss is taken into account [96].
- σ_s/σ'_s is a cross section correction to account for recent updates to effective field theory cross sections in the literature [94]. A correction is made to the weak axial coupling g_A and for the two-body axial exchange current counter term, $L_{1,A}$. The combined corrections are given in Table 8.4.
- $\mathcal{N}_{\text{O,Na,Cl}}$ is a correction for (ν_e, N) charged current interactions, where $N = {}^{17}$O,Na,Cl.
- $\mathcal{N}_t/\mathcal{N}'_t$ is a correction for the number of targets in the fiducial volume because SNOMAN assumes slightly fewer deuterons and electrons.
- $\mathcal{R}_{\text{NC}}$=13.107738 neutrons/day is the total predicted rate assuming SSM ^{8}B and *hep* fluxes [1].
- N_{IntN} is the estimated number of internal neutron background (see Sections 2.5 and 8.7.1).
- ϵ_{NC}=0.398 is the neutron detection efficiency after all cuts (including fiducial volume).

Table 8.4 lists the corrections which differ for the various signal types.

Correction	CC	ES	NC
MC_{corr}	1.005340	1.004538	-
Sacrifice	0.0057	0.0086	0.0068
σ_s/σ_s'	1/(1.0111×0.984)	1	1/(1.0111×0.979)
$\mathcal{N}_{\mathrm{O,Na,Cl}}$	1.0081	-	-
$\mathcal{N}_t/\mathcal{N}_t'$	1/1.01228	1/1.0151	1

Table 8.4: Corrections to predicted numbers of events.

Signal	Expected from MC
CC	1334767
ES	122710
NC	271045

Table 8.5: Expected number of events within neutrino signal region from Monte Carlo assuming no neutrino flavor change.

8.7.1 Background Subtraction

Background neutrons are produced within the D_2O volume from a variety of sources other than solar neutrinos (see Section 2.5 and [1]). These *internal neutrons* have the same signal as neutrons from NC interactions. For the first results of the SNO salted D_2O phase, which contained data from within a total livetime of 254.2 days, there was an estimated total internal neutron background of $111.3^{+25.3}_{-24.9}$. No updated number for the entire salt data set had been released at the time of writing. As an estimate, the number given in [1] is scaled by the ratio of the livetimes in the two data sets to give $N_{\mathrm{IntN}} = 171.4^{+39.0}_{-38.3}$ in the full salt data set used in this thesis. This number must be subtracted from the number of extracted NC events to obtain the total ^{8}B flux.

Backgrounds other than external neutrons (including internal neutrons and γ's, Čerenkov events, and AV events) contribute to systematic uncertainties on the neutrino fluxes. The relative uncertainties due to these backgrounds are assumed to be the same as in [1] (the estimated number of backgrounds will be higher since the data set is larger, but the percentage uncertainty should remain about the same). These uncertainties are found in Table 8.6.

8.7.2 Systematic Uncertainties on Fluxes

A comprehensive list of sources of systematic uncertainties which contribute to uncertainties on the fluxes may be found in [1, 92, 97]. The percentage uncertainties on the fluxes due to the various sources are summarized in Table 8.6 which was taken from [1], except for the values pertaining to isotropy which are highlighted. The uncertainties from each individual source are added in quadrature to obtain the total experimental

Source	CC uncert. (%)	ES uncert. (%)	NC uncert. (%)
Uncalibrated isotropy mean	±3.0	-0.8,+1.0	-3.2,+3.3
Uncalibrated isotropy resolution	-0.2,+0.1	-0.2,+0.0	-0.2,+0.1
Calibrated isotropy mean	-1.9,+2.0	-0.9,+0.7	-2.0,+2.1
Calibrated isotropy resolution	±0.1	-0.1,+0.0	-0.3,+0.2
Energy scale	-1.0,+1.1	±1.8	-3.7,+3.6
Energy resolution	±0.1	±0.3	±1.2
Energy non-linearity	-0.0,+0.1	±0.0	±0.0
Radial accuracy	-2.6,+2.5	-2.6,+2.9	-3.0,+3.5
Vertex resolution	±0.0	±0.2	±0.2
Angular resolution	±0.2	±2.4	±0.2
Radial energy bias	±0.7	-1.3,+1.2	-2.4,+1.9
Vertex Z accuracy	±0.1	±0.1	-0.2,+0.3
Internal background neutrons	±0.0	±0.0	-1.9,+1.8
Internal background γ's	±0.1	±0.0	±0.1
Neutron capture	±0.0	±0.0	-2.5,+2.7
Čerenkov backgrounds	-1.1,+0.0	±0.0	-1.1,+0.0
"AV events"	-0.4,+0.0	±0.0	-0.4,+0.0
Total experimental uncertainty	-4.3,+4.1	-4.3,+4.5	±7.2
Total experimental uncertainty	-3.6,+3.5	-4.3,+4.4	±6.7
Cross section [94]	±1.2	±0.5	±1.1

Table 8.6: Systematic uncertainties on fluxes for the spectral shape unconstrained analysis of the full salt data set. All values except for that pertaining to isotropy are taken from [1]. Pink (blue) values indicate the uncertainties determined using uncalibrated (calibrated) β_{14}.

uncertainty, which is given for both uncalibrated and calibrated β_{14} PDFs. The total experimental uncertainty is then added in quadrature with the uncertainty on the cross sections to give the total percentage systematic uncertainty on the neutrino fluxes.

The highest sources of systematic uncertainty on the CC and NC fluxes are from the accuracy with which an event is reconstructed, the isotropy, and (for the NC flux) neutron capture efficiency and energy scale[5]. With the calibration of β_{14}, the systematic uncertainty from isotropy lies below these other mentioned sources. The β_{14} calibration reduces the total experimental uncertainty on the NC flux from ±7.2% to ±6.7% and on the CC flux from about ±4.2% to about ±3.6%.

[5]The energy scale uncertainty has more of an effect on the NC flux than CC or ES because the 5.5 MeV energy threshold falls within the peak of the NC energy spectrum.

8.7.3 Flux Results

Given the above inputs, the fluxes calculated from the extracted numbers of events are (in units of 10^6 cm^{-2}s^{-1})

Using uncalibrated β_{14} PDFs:

$$\begin{aligned}\phi_{CC} &= 1.66 \pm 0.06(\text{stat.}) \pm 0.07(\text{syst.})\\ \phi_{ES} &= 2.41^{+0.24}_{-0.23}(\text{stat.})^{+0.11}_{-0.10}(\text{syst.})\\ \phi_{NC} &= 5.15^{+0.23}_{-0.22}(\text{stat.}) \pm^{+0.38}_{-0.37}(\text{syst.})\end{aligned} \tag{8.9}$$

Using calibrated β_{14} PDFs:

$$\begin{aligned}\phi_{CC} &= 1.65 \pm 0.06(\text{stat.}) \pm 0.06(\text{syst.})\\ \phi_{ES} &= 2.40^{+0.24}_{-0.23}(\text{stat.})^{+0.11}_{-0.10}(\text{syst.})\\ \phi_{NC} &= 5.21^{+0.23}_{-0.22}(\text{stat.}) \pm 0.36(\text{syst.}).\end{aligned} \tag{8.10}$$

These values are consistent with those found in the published analysis of a smaller data set from the SNO salt phase [1]. The NC flux provides a measure of the total ^{8}B solar neutrino flux and is in good agreement with the Standard Solar Model prediction [13]:

$$5.82 \times (1 \pm 0.23) \times 10^6 \text{cm}^{-2}\text{s}^{-1}.$$

8.8 Summary

Using uncalibrated or calibrated β_{14} PDFs in maximum likelihood results in very little difference in the extracted fluxes. A large difference was not expected because the correction to the β_{14} values is actually quite small and changes sign with radial fit position. It is clear from Figure 6.3 that for approximately half of the detector volume the MC lies below the data and it lies above the data for the other half. Thus, the discrepancy between data and Monte Carlo averages out to a large extent.

Making the small corrections to the β_{14} values does have the obvious advantage of reducing the systematic uncertainty on the flux results. This analysis is preliminary since the systematic uncertainties from sources other than isotropy have not been finalized at the time of writing[6]. Using results from this approach, which obtains fluxes with lower systematic uncertainty, in a global analysis of all solar neutrino (and KamLAND) data would further reduce the limits on the MSW mixing parameters Δm^2_{12} and $\tan^2\theta_{12}$.

[6] The neutrino runs in the final data set were determined just a month before the submission of this thesis.

Conclusions

^{8}B Solar Neutrino Flux

In the previous chapter, the flux of ^{8}B solar neutrinos was derived from the data from the entire salted D_2O phase of SNO to be (all fluxes presented are in units of 10^6 cm^{-2}s^{-1})

$$5.21 \, ^{+0.23}_{-0.22} \text{ (stat.)} \pm 0.36 \text{ (syst.)}$$

using calibrated values of β_{14}. This number is preliminary because the best estimates for the systematic uncertainties of the entire salt phase were not available at the time of writing. The measured flux is in very good agreement with the previously published values of

$$\begin{array}{ll} 5.21 \pm 0.27 \text{ (stat.)} \pm 0.38 \text{ (syst.)} & \textbf{Partial Salt Phase } [1] \\ 5.13 \, ^{+0.44}_{-0.43} \text{ (stat.)} \, ^{+0.46}_{-0.43} \text{ (syst.)} & \textbf{Pure D}_2\textbf{O Phase } [26]. \end{array}$$

This measurement is also in excellent agreement with the Standard Solar Model prediction for the ^{8}B solar neutrino flux [13],

$$5.82 \pm 1.34,$$

and the combined statistical and systematic uncertainties are well below the theoretical uncertainty.

Because the entire salt data set was used, it is not possible to reduce statistical uncertainty using the salt data alone. The statistical uncertainty could be decreased by combining data available from running with pure D_2O and the data now being taken with the neutral current detectors (NCDs) which have recently been installed in the pure D_2O. However, this is non-trivial since there are differences in the analysis of the data from each of these three phases and different systematic uncertainties for each phase.

The NCDs allow for nearly independent neutron (NC signal) and electron (CC and ES signals) detection. Roughly 14% of the neutrons are detected by the NCDs whereas capture on deuterium has a detection efficiency of about 8% in this phase [98]. The neutrons which are captured on D_2O (subsequently leading to Čerenkov radiation) will need to be statistically separated from the CC and ES events. As in the pure D_2O phase, isotropy is not a strong parameter for distinguishing CC and NC events because neutron capture on deuterium results in the release of just one γ-ray with energy of 6.25 MeV, but the radial distributions are significantly different.

In the NCD phase, the systematic uncertainty is expected to be reduced overall. One of the largest sources of uncertainty on the NC flux is the energy threshold, but the NCDs eliminate this problem.

SNO will undoubtedly produce the best measure of the ^{8}B solar neutrino flux above the detector energy threshold of ~ 5 MeV. Other experiments, such as BOREXINO, have been designed to measure neutrino fluxes from other reactions in the pp-chain which produce lower energy neutrinos.

The data from the salt phase of SNO allows for a model-independent measurement of the ^{8}B solar neutrino energy spectrum since isotropy, rather than energy, is used to statistically separate the CC and NC events. The ^{8}B energy spectrum measured in the salt phase will be released shortly by the SNO collaboration. From simulations made with the current best fit MSW parameters, a significant distortion of the energy spectrum is unlikely to be observed.

Future of Neutrino Oscillation Physics

Reducing the uncertainty on the ratio of the fluxes inferred from the CC and NC measurements narrows the acceptable range of θ_{12} while results from the KamLAND experiment are the most powerful at closing in on Δm^2. Discrepancies between the signal rates measured during the day and the night (the difference being that the neutrinos are traveling through the Earth before reaching the detector at night) in SNO or Super-K will also reduce the allowed region of Δm^2. Contours of the CC/NC ratio and the day-night asymmetry are overlaid on the $(\tan\theta_{12}, \Delta m^2)$ phase space in Figure 8.4.

The CC/NC ratio obtained using the analysis in this thesis is

$$0.317 \pm 0.018 \quad \text{(statistical uncertainty only)}.$$

This ratio is in good agreements with the previously published CC/NC ratio [1] and with the LMA MSW solution.

Solar neutrino oscillations are described by the difference in mass-squared of the first and second neutrino mass states (m_1 and m_2). For atmospheric neutrino oscillations it is the difference in mass-squared between m_3 and $m_{1,2}$. Oscillations have also been searched for in reactor data and the mixing of ν_e in m_3 has been limited to be small, but this number needs to be precisely measured. To a good approximation ν_3 is a mixture of ν_μ and ν_τ, and ν_2 and ν_1 are mixtures of ν_e and the orthogonal mixture of ν_μ and ν_τ.

Many efforts are underway to accurately determine all of the parameters involved in neutrino mixing. The most recent experiments involve creating neutrinos at accelerators

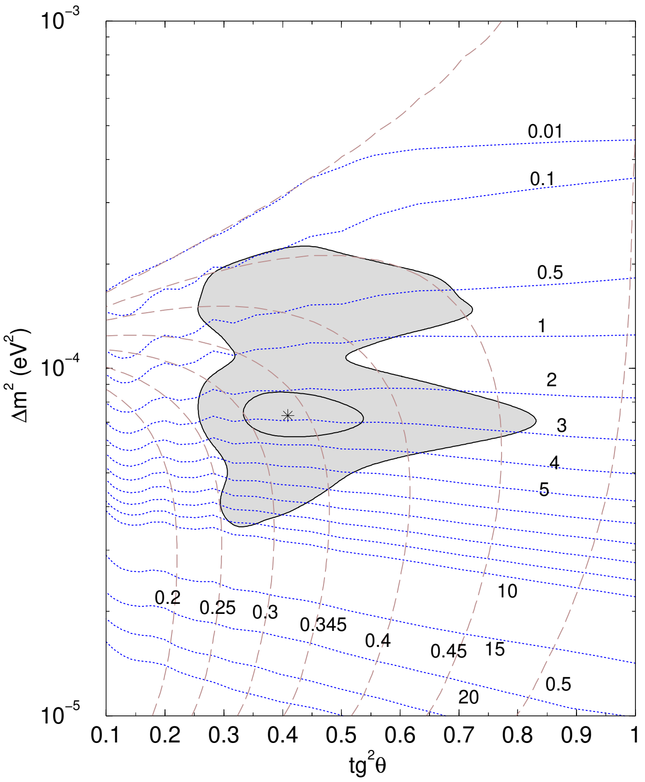

Figure 8.4: Predictions for the CC/NC ratio and the Day-Night asymmetry at SNO, taken from [99]. The dashed lines are lines of constant CC/NC ratio and the dotted blue lines show the percentage of the Day-Night asymmetry. The best fit $(\tan\theta_{12}, \Delta m^2)$ point is indicated by a star.

and detecting them hundreds of kilometers away or detecting neutrinos at locations optimal distances away from nuclear reactor sources. The accelerator experiments, run in an off-axis configuration to obtain a beam with a narrow energy range and small contamination of other neutrino types, are looking for ν_e appearance from a ν_μ beam. The reactor experiments are looking for $\bar{\nu}_e$ disappearance. The accelerator experiments are affected by possible matter oscillations so the information from the two types of experiments are complimentary.

Perhaps the most compelling reason for future neutrino oscillation experiments is that they may be a probe for finding CP-violation in the lepton sector. CP-violation has already been observed amongst the quarks, but not enough to explain the matter-antimatter asymmetry of the Universe. Precise measurements of all neutrino mixing parameters, especially θ_{13}, could lead to a measurement of the CP-violating phase δ which, if non-zero, could give insight into this phenomenon. There is clearly an exciting range of neutrino experiments to be undertaken in the near future.

Appendix A

Decay Chains

The decay chains of ^{232}Th and ^{238}U are displayed on the following pages.

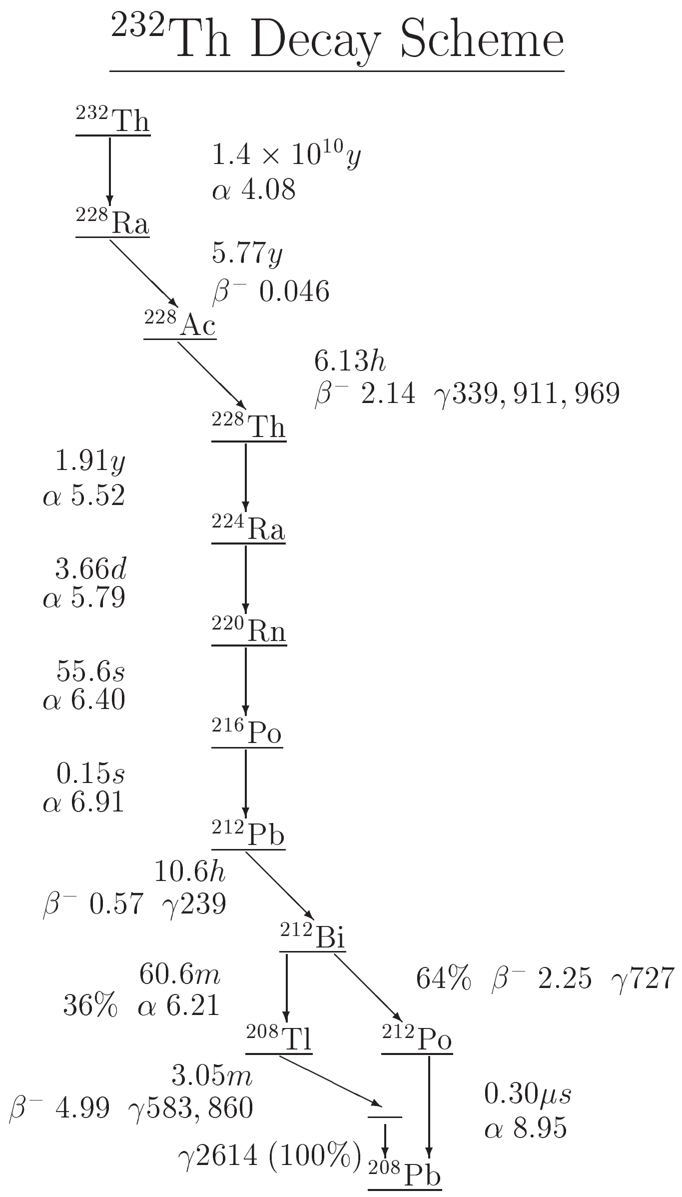

Figure A.1: The decay chain of ^{232}Th. All half-lives are shown, with the Q-values of beta and alpha decays in MeV, and gamma rays in keV. Taken from [78].

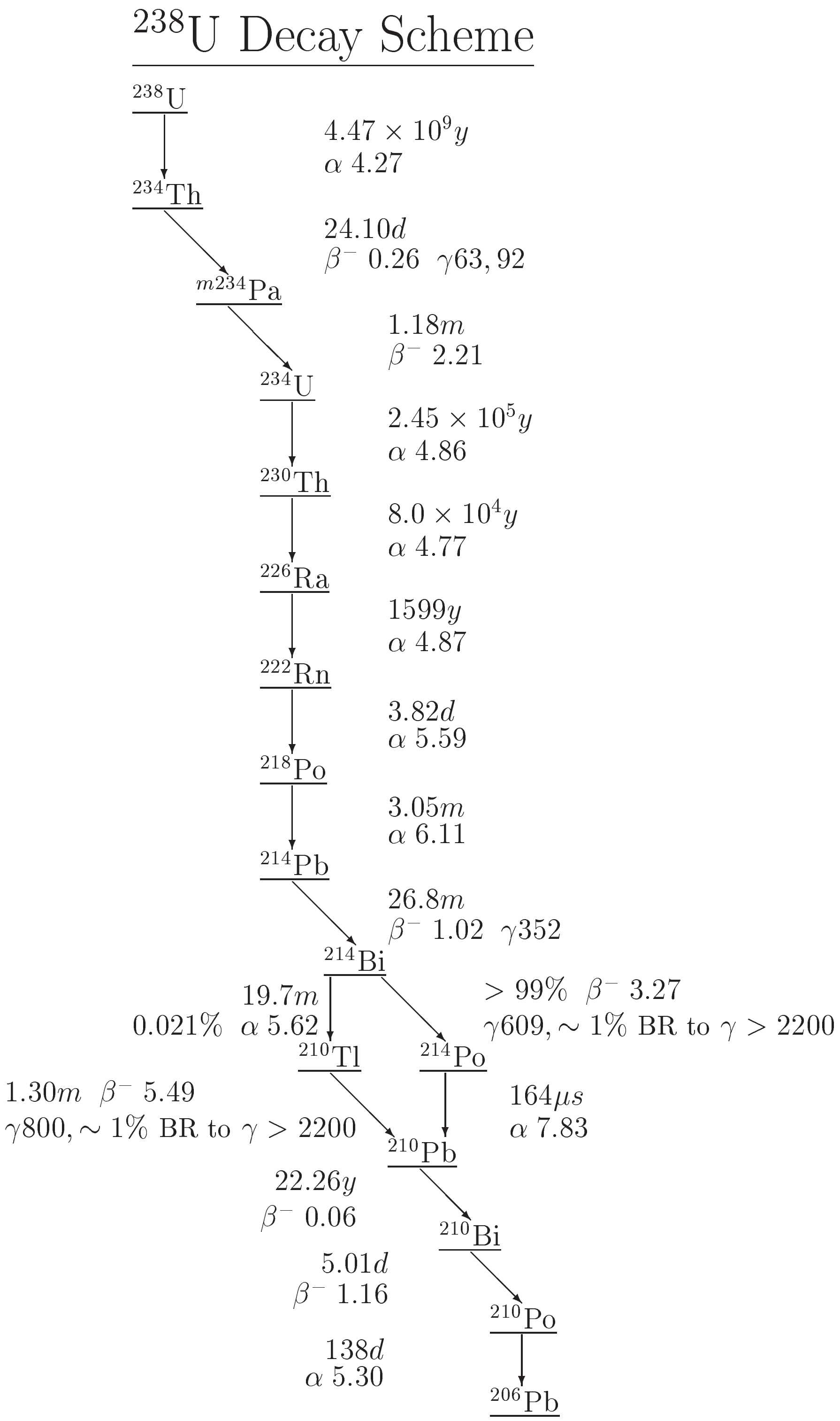

Figure A.2: The decay chain of ^{238}U. All half-lives are shown, with the Q-values of beta and alpha decays in MeV, and gamma rays in keV. Taken from [78].

Appendix B

Statistical Separation Power

A set of data D is comprised of two event types[1]. There is some parameter (such as energy or isotropy) which characterizes each of the two event types. The parameter for each type is described by probability density functions (PDFs) P_1 and P_2, which are known by theory or Monte Carlo. The data contains fractions a_1 and a_2 of the two types, so that

$$D_i \approx a_1 N P_{1i} + a_2 N P_{2i} \equiv N_1 P_{1i} + N_2 P_{2i}, \tag{B.1}$$

where the data and PDFs are histogrammed and P_{1i} and P_{2i} are the probabilities of an event of the corresponding class lying in bin i. D_i is the number of data in bin i, N is the total number of events in the data set and N_1 and N_2 are the total numbers of events belonging to the two event classes. The PDFs are normalized to unity such that $\sum_i P_{1i} = \sum_i P_{2i} = 1$.

The sum of a_1 and a_2 is 1, but the individual values are unknown. The number of events belonging to each event class may be determined using maximum likelihood extraction or χ^2 minimization. In the limit of large statistics, the two methods yield the same result [76].

The χ^2 is defined as

$$\chi^2 = \sum_i \frac{(D_i - N_1 P_{1i} - N_2 P_{2i})^2}{\sigma_i^2}. \tag{B.2}$$

The error for each bin, σ_i, may be estimated as $\sigma_i^2 = \sigma^2(D_i) = D_i$ as long as the contents of the bins have a sufficiently large number of events to allow the use of a Gaussian approximation to the Poisson errors.

The uncertainty on N_k is given by the maximum amount that it can be changed (allowing N_l to vary) to increase $\chi^2(N_k, N_l)$ by 1 from the minimum value at $\chi^2(N_k^{min}, N_l^{min})$ (this is equivalent to decreasing the maximum likelihood by 1/2). The estimation may be determined by expanding the χ^2 in a Taylor series about the minimum value:

[1]The following may be expanded to describe any number of event types.

$$\chi^2(N_k, N_l) = \chi^2(N_k^{min}, N_l^{min}) + \frac{1}{2!}\frac{\partial^2\chi^2(N_k^{min}, N_l^{min})}{\partial N_k \partial N_l}\partial N_k \partial N_l, \tag{B.3}$$

where the first derivatives have been omitted because χ^2 is at a minimum. Thus, the covariance matrix is given by

$$\mathbf{C} = \sigma_{kl}^2 = \partial N_k \partial N_l = \left(\frac{1}{2}\frac{\partial^2\chi^2}{\partial N_k \partial N_l}\right)^{-1}. \tag{B.4}$$

The elements of the inverse covariance matrix $\mathbf{C}^{-1}$ are found by differentiating the χ^2 found in (B.1) and given by

$$C_{kl}^{-1} = (\sigma_{kl}^2)^{-1} = \frac{1}{2}\frac{\partial^2\chi^2}{\partial N_k \partial N_l} = \sum_i \frac{P_{ki}P_{li}}{\sigma_i^2}. \tag{B.5}$$

For the elements of the inverse covariance matrix $\mathbf{C}^{-1}(N_1, N_2)$ we have

$$\begin{aligned} C_{11}^{-1} &= \sum_i \frac{P_{1i}^2}{\sigma_i^2} \approx \frac{P_1 \otimes P_1}{N}, \\ C_{22}^{-1} &\approx \frac{P_2 \otimes P_2}{N}, \\ C_{12}^{-1} &\approx \frac{P_1 \otimes P_2}{N}, \end{aligned} \tag{B.6}$$

where $P_k \otimes P_l$ is defined [75] as the *overlap* of the two PDFs and is given by

$$P_k \otimes P_l = \sum_i \frac{P_{ki}P_{li}}{a_k P_{ki} + a_l P_{li}} \tag{B.7}$$

and

$$P_k^2 \equiv P_k \otimes P_k = \sum_i \frac{P_{ki}^2}{a_k P_{ki} + a_l P_{li}}. \tag{B.8}$$

It is useful to note that

$$\begin{aligned} a_1 P_1^2 &= 1 - a_2 P_1 \otimes P_2, \\ a_2 P_2^2 &= 1 - a_1 P_1 \otimes P_2. \end{aligned} \tag{B.9}$$

From (B.6), the inverse covariance matrix is

$$\mathbf{C}^{-1}(N_1, N_2) = \frac{1}{N}\begin{pmatrix} P_1^2 & P_1 \otimes P_2 \\ P_1 \otimes P_2 & P_2^2 \end{pmatrix}, \tag{B.10}$$

and the covariance matrix is then given by

$$\mathbf{C}(N_1, N2) = \frac{N}{(P_1 \otimes P_1)(P_2 \otimes P_2) - (P_1 \otimes P_2)^2}\begin{pmatrix} P_2^2 & -P_1 \otimes P_2 \\ -P_1 \otimes P_2 & P_1^2 \end{pmatrix}. \tag{B.11}$$

Using the relations found in (B.9) and the condition $a_1 + a_2 = 1$,

$$\mathbf{C}(N_1, N2) = \frac{N}{(1 - P_1 \otimes P_2)} \begin{pmatrix} a_1(1 - a_1 P_1 \otimes P_2) & -a_1 a_2 P_1 \otimes P_1 \\ -a_1 a_2 P_1 \otimes P_1 & a_2(1 - a_2 P_1 \otimes P_2) \end{pmatrix}. \tag{B.12}$$

The errors on N_1 and N_2 are

$$\begin{aligned} \sigma^2_{N_1} &= C_{11} = \frac{a_1 N(1 - a_1 P_1 \otimes P_2)}{1 - P_1 \otimes P_2}, \\ \sigma^2_{N_2} &= C_{22} = \frac{a_2 N(1 - a_2 P_1 \otimes P_2)}{1 - P_1 \otimes P_2}. \end{aligned} \tag{B.13}$$

The *separability* is defined as $\mathcal{S} = (1 - P_1 \otimes P_2)$. A value of $\mathcal{S} = 0$ means that the PDFs completely overlap; a value of $\mathcal{S} = 1$ means that they are completely distinguishable and event-by-event separation may be achieved. This measure is used in Chapter 3 to determine the statistical separation power of various isotropy PDFs.

Appendix C

Legendre Polynomials

The first six Legendre polynomials are as follows:

$$\begin{aligned}
P_0(\cos\theta) &= 1 \\
P_1(\cos\theta) &= \cos\theta \\
P_2(\cos\theta) &= \frac{1}{4}(1 + 3\cos 2\theta) \\
P_3(\cos\theta) &= \frac{1}{8}(3\cos\theta + 5\cos 3\theta) \\
P_4(\cos\theta) &= \frac{1}{64}(9 + 20\cos 2\theta + 35\cos 4\theta) \\
P_5(\cos\theta) &= \frac{1}{128}(30 + 20\cos\theta + 35\cos 3\theta + 63\cos 5\theta)
\end{aligned} \tag{C.1}$$

These are pictured in Figure 3.7.

Any azimuthally symmetric angular distribution $f(\cos\theta)$ may be expanded in terms of the infinite set of Legendre polynomials:

$$f(\cos\theta) = \sum_l^\infty C_l P_l(\cos\theta). \tag{C.2}$$

To get the expansion coefficients, C_l, multiply both sides by $P_k(\cos\theta)$ and integrate over the range (-1,1),

$$\int_{-1}^{1} P_k(\cos\theta) f(\cos\theta)\ d\cos\theta = \sum_l^\infty C_l \int_{-1}^{1} P_k(\cos\theta) P_l(\cos\theta)\ d\cos\theta. \tag{C.3}$$

Using the orthonormality condition for Legendre polynomials, we have

$$\int_{-1}^{1} P_k(\cos\theta) f(\cos\theta)\ d\cos\theta = \sum_l^\infty C_l \left(\frac{2}{2l+1}\right) \delta_{lk}, \tag{C.4}$$

and

$$C_l = \left(\frac{2l+1}{2}\right)\int_{-1}^{1} P_l(\cos\theta) f(\cos\theta) d\cos\theta. \tag{C.5}$$

For a discrete set of N PMT hits, the above integral is simply the average value of $P_l(\cos\theta)$,

$$C_l = \left(\frac{2l+1}{2N}\right)\sum_{i=1}^{N} P_l(\cos\theta). \tag{C.6}$$

A nice example of this expansion is to take a large number of CC and NC events and to expand the distribution of the cosines of the angles between all pairs of PMT hits for each event, $\cos\theta_{ij}$, using the Legendre Polynomial Parameters. Recall Equation 3.15,

$$\beta_l = \frac{2}{N(N-1)}\left[\sum_{i=1}^{N-1}\sum_{j=i+1}^{N} P_l(\cos\theta_{ij})\right], \tag{C.7}$$

which is essentially $\frac{2}{2l+1}C_l$ (but $\frac{N(N-1)}{2}$, rather than N, is the total number of angles). The expansion coefficients for each event are given by

$$C_l = \left(\frac{2l+1}{2}\right)\beta_l. \tag{C.8}$$

For a large number of CC and NC events, the average of the β_l values (obtained through Monte Carlo) were taken as the expansion coefficients, so that the angular distributions could be described by

$$f(\cos\ \theta) = \sum_{l=0}^{5}\left(\frac{2l+1}{2}\right)\langle\beta_l\rangle P_l(\cos\ \theta). \tag{C.9}$$

Only the first five Legendre polynomials were used because only β_1 through β_5 were calculated in the Monte Carlo. The results are shown in Figure C.1 and may be compared with Figure C.2 (also shown in Figure 3.8). Including higher order Legendre polynomials would likely flatten out the distribution near $\cos\theta_{ij}$=-1 and create a sharper peak near $\cos\theta_{ij}$=+1, but one can see that essentially all the information of the distributions and their differences is calculated with the first five β parameters.

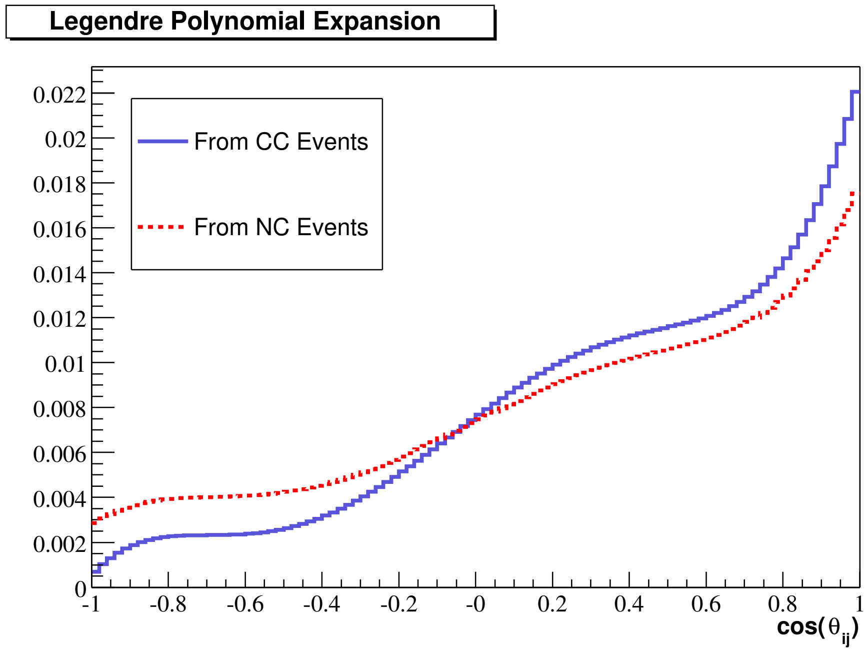

Figure C.1: Legendre Polynomial expansion of $\cos\theta_{ij}$ values for CC and NC events.

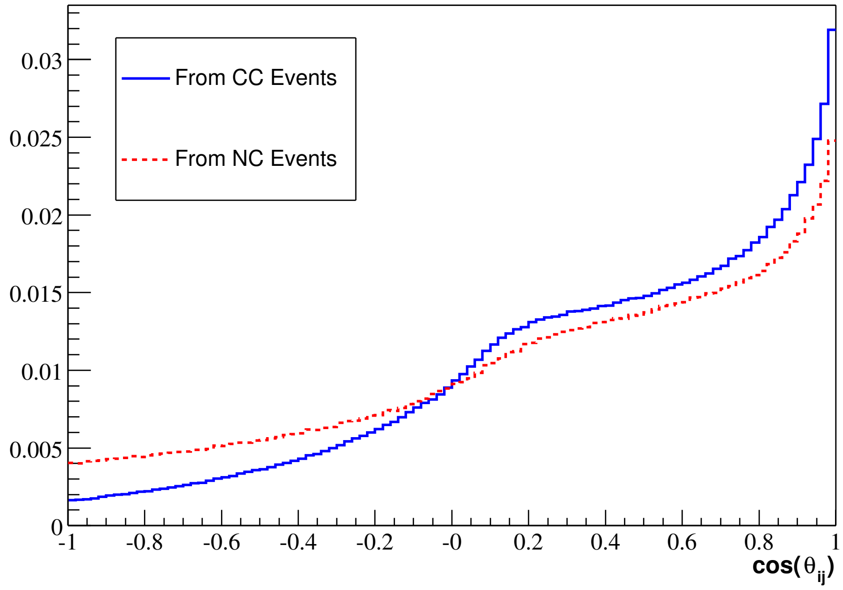

Figure C.2: Distribution of $\cos\theta_{ij}$ values from Monte Carlo simulated CC and NC events.

Appendix D

Correction to EGS4 AUSGAB Code

`AUSGAB` [56] is a user-written routine called by EGS4 subroutines to keep track (score) of transported particle (electron or photon) properties (such as energy) and output results. The AUSGAB routine utilized in SNOMAN does a "scoring" before and after each step to determine whether a particle will move on, be discarded (this might happen if the particle falls below some energy cutoff) or produce some calculated amount of Čerenkov light. It also scores the energy deposited by the particle in various regions of the SNO detector. This routine is called after an electron undergoes various types of interaction including

- A standard multiple scattering step
- Møller (e^-e^-) scattering
- Bhabha (e^+e^-) scattering
- Positron-electron annihilation at rest
- Bremsstrahlung radiation

and also after various photon interactions. It is within the SNOMAN `AUSGAB` routine that Čerenkov light vertices are produced.

The `egs4_ausgab.for` program (written by S. Biller) has been modified to call a subroutine `egs4_mott_corr.for` which makes the correction to the EGS4 electron multiple scattering angles. The program `egs4_ausgab.for` calls `egs4_ausgab1.for` which is where the scoring and Čerenkov light production are actually done. Before this subroutine is called, the multiple scattering angles are altered. The codes `egs4_ausgab.for` and `egs4_mott_corr.for` are found on the following pages.

```
      SUBROUTINE EGS4_AUSGAB(Iarg)
*     SNOMAN: Frontend routine to EGS4 scoring, datastructure handling
*             and Cerenkov production.

      IMPLICIT NONE
      INCLUDE 'constants.inc'
      INCLUDE 'egs4_params.inc'
      INCLUDE 'egs4_sno.inc'
      INCLUDE 'egs4_stack.inc'
      INCLUDE 'egs4_physics.inc'
      INTEGER Iarg

*     Save current stack number
      NP_EGS4_OLD=NP_EGS4

*     Return if photoelectric or Rayleigh is about to happen
      IF(IARG.EQ.19.OR.IARG.EQ.23) RETURN
```

Applies Mott correction only if the particle has a charge of -1.

```
*     Correction for missing Mott term in scattering cross section.
*     Apply only after multiple scattering and if particle is electron.
      IF(IARG.EQ.0.AND.IQegs4(NP_egs4).EQ.-1.AND.MOTT.EQ.1)THEN
        CALL EGS4_MOTT_CORR()
      ENDIF
```

Corrected angles are then passed into `EGS4_AUSGAB1`.

```
*     Do scoring, cerenkov production etc.
      CALL EGS4_AUSGAB1(IARG)

*     If the EGS4 data structure logging is on, go to it.....
      IF(LEGS_DS)THEN
        IF(LAUSFL_MASK(IARG+1))THEN
          CALL EGS4_DSLOG(IARG)
        ENDIF
      ENDIF
      RETURN
      END
*ENDFILE MEMBER=EGS4_AUSGAB
```

```
      SUBROUTINE EGS4_MOTT_CORR()
*     SNOMAN: Corrects resultant angle from multiple scattering to account
*             for Mott term missing in the scattering cross section.

      IMPLICIT NONE

      INCLUDE 'constants.inc'
      INCLUDE 'egs4_params.inc'
      INCLUDE 'egs4_sno.inc'
      INCLUDE 'egs4_stack.inc'
      INCLUDE 'egs4_physics.inc'

*     Local Variable Declarations:-
*     ===========================
      REAL cthet, KEegs
      INTEGER lcthet , ltheta
```

Convert to kinetic energy.

```
      KEegs = EEGs4(NP_egs4) - 0.511
```

MOTTscale is set to 1.1 in the titles file `egs4.dat`. This correction is the same as found in Equation 4.8.

```
      THETA_egs4 = THETA_egs4 - MOTTscale*
     & 0.28*(1-exp(-KEegs/(KEegs+0.19)))*
     & ((PI-THETA_egs4)**(0.78*KEegs**-0.25))*(THETA_egs4**2.2)*
     & (1.0-1.1*exp(-1*THETA_egs4/(THETA_egs4+0.58*KEegs**-0.75)))

      ltheta     = SINc1*THETA_egs4 + SINc0
      SINTHE     = SIN1(ltheta)*THETA_egs4 + SIN0(ltheta)
      cthet      = PI5d2 - THETA_egs4
      lcthet     = SINc1*cthet + SINc0
      COSTHE     = SIN1(lcthet)*cthet + SIN0(lcthet)

      RETURN
      END
*ENDFILE MEMBER=EGS4_MOTT_CORR
```

Appendix E

Event Rate (HCA) Calibration

The rate at which events are read out from a cell in a channel affects the calibration of that channel. As the time since the channel was last read out increases, the fully ECA[1] calibrated times get later [77].

The HCA (for History CAlibrator)[2] applies a correction to ECA calibrated PMT times of low rate data to give an ECA calibrated time that would be consistent with high rate data. The rate of neutrino data is approximately 20 Hz, while ^{16}N calibration data occurs at about 150 Hz.

The size of the HCA correction is largely dependent on the temperature of the electronics. To cool the electronics, the current sources used to fine tune the TAC slopes were turned off and there was a fan upgrade in December 2000. Therefore, it was expected that the HCA correction would be less for data since this time. Collection of data from the salted D_2O phase of the experiment began in June 2001, so the analysis of this data might not require the HCA correction.

PMT timing resolution is approximately 1.5 ns, so unless the HCA correction is considerably greater than this, it is not a necessary calibration. Since the HCA correction involves collecting data from dedicated pedestal runs and an extra step in data processing, the following study was performed to determine if this correction is significant enough to maintain.

E.1 HCA Studies

Neutrino runs in pure D_2O and neutrino and low-rate ^{16}N ($\sim$12 Hz) runs in salted D_2O were processed both with and without the HCA correction applied. The amount by which the ECA calibrated PMT time is altered by the HCA correction is displayed in

[1] ECA stands for Electronic CAlibration and encompasses the pedestal and time slopes corrections discussed in Section 2.8.1.

[2] For more information on the history and creation of the HCA correction, see G. McGregor's thesis [77]

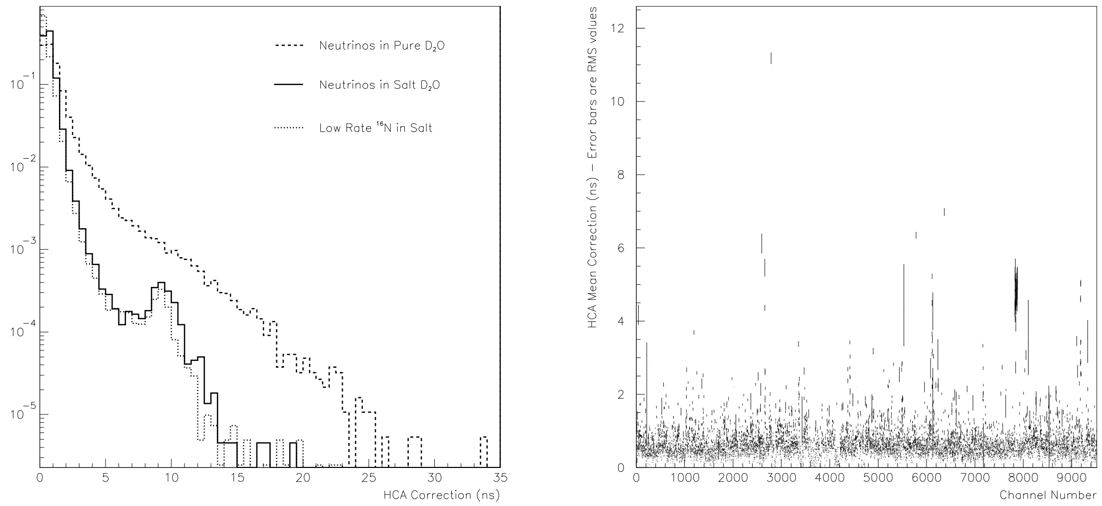

(a) (b)

Figure E.1: (a) HCA correction in ns for each hit in an event. Shown for early neutrino data in the pure D_2O phase and neutrino and low rate ^{16}N data in salt D_2O. (b) The mean value of the HCA correction is plotted for each channel and the error bars show the RMS values.

Figure E.1(a). Note that the width of the HCA correction for salt data is considerably less than that for pure D_2O data, however, there is a tail out to about 20 ns. There is also a peculiar bump around 10 ns in the salt distributions. This bump may be attributed to particular channels as displayed in Figure E.2. Figure E.1(b) shows a profile plot of the mean HCA correction for each channel. The error bars are RMS values.

Figure E.3 shows the HCA correction for neutrinos in salt D_2O for both the particular channels giving high HCA correction, highlighted in Figure E.2 (referred to as “bad channels”), and the distribution without those channels. From these plots, it is clear that the tail in the HCA correction comes entirely from these few channels. It is unknown whether the HCA correction is being calculated correctly for these channels or if an already unreliable time measurement is just randomly being altered.

E.2 Effects on Neutrino Analysis

Timing Resolution

Figure E.4 shows the time-of-flight (TOF) corrected PMT time for a central low-rate ^{16}N run and a neutrino run taken in the salt phase with and without the HCA correction

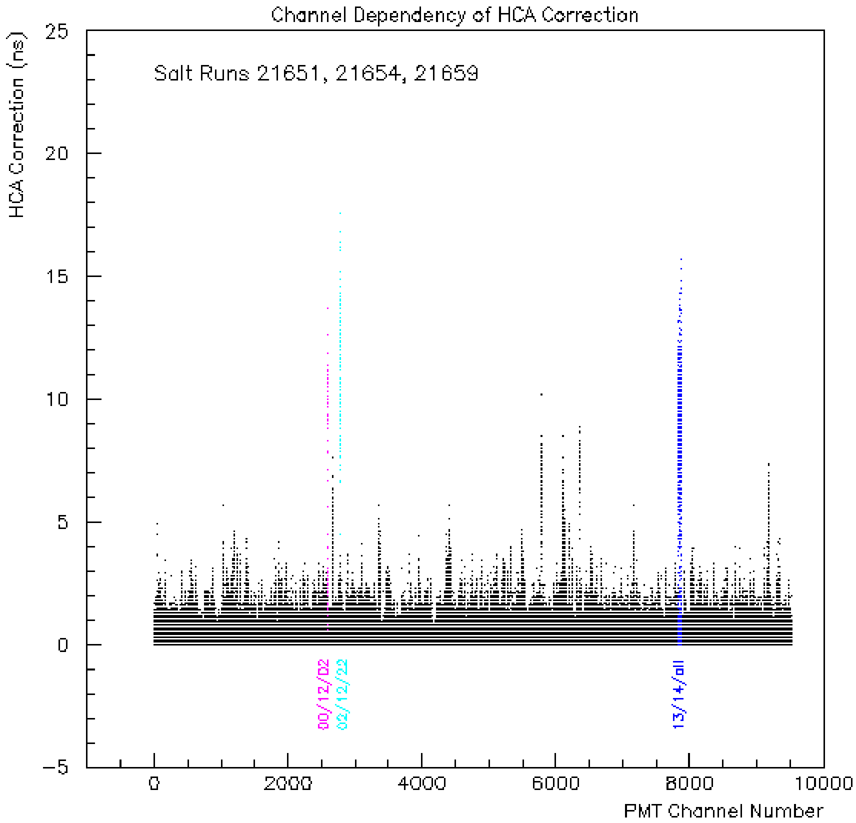

Figure E.2: Channel dependency of HCA Correction.

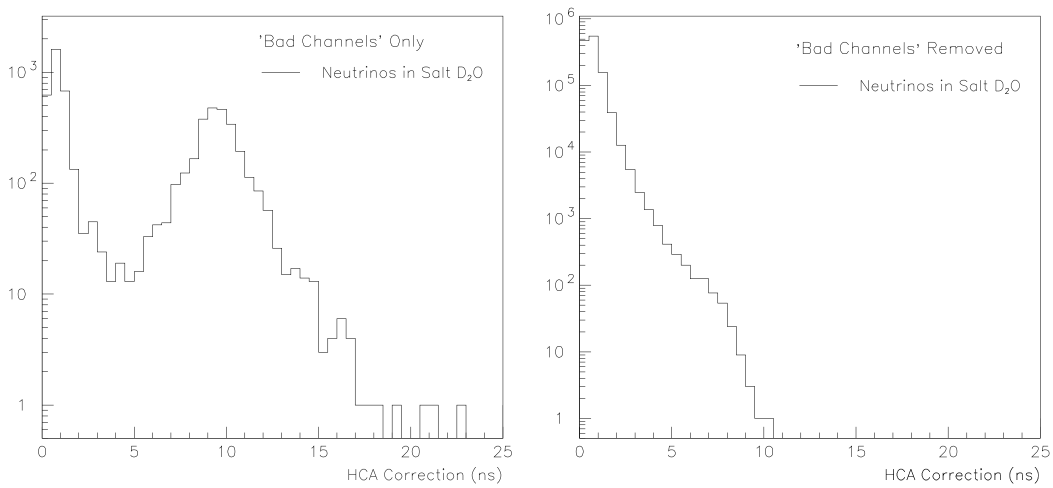

Figure E.3: Left-hand plot shows the HCA Correction for "bad channels" highlighted in Figure E.2. Right hand plot shows HCA correction for neutrino data in salt with the "bad channels" removed.

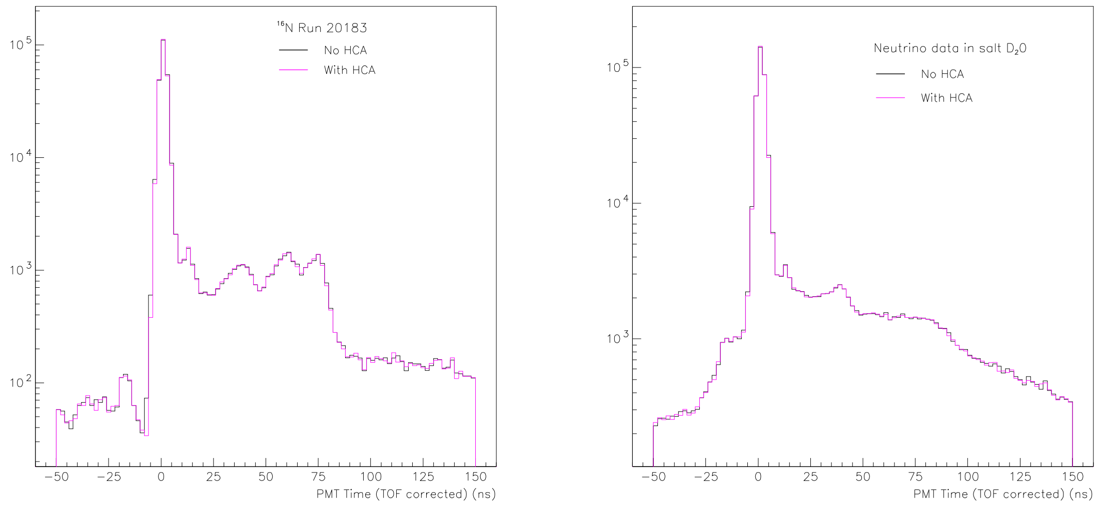

(a) Low rate ^{16}N data.

(b) Neutrino data.

Figure E.4: TOF-corrected PMT time for low-rate ^{16}N and neutrino data in salted D_2O with (pink) and without (black) HCA correction.

applied.

TOF-corrected PMT time is defined in the same way as the timing residual defined in Chapter 2,

$$t^i_{TOF} = (t_i - t_{fit}) - \frac{d}{c}, \tag{E.1}$$

where d is the distance between the fit vertex and the PMT position. Distributions of average TOF-corrected PMT times for individual events are found in Figure E.5 for both pure D_2O and salt neutrino data. It is apparent that there is much less of an effect on the time residuals when HCA is applied in salt data.

Vertex Shift

Low rate ^{16}N runs were studied to find out if the HCA correction has a large effect on vertex reconstruction. In G. McGregor's thesis [77], it is shown that the HCA corrects for an inward shift seen in low rate ^{16}N data. This shift was as large as about 18 cm at R=± 600 cm, and was reduced to 10 cm or less with the application of HCA. Figure E.6 shows the reconstructed z-position for central run 20183 for data with and without the HCA correction. Figure E.7 shows the difference between the mean fit position and source position for runs in different positions of the detector. This plot shows that the HCA correction is not helping to improve this difference.

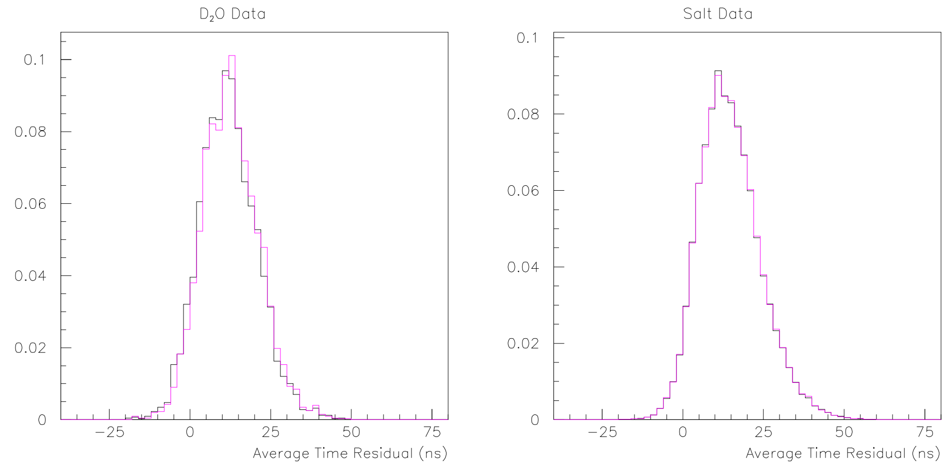

Figure E.5: Average time residuals with (pink) and without (black) HCA correction for pure (left) and salted (right) D_2O.

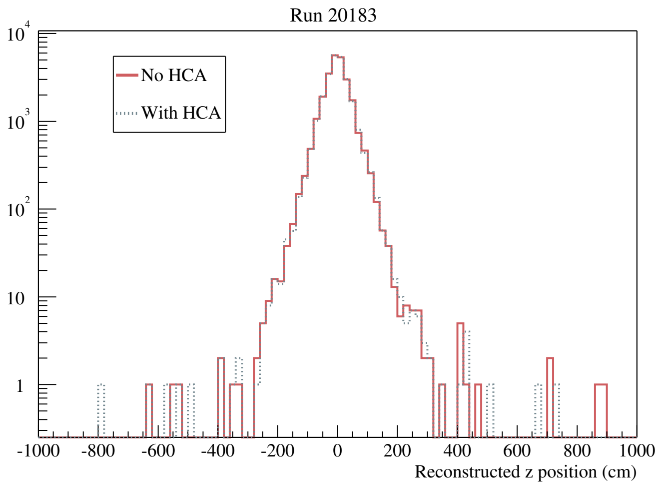

Figure E.6: Reconstructed z-position of low rate ^{16}N Run 20183.

E.3 Discontinuation of HCA Correction

As expected, the HCA correction to the data is less since actions were made to cool the electronics. A correction still exists, but one that seems to only be particularly significant for the problem channels displayed in Figure E.2. This, however, does not appear to have a significant effect on the analysis of neutrino data in salt. Timing distributions do not appear to differ when the HCA correction is applied to salt data. Applying HCA does not improve the vertex reconstruction of ^{16}N data. Because the HCA correction is not improving this systematic, it is unnecessary to maintain this correction. The HCA correction is not included in the analysis of data from the salted D_2O phase.

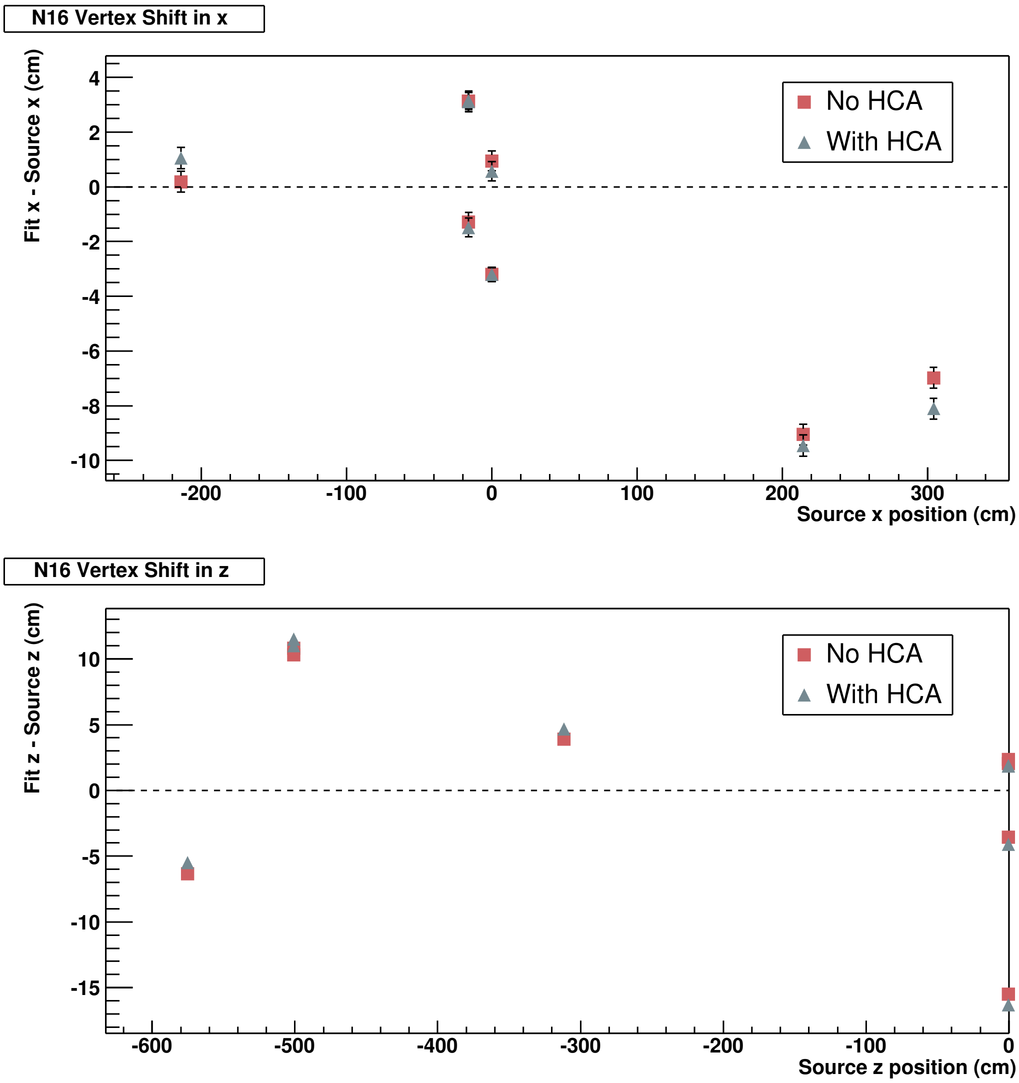

Figure E.7: Mean shift in reconstructed position of low rate ^{16}N runs. Note that the two plots contain data from the the same runs.

Bibliography

[1] The SNO Collaboration, *Measurement of the Total Active ^8B Solar Neutrino Flux at the Sudbury Neutrino Observatory with Enhanced Neutral Current Sensitivity*, Phys. Rev. Lett. **92**, 181301 (2004).

[2] W. Pauli in a letter to the Physical Institute of the Federal Institute of Technology in Zürich, Physics Today (1978).

[3] An excellent description of the neutrino is given in *Celebrating the Neutrino*, Los Alamos Science, Number 25, Los Alamos National Laboratory (1997).

[4] C.S. Wu, *et al.*, Phys. Rev. **105**, 1413 (1957).

[5] R.P. Feynman, M. Gell-Mann, Phys. Rev. **109**, 193 (1958).

[6] F. Reines and C.L. Cowen, Jr., *The Neutrino*, Nature (1956).

[7] M. Apollonio, *Limits on neutrino oscillations from the CHOOZ experiment*, Phys. Lett. B **466**, 415 (1999).

[8] K. Eguchi *et al.*, *First Results from KamLAND: Evidence for Reactor Antineutrino Disappearance*, Phys. Rev. Lett. **90**, 021802 (2003).

[9] K. Hagiwara *et al.*, Phys. Rev. D **66**, 010001 (2002). http://pdg.lbl.gov/2003/

[10] F. Halzen and A. Martin, *Quarks & Leptons: An Introductory Course in Modern Particle Physics*, John Wiley & Sons, Inc. (1984).

[11] J.N. Bahcall, *How Uncertain are Solar Neutrino Predictions?*, Phys. Rev. B **433**, 1 (1998).

[12] J.N. Bahcall, *Nuclear Astrophysics*, Cambridge University Press, Cambridge (1988).

[13] J.N Bahcall and M. Pinsonneault, *What do we (not) know about solar neutrino fluxes?*, arXiv:astro-ph/0402114v1 (2004).

[14] J.N Bahcall and M. Pinsonneault, *Solar models with helium and heavy-element diffusion*, Rev. Mod. Phys. **67**, 781 (1995).

[15] J.N Bahcall, M.H. Pinsonneault, and S. Basu, *Solar Models: Current Epoch and Time Dependences, Neutrinos, and Helioseismological Properties*, Astrophys. J. **555**, 990 (2001).

[16] B.T. Cleveland *et al.*, *Measurement of the solar electron neutrino flux with the Homestake chlorine detector*, Astrophys. J. **496**, 505 (1998).

[17] J.N. Bahcall and C. Pena-Garay, *A road map to solar neutrino fluxes, neutrino oscillation parameters, and tests for new physics*, arXiv:hep-ph/03/05/159v2 (2003).

[18] V.N. Gribov and B. Pontecorvo, *Neutrino Astronomy and Lepton Charge*, Phys. Lett. **B28**, 493 (1969).

[19] B. Kayser, Phys. Rev. D **24**, 110 (1981).

[20] L. Wolfenstein, *Neutrino Oscillations in Matter*, Phys. Rev. **D** (1978) 2369; S.P. Mikheyev and A.Y. Smirnov, *Resonance enhancement of oscillations in matter and solar neutrino spectroscopy*, Sov. Jour. Nucl. Phys. **42**, 913 (1985).

[21] S.P. Rosen and J.M. Gelb, *Mikheyev-Smirnov-Wolfenstein enhancement of oscillations as a possible solution to the solar-neutrino problem*, Phys. Rev. **D34**, 969 (1986).

[22] V. Barger, R.J.N. Phillips, and K. Whisnant, *Level crossings in solar-neutrino oscillations*, Phys. Rev. **D34**, 980 (1986).

[23] A. Yu. Smirnov, *The MSW effect and Solar Neutrinos*, from the 11^{th} workshop on Neutrino Telescopes, Venice, arXiv:hep-ph/0305106 (2003).

[24] H.A. Bethe, *Possible explanation of the solar-neutrino puzzle*, Phys. Rev. Lett. **56**, 1305 (1986).

[25] J.N. Bahcall, *How the Sun Shines*, `http://www.nobel.se/` (2000).

[26] The SNO Collaboration, *Direct Evidence for Neutrino Flavor Transformation from Neutral-Current Interactions in the Sudbury Neutrino Observatory*, Phys. Rev. Lett. **89**, 011301 (2002).

[27] The SNO Collaboration, *Measurement of the Day and Night Neutrino Energy Spectra at SNO and Constraints on Neutrino Mixing Parameters*, Phys. Rev. Lett. **89**, 011302 (2002).

[28] S.J. Parke, *Nonadiabatic level crossing in resonant neutrino oscillations*, Phys. Rev. Lett. **57**, 1275 (1986).

[29] S.T. Petcov and S. Toshev, *Three neutrino oscillations in matter: analytical results in the adiabatic approximation* , Phys. Lett. B **187**, 120 (1987).

[30] G.L. Fogli *et al.*, *Three-flavor solar neutrino oscillations with terrestrial neutrino constraints*, Phys. Rev. D **66**, 093008 (2002).

[31] The Super-Kamiokande Collaboration, *Evidence for oscillation of atmospheric neutrinos*, Phys. Rev. Lett. **81**, 1562 (1998).

[32] The Super-Kamiokande Collaboration, *Tau neutrino favored over sterile neutrinos in atmospheric muon neutrino oscillations*, Phys. Rev. Lett. **85**, 3999 (2000).

[33] The MINOS Collaboration, *MINOS Technical Design Report* (1998). `http://www.hep.anl.gov/ndk/hypertext/minos_tdr.html`

[34] The K2K Collaboration, M.H. Ahn *et al.*, *Indications of Neutrino Oscillation in a 250 km Long-baseline Experiment*, Phys. Rev. Lett. **90**, 041801 (2003).

[35] *Letter of Intent: Neutrino Oscillation experiment at JHF* (2003).

[36] M.H. Shaevitz, J.M. Link, *Using Reactors to Measure* θ_{13}, arXiv:hep-ex/0306031 (2003).

[37] The LSND Collaboration, *Evidence for Neutrino Oscillations from the Observation of Electron Anti-neutrinos in a Muon Anti-Neutrino Beam* Phys. Rev. D **64**, 112007 (2001).

[38] The KARMEN Collaboration, *Upper limits for neutrino oscillations* $\bar{\nu}_\mu \to \bar{\nu}_e$ *from muon decay at rest*, Phys. Rev. D **65**, 112001 (2002).

[39] K. Zuber, *Neutrino Physics*, IoP Publishing, London (2004).

[40] S.A. Bludman, D.C. Kennedy, and P.G. Langacker, *Seesaw model solutions of the solar neutrino problem*, Nucl. Phys. B **374**, 373 (1992).

[41] R.N. Mohapatra, *Theories of Neutrino Masses and Mixings*, arXiv:hep-ph/9910365 (1999).

[42] Y. F. Wang *et al.*, *Probing neutrino oscillations jointly in long and very long baseline experiments*, Phys. Rev. D **65**, 073021 (2002); A. Asratyan *et al.*, *Neutrino Superbeams and the Magic Baseline*, arXiv:hep-ex/0303023 (2003).

[43] J.V. Jelley, *Čerenkov Radiation and its applications*, Pergamon Press, London (1958).

[44] The SNO Collaboration, *The Sudbury Neutrino Observatory*, Nucl. Instr. and Meth. **A449**, 172 (2000).

[45] F. Duncan *et al.*, *SNO Detector Operator Manual, Ver. 0.96* (2002).

[46] P. Vogel and J. Beacom, *The angular distribution of neutron inverse beta decay, $\bar{\nu}_e + p \rightarrow e^+ + n$*, Phys. Rev. D **60**, 053003 (1999).

[47] The SNO Collaboration, *Measurement of the charged current interactions produced by ^8B solar neutrinos at the Sudbury Neutrino Observatory*, Phys. Rev. Lett. **87**, 071301 (2001).

[48] G. t'Hooft, *Prediction for Neutrino-Electron Cross-Sections in Weinberg's Model of Weak Interactions*, Phys. Lett. B **37**, 195 (1971).

[49] J. Schechter and J.W.F. Valle, *Majorana neutrinos and magnetic fields*, Phys. Rev. D **24**, 1883 (1981).

[50] The SNO Collaboration, *Solar Electron Antineutrino Search at the Sudbury Neutrino Observatory*, to be submitted shortly (2004).

[51] N.K. McCauley, *Producing a Background Free Data Set for Measurement of the Charged Current Flux and Day-Night Asymmetry at the Sudbury Neutrino Observatory.* D.Phil. Thesis, University of Oxford (2001).

[52] M. Dunford *et al.*, *Updates to Data Cleaning for the Salt Phase, Version 1.2*, SNO analysis note (2004).

[53] Private communication with Nick Jelley and Neil McCauley.

[54] The SNO Collaboration, *The SNOMAN Companion.* Available with the latest SNOMAN release.

[55] *The ZEBRA System*, CERN Program Library Long Writeups Q100/Q101, CERN, Geneva (1995). `http://wwwinfo.cern.ch/asdoc/zebra_html3/zebramain.html`

[56] W.R. Nelson *et al.*, *The EGS4 Code System*, SLAC-Report-265 (1985).

[57] *MCNP, A Monte Carlo N-Particle Transport Code System, version 4C*, Los Alamos National Laboratory (1993). `http://www-xdiv.lanl.gov/XCI/PROJECTS/MCNP/`

[58] J.R. Wilson, M.G. Bowler, and S. Biller, *Analytical Calculation of the Energy Scaling in the SNO Detector*, SNO Analysis Report (2001).

[59] M.G. Boulay, *Direct Evidence for Weak Flavour Mixing with the Sudbury Neutrino Observatory*, PhD. Thesis, Queen's University (2001).

[60] M. Moorehead, *Grid Fitter for Reducing Tails in Spatial Distributions*, SNO-STR-95-042 (1995).

[61] X. Chen, *An Improved Grid Fitter*, SNO-STR-00-004 (2000).

[62] M. Neubauer, *'Evidence for Electron Neutrino Flavor Change Through Measurement of the ^{8}B Solar Neutrino Flux at the Sudbury Neutrino Observatory*, PhD Thesis, University of Pennsylvania (2001).

[63] F. James, *MINUIT Function Minimization and Error Analysis Reference Manual*, Version 94.1, CERN Program Library Long Writeup D506, CERN, Geneva (1998).

[64] J.R.N. Cameron, *The Photomultiplier Tube Calibration of the Sudbury Neutrino Observatory*, D.Phil. Thesis, Oxford University (2001).

[65] J. Wilson, *Laserball Mask Analysis*, SNO analysis note (2003).

[66] M.R. Dragowsky *et al.*, *Measurement of the ^{252}Cf Acrylic Source Standard*, SNO-STR-2001-009 (2001).

[67] M. Kos, *Neutron Capture Efficiencies with Systematics at Various Cf Positions in Salt*, SNO analysis note (2002).

[68] T.C. Anderson *et al.*, *A radium assay technique using hydrous titanium oxide absorbent for the Sudbury Neutrino Observatory*, Nucl. Instrum. Meth. A501, 386 (2003).

[69] T.C. Anderson *et al.*, *Measurement of radium concentration in water with Mn-coated beads at the Sudbury Neutrino Observatory*, Nucl. Instr. and Meth. A501, 399 (2003).

[70] Private communication, C. Sims.

[71] B. Krusche *et al.*, *Gamma Ray Energies and ^{36}Cl Level Scheme From the Reaction $^{35}Cl(n,\gamma)$*, Nuclear Physics **A386**, 245 (1982).

[72] A. Marino, *Studies on the Separation of Signals in Salt by Isotropy Patterns*, SNO analysis note (2002).

[73] W. Heintzelman, *CC/NC Separation Using Angular Information*, SNO-STR-2002-004 (2002).

[74] W. Heintzelman, *Use of Angular Correlation Function to Identify Background SNO Events*, SNO-STR-2000-031 (2001).

[75] M. Thorman, D.Phil. Thesis, not yet submitted.

[76] P. Bevington and D. Robinson, *Data Reduction and Analysis for the Physical Sciences*, 2^{nd} Ed., McGraw-Hill (1992).

[77] G. McGregor, *The Measurement of the Neutral Current Interaction at the Sudbury Neutrino Observatory*, D.Phil. Thesis, Oxford University (2002).

[78] Xin Chen, *Monte Carlo Simulations and Analysis of Backgrounds in the Sudbury Neutrino Observatory*, DPhil. Thesis, Oxford University (1997).

[79] S.J. Brice, *Monte Carlo and Analysis Techniques for the Sudbury Neutrino Observatory*, D.Phil. Thesis, University of Oxford (1996).

[80] H.A. Bethe, *Molière's Theory of Multiple Scattering*, Phys. Rev. **89**, 1256 (1953).

[81] N.F. Mott, *Scattering of Fast Electrons by Atomic Nuclei*, Proc. Roy. Soc. **A 124**, 425 (1929).

[82] W.A. McKinley and H. Feshbach, Phys. Rev. **74**, 1759 (1948).

[83] I. Kawrakow and D.W.O. Rogers, *The EGSnrc Code System: Monte Carlo simulation of electron and photon transport*, Technical Report PIRS-701, National Research Council of Canada, Ottawa, Canada (2000).

[84] M.G. Bowler and M.D. Lay, Nucl. Instr. and Meth. **A378**, 468 (1996).

[85] M.G. Bowler, N.A. Jelley, and S. West, *The effect of the Mott cross section terms on the distribution of Cherenkov light from electrons multiply scattered in water*, SNO Internal Report (2002).

[86] J.A. Dunmore, N.A. Jelley, and S. West, *Correction to SNOMAN to account for missing Mott terms and approximations used in the EGS4 treatment of multiple scattering*, SNO analysis note (2003).

[87] Many thanks to Dave Rogers for running the EGSnrc code.

[88] J.R. Wilson, D.Phil. Thesis, to be submitted shortly.

[89] The SNO Collaboration, Long write-up of D_2O results.

[90] P.K. Sinervo, *Definition and Treatment of Systematic Uncertainties in High Energy Physics and Astrophysics*, PHYSTAT2003, SLAC (2003).

[91] N. Tagg, *The ^{8}Li Calibration Source and Through-Going Muon Analysis in the Sudbury Neutrino Observatory*, PhD. Thesis, University of Guelph (2001).

[92] V. Rusu, *Measurement of the Total ^{8}B Solar Neutrino Flux at the Sudbury Neutrino Observatory*, PhD. Thesis, University of Pennsylvania (2003).

[93] G. Cowan *Statistical Data Analysis*, Clarendon Press, Oxford (1998).

[94] S. Nakamura *et al.*, *Neutrino reactions on the deuteron*, Phys. Rev. C **63**, 034617 (2001); M. Butler *et al.*, *Neutrino-deuteron scattering in effective field theory at next-to-next-to-leading order*, Phys. Rev. C **63**, 035501 (2001); A. Kurylov, M.J. Ramsey-Musolf, and P. Vogel, Phys. Rev. C **65**, 05501 (2002). J.N. Bahcall *et al.*, *Solar neutrinos: Radiative corrections in neutrino-electron scattering experiments*, Phys. Rev. D **51**, 6146 (1995).

[95] The SNO Collaboration, *CC Unidoc* (2000).

[96] K. Miknaitis and S. Oser, *Livetime for the Full Salt Data Set*, SNO analysis note (2003); K. Graham *et al.*, *Final Run List for NSP*, SNO analysis note (2004).

[97] The SNO Collaboration Salt Flux Working Group, *SNO Salt Phase Neutrino Flux Analysis*, Draft version 0.5 (2003).

[98] Private communication, Hok Wan Chan Tseung.

[99] P.C. de Holanda and A.Yu. Smirnov, *LMA MSW solution of the solar neutrino problem and first KamLAND results*, JCAP 0302, 001 (2003).